Dynamic dewetting of surfactant solutions

Dynamische Entnetzung von Tensidlösungen

Am Fachbereich Maschinenbau
an der Technischen Universität Darmstadt
zur
Erlangung des Grades eines Doktor-Ingenieurs (Dr.-Ing.)
genehmigte

DISSERTATION

vorgelegt von
Franziska Monika Henrich aus Ludwigshafen am Rhein

1. Gutachter: Prof. Dr. Steffen Hardt
2. Gutachter: Prof. Dr. Hans-Jürgen Butt

Tag der Einreichung: 27.04.2017
Tag der mündlichen Prüfung: 28.06.2017
Darmstadt
D 17

TECHNISCHE
UNIVERSITÄT
DARMSTADT

Franziska Monika Henrich : Dynamic dewetting of surfactant solutions
Dynamische Entnetzung von Tensidlösungen
Darmstadt, Technische Universität Darmstadt
Jahr der Veröffentlichung der Dissertation auf TUprints: 2018
Tag der mündlichen Prüfung: 28.06.2017

"I have never tried that before, so I think I should definitely be able to do that"

Pippi Longstocking (Astrid Lindgren)

Erklärung

Hiermit erkläre ich, dass ich die vorliegende Arbeit, abgesehen von den in ihr ausdrücklich genannten Hilfen, selbständig verfasst habe.

Franziska Monika Henrich Mainz, den 26.04.2017

Abstract

Wetting and dewetting play a significant role in many natural processes as well as in many technical applications like in printing or cleaning procedures. To optimize these kind of processes the understanding of the dewetting behaviour of surfactant solutions is important. Previous investigations showed, that an addition of surfactant to a solution changes the dewetting behaviour. Those studies revealed, that the dewetting behaviour is depending on the surfactant concentration, even if the concentration is below the critical micelle concentration (CMC). Nevertheless the effects due to the presence of surfactants are not well understood. Therefore, I investigated in this work, how surfactants influence the dewetting behaviour on smooth and structured surfaces.

The dewetting behaviour of various surfactant solutions (non-ionic, cationic and anionic) on a smooth polystyrene surface were compared at different concentrations well below the CMC. All surfactants show the same tendency, independent of their charge: the higher the surfactant concentration, the lower the receding contact angle as well as the film formation velocity. Scaling with the CMC leads almost to a master curve. The change in contact angle can be interpreted by local surface gradients, e.g. Marangoni stresses. At velocities $>10\,\mathrm{mm\,s^{-1}}$ the experimental results can be described by the hydrodynamic theory.

Additionally to the wetting behaviour on smooth surfaces, the influence of a structured surface in the presence of surfactant was studied. A custom made printing plate with different structured areas was used as model surface. The dewetting behaviour is comparable to dewetting on smooth surfaces, the higher the surfactant concentration the lower the contact angle as well as the critical film formation velocity. The influence of the structured surface decreases with increasing concentration. The decreasing influence of the structured surface is due to the fact, that with increasing concentration the Marangoni stress towards the three phase contact line increases. These Marangoni stresses dominate the stress due to pinning on the structured surface.

Since a direct measurement of the Marangoni stresses is not easily possible, I measured instead the flow profile on a microscopic lenght scale close to the contact line. A newly developed setup is able to image of a moving contact line over a long time period. The measurement of the flow profile showed that at a distance smaller than 30 µm the flow from surfactant solution differs from the one of pure water. This is in agreement with the model of the Marangoni force towards the contact line, which results in the decrease of the contact angle macroscopically.

Zusammenfassung

Be- und Entnetzung spielt in vielen natürlichen Prozessen, aber auch in vielen technischen Anwendungen eine signifikante Rolle. Beispiele sind die industriellen Reinigung, aber auch die Druckindustrie. Um diese Prozesse zu optimieren, ist ein Verständnis des Entnetzungsverhaltens von Tensidlösungen wichtig. Frühere Untersuchungen zeigen einen Einfluss von Tensiden auf das Entnetzungsverhalten, welcher mit steigender Tensidkonzentration zunimmt. Dies ist schon für Konzentrationen weit unterhalb der kritischen Mizellenkonzentration (CMC) der Fall. Der genaue Einfluss von Tensiden auf das Entnetzungsverhalten ist noch nicht bekannt, daher untersuchte ich in dieser Arbeit den Einfluss verschiedener Tenside auf das Entnetzungsverhalten auf glatten und strukturierten Oberflächen.

Dafür wurde der Einfluss von verschiedenen Tensiden (nichtionisch, kationisch, anionisch) auf das Entnetzungsverhalten auf einer glatten Polystyrol Oberfläche untersucht. Die Konzentration der Tenside wurde dabei unterhalb der CMC variiert. Mit steigender Tensidkonzentration sinkt sowohl der Kontaktwinkel als auch die Filmbildungsgeschwindigkeit, unabhängig von der Ladung der Tenside. Durch die Skalierung mit der CMC wird nahezu eine Masterkurve erreicht. Die Änderung des Kontaktwinkels kann durch einen Gradienten in der Oberflächenspannung erklärt werden. Für Geschwindigkeiten $>10\,\mathrm{mm\,s^{-1}}$ stimmen die experimentellen Daten mit der hydrodynamischen Theorie überein.

Zusätzlich wurde der Einfluss von strukturierten Oberflächen auf das Entnetzungsverhalten untersucht. Dafür wurde eine neue Druckplatte mit unterschiedlich strukturierten Bereichen verwendet. Vergleichbar zu glatten Oberflächen sinkt der Kontaktwinkel sowie die Filmbildungsgeschwindigkeit mit steigender Konzentration. Ebenso sinkt der Einfluss der strukturierten Oberfläche. Dies kann durch einen steigenden Gradienten in der Oberflächenspannung, zum Beispiel Marangoni Kräfte, mit steigender Konzentration erklärt werden. Diese Marangoni Kräfte dominieren die Kräfte, die aufgrund der Strukturierung das Entnetzungsverhalten beeinflussen.

Da eine direkte Messung der Marangoni Kräfte nahe der Kontaktlinie nicht möglich ist, wurde stattdessen das Flussprofil nahe der Kontaktlinie auf mikroskopischer Längenskala vermessen. Der neu enwickelte Aufbau erlaubt das Aufnehmen der Kontaktline über einen langen Zeitraum. Die Messergebnisse zeigen eine Änderung des Strömungsprofils innerhalb der letzten 30 µm. Diese Änderung des Strömungsprofils nahe der Kontaktline kann als Indiz für die Marangoni Kräfte angesehen werden.

Contents

1 Introduction and Motivation

Wetting and dewetting on solid surfaces play an important role in many natural processes and technical applications. Natural phenomena are, for example, the wetting of water drops on leaves. Previous studies showed, that the wetting behaviour depends on the specific surface and differs from species to species. The leaves of some plants are wetted nicely if a water drop falls on the leaf. This means the contact angle is relatively low. The contact angle is defined as the angle, between a liquid drop, sitting on a solid surface, and this surface. In the other cases, when the contact angle is relatively high, the leaf has just a water drop on it, that does not spread [58]. But also in many technical applications wetting on solid surfaces is an important issue. In cleaning process, like the cleaning of windows, but also in industrial cleaning processes, e.g. the cleaning of silicon wafers, the understanding of the wetting properties is important. Other examples, where the wetting properties play an important role, are spreading of pesticides on leaves, industrial printing or any cooling processes [23].

Wetting phenomena can be divided in two main fields - the static wetting and the dynamic wetting. In case of the static wetting the liquid is in a local energy minimum and does not move on a solid surface. Thereby the static contact angle (see section 2.1.1) is one important parameter, which describes the wetting on surfaces. A large number of studies investigate the wetting on hydrophilic and hydrophobic materials [10, 12, 23, 66, 75, 127, 149].

One goal of this studies is to understand the wetting on complex surfaces. These surfaces are structured and allow in some cases the inclusion of air gaps under the liquid drop (Cassie state). Therefore the transition between the Cassie state [30] of a droplet, where the droplet wets just the peaks of a structured surface, to the Wenzel state [167], where the complete surface is wetted [82, 118] is investigated.

Another goal in this area of research is to achieve self-cleaning surfaces. On these surfaces the contact angle is close to 180°, therefore the surface is called super hydrophobic. These surfaces provide a low roll-off angle for water drops. The roll-off angle is defined as the angle which a surface has to be tilted, that a liquid drop sitting on this surface, begins to move. Dust on the surface will attach to the water drops and so the surface will be cleaned by itself. This effect is also known as Lotus effect [22, 106, 117]. A special kind of these surfaces is not only water repellent, but also oil repellent and is called super amphiphobic [37, 44].

If the droplets start to move over the surface, the wetting behaviour is not static wetting anymore. Since the drop starts to move it is part of the dynamic wetting behaviour.

The dynamic wetting of simple one component liquids is well studied. Several theories try to explain the dynamic wetting behaviour macroscopically as well as microscopically: the molecular kinetic theory [16, 17] (see section 2.3.1), the hydrodynamic theory [16, 164] (see section 2.3.2) and more models, which are for example combinations of the hydrodynamic and the molecular kinetic model [124]. Not only the theory has been investigated in some detail, also a lot of experimental work has been done on the wetting behaviour of single component liquids. One big goal is to determine the contact angle depending on the measurement length scale [35].

The dynamic wetting of more component liquids, like surfactant solutions, is less understood. Nevertheless in the last years an increasing amount of research is done on that topic [3, 23, 32, 48, 55, 56, 57, 59, 64, 68, 74, 83, 84, 93, 103, 107, 110, 149, 151, 160, 161, 162, 166]. For these liquids surfactant molecules absorb at the interfaces [134]. Therefore they influence the dynamic behaviour of the liquid and can change for example the hydrodynamic boundary condition [3, 32, 103] or the flow profile inside the liquid [84, 110] (see section 2.8.2). Other studies investigate the influence of surfactant on the motion of bubbles in a liquid. For these experiments a bubble rises in a channel, which is filled with a liquid enriched with surfactant molecules. Thereby the surfactant influences the rising velocity of the bubble, the bubble shape, as well as the liquid flow around the bubbles [40, 102, 156]. By using surfactant in a solution it is possible to control the wetted area and the speed of the wetting process, since surfactant reduces the contact angle between a liquid and a solid - which results in some cases in spreading on solid surfaces [23, 149, 162]. The majority of the studies investigate spontaneous wetting. In this case the liquid begins to spread in contact with a solid without external forces [149]. The process of spontaneous wetting depends on the properties of the solid surface as well as on external conditions like the humidity or the temperature. During the spontaneous wetting process a liquid drop is placed carefully on a solid surface. Since the interfacial forces are not in equilibrium the drop starts to spread as long as the interfacial forces reach a steady state. The spreading area depends on the kind of used surfactant, the concentration of the surfactant in the drop as well as on properties of the solid and the liquid [83, 93, 163, 166]. This effect is used for example to change the spreading behaviour of herbicide solutions on leaves to optimize the results and to minimize the necessary amount of herbicides.

Less investigated is the forced wetting behaviour. Thereby a liquid moves over a solid surface due to external forces. For example a plate is pulled out or pushed in a

liquid reservoir. The contact angle thereby is depending on the velocity [47] (see section 2.1.3). The contact angle decreases with increasing velocity. At a critical velocity the contact angle is 0° and a film formation starts. Since a good understanding of the forced wetting and dewetting process is necessary for many industrial processes, as mentioned above, the forced wetting behaviour of different solutions and on different solids was studied in the last years [34, 55, 56, 57]. For example Blake et al. [20] studied the wetting behaviour of liquids with different viscosity.

Since the wetting of surfactant solution appears in most cleaning processes as well as in many other processes, an understanding of this wetting and dewetting behaviour is of great interest. While Hopf et al. [69, 70] studied the wetting behaviour of a surfactant solution at different pH-values for forced wetting, but also for spontaneous wetting. The wetting behaviour of surfactant solutions is studied during the last year in some detail [56, 57]. Also other studies [34] were done in this field but the results have to be critically examined, since the measurement results are not completely explained.

All studies showed that with increasing concentration the contact angle decreases. That happens for different kinds of surfactants. Thereby the question arises, what exactly happens near the three phase contact line. Fell et al. [56] developed a hypothesis (see section 2.7), which tries to explain what happens in the region close to the three phase contact line. They assume that close to the contact line a fresh surface is generated, which is not covered with the same amount of surfactant molecules than the surface far away from the contact line. This leads to a surface tension gradient, e.g. Marangoni forces. This additional force towards the contact line leads to a reduction of the contact angle.

To verify this hypothesis I investigated the wetting behaviour of different surfactant solutions on a smooth surface. The used surfactants vary in the charge. Their critical micelle concentration differs by five orders of magnitude. To vary the charge of the surfactant I use anionic cationic and nonionic surfactant. The influence of the critical micelle concentration (CMC) of a surfactant on the dewetting behaviour can be investigated by variation of the CMC of the nonionic surfactants. The variation of CMC changes the absolute amount of surfactant molecules, which are present at the same concentration of % CMC. In comparison with previous works, I use a smooth polystyrene (PS) surface with a static contact angle close to 90°. This allows a quantitative comparison of forced dewetting data obtained experimentally with the theoretical hydrodynamic models [38, 49, 143, 164].

The wetting and dewetting behaviour is not only influenced by the liquid, but also by the wetted solid surface. Since in industrial processes many wetted surfaces are not homogeneously smooth, but structured, the influence of the surface structure is one of

the important parameters. For example in the offset printing industry the wetted and dewetted surfaces are structured and unstructured next to each other, depending on the desired printing result. Therefore, I investigated the wetting behaviour on a structured surface in combination with complex liquid like surfactant solution. To do so, a new setup was designed, which allows to mount various surfaces in a rotating drum setup, comparable to [56, 57]. With the help of this setup the influence of the surface structure with and without the presence of surfactant is investigated. This allows to achieve a deeper knowledge on the dewetting of structured surface and may help to improve the results in some printing processes by a better understanding of the physical mechanism of the dewetting behaviour on such a surface.

The measurements mentioned before were done macroscopically. The hypothesis by Fell et al. [56] mentioned, that a change in the flow behaviour must happen. Nevertheless, previous experiments show (section 2.8.3) that the flow profile close to the three phase contact line does not change on the macroscopic length scale ($> 100\,\mathrm{mm}$). Since macroscopic changes due to Marangoni force can be observed in the dynamic contact angle, microscopically something has to change by adding surfactant as well. Estimations of the length scale predicted, that the change due to surfactant happens in the last $20\,\mu\mathrm{m}$ distance to the contact line (section 2.7). To investigate these changes a new setup was designed, which allows to measure the flow profile close to the three phase contact line on this length scale by using a fast confocal microscope (section 2.9) as imaging method.

2 State of the art

2.1 Contact angle

When a liquid is in contact with a solid surface it forms an characteristic angle to the solid surface. This angle is called contact angle Θ (figure 2.1).

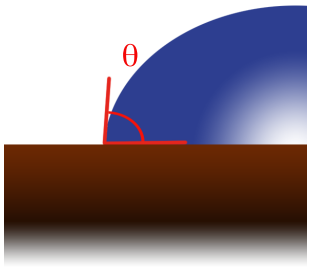

Figure 2.1.: Schematic sketch of drop sitting on a substrate and forming a contact angle Θ with the substrate.

2.1.1 Static and dynamic contact angle

If a drop of a liquid, which is not moving over the solid, is in a local energy minimum, the angle between the liquid and the surface is called static contact angle (CA). The contact angle is depending on the properties of the wetted solid surface as well as on the properties of the liquid of the drop and the surrounding gas or liquid. The contact angle results from a local force equilibrium. For small surface energies the contact angle is high, for a strong surface energy the contact angle is small.

Generally, four different wetting scenarios are distinguished. If the surface is super-hydrophilic and a water drop is deposited on this surface the drop will spread until it completely covers the available surface and has therefore $\Theta \approx 0°$. If the surface is hydrophilic $\Theta < 90°$, a hydrophobic surface would have a contact angle between 90° - 180° and a super-hydrophobic surface of $\Theta > 150°$ [27] (figure 2.2).

The line where the liquid, the gas and the substrate meet is called the three phase contact line (CL). At the CL it is possible to use the Young equation, which relates the contact angle with the interfacial tension γ_S (interfacial tension of the solid), γ_L

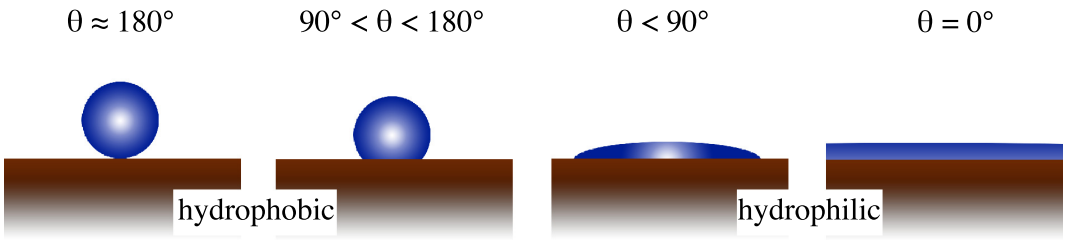

Figure 2.2.: Schematic sketch of water drops on different substrates with different contact angles Θ.

(interfacial tension of the liquid) and γ_{SL} (interfacial tension between solid and liquid) though the balance of the applied lateral forces at the contact line.

$$\gamma_L \cos\Theta = \gamma_S - \gamma_{SL}. \tag{2.1}$$

The solid is hydrophilic if the liquid is water and $\gamma_S > \gamma_{SL}$, the solid is hydrophobic if $\gamma_S < \gamma_{SL}$ [29].

The Young equation is defined for an ideal surface, which is perfectly homogeneous. A real surface is not completely homogeneous, this implicates that the static contact angle, which can be calculated with the Young equation, is rarely observed and the CA varies on the same surface depending on the position. Therefore, it is difficult to define the static contact angle on a surface. To have a comparable CA value, instead of the static contact angle, the receding and advancing contact angle can be measured. These contact angles are defined as the contact angles when the contact line starts to move over the surface.

On the advancing side of the liquid the contact angle is called the advancing contact angle Θ_{adv}, on the receding side the receding contact angle Θ_{adv} (figure 2.3). The CA value at the time when the drop begins to move is the quasi static receding Θ_{0rec} and advancing contact angle Θ_{0adv}. The difference between these two contact angles is called hysteresis and is explained in the following chapter in more detail.

The so called spreading coefficient S specifies if the drop wets or dewets on a specific surface [41, 42].

$$S = \gamma_S - (\gamma_{SL} + \gamma_L) \tag{2.2}$$

Is the spreading coefficient $S > 0$ the liquid spreads completely on the surface to reduce the surface energy. If $S < 0$ the drop does not spread and forms a finite contact angle $\Theta > 0°$.

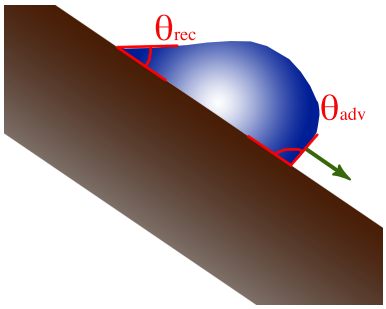

Figure 2.3.: Schematic sketch of a moving drop on a solid surface with the advancing contact angle Θ_{adv} and the receding contact angle Θ_{rec}.

2.1.2 Hysteresis

The difference between the advancing and the receding contact for the velocity $v = 0\,\mathrm{mm\,s^{-1}}$ is called hysteresis H and is defined by:

$$H = \Theta_{adv} - \Theta_{rec} \geq 0°. \tag{2.3}$$

The contact line hysteresis has been studied intensively [7, 41, 46, 53, 61, 78, 126, 174]. A reason for the finite difference between Θ_{adv} and Θ_{rec} is the roughness or the surface heterogeneous of the solid surface. On this kind of heterogeneous surfaces for example areas which are more and less hydrophobic exist. The more hydrophobic areas on the surface pin the contact line and increase therefore the advancing contact angle [174]. A mored detailed description of the pinning can be found in section 2.5.1. Only on a perfectly smooth surface the advancing contact angle Θ_{adv} is equal to the receding contact angle Θ_{rec} [47, 177]. This means that even on a molecular level the surface must be perfectly homogeneous. Various work was done to reach a low hysteresis of the contact angle on a smooth surface of less then 2° [25, 86]. Another way to reach a low contact angle hysteresis it to impregnate the surface with lubricant oil [51, 79, 172].

The dynamic contact angle is velocity dependent [1, 47]. On the advancing side the contact angle increases with increasing velocity (figure 2.4 left side, $v < 0$). The receding contact angle decreases with increasing velocity (figure 2.4 right side, $v > 0$). The theories which describe this depending of the contact angle from the velocity are described in section 2.3.

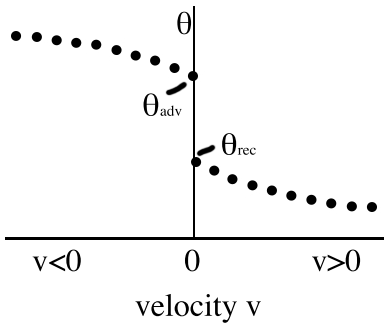

Figure 2.4.: Velocity dependency of the advancing Θ_{adv} and the receding contact angle Θ_{rec} . The contact angle decreases with increasing velocity. (after [47])

2.1.3 Velocity range of dewetting

As described above the contact angle is velocity dependent. If the velocity is high enough, the contact angle is 0°. Therefore, a complete liquid film is built. Those films are called Landau-Levich-Derjaguin films [45, 89]. The thickness h of these films depends amongst others on the surface tension, the density and the viscosity of the liquid. The model which specifies these film formations is described in section 2.3.3. This mechanism is for example used in coating process to reach an uniform film thickness [81, 101].

For low dewetting velocity of a complex liquid (liquid with particles, surfactants,etc.) it is possible to deposit a mono-molecular film (of the particles, surfactants, etc.) on a solid surface [21, 91], these films are called Langmuir Blodgett films [60]. This technique is for example used to investigate the surface structure of a film on a solid surface. Thereby the velocity must be slow enough that the transfered films stay in equilibrium [131]. The shape of the meniscus close to the dewetting area is shown in figure 2.5. The velocities used in this thesis are between the velocities for Langmuir-Blodgett film formation and the one for Landau-Levich-Derjaguin film formation. In this velocity region the hydrodynamic plays an important role in the dewetting behaviour. The particles or surfactants which are presence in the liquid are in contrast to case of Langmuir Blodgett film formation not in equilibrium on the surface. Therefore, the studied velocity range investigate the non equilibrium phenomenons close to the contact line.

Since the contact angle is not only velocity dependent, but also depends on the surface tension and the viscosity of a liquid, it is necessary to define a dimensionless number to

define the ranges where the different above described wetting phenomena happen. One of these dimensionless numbers is the capillary number Ca

$$Ca = \frac{\eta\, v}{\gamma}, \tag{2.4}$$

which represents the ratio of the viscous force and the surface tension γ. The viscous forces are calculated using the velocity v and the dynamic viscosity η [29]. The capillary numbers used in this report vary between 10^{-6} and 10^{-3}. This results in a velocities in between the Langmuir-Blodgett transfer and the Landau-Levich-Derjaguin film formation.

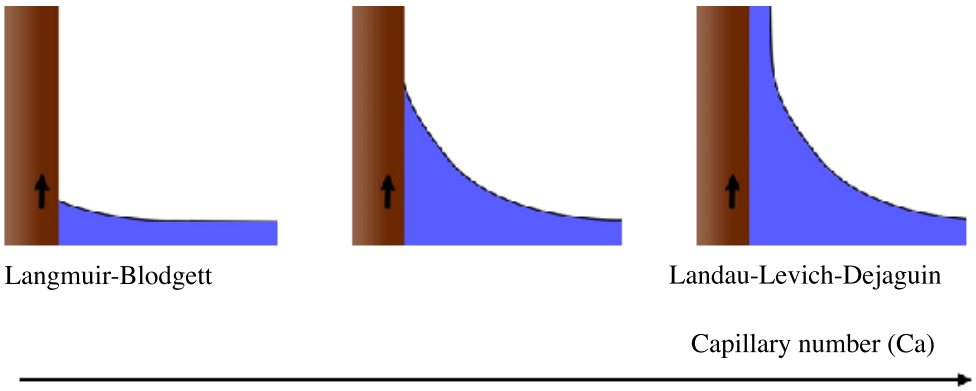

Figure 2.5.: Dewetting at different capillary numbers: For Langmuir-Blodgett transfer of a surface layer low capillary numbers are used, Landau-Levich-Derjaguin film formation happens at high Ca. The velocities used in this report lie in between these two extremes.

Another of these dimensionless numbers is the Reynolds number Re. It helps to compare the flow behaviour in different flow situations. It describes the ratio between the initial force F_i and the viscous force F_v [130].

$$Re = \frac{F_i}{F_v} = \frac{\rho\, v\, \lambda}{\eta}, \tag{2.5}$$

Thereby ρ is the density, η the viscosity and v the velocity of the flowing liquid. λ is the characteristic length of the geometry. The Reynolds number can be used to calculate if a flow is laminar or turbulent. Re above a critical value of approximately Re_{crit} ≈2300 describes a turbulent flow, while Re below this critical value describes a laminar flow [147].

2.2 Measurement techniques

2.2.1 Static contact angle

To measure the static contact angle a liquid drop is deposited on a solid surface. A light source is placed behind the drop and a picture is taken from the front. The positioning of the light source is important to guarantee a good contrast between the drop and the background in the final image. The contact angle is measured in the image of the drop sitting on a surface as shown in figure 2.6.

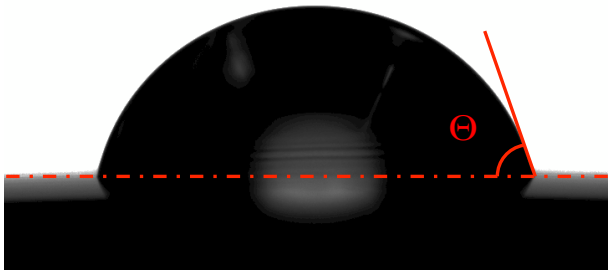

Figure 2.6.: Picture of a static contact angle with backlight illumination.

2.2.2 Receding and advancing contact angle

There are many different methods to measure the receding and advancing contact angle [174], which are presented in the subsequent list. The symbols in brackets show the kind of receding contact angle which is measurable, the quasi static and dynamic contact angle Θ_{0adv}, Θ_{0rec} or the dynamic contact angle Θ_{adv} and Θ_{rec}.

- Tilted plate method: A drop is deposited on a tilted plate and the contact angle is detected when the drop starts to move [98]. (Θ_{0adv}, Θ_{0rec})
- Tilting plate: A plate is tilted in a water bath until the meniscus of the water is horizontal. The angle of the plate is the contact angle [2]. (Θ_{0adv}, Θ_{0rec})
- Wilhelmy balance method: This is an indirect measurement of the contact angle. A thin solid plate is pulled vertically out of a water bath. The change in weight is measured, which enables a calculation of the contact angle if the surface tension is known [24, 77, 129, 132, 170]. (Θ_{0adv}, Θ_{0rec})

- Sessile drop method: A drop is deposited on a surface and is inflated or deflated from the top or the bottom, with the help for example of a syringe pump. The contact angle is detected while the drop is growing or shrinking. By changing the flow rate of the in- and deflating liquid, the velocity can be changed in a small velocity range [13, 87, 88, 132]. (Θ_{0adv}, Θ_{0rec}, Θ_{adv}, Θ_{rec})

- Captive bubble method: Similar to the sessile drop method, but here an air bubble is inflating and deflating which is deposited in the liquid next to the solid. The contact angle between the air, the liquid and the solid is measured [175]. Comparable to the Sessile drop method the velcoity can be changed in a small velocity range. (Θ_{0adv}, Θ_{0rec}, Θ_{adv}, Θ_{rec})

- Rotating drum method: A rotating cylinder is placed in a liquid container which is filled up to the axis of the cylinder. The contact angle can be imaged in the side view of the drum with a camera. This setup allows to change the velocities in a wide range. This setup is primarily used in this thesis and is described in more detail in section 2.6 [1, 50, 55, 56, 57, 64, 161]. (Θ_{adv}, Θ_{rec})

- Plunging tape method: A continuous tape is moved through a liquid bath via rollers. At the position were the tape immerses in the liquid the advancing contact angle and at the position where the tape emerges from the liquid the receding contact angle can me measured [8, 18, 19, 20, 26, 62]. This setup allows comparable measurements to the rotating drum setup to change the velocities in a wide range. Due to the necessary continuous tape the kind of surfaces is more limited compare to the rotating drum setup. (Θ_{adv}, Θ_{rec})

- ...

2.2.3 Apparent contact angle

Due to the bending of the meniscus, the contact angle strongly depends on the length scale at which it is measured [23]. A contact angle on the nanometer length scale (microscopic) can differ from the one on the macroscopic contact angle (millimeter length scale). Schellenberger [137] showed for example that the contact angle changes on a micro pillar surface during receding and advancing more than 20° on a mesoscopic length scale. In macroscopic measurements this change is not detectable. The contact line is pinned on the edge of an inhomogeneity and changes until the same contact angle on the new area of the surface is reached [67].

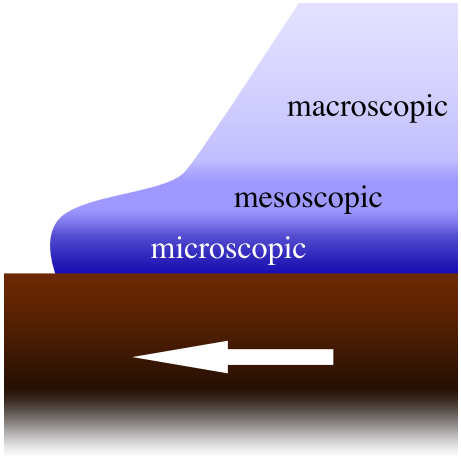

Figure 2.7.: Schematic drawing of the length scale dependence of the contact angle, after [16].

2.2.4 Shape of menisci

The static shape of the menisci of a liquid pulled out of a liquid bath by a solid plate is dependent on the equilibrium between the gravitational forces and the capillary forces [42]. The pressure between the liquid and the gas can be calculated with

$$P_z = P_0 - \rho g h. \tag{2.6}$$

thereby P_0 is the outer pressure, h is the height above the equilibrium surface of the liquid, g the gravitational acceleration and ρ the density of the liquid (figure 2.8). The force resulting of this pressure is

$$F_P = \frac{1}{2}\rho g h^2 \tag{2.7}$$

The horizontal balance of the forces can be written as

$$\gamma = \gamma \sin\Theta + \frac{1}{2}\rho g h^2. \tag{2.8}$$

With this equation it is possible to calculate the height of a static meniscus above the unpertubed liquid level [42].

For the dynamic case of a moving plate it is also possible to use this calculation to describe the shape of the meniscus, but only for a large distance to the contact line (in

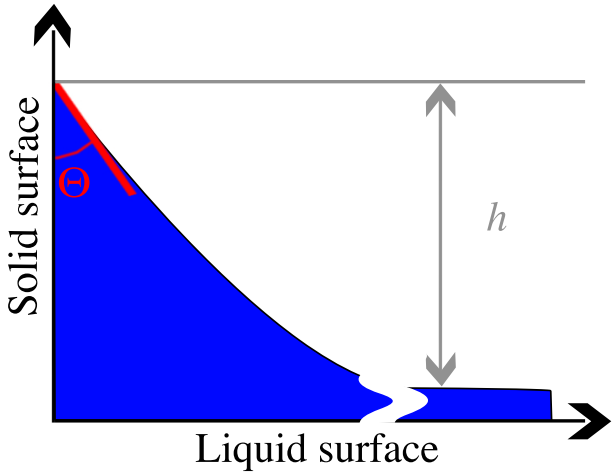

Figure 2.8.: Schematic drawing of the area near the three phase contact line.

comparison to the slip length, which is typically less than 10 nm) [33]. Since the viscous bending of the meniscus happens below the macroscopic length scale (figure 2.7).

2.2.5 Wetting mechanism:

There are two kinds of mechanisms causing a liquid to wet or dewet on a surface: the spontaneous wetting and the forced wetting.

Spontaneous (de)wetting

The spontaneous wetting is also called spreading. Thereby a drop, which is placed on a substrate starts to move or spread without external forces to reach the thermodynamic equilibrium. Thereby the spreading coefficient $S > 1$ and velocity during the spreading is not constant.

Forced (de)wetting

In contrast during the forced wetting an external force is applied, which results in a wetting or dewetting. This happens for example at all in section 2.2.2 mentioned measurement techniques. But also in industrial processes it is the important wetting mechanism, for example wetting and dewetting of ink in the offset printing. The biggest advantage of the forced wetting process is a constant and variable velocity. Furthermore the wetting and dewetting behaviour can be investigated over a longer time scale. This allows to investigate the velocity depending wetting behaviour on surfaces with a finite contact angle.

2.3 Modeling

Until now a theory to describe the exact mechanism of the movement near the three-phase contact line on all length scales is not developed. To explain the wetting properties near the CL different models were developed in the past, which ares presented subsequently.

2.3.1 Molecular-Kinetic Model

The molecular-kinetic model, called molecular kinetic theory (MKT), was developed by [17, 36]. It describes the motion of the contact line due to a hopping of molecules near the CL [16] (figure 2.9). It assumes that the liquid is saturated with gas and the gas saturated with liquid and that on the solid surface molecules of both liquid and gas can adsorbed. Since neither gas nor liquid wet the solid surface completely the adsorption behaviour of gas and liquid area differs from the one at the contact line region. The thickness of the contact line region is not more than two adsorption sites. This adsorption situation at the contact line is never static. If in average the same amount of liquid and gas molecules adsorb and desorb on the surface at the contact line region the contact line is static. If more liquid molecules adsorb on the surface in the contact line region, the contact line moves away from the bulk (advancing). Considering that more liquid molecules desorb from the liquid phase, the contact line moves in direction of the liquid bulk (receding) [20, 16]. The model describes the dependency of the contact angle on the wetting line velocity:

$$v = 2\,\kappa^0\,\lambda^3 \sinh\left(\frac{\gamma\,(\cos\Theta_0 - \cos\Theta)}{2\,k_B\,T}\right). \tag{2.9}$$

Thereby κ^0 is the characteristic frequency, λ the distance between adsorption sides on the solid surface, γ the surface tension of the liquid, Θ_0 the contact angle at no velocity, Θ the contact angle at the velocity v, k_B the Boltzmann constant and T the absolute temperature [16].

This theory describes some parts of the dependency between the contact angle and the velocity, but the model misses the link to the hydrodynamics. For this model the wetting behavior is not allowed to have an influence on hydrodynamic length scale, since the wetting depends on the hopping of single molecules.

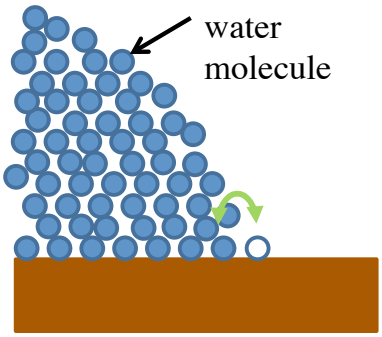

Figure 2.9.: Liquid molecules hop from the gas phase solid surface to the liquid phase solid surface (advancing side) or hop from the liquid phase solid surface to the gas phase solid surface (receding side), after [16].

2.3.2 Hydrodynamic model

In contrast to the MKT, the hydrodynamic theory (HDT) describes the wetting mechanism from the hydrodynamic point of view. It describes the wetting behavior near the three-phase contact line with energy dissipation due to viscous flow near the CL. The classical hydrodynamic approach can not describe the flow near the CL. The problem is the assumption of a moving contact line and the non-slip boundary condition between the liquid and the solid. This results in unbounded shear stresses at the CL and infinite forces by the liquid on the solid [73]. To solve this problem different approaches were developed to deal with the singularity. A possibility is to truncate the solution at the molecular scale [164], another one is to modify the flow equation and boundary conditions by relaxing the non slip boundary condition [47, 73]. The simple form of this solution describes the contact angle depending on the capillary number Ca (see Eq. 2.4):

$$\Theta = \left(\pm 9\, Ca \ln\left(\frac{\alpha h}{\lambda} \right) + \Theta_0^3 \right)^{\frac{1}{3}}. \tag{2.10}$$

Thereby Θ_0 is the contact angle obtained for zero velocity, α is a numerical constant depending on the geometry, λ is depending on the assumption the characteristic distance or the slip length and h the characteristic macroscopic length scale which is also given by the specific geometry. The sign is positive for the advancing contact angle and negative for the receding one [16, 20, 38, 53, 123, 124, 157, 164]. This theory has been used to describe the wetting behaviour for a wide range of capillary numbers [38, 123, 124, 164], only at very low $Ca \leq 10^{-4}$ the model fails [63, 70, 138, 139]. For

higher velocities ($Ca \geq 10^{-2}$ [100, 122, 125, 139]) the CL gets unstable and a contentious film, a so called Landau-Levich Film, is formed [100, 89, 45, 146](see section 2.3.3). On the basis of this hydrodynamic model for example Shikhmurzaev [140, 141] and Billingham [14, 80] developed a model with more physical boundaries at the surface.

The major difference between the MKT and the HDT is, that in the MKT no contact line exists, while in the HDT a contact line exists. On the basis of the MKT and the HDT Petrov and Petrov [124] developed a model, which combines both theories [16, 23, 124].

Snoeier and Andreotti [143] pointed out that equation 2.10 was only developed for the advancing, not for the receding case. Eggers [49] developed an approximate solution for small Θ_0. The apparent contact angle follows the equation [49, 143]:

$$\frac{\Theta}{\Theta_0} = \frac{2^{\frac{2}{3}}\delta^{\frac{1}{3}}}{Ai(\sigma)} \frac{\mathrm{d}Ai(x)}{\mathrm{d}x}\bigg|_{x=\sigma} \tag{2.11}$$

Thereby all lengths are rescaled using the capillary length and

$$\delta = \frac{2Ca}{{\Theta_0}^3}, \tag{2.12}$$

σ is the largest solution of the equation [49, 143]

$$\frac{2}{\Theta_0 \delta^{\frac{1}{3}}} + \frac{2^{\frac{2}{3}}}{Ai(\sigma)} \frac{\mathrm{d}Ai}{\mathrm{d}x}\bigg|_{x=\sigma} - \frac{2^{\frac{1}{6}} e^{-\frac{1}{3\delta}} \Theta_0}{3\pi Ai^2(\sigma)\lambda} = 0, \tag{2.13}$$

Ai is the Airy function and $\frac{\mathrm{d}Ai}{\mathrm{d}x}$ the first derivation of the airy function. In this model two adjustable parameters exist: (1) the characteristic length of the microscopic regime λ, (2) the contact angle at zero velocity Θ_0. The other parameters can be independently determined.

2.3.3 Landau-Levich-Dejaguin Model

In contrast to the hydrodynamic and the molecular kinetic model the Landau Levich Dejaguin model describes the film formation behaviour as shown in figure 2.10.

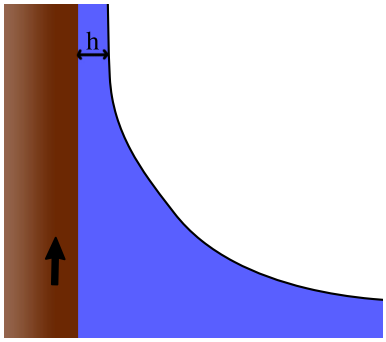

Figure 2.10.: Schematic sketch of the Landau-Levich-Dejaguin film formation, thereby a solid is pulled out of a liquid whereat a film with the thickness h is created.

Above a critical velocity the contact angle is 0° and a complete film is pulled out of the liquid on the solid [45, 89]. The thickness of the film h_F is depending on the surface tension γ, the density ρ, the gravity acceleration g and the capillary number Ca [101]:

$$h_F \backsimeq 0.94 \sqrt{\frac{\gamma}{\rho\, g}}\, Ca^{\frac{2}{3}}. \tag{2.14}$$

The transition between the case of complete dewetting (endless contact angle) and the film formation is called Landau-Levich-Dejaguin-transition. As described above the contact line starts to get unstable and shows often a V shaped corner [18, 122, 171].

2.4 Surfactants

Surfactants are substances which reduce the interfacial tension. Surfactant molecules are amphiphilic and consist of a hydrophilic and a hydrophobic part (figure 2.11). In an aqueous surfactant solution the hydrophobic part tries to stick out of the water.

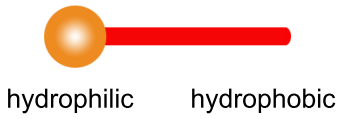

Figure 2.11.: Schematic structure of a surfactant molecule.

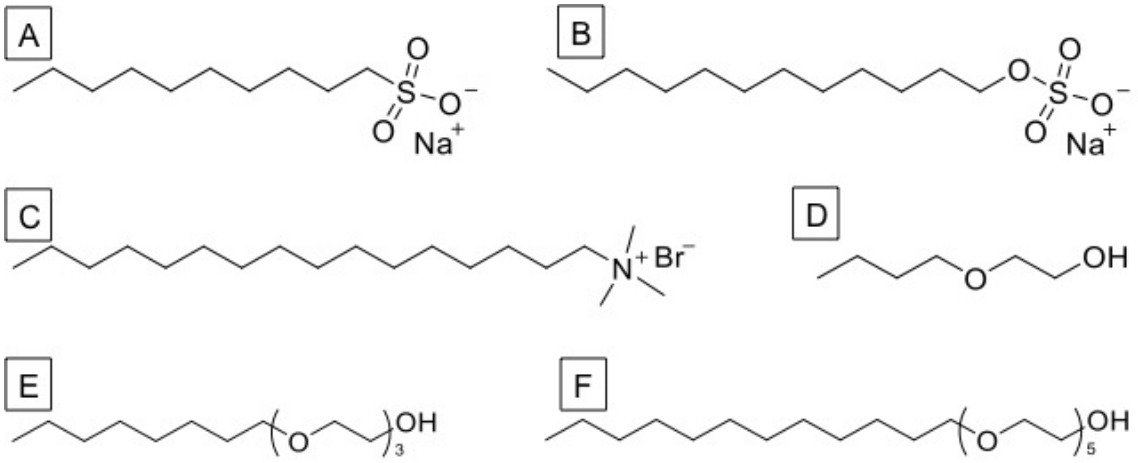

Figure 2.12.: Chemical structure of the used surfactant [A] S-1DeS, [B] SDS, [C] CTAB, [D] C_4E_1, [E] C_8E_3, [F] $C_{12}E_5$.

Depending on the head group surfactants can be divided in different groups [92]. The surfactants used in this work can be divide in the following groups according to the charge of the hydrophilic parts in water:

- anionic: negatively charged head group, for example SDS, S-1DeS
- cationic: positively charged head group, for example CTAB
- nonionic: non charged head group, for example C_4E_1, C_8E_3, $C_{12}E_5$

The structure of used surfactants in this work is shown in figure 2.12

2.4.1 Critical micelle concentration

Since the hydrophobic part tries to stick out of the aqueous solution, surfactant molecules have the tendency to cover the water-air surface and reduce the surface tension. If the whole surface is covered with surfactant molecules the so called CMC is reached. The surfactant molecules build micelles for concentration above the CMC. In the center of the micelles for example oil can be included and therefore with the help of surfactant it is possible to mix two immiscible liquids like for example oil and water (figure 2.13) [85, 92]. Due to this, they are used in many cleaning agents [85].

To measure the critical micelle concentration the surface tension of different surfactant concentrations has to be measured. With increasing surfactant concentration the surface tension decreases (figure 2.14). As soon as the whole surface is covered with surfactant molecules and the CMC is reached, the surface tension is constant with

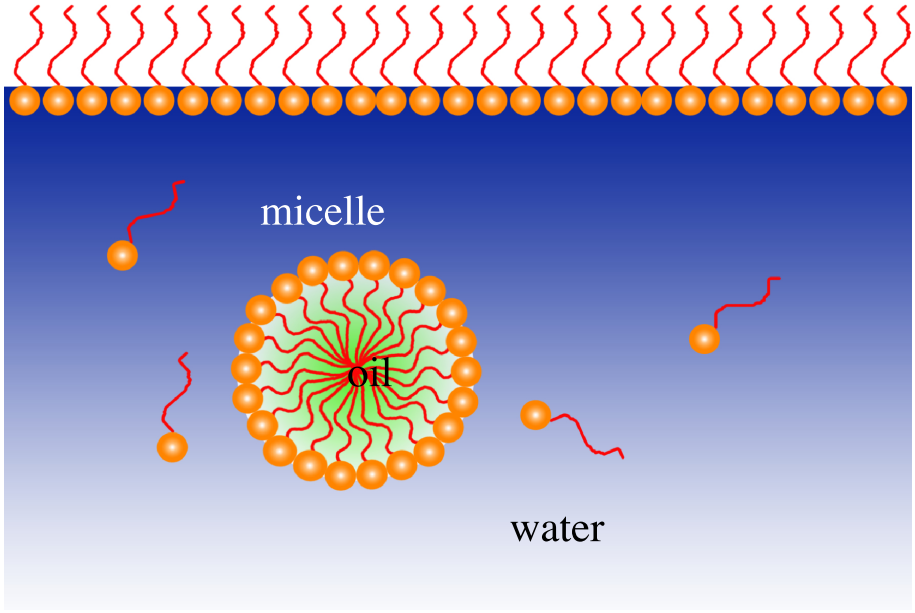

Figure 2.13.: With the help of surfactant molecules it is possible to mix two immiscible liquids like oil and water by surrounding oil drops with surfactant molecules. These structures are called micelles.

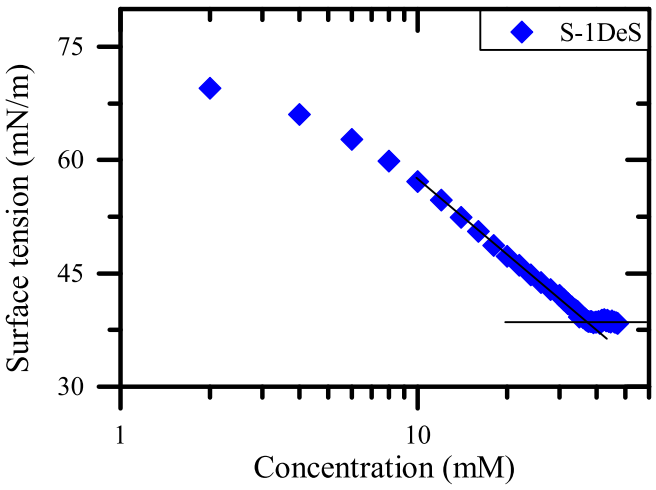

Figure 2.14.: The surface tension is depending on the surfactant concentration. Above the critical micelle concentration (CMC) the surface tension is constant, here for the anionic surfactant S-1DeS. The straight black lines symbolize the fits of Eq. 2.15 and Eq. 2.16 .

increasing surfactant concentration. To determine the CMC out of the measurement points the concentration depending part is fitted with

$$\gamma = m \log c + n. \tag{2.15}$$

The constant part is fitted with

$$\gamma = \gamma_{constant}. \tag{2.16}$$

Thereby $\gamma_{constant}$ is the average of the constant measurement point. The crossover of these two equation is the measured CMC.

2.4.2 Gibbs adsorption isotherm

The absorption of surfactant molecules on the liquid surface reduces, as already mentioned, the surface tension. This can be described with the the Gibbs adsorption isotherm, which calculates the surface tension correlation to the surface excess [28, 29]. The described Gibbs adsorption isotherm is valid for surfaces, which can deform reversible like solid surfaces

For a two component system consisting of a solvent 1 and a solute 2, for example water and surfactant, it can be described with:

$$\mathrm{d}\gamma = -\Gamma_1 \mathrm{d}\mu_1 - \Gamma_2 \mathrm{d}\mu_2. \tag{2.17}$$

Thereby is γ the surface tension, Γ the surface excess, which describes how many molecules are adopted per unit area, and μ the chemical potential of the surfactant solution:

$$\mu_i = \mu_i^0 + RTln\frac{a}{a_0}. \tag{2.18}$$

Here μ_i^0 is the chemical potential at a reference state, a the activity and a_0 the standard activity [28]. For a constant temperature this can be simplified to

$$\mathrm{d}\mu_i = RT\frac{\mathrm{d}a}{a}. \tag{2.19}$$

Gibbs assumes that the surface of an ideal model has no thickness, the so called Gibbs divining interface. In a real system the bulk close to the surface also includes molecules of the other phase, therefore the thickness of the interface is not zero. Nevertheless it is

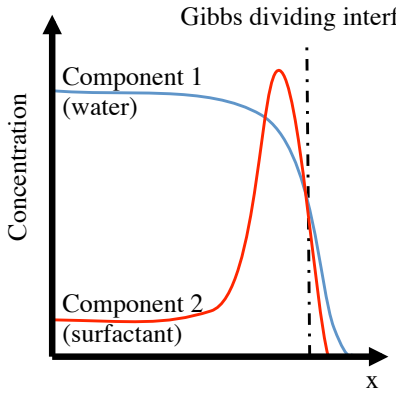

Figure 2.15.: Concentration profile for a surfactant solution, after [28].

a convenient assumption. Therefore, the surface excess of component 1 is zero. Using this and equation 2.19, the surface excess of component 2 can be calculated with

$$\Gamma_2 = -\frac{a}{RT}\left.\frac{\partial \gamma}{\partial a}\right|_T . \tag{2.20}$$

The calculation of the surface excess allows to calculate the amount of surfactant absorbed on the interface. Figure 2.15 shows how the concentration profile of a surfactant solution would look like.

2.4.3 Marangoni effect

The Marangoni effect is a mass transfer due to a surface tension gradient along an interface. The surface tension tries to minimize the surface area. On a surface area with a high surface tension this effect is stronger than on a surface area with a lower surface tension. If now a surface with a higher surface tension is next to one with a lower surface tension, the area with the higher surface tension is pulling stronger on the liquid molecules than the one with the lower surface tension. This leads to a flow towards the area with the stronger surface tension, the Marangoni effect. One of the first who described this effect was the physicist James Thomson in 1855 [158]. The effect is named after the physicist Carlo Marangoni, who published a study on that topic in 1865 [104].

A good example to see the Marangoni effect are the tears of wine (figure 2.16). Wine can be simplified as a mixture of ethanol and water. The surface tension of these two component differs, water has a higher surface tension than ethanol. In the area close to the contact line the wine evaporates. Since ethanol evaporates faster than water,

(a) (b)

Figure 2.16.: (a) The tears of wine are clearly visible in the shadow of the glass. (b) Schematic drawing of the tears of wine mechanism.

this leads to a concentration gradient in this area. Close to the contact line more water molecules exist than in the bulk, which results in a higher surface tension close to the contact line than on the bulk surface. This gradient in surface tension leads to the flow towards the contact line, acting against the gravitational force and generates the so called tears of wine.

But not only the tears of wine are investigated, also other effects can be explained by the Marangoni force, for example the building of micrometer rings and hexagonal arrays made of nanocrystals, etc. [71, 99, 115]. The Marangoni force can for example also be used for a directed motion of an object. An easy example is a small aluminum piece, cut in boat shape with a hole in the middle and a cut out to the end of the boat, is paced in clean water. By placing a drop of surfactant solution in the hole, the boat will move frontwards. Also in the recent scientific investigation the Marangoni force plays an important role, for example the movement of liquid marbles by laser light (heat induced Marangoni force) [120].

Another area where Marangoni forces plays a important role is the spreading of surfactant solution [83, 151, 159, 160] and superspreader solutions [116, 128, 166]. Due to the presence of surfactant the drop deposited on a surface spreads amongst others due to the Marangoni force.

2.5 Influence of surface roughness

The surface roughness has a strong influence on the contact angle of a liquid on a substrate. Most natural structures have a structure in the sub millimeter range [67]. A liquid drop on this surfaces results in a contact angle at which the interfacial free energy shows a local minimum [95]. Therefore, depending on the surface roughness and structure the wetting and dewetting behaviour changes.

2.5.1 Contact line pinning

Deformations of the surface or chemical inhomogeneities have the possibility to pin the contact line. If a liquid moves over a solid surface it has a specific contact angle (Θ). This case is shown in figure 2.17 at position 1 and 4. If the CL reaches now a deformation of the surface, like at position 2 and 3, the contact line is pinned until it reaches the same contact angle on the new surface [67].

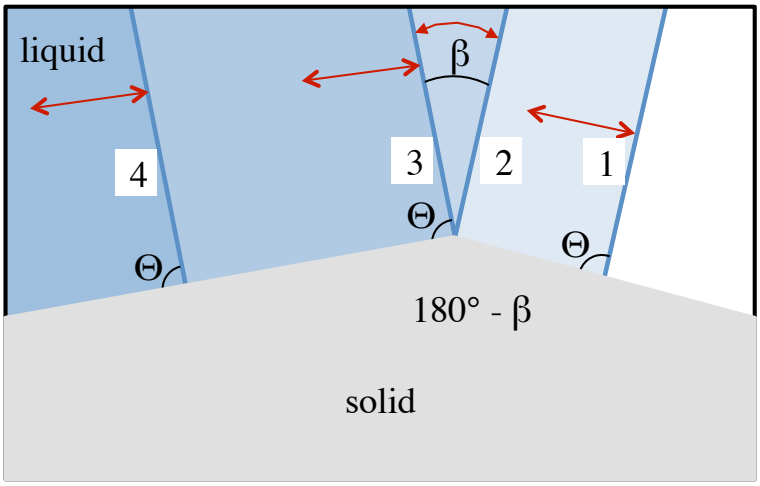

Figure 2.17.: The liquid moving over a solid surface has a specific contact angle (1 and 4). By reaching a deformation the contact line is pinned as long as it has the same contact angle on the new surface (2 and 3). After [67].

2.5.2 Cassie and Wenzel state

Depending on the liquid, the surface roughness and the surface chemistry two main phenomena can happen on a structured surface. Either the area between the drop and the solid is completely wetted or some gas is enclosed in some parts between the liquid and the solid. The first case is the so called Wenzel state [167] (figure 2.18 B).

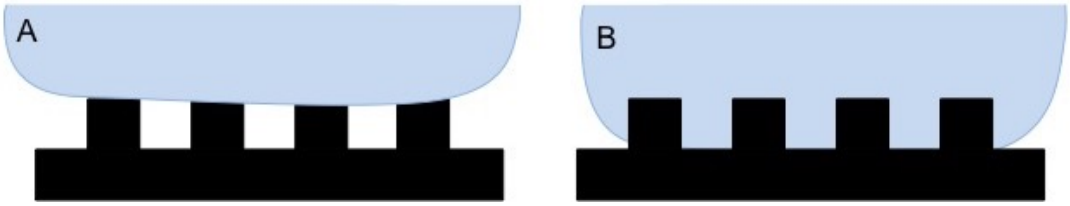

Figure 2.18.: A drop is sitting in an A) Cassie Baxter state, B) in a Wenzel state on a structured surface.

The apparent contact angle on a rough surface for the Wenzel model is calculated to be:

$$\cos\Theta_0 = r\cos\Theta, \tag{2.21}$$

where r is the roughness ratio. The roughness ratio describes the ratio of the structured surface to its projected surface.

In the other case the drop is resting only on parts of the surface, the so called Cassie-Baxter state (figure 2.18). Thereby air pockets are embedded between the liquid drop and the surface. For this case the apparent contact angle can be described with:

$$\cos\Theta_{CB} = f_1\cos\Theta - f_2. \tag{2.22}$$

Thereby f_1 is the total area of the solid liquid interface and f_2 the total liquid interfaces in a plane geometry area [30].

2.5.3 Hydrophobic and hydrophilic materials

As described before the surface is called hydrophilic if the contact angle $\Theta < 90°$ and called hydrophobic if $\Theta > 90°$. If the static contact angle is more than 150° and the contact angle, where the drop starts to move over the surface, the so called roll off angle $\Theta_{rolloff}$, is smaller than 10° the surface is called superhydrophobic.

These superhydrophobic materials can be found on various natural surfaces, like lotus leaves, water strider leg,Macroscopy...[127, 152]. Due to the superhydrophobic surface a water drop pearls off easily on a lotus leaf and the water strider and other small animals like spiders can walk on water (figure 2.19).

These surfaces have mostly a nano and micro structure on the surface. If a water drop sits on such a surface the drop will mostly stay in the Cassie state. In recent years a lot

(a) (b)

Figure 2.19.: (a) show a spider walking on water. (b) show various water drops on a lotus leave.

of work was done to build this kind of super hydrophobic surfaces artificially. Thereby the nano and micro structure were built by various kinds of techniques (candle sout, pillars, nanofibers,...) [11, 44, 54, 94, 97, 176]. The opposite of a superhydrophobic surface, which repels water, is the superhydrophilic surface, which repels the air and prefers to be wetted.

2.5.4 Spontaneous wetting on rough surfaces

Spontaneous wetting, also called spreading, on a rough surface, depends on the kind of surface roughness [165]. By the spreading on a smooth surface the radius of the contact line over the time correlated with a power law [5, 31, 96, 105].

The spreading on a rough or structured surface is more complex. By using variations of the micostructured surfaces the spreading behaviour on a more complex surface was investigated by [165]. By defining a roughness parameter depending on the wetted geometry they showed that with increasing roughness on the surface the spreading velocity decreases. This indicates that the structure on a surface counteracts the spreading.

2.5.5 Forced wetting on structured surfaces

As already mentioned there is a difference between spontaneous and forced wetting. It is the same on structured surfaces. Various studies were done on the investigation of the influence of defects on the surface on the wetting behaviour [43, 108, 144]. The contact

line pins at the defect, therefore the dewetting of a solid on a surface can be used to find imperfections on the surface. For periodic defects the deformations of the contact line were for example developed by [43]. They describe, that immediately after the contact line depinns from the defect, the shape of the contact line is almost sinusoidal.

2.6 Rotating drum setup

To measure the dynamic contact angle a rotating drum setup was used in previous investigations [1, 55, 56, 57] (section 2.2.2).

2.6.1 Setup

The setup consists of a container made of polyvinyl chloride (PVC) (width: 100 mm, depth: 170 mm, height: 150 mm), which has three windows, which allow the investigation of the contact angle (side view) and also the shape of the contact angle (front view) [55] (figure 2.20). Inside the container exchangeable drums can be mounted. These drums are build out of stainless steel. Two different drums were used in the previous experiments [55, 56, 57], one is a cylinder with a diameter of 120 mm and a width of 60 mm, the other one is a segment of a sphere. The diameter of this sphere is also 120 mm. The flat surface allows to glue different surfaces on the drum like for example thin glass slides [50, 55]. The segment of a sphere drum allows an easier and more precise measurement of the contact angle, since it is possible to focus on one part of the CL without optical perturbation.

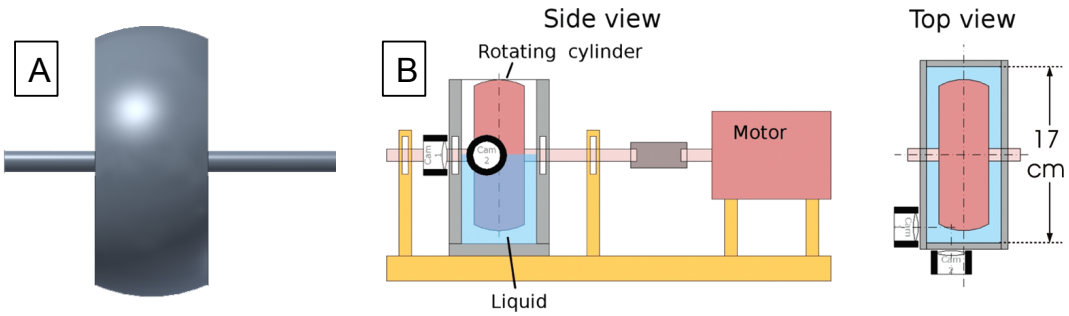

Figure 2.20.: [A] 3D image of the rotating drum (segment of a sphere drum). [B] Sketch of the rotating drum setup. Reprinted with permission from [56]

The drum can be connected to four different linear motors, to vary the velocities between 10^{-4} up to $1\,\mathrm{m\,s^{-1}}$. The velocities of the different motors are listed in table 2.1.

Table 2.1.: Velocities and velocity steps of the four motors, which can be connected to the rotating drum setup to vary the velocity between 10^{-4} up to $1\,\mathrm{m\,s^{-1}}$. after [55]

motor	velocity range $[\mathrm{m\,s^{-1}}]$	velocity steps $[\mathrm{m\,s^{-1}}]$
1	10^{-4} - 10^{-3}	5x10^{-5}
2	10^{-3} - 10^{-2}	5x10^{-4}
3	10^{-2} - 10^{-1}	5x10^{-3}
4	10^{-1} - 1	5x10^{-2}

The contact angle is detected with a high speed camera and analyzed manually from the videos with ImageJ [1]. On the side where the rotating drum moves in the water, the advancing contact angle can be measured. On the other side of the drum, where the rotating drum moves out of the liquid, the receding contact angle can be measured (see figure 2.21).

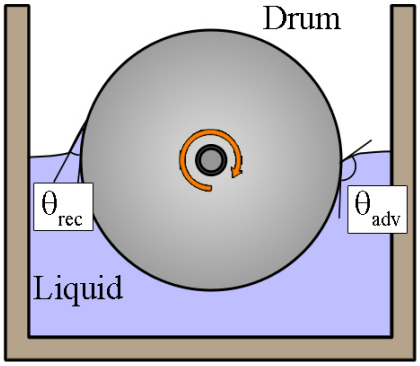

Figure 2.21.: Schematic sketch of the rotating drum setup with advancing and receding contact angle. [64] - Published by the Royal Society of Chemistry.

The segment of a sphere drum is coated with polystyrene to guarantee a homogeneous and smooth surface. Therefore, the drum is first cleaned with ethanol, acetone and tetrahydrofuran (THF) and afterwards placed in 0.8 wt% solution of PS in THF and rotated inside of the solution with a velocity of $100\,\mathrm{mm\,s^{-1}}$. After five minutes the solution is removed as fast as possible. The film was dried under rotation for one hour at room temperature and then for 16 h at 60 °C. This results in a homogeneous PS film at the surface of the cylinder [55, 56].

[1] ImageJ, https://imagej.nih.gov/ij/

The disadvantage of this setup is the limitation in the cleaning of the setup. The complete container is glued together, which makes a cleaning of the setup difficult. Since in the corners of the setup the dust can not easily be washed away. Additionally, the material of the bath is not stable against a lot of solvents. This is not only a problem for the cleaning of the setup, but also limits the liquids which can be measured in this setup. The three windows allow an imaging of the contact angle as well as the contact line, but no imaging of the receding and advancing contact angle at the same time. The covering of the setup allows measurements in saturated atmosphere (90 %) and with an open container at room conditions (30 %) [55], but it does not allow to adjust the atmosphere somewhere in between.

2.6.2 Water

For pure water measurements 0.9 L milli-Q water is filled in the container. With this amount of water the bath is filled to the axis of the drum. The setup is covered with a glass plate to ensure a homogeneously saturated air during the measurement. The change in contact angle can be compared to the illustration shown in figure 2.4. With increasing velocity the advancing contact angle increases and the receding contact angle decreases. As described in section 2.1.2 the measurements show a hysteresis ($\approx 30°$) since the surface is not perfectly smooth. The pure water measurements are the black squares in figure 2.22.

2.6.3 Surfactant solution

If a small amount of surfactant molecules, well below the CMC, is added to the pure water the wetting behaviour changes. This amount of surfactants changes the surface tension slightly, for example for the surfactant CTAB only by 15 %. Nevertheless the wetting behaviour is changed significantly. At any given velocity, the contact angle decreases with increasing surfactant concentration. In the same way the velocity, where the contact line starts to get unstable, and the film formation begins, decreases. Due to the beginning film formation at this velocity, the contact angle can not be measured at higher velocities.

[55] showed that this behaviour is not only typical for cetyl trimethyl ammonium bromide (CTAB, anionic) solution (figure 2.22). Also sodium dodecyl sulfate (SDS, cationic) solutions as well as neutral surfactant solutions like butyl glycol C_4E_1, octyl triglycole trimethyl C_8E_3 and dodecyl pentaglycole $C_{12}E_5$ show the same tendency [55].

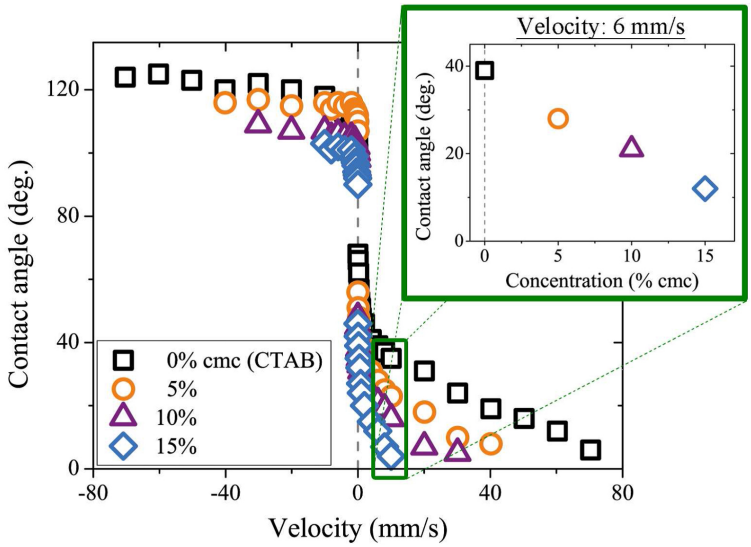

Figure 2.22.: Contact angle vs velocity for CTAB solution well below CMC . The contact angle decreases with increasing velocity as well as with increasing CTAB concentration (blow-up at 6 mm/s). Reprinted from [55]

2.7 Hypothesis

The question arises why we see the change in the contact angle, if we add only a small amount of surfactant (well below the CMC). Fell et al. [56, 55] described a hypothesis why the change in contact angle happens. For pure water, the water should pull upwards with the solid to the CL and flows on the surface back to the bulk near the surface. This flow is shown in figure 2.23 with arrows.

By adding surfactant molecules to the liquid the contact angle changes. Fell et al. [55] assumed that directly behind the CL a fresh surface is created. This fresh surface is covered with less surfactant molecules than the bulk surface. This happens, since on one hand that not all surfactant molecules transfer from the solid surface to the liquid interface, on the other hand the surfactant molecules need less space on the liquid air interface than on the solid liquid interface, which results in a less covered surface even if all surfactant molecules will be transfered from the solid interface to the liquid interface at the CL.

A calculation of the length scale of the surface tension gradient is complex since different processes work at the same time and length scale - amongst others the diffusion of the single molecules, the adsorption kinetic as well as hydrodynamic flow effects. A simple approximation allows to estimate the length scale. This assumption is a simple diffusion model neglecting all hydrodynamic flow effects. By considering that the liquid

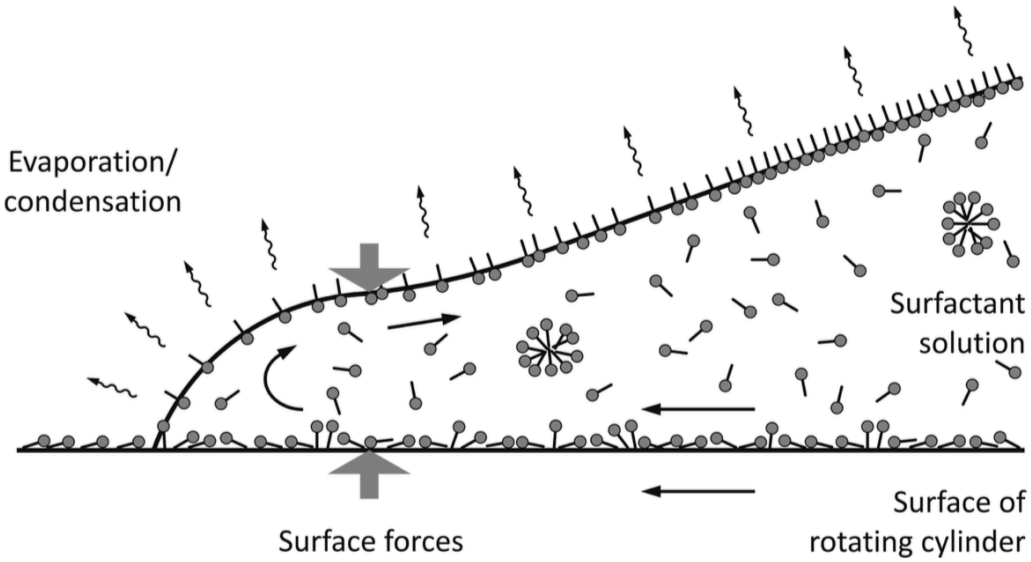

Figure 2.23.: Hypotheses of the flow profile. The black arrows sketch the flow of pure water. After adding of surfactant solution, fresh surface is created near the CL, which is not covered with surfactant molecules. Due to Marangoni stresses a force is pointing in the direction of the CL. Reprinted with permission from [56]. Copyright 2011 American Chemical Society.

meniscus near the three phase contact line has the shape of a wedge (see figure 2.24), the distance x can be calculated with

$$x = h \cos \Theta. \tag{2.23}$$

By assuming that the surfactant molecules only diffuse from the bulk to the surface and not along the surface the thickness α represents the thickness in which enough molecules exist to get the same surface coverage of surfactant molecules like far away from the CL. By assuming a linear absorption Γ it can be assumed, that below the CMC the surface excess Γ is proportional to the surfactant concentration c just below the surface

$$\Gamma = \alpha c. \tag{2.24}$$

With the Gibbs adsorption isotherm

$$\Gamma = \frac{c}{2RT}\frac{\mathrm{d}\gamma}{\mathrm{d}c} \tag{2.25}$$

it is possible to calculate the distance α by using equation 2.24:

$$\gamma_0 - \gamma = 2\alpha cRT. \tag{2.26}$$

Thereby T is the temperature and R the universal gas constant. To estimate the distance x we can assume that the thickness α is equal to the thickness h:

$$x = \frac{\gamma_0 - \gamma}{2cRT}\cos\Theta. \tag{2.27}$$

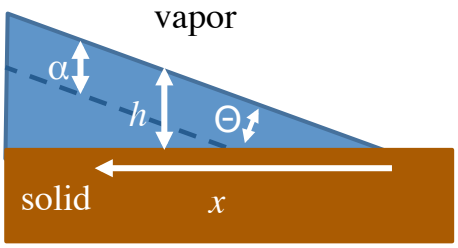

Figure 2.24.: Estimation of the distance to cover the fresh surface with the same amount of surfactant molecules like the bulk surface. After [56]

The freshly built surface has a higher surface tension than the surface far away from the contact line, which leads to a gradient in the surface tension. As a consequence of the Marangoni force the contact angle changes.

This hypothesis can explain the measured effects of the change in the contact angle by adding surfactant to the liquid. The stronger effect for higher surfactant concentration can be explained with the higher gradient in surface tension. To proof these hypothesis for example the surface tension gradient close to the contact line should be measured. Since this is not easily possible instead of the surface tension gradient the flow profile near the CL can be measured. Since the surface tension gradient close to the contact line influences the flow behaviour close the CL.

2.7.1 Flow behaviour inside the container

Depending on the amount of liquid in the setup the container is filled above / under the axis (A,C) or up to the axis (B). This filling height influences the flow possibilities of the liquid in the setup. In the first case the liquid can flow along the surface as well as through the bulk. Is the liquid filled up to the axis of the drum, the surface is interrupted by the axis of the drum and therefore the flow along the surface is blocked. To reduce also the flow through the bulk an external barrier can be placed in the setup, this barrier has only a small gap ($\approx 1\,\mathrm{mm}$) to the rotating drum. This barrier is described in more detail in [55]. For water the flow behaviour inside the container has no significant result on the measured dynamic contact angle. Nevertheless for surfactant solution the filling height influences the measured dynamic contact angle [55]. The exchange of the surfactant molecules from the advancing and receding side can be blocked along the surface, which results in a stronger decrease of the contact angle for the same surfactant concentration. To have comparable results in this work all measurements were done for the case (B), were the liquid is filled up to the axis.

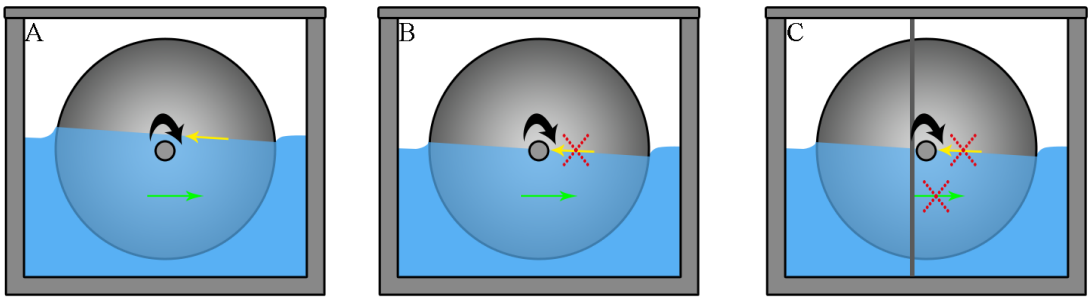

Figure 2.25.: [A] liquid is filled above the axis, which allows a flow along the surface and through the bulk [B] liquid is filled up to the axis, which blocks a flow along the surface and allows the flow through the bulk. [C] liquid is filled to the axis, an external barrier blocks additionally the flow through the bulk. After [55]

2.8 Flow-profile

To measure the flow profile of a laminar flow, some kind of tracers, for example particles dispersed in the liquid are required. These particles must be small enough to avoid changes in the flow by the particles and they must be visible. Furthermore the motion on the particles induced by the flow must overcome the Brownian motion of the particle

[52, 90, 121, 153]. Additionally the density of the particle and the liquid must be similar ($\Delta\rho = 0$) to the liquid, to avoid sedimentation and flotation.

2.8.1 Particle tracking

In this work the tracers are either imaged with an optical high speed camera or with a fast confocal microscope (see section 2.9). To analyze the flow from the video, the particles and their trajectories must be clearly detectable. This implies that the volume concentration must be relatively low, that the inter-particle distance is at least one particle diameter. Additionally, the motion of the particles between two frames should be less than half of the particle diameter [39].

2.8.2 Landau-Levich flow-profile

Mayer et al. [110] measured the flow profile for Landau-Levich film formation [89], i.e., for the case that no contact line exists anymore and a complete film is pulled out of the liquid (compare section 2.3.3). In this experiment they used a plexi glass tank and pulled out a glass plate. To visualize the flow profile they placed tracer particles in the liquid. By using a laser sheet to illuminate the particles in one focal plane vertical to the glass plate, they imaged the flow profile. Instead of tracking the particles they chose a longer exposure time so the flow can be seen due to motion blurring, figure 2.26. This technique of measurement has the advantage, that the flow profile can be seen directly in the picture. However, it has the disadvantage that the exact velocity at a defined position can not be determined.

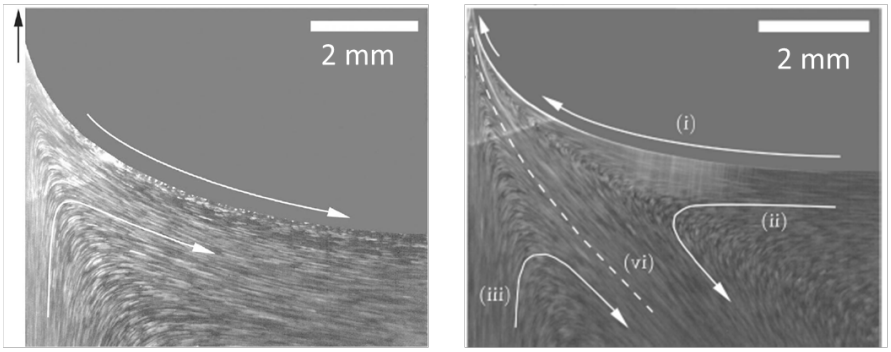

Figure 2.26.: Flow profile for Landau-Levich film formation at a velocity of $1.27\,\mathrm{mm\,s^{-1}}$. Left: pure water measurement, right 50 % CMC of SDS. Reprinted with kind permission from [110]

For pure water solutions the liquid moves with the solid up and flows back to the bulk on the surface (figure 2.26, left). By adding surfactant molecules (50 % CMC of SDS) to the solution the flow field for Landau-Levich flow changes. Instead of a flow on the surface back to the bulk the flow on the surface is in the opposite direction towards the film (figure 2.26, right).

2.8.3 Flow profile with contact angle

To proof the hypothesis described in section 2.7 the flow behaviour close to the CL can be measured. In contrast to the Landau Levich film formation in all the measurements shown in this work a contact angle is presence which results in a different flow profile. As already mentioned the addition of surfactants to the pure liquid should change the flow profile. For the case that the flow profile changes in the same way like for the film formation, the earlier described hypothesis can not be true. Especially, a surfactant-induced change in the flow profile like shown by Mayer et al. [110] would be incompatible with the hypothesis. If the flow profile would change in a similar way no fresh surface would be created, which results in the Marangoni stress towards the three phase contact line. [55, 64] measured the flow profile inside the rotating drum setup near the three phase contact line. To do so they added silica particles to the rotating drum setup in pure water and 10 % CMC CTAB solution. In contrast to [110] they track the tracer particles. By measuring the trajectories of the particles the flow profile can be determined (figure 2.27 A and B).

The flow inside the liquid follows the solid drum surface and goes up to the CL. Along the liquid surface the liquid flows away from the contact line. This flow in the dewetting case did not change within the measuring resolution irrespective of the presence and concentration of surfactant (CTAB). Possible aggregations of the silica particles due to charging effects with the CTAB surfactant molecules do not play a role while analyzing the flow profile. Due to reflections from the air-liquid interface and the small quantities (≈ 0.05 wt %) of particles the flow closer than ≈ 300 µm to the CL could not be clearly visualized.

To visualize the flow closer to the CL a micro tube system is used as described in [4]. The setup consists of a micro tube, where liquid slugs separated by air bubbles flow though (figure 2.28). With this setup the flow profile close to the contact line can be resolved up to 100 µm. The micro tube has a better resolution than the rotating drum setup. One disadvantage in comparison with the rotating drum setup is, that the contact line is moving and can only be imaged for the time that it moves across

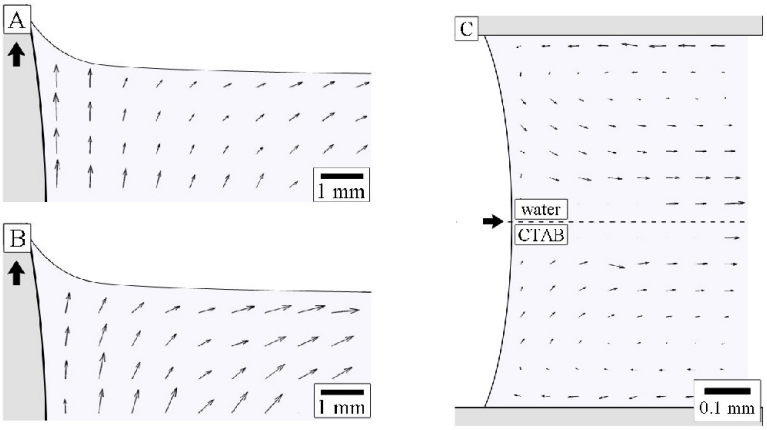

Figure 2.27.: Measured flow profile. A: in the rotating drum setup for pure water, B in the rotating drum setup for 10 % CMC CTAB solution at a velocity of 20 mm s^{-1}, C: in the micro tubing system at a velocity of 0.3 mm s^{-1}. The flow profile for pure water is shown at the top, the flow profile for 100 % CMC CTAB is shown at the bottom. In both setups the flow profile did not change by adding surfactant to the liquid within the measurement resolution [64]-Published by the Royal Society of Chemistry.

the picture. Therefore, the velocities were with around 0.3 mm s^{-1} slower than for the rotating drum setup to increase the observation time.

The flow profile inside the micro tube near the air liquid interface was measured by adding carboxylated polystyrene micro particles and analyzing the trajectories of the particles [64]. The flow was symmetric and showed one circular vortex. By adding the surfactant CTAB the flow profile did not change as well in the visible measurement range (figure 2.27; top: water, bottom: 100 % CMC CTAB). Also variations of the absolute value of the flow velocity did not influence the flow profiles close to the contact line, as long as the critical velocity of film formation was not exceeded. So in the measuring resolution of this setup (approximate 100 µm) the flow profile does not change by adding surfactant to the liquid. This implies that the flow profile for the presence of a contact angle differs from the flow profile measured by Mayer et al. [110] for the case of film formation (see section 2.8.2).

In these setups it is not possible to measure a change in the flow profile by adding surfactant solution. To understand, why it is not possible, it is interesting to know the equilibrium distance between the surfactant in the bulk and the area near the three phase contact line. As described in section 2.7 it is possible to approximate by a simple diffusion model the distance to the CL at which enough surfactant molecules are presence to reach an equilibrium surface coverage than far away from the CL. For

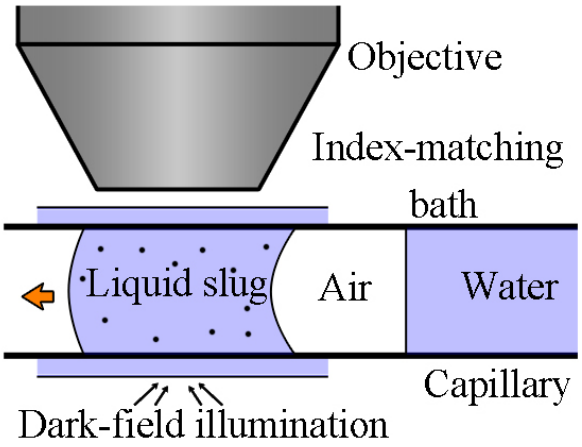

Figure 2.28.: Sketch of the micro tube setup to measure the flow profile close to the CL. [64] - Published by the Royal Society of Chemistry.

a CTAB solution with 0.9 mmol L^{-1} they estimated an equilibrium distance of 20.3 µm [56]. So the change caused by the surfactant happens in a region of a characteristic size of 20 µm. Therefore, the region, where the change in the flow profile is assumed to happen by adding surfactant to water, is smaller than the measurement resolution. Nevertheless the measurements show that all neglected effects in the assumption do not show up in the change of the flow profile at a length scale of 100 µm.

2.9 Confocal microscopy

For a higher image spatial resolution of the flow profile a confocal microscope is used in this work. A confocal microscope is a special kind of a light microscope. Instead of acquiring a whole picture instantaneously, the picture is scanned point by point. In a confocal microscope a whole picture is never taken at the same time. The first confocal microscope, which took the picture point by point, was constructed by Marvin Minsky 1955 [112] and patented 1957 [111].

The used light goes trough the microscope and is reflected on the surface back to the microscope. The reflected light goes back in the microscope and passes a pinhole. Only the light reflected by the surface which is in focus height can pass the pinhole, all reflected light on other surface height than the focus one gets blocked. By moving the sample or the microscopes objective the sample can be imaged in different height positions.

2.9.1 Laser confocal microscope

As light source a laser is used which rasters through the sample by using scanning mirrors. The scanning mirrors can move the detection volume horizontal and vertical to scan the whole 2D frame. For a 3D images additionally the objective or the sample can be moved to generate 2D images at different heights, which results in a 3D image.

For this work a home built laser scanning microscope is used. The working procedure of a confocal microscope will be explained on the example of the home built laser scanning microscope, but other laser scanning microscope work in a similar way. This setup was used for a series of earlier publications [6, 72, 135, 136, 168, 169].

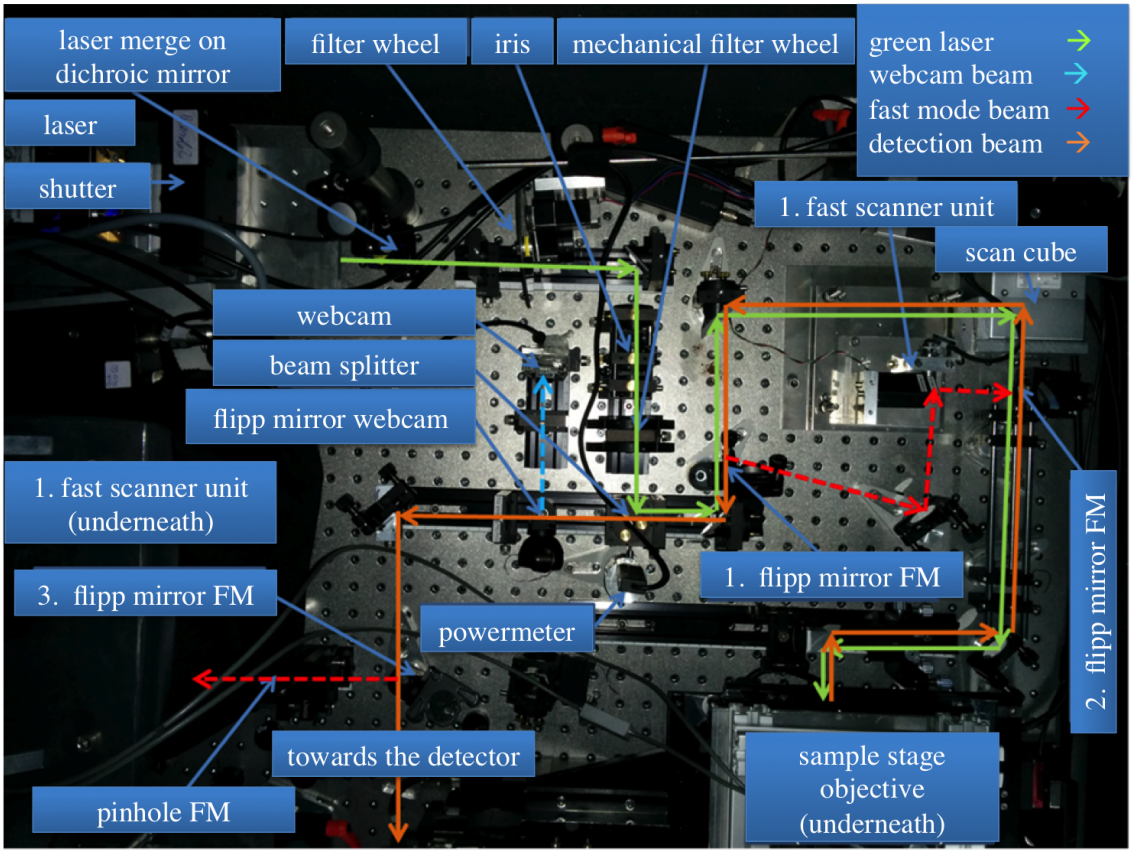

Figure 2.29.: Picture of the home build microscope, with schematically indrawn beam lines. The green line shows the excitation beam path, the orange one the detection beam path. The red dashed line represents the alternative beam path of the fast mode and the blue one is the beam path towards the webcam.

An image of the used confocal microscope and its optical path is shown in figure 2.29. The laser (Cobolt Samba™, wavelength: 532 nm, maximum power: 25 mW, Cobold

AB[2]) is used as light source. At first the laser goes through a shutter, which allows to shut of the laser from the rest of the optical path, which is necessary due to safety reasons, e.g. to place for example the sample on the microscope. Afterwards the laser pases a filter wheel that allows varying the laser intensity over four orders of magnitude. Next the laser beam passes some optical components to optimize the quality of the laser beam (a telescope with two lenses and one iris). Behind this the laser beam passes an additional filter wheel to adjusted the laser strength further. The laser beam is now splitted in two parts by a beam splitter cube (50/50). One part of the beam is going to a power meter, which allows to detect the laser strength which reaches the sample. The other part is going to the scanning galvanic mirrors (SCANcube®7[3]) in this setup. This scan cube consists of two movable mirrors, which move the laser beam horizontal and vertical to scan the whole sample. The laser beam passes through a telescope and enters afterwards the objective. Due to the telescope, the divergent scanning of the scan cubes is transfered in a rotation of the laser at the entrance of the objective. The objective is mounted on a piezo stage and allows therefore the movement of the focus plane in z direction. Together with the scan cubes this allows the 3 dimensional imaging of objects.

There are two different options to image an sample in a confocal microscope. In the refection mode, the light is reflected at interfaces between materials with different indices of refections. The reflected light is collected by the objective. Alternatively, in the fluorescent mode, the laser beam excites a fluorescent dye that emits light at a higher wave length, which is again collected by the objective. The detection beam path uses the same optical path back to the beam splitting tube like the laser going to the objective. Behind the beam splitter the detection beam is going to the detectors. Inbetween the detection beam can be redirected by the help of a flip mirror to a webcam to control the laser beam quality during alignment. Two independent photon counters were used as detectors, which allow the detection of the reflecting and fluorescent light simultaneously by using filters to separate the different wave lengths. The usual pixel rate is 200 kHz (0.7 fps for 512x512 pixels image). An example image of this mode is shown in figure 2.30 on the left side.

Additionally to the explained beam path the home made confocal microscope has an additional mode, the so called fast mode. Instead of counting photons the whole image is scanned directly on a 2D detector. To do so two 2D-scanning units are necessary which scan the sample and the detector synchronized. The fast mode has therefore one synchronized pair of resonant mirrors working together with two galvanic mirrors to

[2] Cobold AB, Vretenvägen 13, SE-171 54 Solna, Sweden, www.cobolt.se
[3] SCANLAB GmbH, Siemensstraße 2a, 82178 Puchheim, Germany,www.scanlab.de

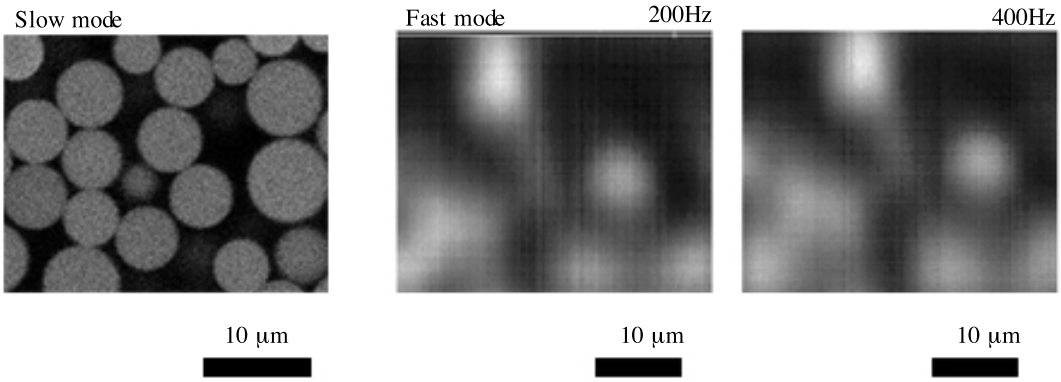

Figure 2.30.: Pictures acquired in the two modi of the home built microscope. Left side is a picture done in the slow mode and right two pictures made with the fast mode with 200 fps and 400 fps.

back scan the image on a CCD chip [6]. In the slow mode, the single photon detection units work as pinhole. Since in the fast mode this is not possible, an additional pinhole is used to vary the focal depth of the 2D image. This mode has a much higher frame rate of 2D images, but does not allow 3D images (at the moment). For a 3D image the objective could be moved by the piezo, but this is on one hand too slow and on the other hand the fast movement of the objective close to the sample generates distortions in the sample. The frame rate of the fast mode is between 50 - 400 Hz. Images done with the fast mode are shown in figure 2.30 on the right side. To allow the usage of two modes on one confocal setup the fast mode is switched on by using flippable mirrors. This means, that if the fast mode is used some mirrors are flipped into the optical path of the slower mode to change the optical path partially. This flipping of the mirrors is one of the biggest challenges in the aligning of the fast mode setup, since the fast and the slow mode cannot be aligned independently.

2.9.2 Confocal white light microscope

For measuring the topography of surfaces, a confocal white light microscope can be used. This microscope works with white light. Instead of moving the focus point by mirrors a so called Nipkow disk is used. This is a rotating disk with multiple pin holes inside. Therefore, various focus points are used, which decrease the measurement time significantly. The remaining light is detected on a CCD chip. The used confocal white light microscope in this thesis is a Nano Focus μsurf®[4].

[4] NanoFocus Ag, Max-Planck-Ring 48, 46049 Oberhausen, Germany,www.nanofocus.de

2.10 Aim of the present work

In many application the dewetting of complex liquids like surfactant solutions plays an important role, for example in the cleaning industry as well as the printing industry. Therefore, I want to investigate in this thesis the influence of surfactant on the dewetting behaviour.

On one side I want to investigate the wetting behaviour on a smooth surface. Therefore, I measure the wetting behaviour of different surfactants. The influence of the charge of the surfactant was investigated. Therefore, I use anionic cationic and nonionic surfactant. To investigate the influence of the critical micelle concentration CMC of a surfactant on the dewetting behaviour I use various of nonionic surfactants with four orders of difference in the CMC. The variation of CMC changes the amount of surfactant molecules, which are presence at the same concentration of % CMC. In comparison with previous work I use a smooth surface with a static contact angle close to 90°. This allows a quantitative comparison of forced dewetting experimental data with the theoretical hydrodynamic models.

The wetting and dewetting behaviour is not only influenced by the liquid, but also by the surface. The influence of the surface structure is one of the important parameters, since in the most industrial processes the surface is not homogeneously smooth, but structured. One example is the offset printing industry, where structured as well as smooth surfaces are wetted and dewetted several times during the printing process. To investigate the influence of the structure in combination with complex liquids, like surfactant solution, a new setup is designed which allows to mount various surfaces in a rotating drum setup. With the help of this setup the influence of the surface structure with and without the presence of surfactant is be investigated. This helps to create a deeper knowledge on the dewetting of structured surfaces and helps most likely to improve the results in some printing processes by a better understanding of the physical mechanism of the dewetting behaviour on such a surface.

All these previously mentioned experiments are done on a macroscopic length scale, but previous experiments show (section 2.8.3) that the flow profile close to the three phase contact line does not change on the macroscopic length scale. Even on a 100 µm length scale the flow behaviour does not change by adding surfactant to the solution. But since macroscopic changes by adding surfactant, due to Marangoni force, can be observed, something must happen on a microscopic length scale. Estimations of the length scale show, that the change should happen in the last 20 µm (section 2.7). Therefore, a new setup is designed, which allows to measure the flow profile close to the three

phase contact line on this length scale by using a fast confocal microscope (section 2.9) as imaging method.

3 Macroscopic study

Most of the content in the following section of the macroscopic dewetting on smooth surfaces is published in [64]. The measurements of the surfactants were all done by myself, excluding the NMR measurements (section 3.3), which are done by Manfred Wagner (Max Planck Institute for Polymer Research), where only the sample preparation was done by myself. The software to fit using the equations 2.11, 2.12, 2.13 was written by Günter Auernhammer. The fitting of the data was done by myself. The section of the dewetting on structured surfaces is based on the work published in [65]. All of these measurements were done by myself.

3.1 Material

In the following chapter, I compare six different surfactants to investigate the influence of the charge as well as of the critical micelle concentration (CMC). I used cetrimonium bromide (CTAB) as a cationic surfactant (positively charged), sodium 1-decanesulfonate (S-1DeS) and sodium lauryl sulfate (SDS) as anionic surfactants (negatively charged) and three nonionic surfactants (non charged): butyl glycole (C_4E_1), octyl triglycole (C_8E_3) and dodecyl pentaglycole ($C_{12}E_5$) with a variation of the CMC of four orders of magnitude. Cetyl trimethylammonium bromide ($(C_{16}H_{33})N(CH_3)_3Br$), sodium 1-decanesulfonate ($C_{10}H_{21}SO_3Na$), sodium dodecyl sulfate ($C_{12}H_{25}OSO_3Na$), Octyl triglycol ($C_8H_{17}(OCH_2CH_2)_3OH$) and dodecyl pentaglycol ($C_{12}H_{25}(OCH_2CH_2)_5OH_4$) were purchased from Sigma-Aldrich[1] and butyl glycol ($C_4H_9OCH_2CH_2OH$) from Alfa Aesar[2]. All surfactants were used without further purification.

The milli-Q Water was prepared by using an Arium®611 ultrapure water system (Sartorius[3]) or Arium ®pro VF/UF & DI/UV (Sartorius) at a resistivity of 18.2 MΩ m.

The molecular weights of surfactants are provided by the manufacturer Sigma Aldrich and Alfa Aesar. The CMC is measured with the Wilhelmy plate method (section 3.2). The diffusion coefficient is measured by nuclear magnetic resonance spectroscopy (NMR) (section 3.3). The important properties of the surfactants are summarized in

[1] Sigma-Aldrich Chemie GmbH, Eschenstrasse 5, 82024 Taufkirchen bei München, Germany, www.sigmaaldrich.com

[2] Alfa Aesar, Thermo Fisher (Kandel) GmbH, Postfach 11 07 65, 76057 Karlsruhe, Germany, www.alfa.com

[3] Sartoris AG, Weender Landstraße 94-108, 37075 Göttingen,www.satorius.de

Table 3.1.: Properties of the used surfactants.

	name	type	CMC [mM]	molecular weight [$g\,mol^{-1}$]	surface tension at CMC [$mN\,m^{-1}$]	diffusion coefficient [$10^{-10}\,m\,s^{-2}$]
SDS	Sodium dodecyl sulfate	anionic	8	288.4	-	-
CTAB	Cetrimonium bromide	cationic	1	364.45	35.2	5.4
S-1DeS	Sodium 1-decane sulfonate	anionic	38.5	244.33	39.7	6.98
C_4E_1	Butyl glycole	nonionic	1200	118.17	27.9	9.3
C_8E_3	Octyl triglycole	nonionic	7.5	262.39	27.3	4.6
$C_{12}E_5$	Dodecyl pentaglycole	nonionic	0.07	406.60	30.7	2.9

table 3.1. The measuring method for the diffusion coefficient as well as of the surface tension and of the CMC are explained in more detail in the following sections.

3.2 Wilhelmy plate measurements

For measuring the CMC of the used surfactant the tensiometer DATAPHYSICS[4] DCAT11EC is utilized. This tensiometer consists of a precision electro dynamic compensation weighting system with automatic calibration. The principle of this measuring method is described in section 2.2.2. The used Wilhelmy plate is a thin platinium-idium plate (length l: 19.9 mm; thickness t: 0.2 mm) which is placed in the liquid. The plate is on one side pulled down by the weight force and pushed upwards by the buoyancy force. To measure the the difference between these two forces, this plate is connected

[4] DataPhysics Instruments GmbH, Raiffeisenstrasse 34, 70794 Filderstadt, Germany, www.dataphysics.de

the weighing system, which measures the force needed to keep the plate at a fixed position. This force is given by:

$$F_{\gamma\Theta} = 2l\gamma\cos\Theta. \tag{3.1}$$

The use of a roughened platinum-indium on which the most liquids have a contact angle of 0° ($\cos\Theta = 1$) allows calculating directly the surface tension γ from the measured force. To do so, it is important to have a really clean surface, since every contamination would increase the contact angle. With this setup the surface tension of all used surfactant solutions is measured (figure 3.1). Before measuring all used laboratory devices were cleaned for 15 min in an ultrasonic bath with isopropanol, rinsed with milli-Q water afterwards and dried with ultra pure gaseous nitrogen. At the beginning of every measurement the surface tension of milli-Q water was measured at least twice with a 5 min break between the measurements. Only if the surface tension was stable at $72 \pm 0.5\,\mathrm{mN\,m^{-1}}$ the measurement was started. The surfactant solution was stepwise added with an eppendorf piped (with epT.I.P.S®) [5] to the liquid and stirred with a magnetic stirring bar for two minutes. Afterwards I waited for additional two minutes before the next surface tension was measured. The eppendorf tips were used since their usage show no measurable contamination of the liquid.

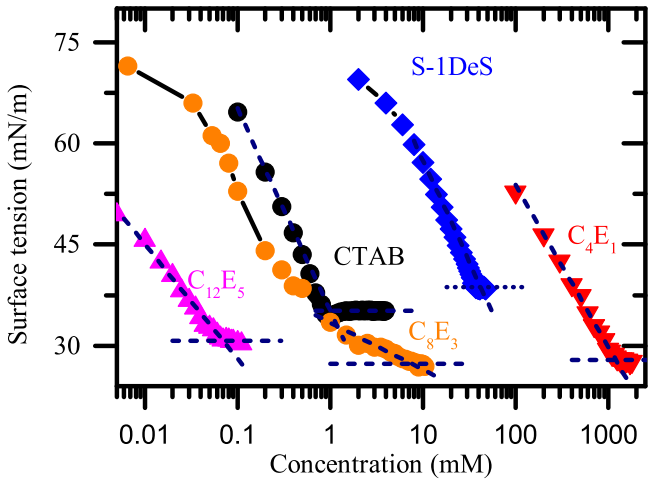

Figure 3.1.: The surface tension is measured with a Wilhelmy plate. The critical micelle concentration of CTAB is 1 mM, of S-1DeS 28.5 mM, of C_4E_1 1200 mM, of C_8E_3 7 mM and of $C_{12}E_5$ 0.07 mM.

[5] Eppendorf Vertrieb Deutschland GmbH, Peter-Henlein-Straße 2, 50389 Wesseling-Berzdorf, Germany, www.eppendorf.com

The results are summarized in table 3.1. To determine the critical micelle concentration a logarithmic concentration dependence and a constant surface tension are fitted on the measured data. The logarithmic fit to the decreasing part of the curve and the constant surface tension to the flat part of the curve (see section 2.4.1). The intersections of these two fitted curves represent the critical micelle concentration. The results are summarized in table 3.1. The measured values of the critical micelle concentration are comparable with the literature values [133, 119, 114].

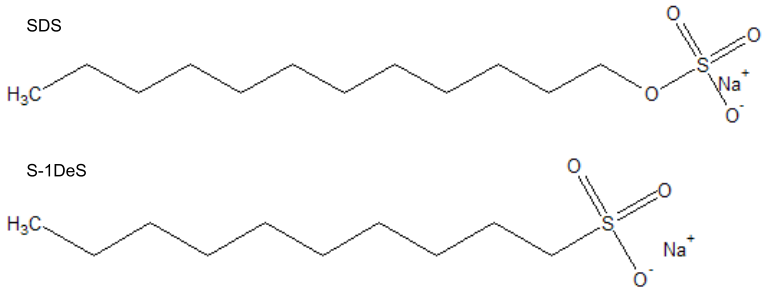

Figure 3.2.: Chemical structure of SDS and S-1DeS.

The S-1DeS was chosen, because the more common surfactant SDS shows an increase of the surface tension of more then $5\,\mathrm{mN\,m^{-1}}$ after it reaches the CMC. This increase might be caused by the hydrolysis of SDS in water. Since I want to be sure that the used surfactant is clean and stable during the whole measurement, I chose the surfactant S-1DeS, which has a similar chemical structure (figure 3.2) and the same charge. In comparison to SDS S-1Des does not show this artifact after reaching CMC (figure 3.3).

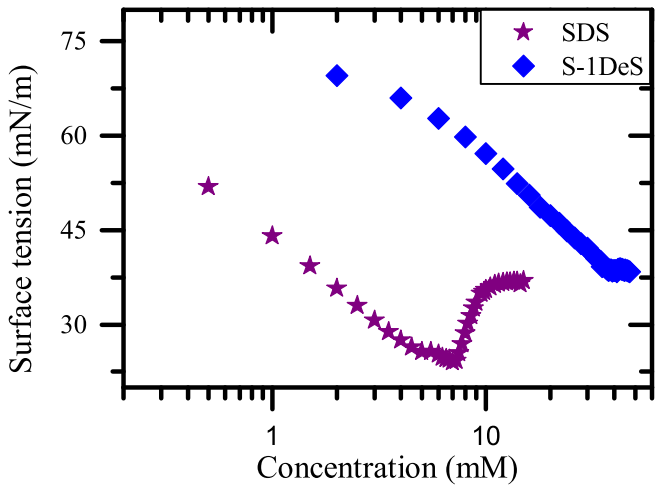

Figure 3.3.: The surface tension of SDS increases after reaching CMC, in comparison S-1Des does not show this artifact after reaching CMC.

3.3 NMR-Measurements

To analyze the diffusion coefficient of the surfactants gradient nuclear magnetic resonance (NMR) measurements were performed. To conduct the ^{1}H-NMR experiments combined with the diffusion measurements (DOSY) [150] a 850 MHz Bruker[6] AVANCE III system equipped with a special 5 mm triple resonance TXI ^{1}H/ ^{13}C/^{15}N probe with a z-gradient was used. To enable diffusion measurements a 2D sequence (DOSY, stebpgp1s19) with a stimulated echo has been utilized with a stimulated echo and additionally water suppression (3-9-19 pulse sequence with gradients) [76]. The temperature was regulated with a standard 1H methanol NMR sample using the topspin 3.1 software (Bruker) at a temperature of 25.1 °C with a accuracy of ± 0.1 K by using a VTU (variable temperature unit). The respective strength of the gradient was varied in 16 steps between a minimum of 2 % and a maximum of 100 %. For the optimization of the diffusion time 30 ms and a gradient length of 1.2 ms were adjusted. The latter was calibrated by analyzing a sample $^{2}H_2O/^{1}HH_2O$ and comparing it with the theoretical diffusion coefficient of this element. To guarantee a strong diffusion weighting the diffusion gradient amplitudes were alternated during 16 experiments linearly from 1 to 53 G/cm (10 up to 470 mT m^{-1}). The resulting coefficients of the diffusion were in this work calculated for the integrated peak areas, making use of an exponential decay fit function covering all 16 spectra:

$$S_i = S_0 exp(-D b_i). \tag{3.2}$$

The diffusion sensitivity factor b_i was calculated using

$$b_i = (2\pi g_L G_i)^2 \left(\Delta - \frac{d}{3}\right). \tag{3.3}$$

Here g_L represents the gyro magnetic ratio of the observed nucleus, G_i the gradient strength, d the length of the gradient (1.2 ms), and Δ the diffusion time (30 ms). The analyzed diffusion coefficients are summarized in table 3.1.

[6] Bruker GmbH, Dynamostraße 19, 68165 Mannheim, Germany, www.bruker.com

3.4 Rotating drum setup

3.4.1 Old setup

The old setup is described in section 2.6.1. This setup was used for measuring the contact angle of different surfactant solutions on a smooth PS surface and to compare the measured results with the experimental results described in [55] (see section 4). As described this setup has some disadvantages regarding the possibilities to clean the setup, the flexibility and the observation possibilities. To overcome this problems a new setup was designed, which is described in detail in the following section.

3.4.2 New developed setup

To allow a better cleaning of the setup and to have the possibility to use different solvents than water in the setup a liquid container as well as a new drum was designed, which allow to analyze the wetting and dewetting behaviour on different kinds of solid surfaces.

Liquid container

The old setup is build out of PVC and is therefore not stable against solvents like for example acetone and toluene. Additionally the parts of the container are glued together, which makes the cleaning of the setup even more difficult. Since there were major problems achieving a proper cleaning of the old setup due to the PVC a new setup was designed. This liquid container is built completely of stainless steel and is therefore stable against most solvents. To allow a separate cleaning of every part of the container, the new liquid container is screwed together instead of being glued together.

To allow a better imaging of the contact angle as well as of the contact line the size of the window was increased. Additionally more windows are include in the setup, which allows an imaging of the receding and advancing contact angle at the same time. For measuring both angles at the same time it is also necessary to increase the size of the liquid container. In the old container the drum was placed asymmetrical and only at the side where the contact angle could be measured, the distance between drum and wall of the container was large enough to be sure that no wall effects influence the measurement. In the new setup the drum is placed in the middle of the liquid container and the distance from the drum surface to the wall is on both sides similar to the measuring side in the old setup. The new setup has also a cover with a window, which

has the possibility to connect a humidity control to the setup. This allows to measure not only under room condition (open cover) and saturated atmosphere (closed cover), but also under other atmospheres conditions, regarding humidity, other gases as well as different temperatures. Nevertheless in this work all measurements were done at a relative humidity higher than 90 % at room temperature.

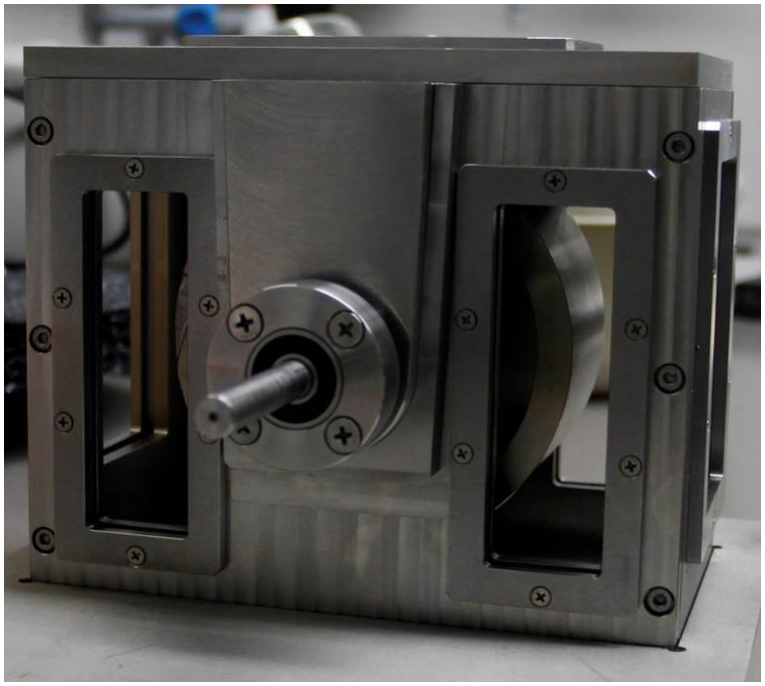

Figure 3.4.: Image of the newly build liquid container

Since we want to have the possibility to measure the wetting and dewetting behaviour of other solvents than water it was necessary to change the sealing system. The new setup is sealed on every fixed connection with polytetrafluoroethylene (PTFE). Therefore, four layers of PTFE tape (width: 12 mm, thickness: 0.1 mm) were placed in-between the side walls and between the side walls and the bottom. Around the windows and the side walls a PTFE thread with a diameter of 2.5 mm was placed to seal this connection. The drum is pivot-mounted in 10 mm ball-bearings. The dynamic connection between the liquid container and the rotating drum is sealed with a packing gland from EagleBurgmann[7]. Each side consists of four rings with thickness of 4 mm and an inner diameter of 10 mm and an outer diameter of 14 mm. The drum itself is rotated with the same motors like the old setup. The packing gland sealing results in a higher initial tension, which results in a smoother motion of the drum at lower velocities, but therefore a higher motor force is necessary. To vary the velocity comparable to the old

[7] EagleBurgmann, Äußere Sauerlacher Straße 6-10, 82515 Wolfratshausen, Germany, www.eagleburgmann.de

setup 4 different motors from the company Faulhaber[8] ,with a more stable gearing for the motor with the lowest velocity range, were used, to allow to vary velocity between 0.015 round/min - 150 round/min. The whole setup is shown in figure 3.4. The technical drawings of this new setup can be found in the appendix figure A.1 - figure A.15

Rotating drum

Curved surfaces

For measuring the contact angle on a smooth surface the same drum like in the old setup could be used. However, the axis must be extended, because the sealing of the rotating axis with packing gland of the drum needs a longer axis. Therefore, the axis of the old segment of a sphere drum is drilled out and a longer axis is forced in. To reach a smooth, homogeneous and hydrophobic surface the drum is coated with PS, the coating procedure is described in section 2.6.1.

Exchangeable surfaces

To allow measuring a broad range of surfaces and an investigatation of their wetting behaviour, a new drum was constructed, which allows fixing more or less any kind of solid and bendable surfaces. This was achieved by constructing a drum on which different surfaces can be fixed and which makes an exchange easily possible. This is realized with different clamping systems on the flat cylinder. The first clamping system is embedded in the drum to have as little perturbation as possible of the clamping system on the wetting behaviour. The exchangeable surface is fixed with a rounded down wedge on one side directly on the drum. On the other side it is fixed between two metal plates. On these metal plates it is fixed with a dovetail joint on the rotating cylinder. To clamp the exchangeable surface on the surface of the drum to the second metal part springs are connected, which are on the other side connected on the drum. Depending on the kind of spring different forces can be achieved to strain the surface on the drum surface. To reach less perturbations a rounded cap is mounted over the fixing part of the drum. A technical drawing shown in figure 3.5 depicts the rotating drum. All other technical drawings of this drum can be found in the appendix figure A.16 - figure A.24. This method of fixing allows only the fixing of material with a width up to 80 mm and a length between 290 to 300 mm. Shorter materials could not be mounted with this

[8] Dr. Fritz Faulhaber GmbH & Co. KG, Daimerstraße 23, 71101 Schöneich, Germany, www.faulhaber.de

fixing mechanism, additionally the material must be relatively bendable, otherwise it will break by clamping.

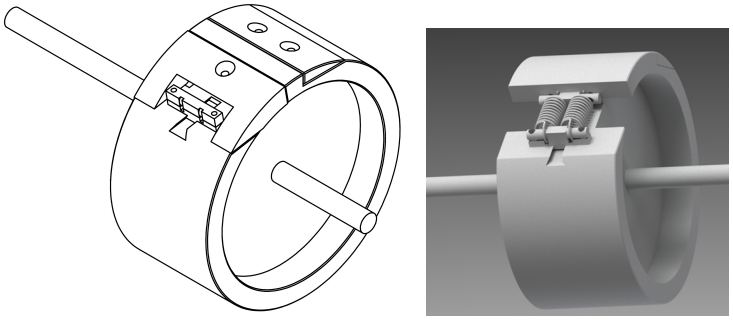

(a) (b)

Figure 3.5.: (a),(b) Technical drawing of the rotating drum, which allows fixing a printing plate on the surface.

To allow also fixing of shorter and/or stiffer surfaces a second fixing system was developed. Thereby the rounded down wedge is exchanged by an wedge with a tangential angle. This allows to fix also stiffer materials to the drum. The other end of the surface is fixed between a metal wedge and a stainless steel plate. The metal wedge is connected to the metal part with the dovetail joint by a stainless steel wire. This allows to fix every length of material on the drum. However, this fixing system generates more hydrodynamic perturbation in the bath than the first fixing system described above. This new drum has the advantage, that an easy fixation of different surfaces on the drum is possible. In this work different printing plates were mounted with the second fixing technique on the drum (section 5).

3.4.3 Motor Speed

For a variation of the velocity four different motors can be connected to the drum of the new and the old setup. With these motors the velocity can be varied between $0.1\,\mathrm{mm\,s^{-1}}$ to $1000\,\mathrm{mm\,s^{-1}}$ theoretically. The real velocities of the drum were checked by tracking some scratches on the surface of the drum. Therefore, the drum was rotated at different velocities in the empty liquid container and the drum surface was imaged with a high speed camera Photron S1 with illumination trough the objetive (frame rate 500-10 000 fps). Since the images of the surface were done at the height of the drum axis the curvature is much smaller then the radius of the drum and therefore the velocity can be measured in the picture directly. To do so the movement of a single defect on the surface of the uncoated drum, from one to the next frame, was measured. With

the help of the frame rate the real velocity can be calculated. This was done for the every velocity for more than one defect and over more than 100 picture pairs. The results were averaged and are shown in figure 3.6. They reveal a good agreement of the adjusted velocities (yellow dashed line) and the measured ones.

The velocities for this comparison were calculated with the diameter of the drum d and the adjusted velocity $v_{adjusted}$.

$$v_{calculated} = 2\pi d\, v_{adjusted} \tag{3.4}$$

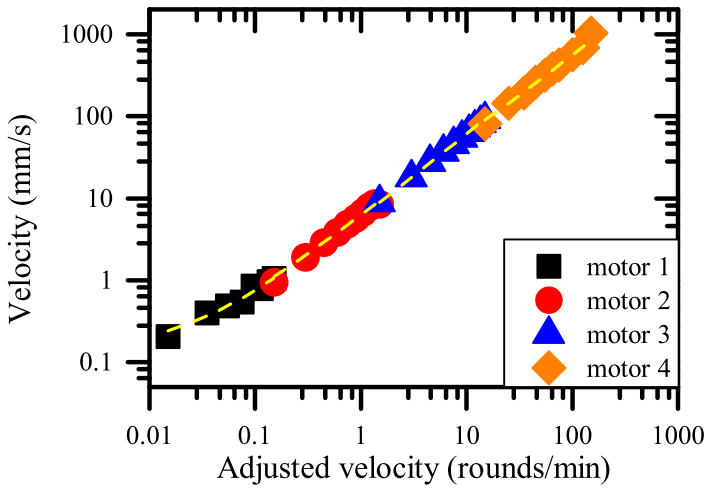

Figure 3.6.: Motor velocities of the rotating drum setup (adjusted vs. measured speed). The dashed yellow line represents the calculated velocities (equation 3.4) and the symbols the measured velocities for different motors.

The single motor velocities can be fitted with a straight line ($v = m v_{adjusted} + n$). The values for m and n are summarized in table 3.2. These fitted velocities were used in this thesis to calculate the velocities of the rotating drum surface.

Table 3.2.: Values of the motor velocity fit ($v = m v_{adjusted} + n$)

motor number	adjusted velocity [round/min]	measured velocity [mm s^{-1}]	m	n
1	0.015 - 0.15	0.24 - 1.07	6.1095	0.1490
2	0.15 - 1.5	1.1 - 9.2	6.0078	0.2093
3	1.5 - 15	9 - 92	6.1378	-0.3612
4	15 - 150	89 - 830	5.4843	7.2146

3.5 Experimental procedure

The milli-Q water was filled up to the axis of the drum, to avoid exchange of molecules along the surface (see section 2.7.1) [55, 56]. For the old liquid container 0.9 L were used and for the new one 1.0 L. For measuring surfactant solution the surfactants were added stepwise in the liquid container and stirred for at least 20 min at 100 mm s^{-1}, to reach an equilibrium state of surfactant molecules adsorbing to and absorbing from the surface. At this rotation velocity I can assume a turbulent flow and therefore a good mixing in the setup. By measuring the contact angle the interesting area is around 2 mm. At this lenght scale a laminar flow can be assumed in the region. The meniscus shape was imaged by a high speed camera (Photron[9], Fastcam SA-1, 12x magnification, working distance about 30 cm, 250 - 500 frame/s) with bright field illumination. To avoid temperature increase due to an infrared component of the illumination, a LED light source (Volpi[10], intraLED 3) was used. All measurements were done at room temperature (21 °C) in a closed setup with water saturated atmosphere. For analyzing the contact angle on smooth surfaces the segment of a sphere drum coated with PS was used, for the structured surface measurements of the drum with exchangeable surfaces was used. The contact angles were measured from the side view image by fitting straight lines to ten randomly selected pictures in the video to the drum surface and the water surface close to the CL with imageJ. The angle between these two lines is the measured contact angle. The error of the measured contact angle is ±3°. An example picture of the contact angle of water at 117 mm s^{-1} is shown in figure 3.7.

After one measurement series the setup was rinsed over night with flowing tap water and afterwards immediately for 1 h with milli-Q water, to avoid calcification in the setup. To guarantee a clean setup I measured after the first coating the surface tension of pure water directly after filling and after a waiting time of one hour. Both times the surface tension was around 72 mN m^{-1}. Since the surface tension did not change a clean setup can be assumed. As indicator for a clean setup after the cleaning procedure I used the fact, that for pure water the contact angle and the film formation velocity does not change over time. Since the surface tensions are stable the contact angle must be stable as well ($\gamma_{lv}\cos(\theta) = \gamma_{sv} - \gamma_{sl}$, whereby lv, sv, sl stands for the liquid vapor, solid vapor and the solid liquid interface [173, 174], see section 2.1.1). If the contact angle does not change a clean setup was assumed and the measurement was started. For the case that the contact angle changes over time the cleaning procedure was started again

[9] Photron, The Barn, Bottom Road,West Wycombe, Bucks, HP14 4BS, United Kingdom, www.photron.com

[10] Volpi AG, Wiesenstrasse 33, CH-8952 Schlieren, Switzerland, www.volpi.ch

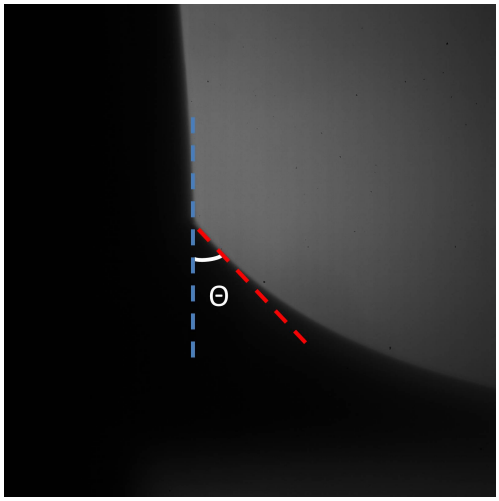

Figure 3.7.: Image of the receding contact angle of pure water at a velocity of $117\,\mathrm{mm\,s^{-1}}$ in the rotating drum setup. The left side is the drum, the right side the liquid. The blue dashed line is the tangent line at the contact angle on the drum surface and the red one on the liquid surface, the contact angle is measured between these two straight lines.

from the beginning and repeated until the contact angle was stable over time. By the time a clean setup can be ensured, the water measurements were done first, afterwards the surfactant measurements were done, starting with the lowest concentration to the higher concentrations.

4 Influence of surfactants on smooth surfaces

As described in section 2.1.2 the contact angle is velocity dependend. By adding surfactant to the solution the contact angle decreases with increasing surfactant concentration as mentioned in section 2.6.3. The receding contact angle of the surfactants CTAB, S-1DeS, C_4E_1, C_8E_3 and $C_{12}E_5$ were measured. The experiments of [55] with a similar setup had a couple of drawbacks that made e.g. comparisons to the hydrodynamic models complicated (if not impossible). The older experiments were made on a surface with a receding contact angle at $0\,\mathrm{mm\,s^{-1}}$ of 67°, leaving a very limited velocity range before film formation started. The measurements described in the following sections were done on a surface with a receding contact angle at $0\,\mathrm{mm\,s^{-1}}$ of 83°. The higher contact angle indicated a smother and more homogeneous surface. This results in a higher film formation velocity, so the velocity range could be increased by the almost a factor of three. The increased velocity range allows a more detailed investigation of the influence of the different surfactants. If not differently mentioned all the contact angle measurements were done on the spherical segment of the drum coated with Polystyrene.

4.1 Experimental results of water

Before the surfactant solutions were measured, every time pure water was measured. During the experiments, presented in this work, the rotating drum was coated twice. The static receding contact angle varies slightly between the two different coatings (83° - M1 and 81° - M2. The coating of M1 was used for the surfactant measurements with CTAB and S-1DeS and the coating of M2 for C_4E_1, C_8E_3 and $C_{12}E_5$ measurements (M2)). The dewetting behaviour of water on these two surfaces is comparable as seen in figure 4.1. With increasing velocity the contact angle decreases until the contact line becomes unstable and starts to buckle (at around $190\,\mathrm{mm\,s^{-1}}$) (figure 4.1). Above this velocity the contact line builds a V shape and single drops were pulled upwards and a constant contact angle can not be measured. Because of this instability of the contact line the measurements were stopped at this velocity. Due to the created V shape of the contact line and the single pulled up drops, as already described in [18, 43, 56, 125], the shape of the curve is calculated by [145]. At even higher speeds the contact line starts to vanish and a complete film is pulled out like described for example in [45, 89, 101, 142].

To test, whether all measurement results can be explained with the hydrodynamic model, I fitted the measurements with the model by Cox and Voinov Eq. 2.10 [38, 164].

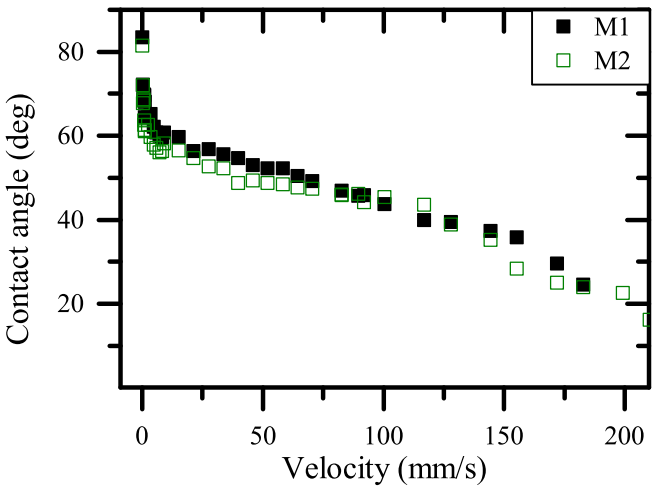

Figure 4.1.: Receding contact angle of pure water. Filled symbols are measured on the surface on which the surfactants CTAB and S-1DeS were measured (M1), open symbols are measured on the surface on which the surfactants C_4E_1, C_8E_3 and $C_{12}E_5$ were measured (M2). The measurement error is approximately the symbol size (±3°).

Since, as described above, only the receding contact angle was measured in this thesis, the sign in Eq. 2.10 is negative.

$$\Theta = \left(-9\,\frac{\mu\,v}{\gamma}\ln\left(\frac{\alpha h}{\lambda}\right)+\Theta_0^3\right)^{\frac{1}{3}} \tag{4.1}$$

The measured curve shape can be divided in two parts; a steep curve for velocities smaller than 10 mm/s and a less steep one for faster velocities. The faster velocities are comparable with the hydrodynamic theory (see figure 4.2 red line, squared symbols) in contrast to the shape of the curve for low velocities. I assume that at low velocities the roughness of the surfaces is the dominant effect and not the hydrodynamic behaviour. Therefore, the shape of the curve differs from the theoretical prediction. By fitting the measurement results I assume, that the logarithmic part of the equation $\ln\left(\frac{\alpha h}{\lambda}\right)$ is one characteristic parameter and it is used as a fitting parameter. The second fit parameter is the apparent contact angle θ_0. Both parameters are can not correlate to the expected values for a smooth surface, since the included parameters are more complex hydrodynamic, for example the pinning on the contact line. Therefore, the slip length as well as the apparent contact angle is smaller than the expected values for pure water on a smooth surface.

For comparison, I also fitted the data published in [55] with the hydrodynamic model. The comparison shows clearly, that these measurements do not reach the regime where the hydrodynamic behaviour is the dominant effect, therefore the fitting with the hydrodynamic model it not working (see figure 4.2). My measurements on the surface with the higher contact angle show for the higher speeds, as already mentioned, a good agreement with the hydrodynamic model.

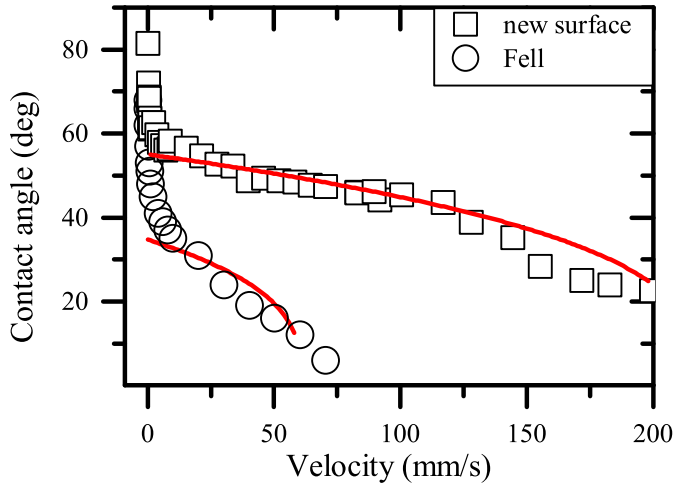

Figure 4.2.: Comparison of the receding contact angle of pure water on the new surface (M2) with the measurements done by [55]. The red lines are the fitting done with Eq. 4.1. Due to visual reasons the error bars are not shown ($\pm 3^{\circ}$).

4.2 Surfactants: Generic behaviour

By adding surfactant in general the behaviour is comparable to water. The contact angle decreases with increasing velocity. The contact line shows a straight line for low velocities, at higher velocities it starts to buckle and at even higher velocities a complete film is formed. In comparison to water the contact angle at zero velocity decreases with increasing surfactant concentration. The plot of the contact angle against the velocities shows with increasing surfactant concentration an increasing steeper slope (see figure 4.3 a). As a result of the lower contact angle also the critical velocity of film formation decreases with increasing surfactant concentration. At any given velocity the contact angle decreases with increasing surfactant concentration. In figure 4.3 b this behaviour is shown as an example for the surfactant CTAB. This tendency was observed for all measured surfactants (figure 4.5).

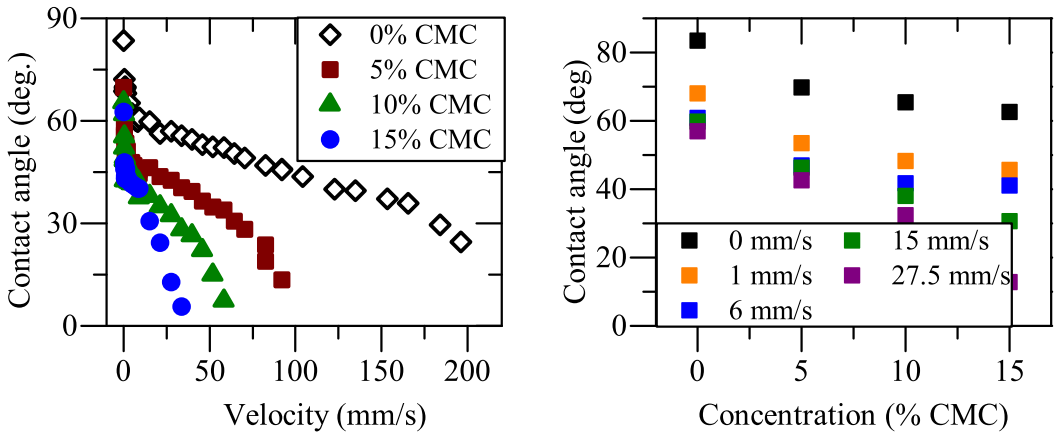

(a) (b)

Figure 4.3.: (a) Comparison of the receding contact angle of different CTAB concentrations. (b) shows the decrease of the receding contact angle with increasing surfactant concentration for the example surfactant CTAB. The measurement uncertainty is ±3°.

4.3 Contact angle at zero velocity

The receding contact angle at zero velocity decreases for all measured surfactants. The behaviour that surfactant reduces the contact angle of pure water is well known and described in earlier publications [9, 15, 148, 155]. Nevertheless a comparison to the Young equation Eq. 2.1 is instructive.

$$\gamma_L \cos\Theta = \gamma_S - \gamma_{SL}.$$

For water the surface tension of the liquid is $\gamma_L = 72.1\,\mathrm{mN\,m^{-1}}$. The measurement of the receding contact angle in this setup is not easily possible. For measuring the contact angle at zero velocity the drum is firstly rotated and after the drum is stopped I waited 30 s before the measurement is started. Since this contact angle at zero velocity depends on the measurement history, I define the receding contact angle as the average of the contact angle at zero velocity and the contact angle at the lowest measured velocity ($0.24\,\mathrm{mm\,s^{-1}}$). For pure water this is 77°. As a help to interpret the data I use the Young equation, which leads to $\gamma_S - \gamma_{SL} = 16.2\,\mathrm{mN\,m^{-1}}$.

The change in the contact angle by adding surfactant can be explained by the adsorption of surfactant molecules at the solid-liquid and the liquid-air surfaces. Since

if no surfactant would adsorb at the solid surface the surface tension of the solid and the solid-liquid interface should be constant. Using the measured values of the surface tension of the surfactant solutions and assuming that $\gamma_S - \gamma_{SL}$ is constant, the contact angle of a 10 % CMC CTAB solution should be at around 75°. The other values for the contact angle of CTAB, calculated and real ones, are summarized in table 4.1.

Table 4.1.: Calculated contact angle of CTAB after the Young equation by assuming no adoption of surfactant molecules to the surface, ($\gamma_S - \gamma_{SL} = 16.1\,\mathrm{mN\,m^{-1}}$) and the calculated values for $\gamma_S - \gamma_{SL}$ for the measured contact angle

Concentration [% CMC]	Surface tension [$\mathrm{mN\,m^{-1}}$]	Contact angle [deg]	Calculated contact angle [deg]	Calculated $\gamma_S - \gamma_{SL}$[$\mathrm{mN\,m^{-1}}$]
0	72.1	77	77	16.1
5	68.4	65	76	28.9
10	64.6	64	75	28.3
15	60.2	53	74	36.2

The difference between the calculated values and the measured ones are explainable by the fact, that surfactant molecules adsorb at the solid-liquid interface, and therefore $\gamma_S - \gamma_{SL}$ increases with increasing surfactant concentration. By calculating the $\gamma_S - \gamma_{SL}$ with the measured receding contact angle it is clearly visible, that the value is not constant, it increases with increasing surfactant concentration, even if it is not possible to extrapolate the change of γ_S and γ_{SL} independed. This conclusion is true for all other measured surfactant solutions as well.

4.4 Marangoni effect

At the moving contact line different possible mechanisms for surfactant transfer can be considered. I assume that a surfactant molecule, which is close to the contact line, has different options (figure 4.4). One option is the molecule adsorbs to the surface of the drum (A), the other option is the molecule adsorbs to the fresh built solid liquid interface (B), a direct transfer of the molecules already adsorbed at the solid liquid interface to the bulk of the liquid is inconceivable.

If more surfactant molecules adsorb to the solid surface, less surfactant molecules are free to adsorb to the liquid-air interface close to the three phase contact line. Therefore, the surface tension close to the contact line is higher than the surface tension far away from the contact line. The gradient in the surface tension increases, which leads to a higher Marangoni stress. The other case, that more surfactant molecules adsorbed to the liquid-air interface, leads to lower surface tension, which is closer to the surface

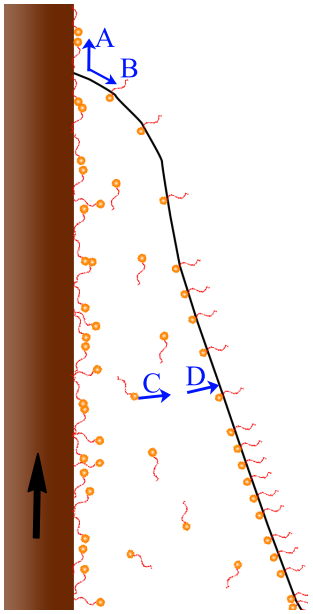

Figure 4.4.: Schematic drawing of the four processes of surfactant molecules close to the three phase contact line.

tension far away from the contact line, therefore the gradient in surface tension is smaller and the resulting Marangoni stress is smaller than for the first case.

The fact that the contact angle decreases with increasing surfactant concentration, points to the existence of a Marangoni stress. Due to this Marangoni stress it is to be expected that the surface tension close to the contact line is higher than the surface tension of the bulk surface. The observed effects are in agreement with the hypothesis described in section 2.7. Close to the contact line a fresh surface is generated, which is not in equilibrium with the surface far away from the contact line regarding the surfactant concentration. Close to the contact line less surfactant molecules are present. To reach an equilibrium surfactant is transfered to the liquid air interface: advection and diffusion from the bulk (process C) and adsorption to the liquid-air interface (process D).

4.5 Comparison with the hydrodynamic theory by Cox and Voinov

Since the shape of the surfactant curve does not vary too much from the shape of water I also fit the measured surfactant with the Cox-Voinov equation Eq. 4.1. The results are shown in figure 4.5. The free fitted parameters were chosen in the same way as for water: θ_0 as the contact angle at zero velocity and the logarithmic part is a friction

parameter. The fit was done by a fitting routine in Origin[1]. It was possible to fit all the measured surfactants for the different concentrations with the Cox-Voinov equation. As described in section 4.1 the velocity vs. contact angle curves consist of two slopes, a steep one for low velocities and a less steep one for higher velocities. These surfactant measurements show the same trend, but the beginning of the second slope is shifted towards slower velocities. Therefore, the fitted velocity range varies with increasing surfactant concentration towards slower velocities.

For a better comparison I plotted the Capillary number Ca against the contact angle to the power of three θ^3 in rad. This results in a straight line in the plot of the Cox-Voinov equation (right side of figure 4.5, dashed line). To calculated the Capillary number the viscosity of Water $\eta = 10^{-3}$ Pa s was used for all fits and the surface tension of the corresponding concentration. As surface tension the measured surface tension (see section 3.2) was used.

As seen in figure 4.5 it is possible to fit also the surfactant solutions with the Cox-Voinov equation above a critical velocity, even if nowhere in the equation the presence of surfactant molecules is plotted. Therefore I assume, that all the influences of the surfactants are considered in the two fitting parameters (the contact angle at zero velocity and the logarithmic part of the equation).

4.6 Comparison of different surfactant solutions

To compare the different surfactant solutions I fix the velocity and compare the dynamic contact angle as a function of concentration for the different surfactants. As described above, the contact angle decreases with increasing concentration. To find out if the CMC of surfactants influences the velocity dependence of the contact angle I compare my measurement results for the five different surfactants. The CMC of these five surfactants varied over five orders of magnitude (table 3.1). As shown in figure 4.6 (a),(c) and (d) the contact angle variation increases with increasing concentration for all of the surfactants, independent how they are charged (positive, negative or neutral). By recalculating the relative concentration depending on the CMC the difference in the wetting behaviour decreases significantly (figure 4.6 (b), (d), and (e). As shown in figure 4.6 the tendency is the same for low velocities ($0.24\,\mathrm{mm\,s^{-1}}$) as well as at higher velocities (15 and $27.5\,\mathrm{mm\,s^{-1}}$).

[1] OriginLab Corporation,One Roundhouse Plaza, Suite 303,Northampton, MA 01060, USA,www.originlab.de

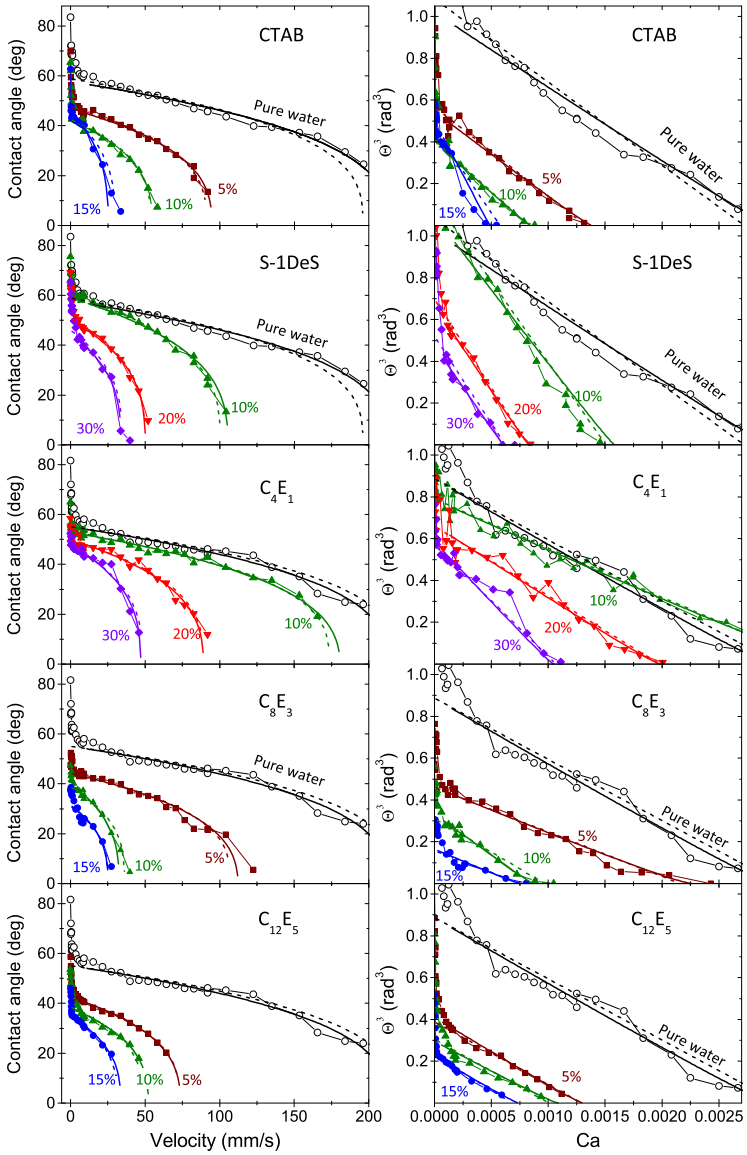

Figure 4.5.: Left: Dynamic receding contact angle of aqueous solutions versus velocity for the surfactants CTAB (cationic), S-1DeS (anionic), and C_4E_1, C_8E_3, $C_{12}E_5$ (nonionic) on a polystyrene-coated cylinder. Right: Contact angle (in rad) cubed versus the capillary number $Ca = \eta U/\gamma_L$. Here, $\eta = 10^{-3}\,\mathrm{Pa\,s}$ is the viscosity of water. Results for pure water are indicated by open black circles. The concentrations (in % CMC) were 5 % (dark red circles), 10 % (green up triangles), 15 % (blue circles), 20 % (light red down triangles), and 30 % (violet diamonds). For pure water I only show two independent measurements; the top two and the bottom three results for pure water are identical. The solid lines are fits using the hydrodynamic model by Eggers and Snoeijer Eq. 2.11,Eq. 2.12 and Eq. 2.13, the dashed lines are fits using the hydrodynamic theory by Cox-Voinov Eq. 4.1. [64]-Published by the Royal Society of Chemistry

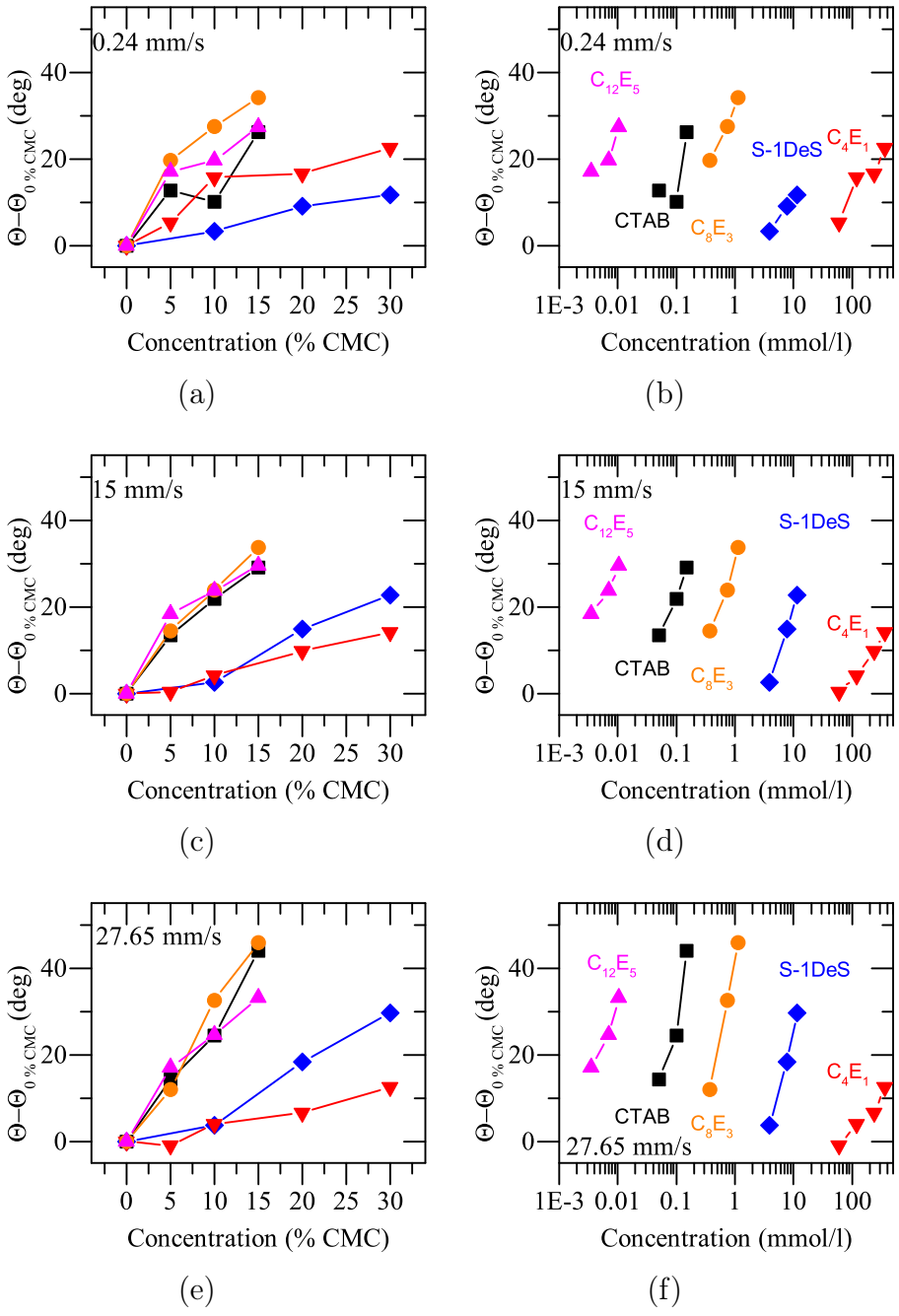

Figure 4.6.: The contact angle difference between the contact angle Θ and the receding contact angle (Θ_0, 0 % CMC). The contact angle increases with increasing surfactant concentration for different surfactant solution. This behaviour is comparable for all velocities (a), (b) $v = 0.24\,\mathrm{mm\,s^{-1}}$, (c), (d) $v = 15\,\mathrm{mm\,s^{-1}}$, (e), (f) $v = 27.65\,\mathrm{mm\,s^{-1}}$

However, even between the two extreme cases of C_4E_1 and $C_{12}E_5$, with almost five orders of magnitude difference in CMC, the receding contact angles differed only by about a factor of two. Thus, the CMC of a surfactant only has a moderate effect on the dewetting behaviour, after rescaling the results with the CMC. The difference in the change of contact angle between the measured surfactant might be affected by the different diffusion times, surface tension difference between water and surface tension at CMC, gradient in surface tension at the respective concentration in the surface tension graph or the adsorption and desorption kinetic of the surfactant molecules. But at the moment it is not clear what exactly causes the remaining difference. But I assume, that the remaining differences could be due to a different behaviour of the adsorption and desorption behaviour described in the processes A,B C and D in figure 4.4. The comparison of the fitting parameter of the hydrodynamic theory is explained in detail in section 4.8.

4.7 Comparison with the hydrodynamic theory by Snoeijer and Eggers

As mentioned in section 2.3.2 Snoeijer and Andreotti pointed out that the hydrodynamic theory by Cox Voinov is developed for the advancing but not for the receding case [143]. Therefore, I compare my data with the hydrodynamic theory developed by Eggers and Snoeijer [49, 33], see section 2.3.2:

$$\frac{\Theta}{\Theta_0} = \frac{2^{\frac{2}{3}}\delta^{\frac{1}{3}}}{Ai(\sigma)} \frac{\mathrm{d}Ai(x)}{\mathrm{d}x}\bigg|_{x=\sigma} \tag{2.11}$$

$$\delta = \frac{2Ca}{{\Theta_0}^3} \tag{2.12}$$

$$\frac{2}{\Theta_0 \delta^{\frac{1}{3}}} + \frac{2^{\frac{2}{3}}}{Ai(\sigma)} \frac{\mathrm{d}Ai}{\mathrm{d}x}\bigg|_{x=\sigma} - \frac{2^{\frac{1}{6}} e^{-\frac{1}{3\delta}} \Theta_0}{3\pi Ai^2(\sigma)\lambda} = 0 \tag{2.13}$$

The fit routine was done in Matlab. The Eq. 2.11, Eq. 2.12 and Eq. 2.13 were therefore implemented in Matlab. The Eq. 2.13 had only one positive root. Finding of the root was proven to be numerically stable by limiting the range of the variable σ to smaller positive numbers, tending to be approximately 60. Using the logarithm of λ

furthermore was more efficient when performing the nonlinear fit for the parameters λ and Θ_0. Regarding the initial values of the parameters it is important, that the initial guesses are close to the final values. In the presented nonlinear fits a discrepancy of 20 for the logarithm of λ and a factor of 1.5 for Θ_0 has to be used. By choosing values in this range the fit does not depend on the initial value.

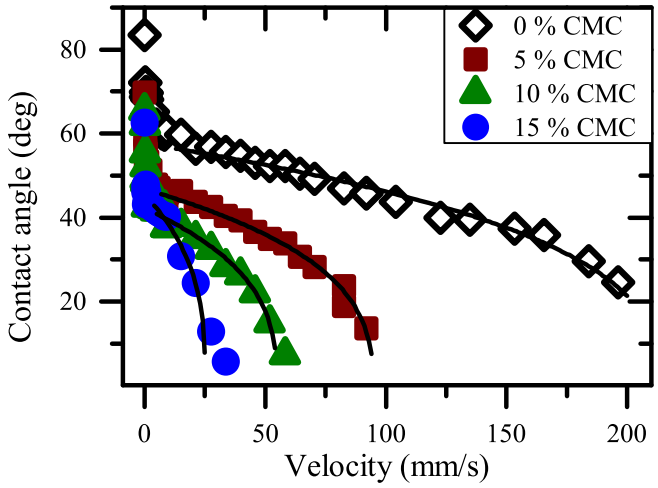

Figure 4.7.: Dynamic receding contact angle of aqueous solutions versus velocity for the surfactant CTAB. Results for pure water are indicated by open black diamonds. The solid lines are fits using Eq. 2.11, Eq. 2.12 and Eq. 2.13.

The fits show a good agreement with the measurement data. In figure 4.7 the results are shown for the surfactant CTAB. The fits of all other measured surfactants are shown in figure 4.5, presented as solid lines.

Comparable to the fit with the hydrodynamic theory by Cox and Voinov the apparent contact angle Θ_0 as well as the logarithmic of λ are the used fit parameters. The logarithmic of λ is the friction parameter, including the slip length as well as the influence of roughness. For the surface tension and viscosity measured values were used. The fit showed good agreement with the experimental data for velocities higher than $10\,\mathrm{mm\,s^{-1}}$. The measurement data of lower velocities could not be fitted with this model. The fitting parameter are discussed in the following section.

4.8 Comparison of the two hydrodynamic models

Since both of the hydrodynamic models show comparable good results, I compared the resulting fitting parameter of the models. The hydrodynamic model by Cox-Voinov was developed for the advancing case in contrast to the model by Eggers and Snoeijer,

which was also developed for the receding case. By comparing the two models for the receding case of the contact angle I can show how good the hydrodynamic model by Cox-Voinov works also for the receding case. Both models use an apparent contact angle at zero velocity which is in both cases not the measured receding contact angle but the extrapolation of the contact angles of high velocities to zero velocities $\Theta_0 = \Theta(v \to 0)$. The logarithmic part in Cox Voinov model Eq. 4.1 $\alpha h \lambda$ as well as $1/\lambda$ in Eq. 2.11, Eq. 2.12 and Eq. 2.13 represent the friction close to the three phase contact line. More details about the friction parameters are explained in section 4.5 and 4.7 . The difference of the prefactors of the friction parameter can be explained by the rescaling of the Eq. 2.11, Eq. 2.12 and Eq. 2.13(see section 4.7)

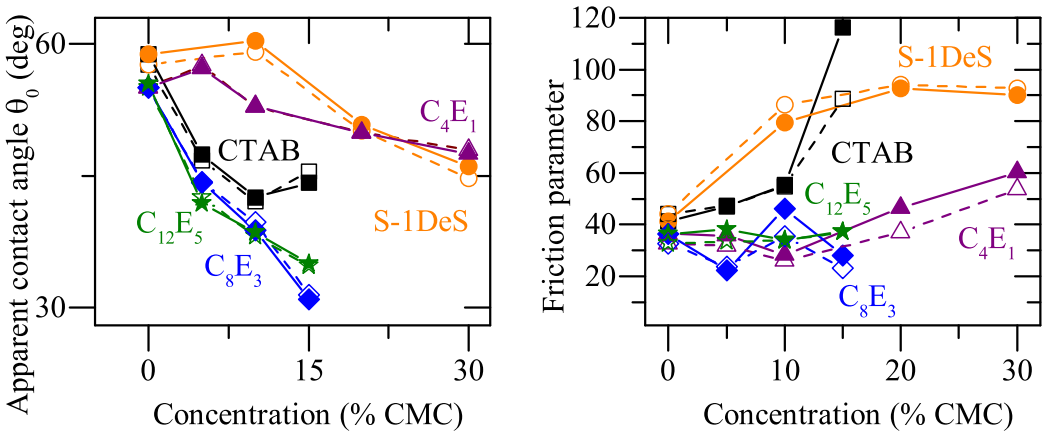

Figure 4.8.: Fitting parameter for the hydrodynamic model. Left: friction parameter, Right: apparent contact angle extrapolated for $v \to 0$. Solid symbol Eq. 2.11, Eq. 2.12 and Eq. 2.13, Open symbols Eq. 4.1. If only the solid line or the solid symbols are visible, both models fits overlap.

The apparent contact angles at zero velocity Θ_0, which result of the fit with both models, show a good agreement between each other (figure 4.8 a). Since the hydrodynamic model developed by Cox and Voinov was only developed for the advancing case and not for the here used receding case this was not obvious. With increasing surfactant concentration the fitted apparent contact angles decreases for all measured surfactant independent of the charge of the respective surfactant. However, the fitted friction parameter is relatively constant up to 15 % CMC and does not show an increase. Only at higher concentration of the lowest of the nonionic surfactant C_4E_1 a slight increase can be measured. The cationic and anionic surfactant CTAB and S-1DeS show an increase. This effect can also be seen in the right figure 4.5. For the nonionic surfactant the fitted dynamic contact angles are more or less only lifted parallel to each other, while

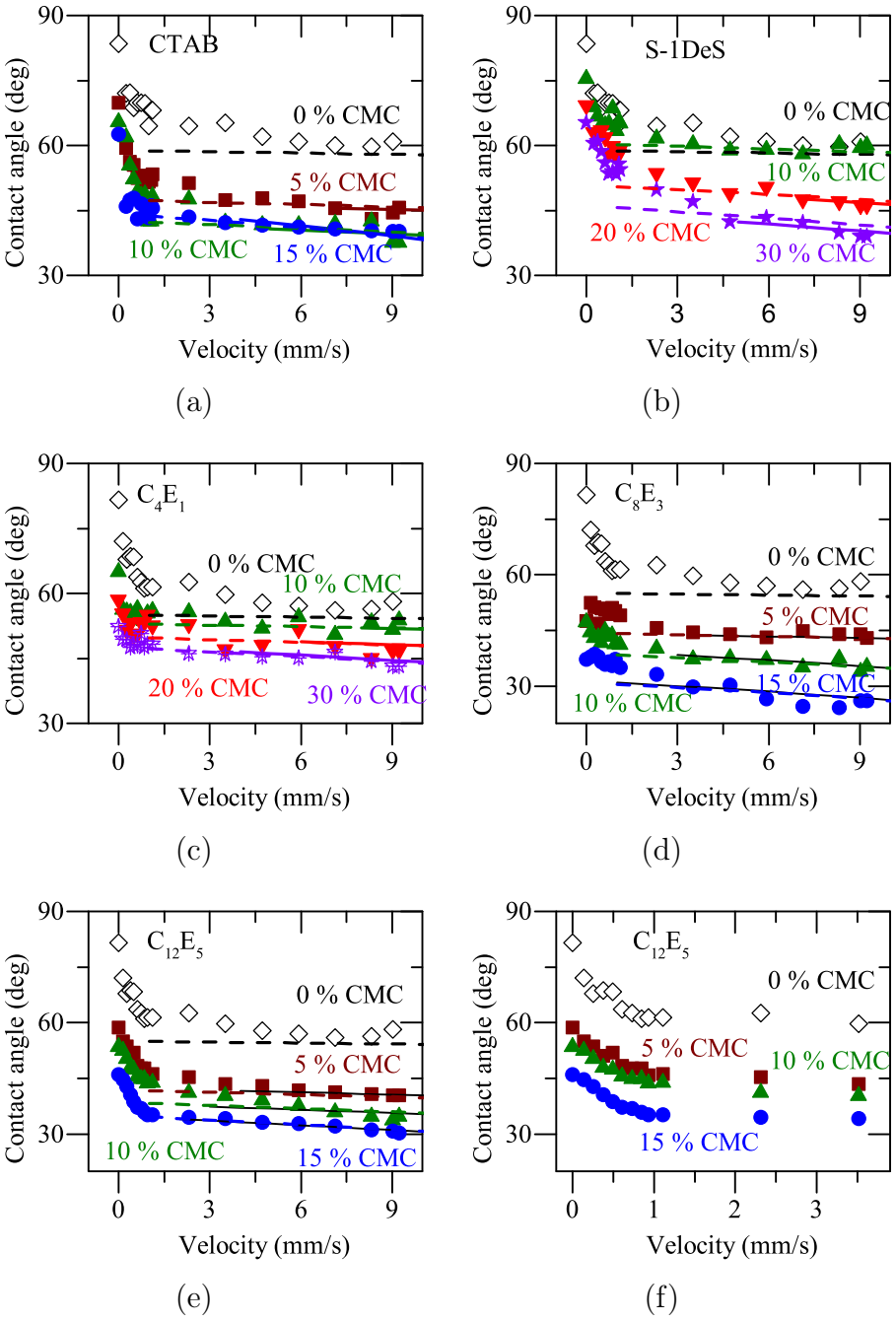

Figure 4.9.: Comparison of the contact angle vs. velocities for low velocities with the hydrodynamic models for different surfactant solutions a)CTAB, b) S-1DeS, c) C_4E_1, d) C_8E_3, e) $C_{12}E_5$, f) magnification of $C_{12}E_5$. Solid line: Eq. 2.11, Eq. 2.12 and Eq. 2.13, dashed line: Eq. 4.1. The models do not work for lower velocities than $10\,\mathrm{mm\,s^{-1}}$ for water. For surfactant solution it is possible to fit also lower velocities, but at a specific velocity fitting is not possible anymore.

the dynamic contact angle for the charged surfactant also changes the slope. I assume, that the higher friction parameter for the charged surfactant depends on the repulsion due to electrostatic effects of the surfactant molecules (between the one sitting already on the surface to the surfactant molecules which try to adsorb at the surface). This repulsion would slow down the adsorption process and increases therefore the friction near the contact line, where the surfactant molecules try to adsorb [154].

As mentioned above both models show only a good agreement with the experimental data for higher velocities. For low velocities $v < 5\text{-}10\,\mathrm{mm\,s^{-1}}$ the model does not show an agreement with the measured data. In figure 4.9 the slow change between the steep slope at low velocity and a less steep slope at higher velocities, which can be fitted with the hydrodynamic models, is shown. The fitting for pure water works only at $v > 10\,\mathrm{mm\,s^{-1}}$ which can be explained by the fact that even at $v = 10\,\mathrm{mm\,s^{-1}}$ the measurement points are still above the fit. With the presence of surfactant the measured results can be fitted down to lower velocities. For the measurement of surfactant solutions it is possible to fit also lower velocities, independent of the kind of surfactant.

Nevertheless, below a specific velocity the measured contact angle cannot be fitted anymore with the hydrodynamic models. By comparing the shape of the curves at low velocities it is detectable, that the shape of these curves at low velocity is independent of the concentration. Figure 4.9 f) shows this exemplarily for the surfactant $C_{12}E_5$. Due to the similar shape I assume that the major reason for this steeper decrease at low velocities is not primarily depending on the Marangoni force due to the presence of surfactant. If a significant dependency would be the case the shape of the curve would depend on the surfactant concentration. Therefore, this must be influenced by an additional parameter like for example the roughness of the surface. Even if the surface is relatively smooth there is still finite roughness on the surface of the drum.

4.9 Conclusion of the wetting on smooth surfaces

By adding surfactant to a solution the receding contact angle decreases with increasing concentration as well as with increasing velocity. The critical velocity, where the contact line starts to get unstable, decreases with increasing surfactant concentration as well. This behaviour is detectable for all kind of measured surfactants (CTAB, S-1DeS, C_4E_1, C_8E_3 and $C_{12}E_5$). One of the main forces resulting in a decrease of the receding contact angle seems to be the Marangoni force. A local gradient of the surface tension is formed close to the three phase contact line. This influences the flow behaviour close to the three phase contact line, but does not influence the flow behaviour in the bulk liquid significantly. The charge of the surfactant does not have an significant influence on

the dewetting behaviour, since all surfactants, independent of their charge, show a comparable effect. The dominating effect of the different surfactants is the relative concentration of the critical micelle concentration. By scaling with the CMC of the surfactant, it is possible to compare the effect of different surfactant molecules, even if the absolute concentration is varied by more than four orders of magnitude. The scaling with the CMC allows to predict the influence of a surfactant on the dewetting behaviour for other surfactants. For velocities higher than $10\,\mathrm{mm\,s^{-1}}$ the hydrodynamic models fit the experimental data even if surfactants are presence. The local effects close to the three phase contact line can be summarized in a friction parameter in the models similar to the dewetting of simple liquid. Since it is possible to fit the data with the hydrodynamic model I can assume, that the dewetting effects can be explained on a bigger length scale than the molecular length scale.

5 Additional influence of structured surfaces

The previous measurements where done on relatively smooth and unstructured surfaces. Here, I concentrate on the question, how a structured surface influences the wetting behaviour for pure water as well as the influence of surfactant solutions. One practical example of dewetting of a complex liquid on a structured surface is the offset printing. Thereby an ink (solution with surfactants and various other materials) wet and dewet on structured and unstructured plates to generate a print product. I investigated the influence of the structured surfaces on the dewetting behaviour. Special focus is set on parameters like the surfactant concentration, the structure of the solid surface and the local and global effects of the surface structure on the velocity-dependent dewetting dynamics.

To do so I used the new rotating drum setup (described previously in section 3.4.2), with the drum which allows mounting different surfaces on the drum. As structured surface I used gravure printing places with different structured areas. These printing plates consisted of unstructured surface areas as well as of differently structured areas. The following section is based on [65].

5.1 Characterization of the structured surface

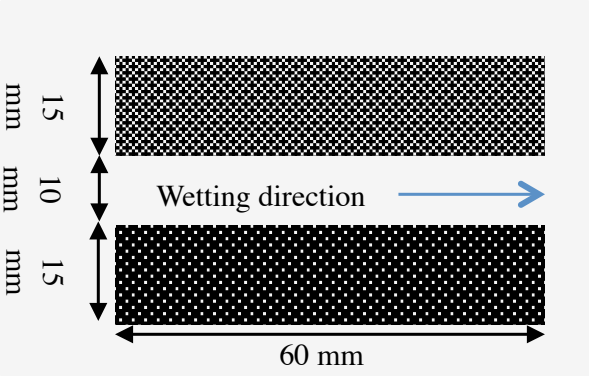

Figure 5.1.: Sketch of the printing plates with two structured areas surrounded by unstructured areas.

As described above, our model system of a structured surface is a custom made gravure printing plate. The plates were produced by GT+W[1] and consist of a copper

[1] GT+W, Paul-Ehrlich-Straße 17, 63322 Rödermark, Germany, www.gtandw.com

layer which is galvanically deposited on stainless steel plates with a thickness of 0.4 mm. Inside the copper layer the structure is mechanically engraved and the grates are removed. These engraved structure is coated and hardened with 5 µm chromium, which is electronically deposited on the surface. These printing plates have eight differently structured areas, which are surrounded by relatively smooth areas.

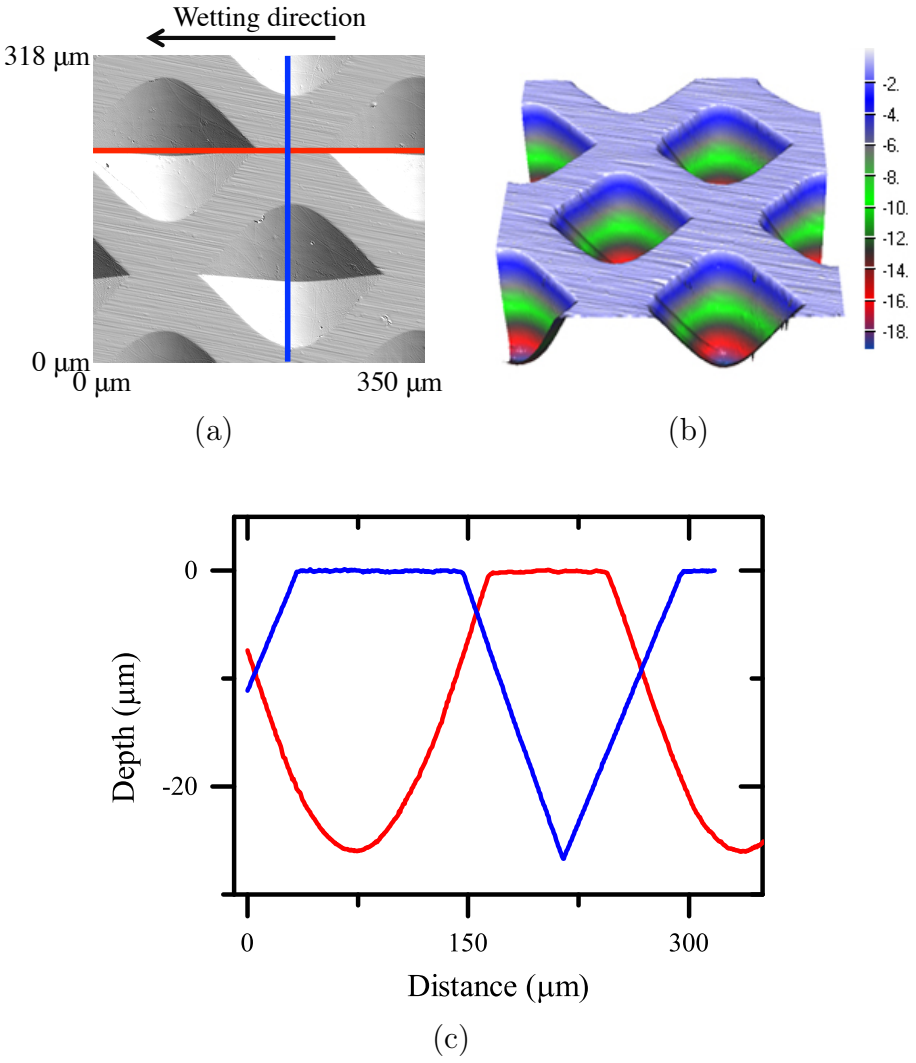

Figure 5.2.: Figure a) and b) show an image of the structure on surface 262x262-25. a) is the photo realistic surface done with a confocal white light microscope. b) is the 3D image, the numbers on the scale are in µm. c) shows the surface profile along the red and blue lines in panel a.

In figure 5.1 a sketch shows the arrangement of the structured area on the plates. The structures consist of gravure cells with different size, height and distance. Inside one structured area the distances and dimensioned of the gravure cells are similar. The lateral size, depth and distance of the gravure cells are analyzed with a white

light confocal microscope (NanoFocus®μSoft® with 50 x magnification). The setup is described in section 2.9.2. To characterize the structures on the surface the dimensions of one of those cells in x, y and z direction as well as the distance of the center of two cells are measured. Therefore, two different areas of each structure were imaged and analyzed (figure 5.2 a, b). The cells inside this surface area were analyzed by measuring the surface profile (figure 5.2 c). The printing plates are mounted on the drum surface, thereby the gravure cells are arranged horizontal to the water surface. The averaged results of those measurements are summarized in table 5.1.

Table 5.1.: Properties of the different structured areas on the printing plates. The name results from the distance of the gravure cells' centers in x an y direction as well as the depth of a single gravure cell.

Name	gravure cells x [µm]	gravure cells y [µm]	gravure cells depth [µm]	distance gravure cells x [µm]	distance gravure cells y [µm]
262x262-7	85.05	45.07	7.11	262	262
262x262-9	98.13	62.40	9.43	262	262
262x262-13	116.70	84	12.53	262	262
262x262-25	192.16	138.2	24.87	262	262
218x212-4	45.9	31.00	3.58	218	212
218x212-7	63.47	48.80	6.54	218	212
218x212-9	81.5	68.20	8.88	218	212
218x212-19	134.70	121.20	18.84	218	212

The unstructured areas of the surface have still a roughness due to the production process. Measured with the optical microscope the roughness was approximately $R_q = 0.04\,\mu m$ (measured on a region of 150x200 μm^2).

5.2 Experimental procedure

The above described printing plates have a length of 340 mm and did not fit on the in chapter 3.4.2 described clamping system. Therefore, the second described clamping system was used and the printing plates were divided into two parts (each has a length of 170 mm and a width of 70 mm). On each of these parts are four structured areas with a length of 60 mm and a width of 15 mm. Two of these structured areas are parallel with a distance of 10 mm (see figure 5.1). The other two structured areas are in wetting direction next to the first one with a distance of 20 mm. On both sides of the printing

plates there are unstructured areas with a width of a 15 mm to fix the plate in the clamps. The structured surface fixed on the drum surface is shown in figure 5.3 (b).

Before the measurements were started the plates were cleaned carefully mechanically with isopropanol and rinsed afterwards with flowing m milli-Q water. Subsequently the plates were mounted in the new rotating drum setup on the drum. Thereby an contamination with any dust has do be avoided. Before the experiments are started the setup is rinsed with flowing milli-Q water for one hour to be sure to have a clean setup. After the experiments the whole setup is rinsed over night with flowing tap water and rinsed immediately with milli-Q water to avoid calcifications. Comparable to the experiments on the smooth surface (section 4), the new setup is filled up to the axis of the drum with milli-Q water (corresponding to 1 L) and the surfactants were stepwise added to the system and stirred by rotating the drum for at least 20 min at a velocity of 100 mm s^{-1}. As surfactant the anionics surfactant S-1DeS was used. All measurements were done well below the critical micelle concentration (maximum 45 % CMC). The CMC of S-1DeS is 38.5 mmol L^{-1} (section 3.2). The measurements were done under saturated atmosphere by closing the setup (figure 5.3 (a)).

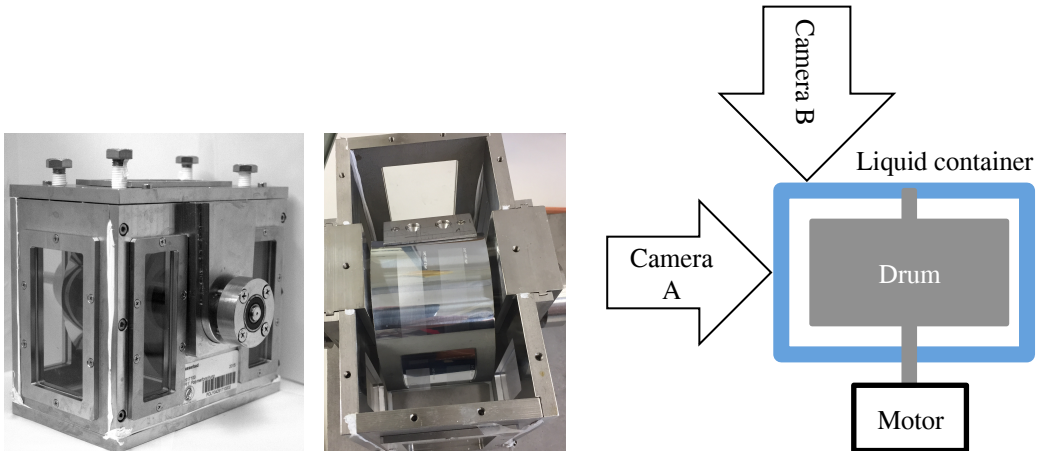

(a) (b) (c)

Figure 5.3.: Panel (a) shows the closed new setup with the rotating drum with the structured surface clamped on the drum surface shown in figure (b). (c) shows the experimental arrangement of the setup with camera A for analyzing of the CL and camera B for measuring the contact angle.

For the measurements a high speed camera (Photron, Fastcam SA-1) with 500 fps was used. To measure the contact angle, camera B in figure 5.3 was used with back light illumination and an optics with 12x magnification and a working distance of 300 mm. To analyze the shape of the three phase contact line the camera in position A was used with light through a 2x objective, with a working distance of 35 mm.

Since the printing plate can only be bended in one direction a direct measurement of the contact angle on the structured area is not easily possible due to optical reasons. In the optical path the contact angle on the structured and the unstructured area can not be clearly separated. Therefore, the contact angle on the structured areas is not measurable. Only on the completely unstructured regions, where no structured area is along the optical path, it is possible to measure the contact angle. Instead of the contact angle therefore the shape of the three phase contact line is measured, more precisely the height difference of the CL on the structured (red line) and unstructured area (blue line) (figure 5.4). The contact angle on the structured areas is approximated afterwards from the height of the meniscus in section 5.3.3.

Figure 5.4.: The height difference is the distance between the CL on the structured area (red line) and the unstructured area (blue line)

5.3 Experimental results of water

5.3.1 Quasi static contact angle

The wetting and dewetting behaviour on the structured surfaces was investigated by measuring the quasi static contact angle. To do so, a 10 µL droplet was placed on the structured area of the surface. To measure the quasi static contact angle the liquid drop was inflated and deflated by additional 10 µL by using a OCA 35 contact angle measuring device[2]. During the movement of the contact line over the surface the contact line is pinned on the gravure cells of the printing plates. Therefore, the quasi static receding contact angle varies during the deflating of the drop more than 15° (figure 5.5 for surface 262x262-25). The contact line is pinned typically on the corner of the gravure cells, therefore the contact line decreases until it jumps to the smooth part between the gravure cells.

The pinning on the edges is well known and for example described in [67, 127]. Due to the variation of the contact angle on the structured surface the contact angle is

[2] DataPhysics Instruments GmbH, Raiffeisenstrasse 34, 70794 Filderstadt, www.dataphysics.de

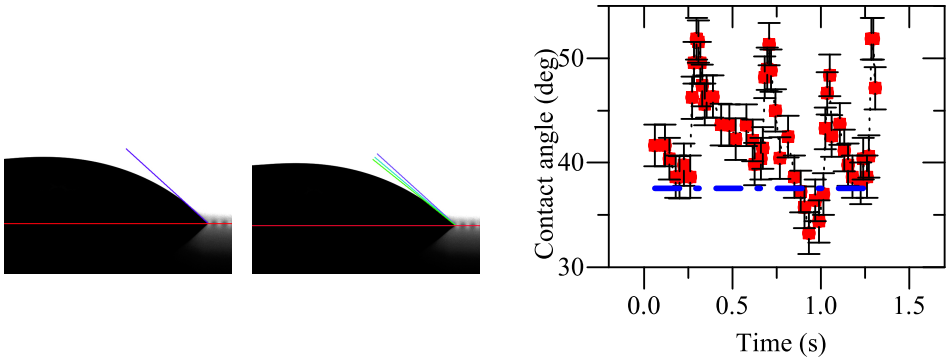

(a) (b) (c)

Figure 5.5.: Panel (a,b) shows the variation of the contact angle by receding over the surface 262x262-25. (a) shows the half droplet when the contact line is pinned at the corner of the gravure cell, (b) shows the half droplet shortly before the contact line is jumping to the next gravure cell corner. The solid lines represent the variation of the contact line during the movement (blue represents the beginning of pining to green which shows the contact angle shortly before the contact line jumps to the next gravure cell). The measurement results are shown in figure (c). The contact angle varies more than 15° by receding over the structured surface. The dashed blue line symbolize the contact angle on the unstructured part of the surface.

not the right parameter to measure in our setup. Instead, as already mentioned, the height difference of the contact line between the structured and the unstructured area is measured. The measurement of the height difference allows to be measured at the same position, shortly before the contact line depinns, to get comparable results.

5.3.2 Dynamic contact angle

The contact angle of pure water on the unstructured part of the printing plate shows the same behaviour like on a smooth PS surface (section 4). Due to the cylindrical and not spherical drum surface the measurement uncertainty increases [50], but on the unstructured surface it is still possible to measure the contact angle with an uncertainty of ±5°. With increasing velocity the contact angle decreases (figure 5.6). The unstructured surface of the printing plates has another chemical surface as the smooth PS surface on which the velocity range, in which the contact angle is measurable and film formation did not started, is smaller ($80\,\mathrm{mm\,s^{-1}}$ instead of $200\,\mathrm{mm\,s^{-1}}$). Nevertheless the dewetting behaviour on both surfaces is comparable.

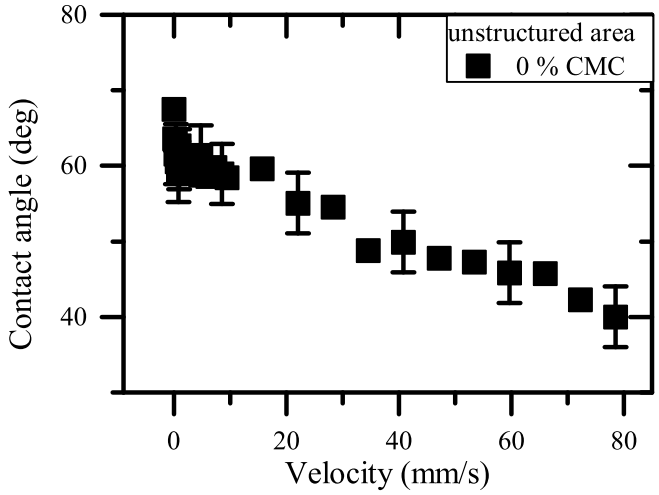

Figure 5.6.: The contact angle on the unstructured area of water decreases with increasing velocity. The errorbars are comperable for all measurement points ($\pm 5°$).

5.3.3 Height difference of the contact line

Since the contact angle is not measurable in side view imaging on the structured part, instead of the contact angle the height difference between the unstructured and the structured part was measured as described above. The CL pinned for all surfaces at the top of the gravure cells during the rotation of the drum until it depinned more or less for all gravure cells in one line simultaneously. For the analysis the position shortly before the depinning is used. With increasing velocity the height difference increases up to a velocity of about $15\,\mathrm{mm\,s^{-1}}$ and reaches a kind of plateau until it comes close to the critical velocity for film formation ($80\,\mathrm{mm\,s^{-1}}$). Beyond this velocity an additional increase can be seen for some structures. This increase is explainable with the fact, that the contact line starts to buckle.

Since the structured areas have two different distances in x an y direction between the center of the single gravure cells, at first I compare the one with the same distance (figure 5.7). Both kinds of structures show, that with increasing depth of the single gravure cell the height difference increases (the last number of the surface name represents the depth of the single gravure cells). The shallower the gravure cell is the smaller is the height difference of the contact line. Figure 5.7(c) shows the direct comparison of the height difference for a velocity of $21\,\mathrm{mm\,s^{-1}}$. Since all of the gravure cells of the different structures have the same corner angle (approximately 160° (see figure 5.7 (d)) the change of the contact angle can not be explained by the change of contact angles

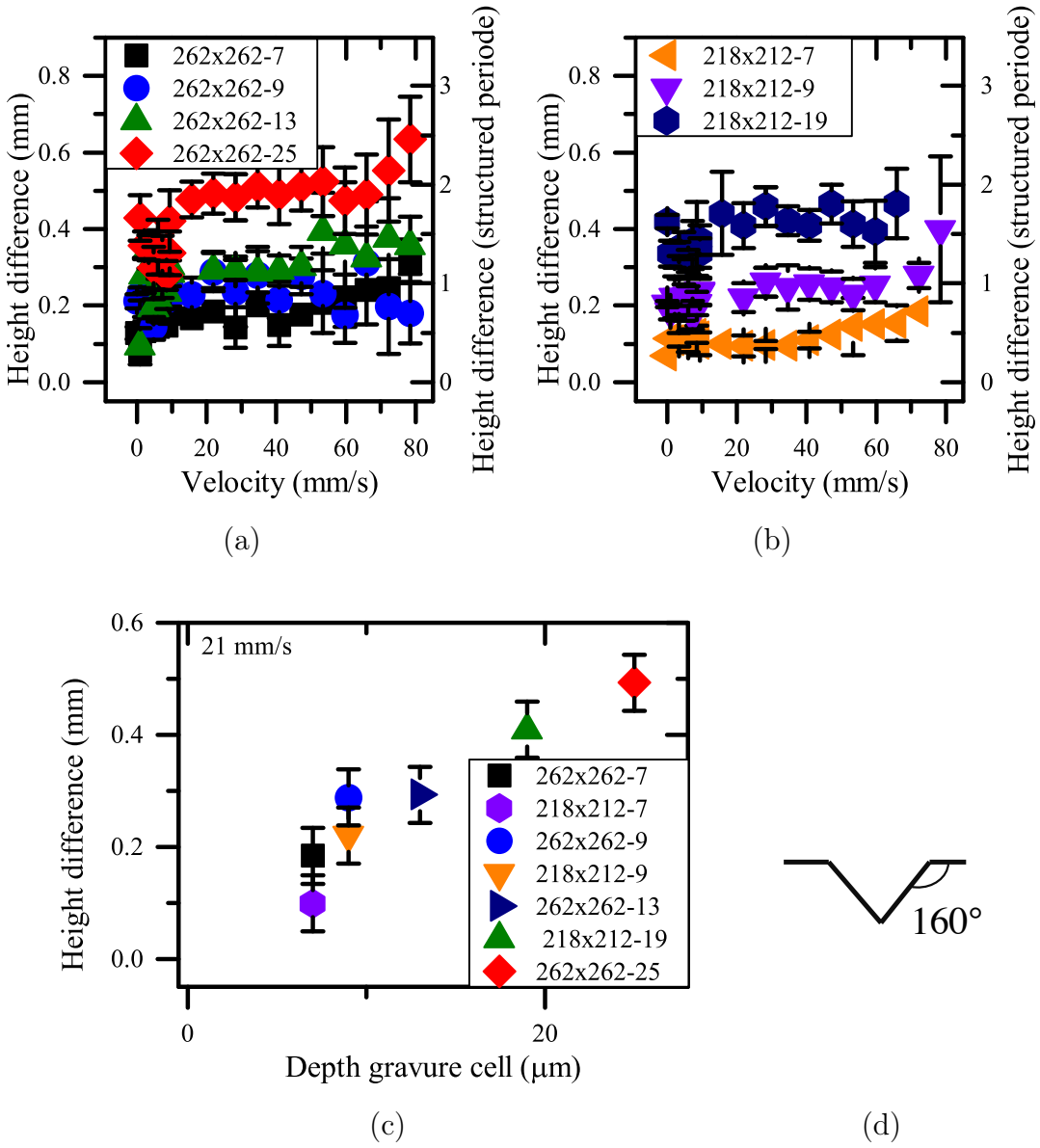

Figure 5.7.: The height difference between the unstructured and the structured area increases with increasing velocity (a) for the surfaces with the distance between the gravure celles of 262x262 µm and (b) 218x212 µm. (c) shows the direct comparison of these two different distances for a velocity of 21 mm s^{-1}.(d) shows the measured angle of the gravure cells, which is similar for all structures.

on corners like it is described in section 2.5.1 [66]. Since a direct measurement of the contact angle on the structured areas is not possible, I use the fact, that far away from the contact line (>100 µm) viscous bending is not visible [33, 109]. Therefore, the shape of the meniscus can be described with the static shape (section 2.2.4). On the smaller length scale the shape of the meniscus of a moving contact line varies from the one of

a static contact line. Since the measurement resolution is due to the optical resolution around 100 µm the observed area is significantly larger as the slip length and even larger as the intermediate length scale. Therefore, the height of the meniscus above the unperturbed liquid level h can be described with [42]

$$\gamma = \gamma \sin\Theta + \frac{1}{2}\rho g h^2. \tag{5.1}$$

The height of the unstructured surface can therefore be calculated by using the surface tension γ of water 72 mN m^{-1}, the density of water ρ =998.2 kg m^{-3}, the gravitational force g =9.81 m s^{-1} and the measured contact angle Θ. By adding the measured height difference between the unstructured and the structured area of the surface Δh, the contact angle on the structured areas can be approximately calculated.

$$h = h_u + \Delta h. \tag{5.2}$$

To calculate the contact angle on the structured surface Eq. 5.2 is inserted in Eq. 5.1.

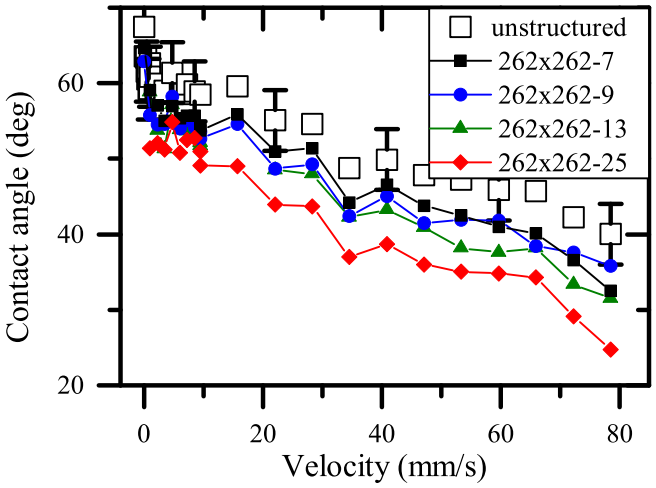

Figure 5.8.: The contact angle on the structured surface areas of water decreases with increasing velocity comparable to the behaviour on unstructured surfaces. The error bars are comparable for all measured points (± 5°).

This calculated contact angle is done for comparable wetting situations, since the height difference is measured at comparable positions, shortly before the contact line is depinned. The wetting situation is comparable to minimum contact angle shown in figure 5.5. Therefore, the calculated contact angle at the different surfaces are for

comparable positions of the contact line relative to the structure of the gravure cells. The contact angle on the structured surface behaves comparable to the one on unstructured surface: with increasing velocity the contact angle decreases until the contact line begins to buckle and film formation starts. But with increasing depth of the surface structure the contact angle itself decreases (figure 5.8). For the structure with gravure cells with a depth of only 7 µm (262x262-7) the contact angle changes at a velocity of 40 mm s^{-1} only by 5°, while at the deepest structure (262x262-25) the contact angle decreases by 11°.

5.4 Surfactant solution

On the unstructured part of the printing plate the contact angle can be measured and compared with the results on the smooth PS surface. The surfactant S-1DeS was added stepwise to the liquid container to measure concentrations of 15 % CMC, 30 % CMC and 45 % CMC (CMC=38.5 mM). The solution was stirred for at least 20 min at a velocity of 100 mm s^{-1} to reach an equilibrium of surfactant molecules adsorbed and desorbed at the surface of the drum and air in the setup is close to a saturated atmosphere. By adding surfactant the contact angle as well as the critical velocity of the unstable contact line decreases with increasing surfactant concentration (figure 5.9). Therefore, I conclude, that on the unstructured part of the drum the wetting behavior is comparable to the behaviour on smooth surfaces described in section 4.

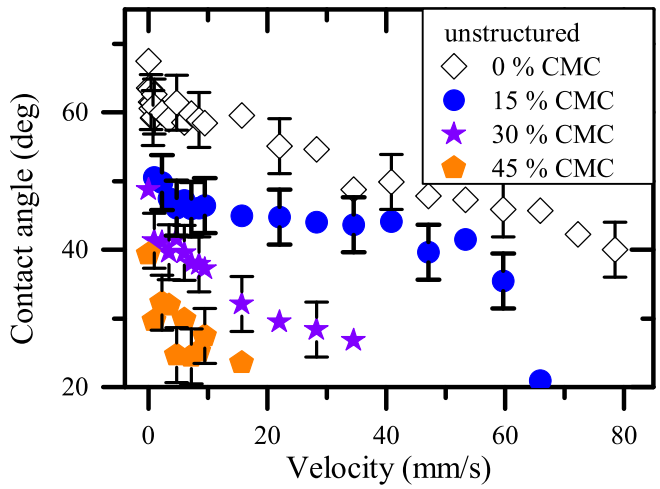

Figure 5.9.: The contact angle as well as the critical velocity of the instable contact line decreases on the unstructured part of the surface with increasing surfactant concentration. The measurement error is approximately ±5° and is shown only exemplarily.

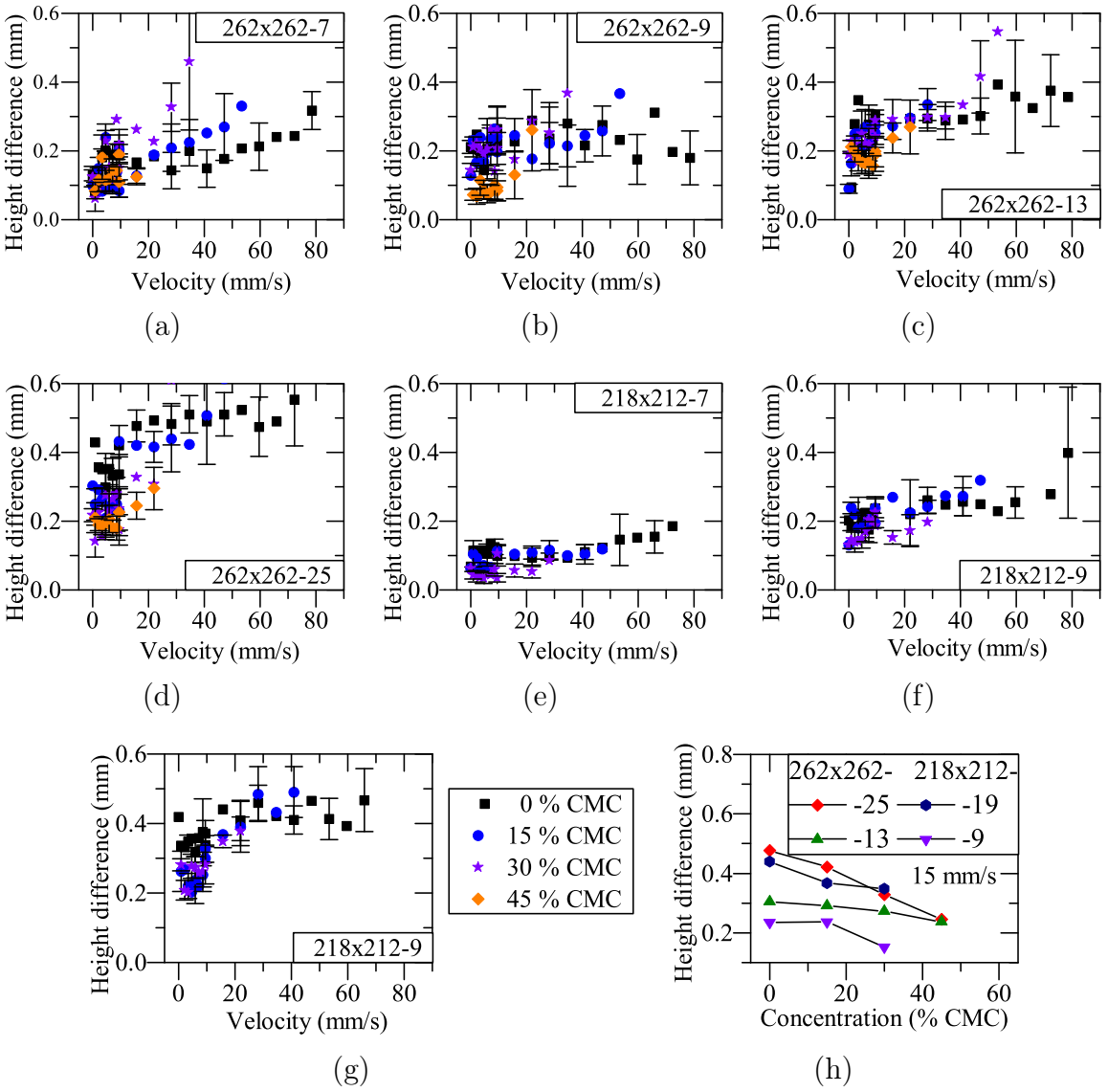

Figure 5.10.: The height difference between the unstructured and the structured area increases with increasing velocity on the different structures. With increasing surfactant concentration the height difference decreases. (a) 262x262-7, (b) 262x262-9, (c) 262x262-13, (d) 262x262-25, (e) 218x212-7, (f) 218x212-9, (g)218x212-19. (h) shows the decrease of the height difference with increasing surfactant concentration at a velocity of 15 mm s^{-1}.

On the structured surface it is, as already mentioned, only indirectly possible to determine the contact angle. Therefore, compared to the water measurements, additionally to the contact angle, the height difference between the unstructured and the structured area was measured (compare figure 5.4). Similar to the water measurements the height difference was measured just before the contact line depinned from the edge of the single gravure cells. Comparable to the water measurement the height difference

increases, reaches a plateau at higher velocities, and increases shortly before the contact line becomes unstable and begins to buckle. However, with increasing surfactant concentration the height difference decreases for all measured structured surfaces (figure 5.10). For a better comparison in figure 5.10 (h) the decrease of the height difference is shown exemplarily for four different structured surfaces at a velocity of $15\,\mathrm{mm\,s^{-1}}$.

Comparable to the calculation for water on the structured surfaces, the contact angle on the structured surfaces for all measured surfactant concentrations and surfaces were calculated. The contact angle behaviour for all surfaces is comparable to the measurement on the unstructured surface (see section 4). With increasing surfactant concentration the contact angle as well as the critical velocity of film formation decreases. Figure 5.11 shows this behaviour on the surface 262x262-15, which is typical for all surfaces.

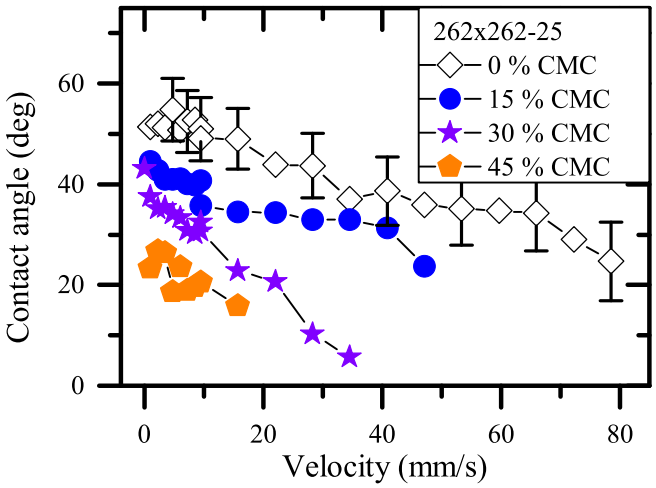

Figure 5.11.: The contact angle as well as the critical velocity of film formation decreases with increasing surfactant concentration on all structured surfaces. As an example (a) shows the calculated contact angle on the surface 262x262-25.

5.5 Comparison to the hydrodynamic considerations

The influence of the surface structure on the wetting behaviour in the presence of surfactant can be investigated by comparing the change in contact angle on different surfaces: the structured surfaces 262x262-25, the unstructured part of the printing plate

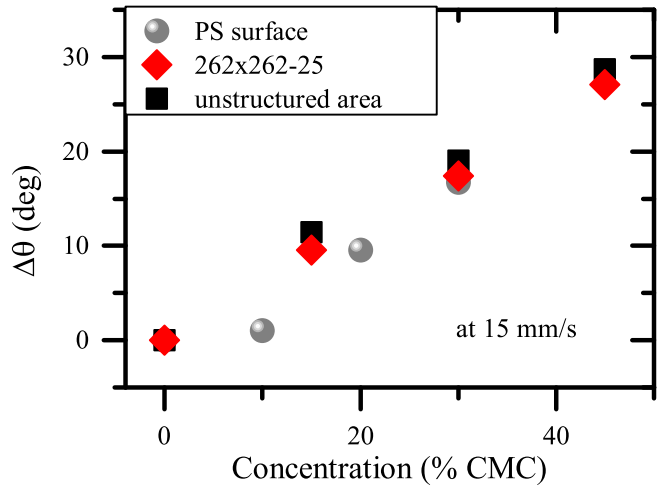

Figure 5.12.: Comparison of the change in contact angle on the unstructured part of the printing plate, the structured surface 262x262-25 as well as the smooth PS surface show a comparable behaviour. With increasing surfactant concentration the change in contact angle increases. With increasing surfactant concentration the differences between the different surfaces decrease.

as well as the smooth PS surface (see section 4). The change in contact angle $\Delta\Theta$ is defined as

$$\Delta\Theta = \Theta_{0\,\%\,\mathrm{CMC}} - \Theta_{X\,\%\,\mathrm{CMC}} \tag{5.3}$$

Thereby $\Theta_{0\,\%\,\mathrm{CMC}}$ is the contact angle of pure water at a given velocity and $\Theta_{X\,\%\,\mathrm{CMC}}$ the contact angle at $X\,\%\,\mathrm{CMC}$ at the same velocity.

By comparing the change in contact angle it is clearly visible, that at low velocity and low surfactant concentration the contact angle, as well as the slope of the contact angle curves, differs from each other. For higher concentrations the difference in the wetting behaviour induced by the roughness and structure of the surfaces vanishes (figure 5.12). That implies, that the higher the contact line velocity is and the higher the surfactant concentration is the more the hydrodynamic effects dominate the dewetting behaviour. This can be explained in the framework of the hypothesis formulated in section 4.4. Close to the CL the liquid moves together with the drum surface towards the three phase contact line. At the CL the liquid changes the direction and flows back on the liquid surface to the bulk. Thereby at the contact line a fresh surface is created, which is not covered with the same amount of surfactant molecules than far away from the contact line. This leads to a gradient in surface tension and therefore to a Marangoni

stress towards to the contact line, resulting in an variation of the flow profile close to the contact line compared to pure water. The change in the flow profile leads to a smaller contact angle and an increasing friction force. This friction force depends on the kind of surfactant (see section 4.8).

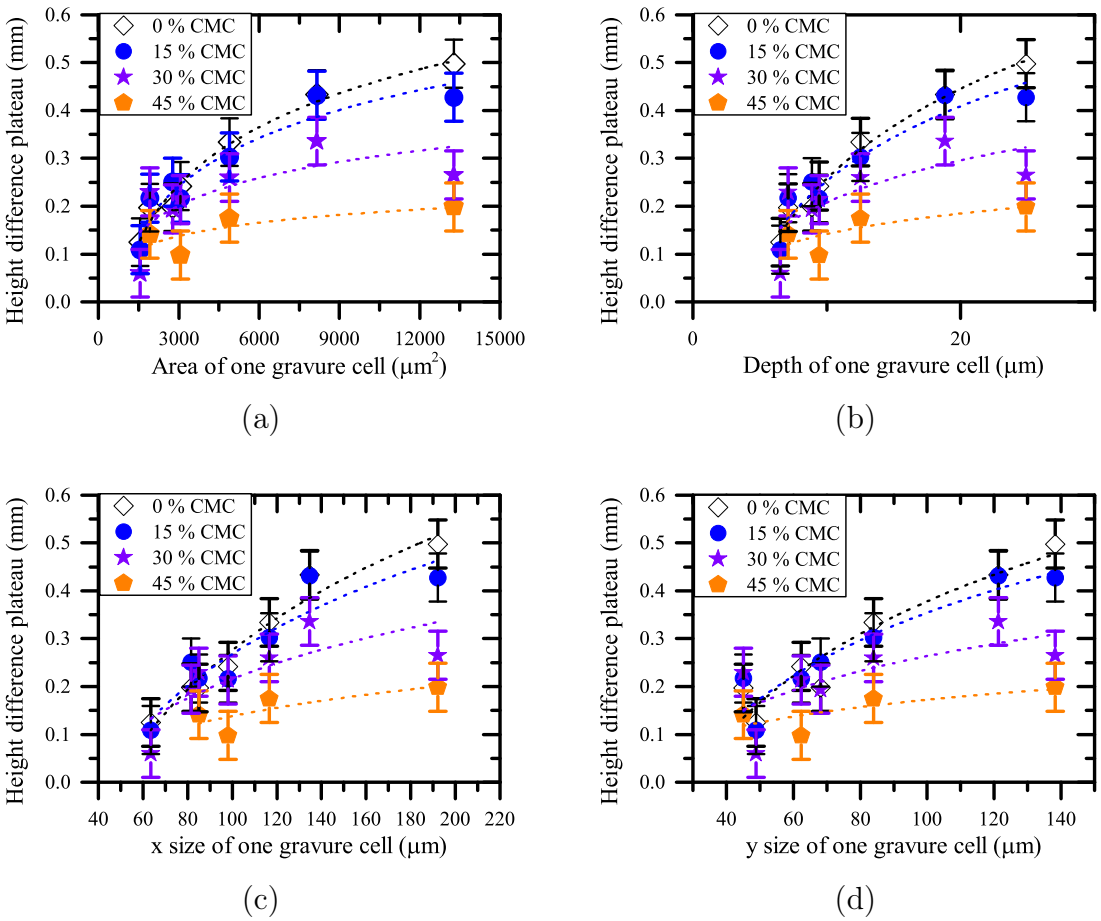

Figure 5.13.: Comparison of the height difference plateau. With increasing surfactant concentration the height difference decreases. The error bars are the standard deviation of the measured points in the plateau. The dashed lines are a guide to the eye.(a) shows the height distance over the area of one single cell (b) over depth of the gravure cell (c) the x-size and (d) the y size of a single gravure cell

The decreasing height difference with increasing surfactant concentration can be explained with the increasing frictional force with increasing surfactant concentration. With increasing surfactant concentration the frictional force due to Marangoni stress dominates the effects due to roughness. Therefore, the influence due to roughness decreases with increasing surfactant concentration.

For a comparison of the influence of the surfactant on the dewetting on the different structured surfaces. I compared the differences in height of the plateaus with the area of one single gravure cell (figure 5.13). Therefore, the plateau was defined as the average of the data points between the initial rise and the increase close to film formation velocity. The height difference of the plateau increases with increasing gravure cell size for pure water as well as for surfactant solution. It is unimportant how the size of the cell is exactly defined - as the area of one gravure cell, as the size of the gravure cells in x and y direction or as the depth of the gravure cell (figure 5.13)- with increasing size the height difference of the plateau increases. Nevertheless, in this comparison it is clearly visible, that the influence of the surface roughness decreases with increasing surfactant concentration.

5.6 Contact line velocity

Since the plateau in the height difference at a specific velocity range might be influenced by the emptying process of the gravure cells, I had a close look at the emptying process of the single gravure cells. Therefore, I used the high speed camera Photron S1 with 50 x magnification and thought objective illumination. For a better illumination of the single gravure cells an additional light was directed on the imaged area. The higher magnification allows to image the passage of the contact line over a single gravure cell. The time span that the contact line needs to come in first contact with a gravure cell until the CL depinns from the boundary of the same gravure cell is defined as passage time (figure 5.14). I measured this passage time for pure water as well as for 15 % CMC of S-1DeS at different velocities.

By assuming a constant CL velocity over the whole structured surface the passage time should decrease proportional to the inverse of the velocity (figure 5.15, dashed red line). The measurement of the passage time of pure water shows a good agreement for velocities slower than $40\,\mathrm{mm\,s^{-1}}$. But for higher velocities the passage time is longer than the expected one. Additionally,the passage time varies little for velocities up to $70\,\mathrm{mm\,s^{-1}}$. The passage time is not directly depended on the average velocity of the contact line. The contact line motion over the structured surface can not be constant. The CL stops at the pinning sides, and has different velocities in the gravure cells and the regions in between the gravure cells. The combination of these effects leads to the variation of the contact line velocities. The stable passage time for $v > 40\,\mathrm{mm\,s^{-1}}$ overlaps with the plateau in the height difference measurements.

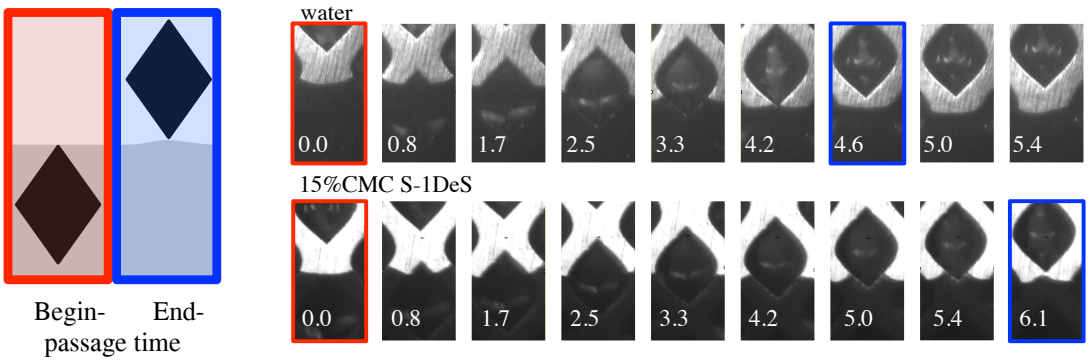

(a) (b)

Figure 5.14.: (a) depicted the definition of the passage time span. The left picture, with the red border, depicted the first contact of the gravure cell with the CL and the right picture, with the red border, depicted the same gravure cell at the ending point of the passage time span, the depinning of the CL of the gravure cell. (b) the top part shows the image passage time process in the top pictures for water and in the bottom pictures for 15 % CMC at a velocity of 20 mm s^{-1}. The numbers are the passage time in ms. The start (red) and ending (blue) of the passage time are marked colored borders.

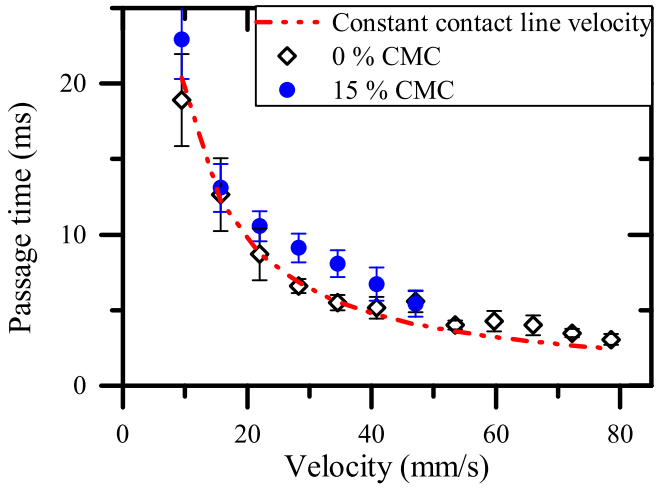

Figure 5.15.: The passage time of the contact line should decrease with increasing velocity by assuming a constant CL-velocity (dashed red line). The measurements show an stable passage time for water (black symbols) at velocities higher than 40 mm s^{-1}. In the presence of surfactant the passage time iseven longer (blue symbols)

5.7 Emptying of a single gravure cell

So far it is not clear if the cells are emptying completely or some liquid remains in the cells after the contact line passes. Due to optical reasons it is not possible to answer this question from the already mentioned measurement techniques. To investigate this, I place a liquid drop of 500 µL on the structured area of a slightly tilted printing plate. Thereby half of the drop is moving over the unstructured surface and the other half of the drop is moving over the structured surface 262x262-25. I image this by using an infrared camera (Infratec, VariocamHD[3]). The drop starts to move over the surface. On the unstructured surface the reflected infrared emission in front of the drop and behind the drop is similar. Which indicates the same temperature in front and behind the drop. During the movement of the drop on the structured part the surface behind and in front of the drop differs. Behind the drop it is colder compared to the front of the drop. This temperature decrease can be explained by liquid, which remains in the gravure cells and evaporates after the contact line has already moved over the drop. An example of this images done with the infrared camera can be seen in figure 5.16. The inhomogeneous temperature distribution behind the drop might depend on variations in the velocities of the contact line.

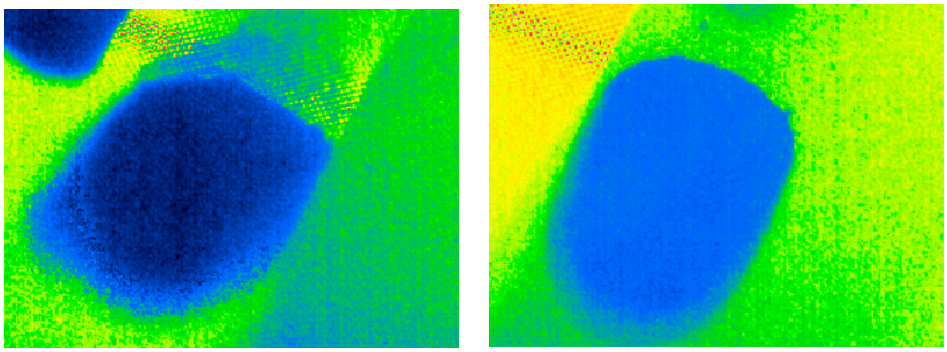

(a) (b)

Figure 5.16.: Infrared image of a drop moving over the printing plate. (a) The drop it moves over the structured surface area, (b) over the unstructured surface area 262x262-25.

For a better image of the process happening in the cells I replaced the printing plate with a transparent structured SU-8 substrate. This substrate had circular holes (diameter 48 µm, depth 11 µm, distance between the center of the holes in x an y direction 52 µm). On this surface I investigate the receding contact line by using an

[3] InfraTec GmbH, Infrarotsensorik und Messtechnik, Gostritzer Straße 61 - 63, 01217 Dresden,www.infratec.de

optical inverted microscope with a connected high speed camera, looking from below on the receding contact line (see figure 5.17). Therefore, a drop is placed on the surface. The volume is reduced by a syringe pump with a needle directly in the drop. As a result of the decreasing volume the contact line moves over the surface and can be imaged.

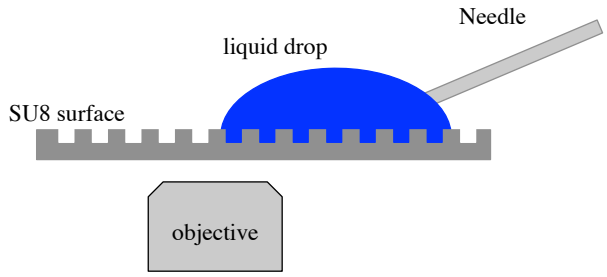

Figure 5.17.: Sketch of the setup to visualize the receding contact line of a drop on the SU8 surface with a microscope.

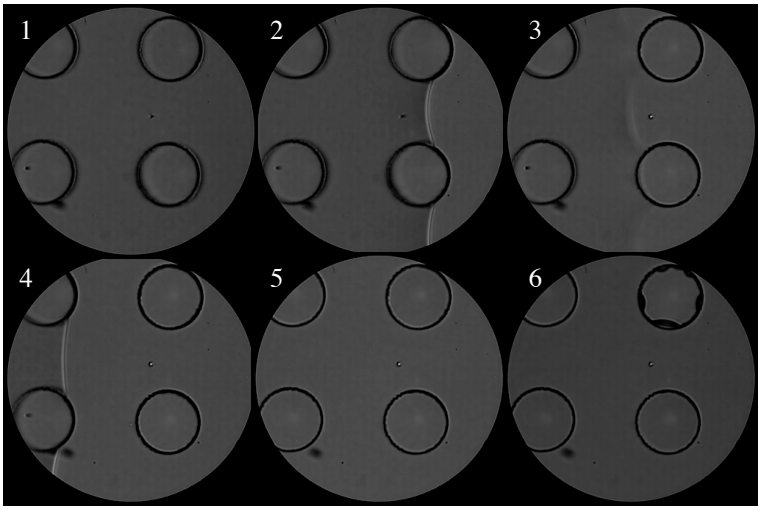

Figure 5.18.: The receding contact line moves from the right side of the image to the left side of the images. The panels show different times of receding of the contact line on a SU8 surface: (1) wetted surface (2-4) receding CL pins at the holes and slips to the next one, (5) the CL already moved over the surface, holes are still filled with liquid and (6) due to evaporation the liquid in the hole in the right corner cracks.

In the images of figure 5.18 the contact line is moving from the right to the left side. Equivalent to the measurements on the printing plate the contact line is pinned at the edge of the holes and slips to the next hole corner afterwards (figure 5.18: 1-4). After the contact line is moved over the hole there is still liquid inside the cell (figure 5.18: 5).

The remaining liquid evaporates afterwards and the cell is only due to the evaporation completely empty in the end (figure 5.18: 6).

5.8 Conclusion of the wetting on structured surfaces

By adding surfactant to a liquid the dynamic dewetting behaviour on a structured surface changes. Comparable to the dewetting on smooth surfaces (section 4), the contact angle as well as the critical velocity, at which the contact line starts to get unstable, decreases [55, 57, 56, 64, 161]. The influence of the structure surface decreases with increasing surfactant concentration. The decreasing influence of the structured surface can be explained by the fact, that with increasing surfactant concentration the Marangoni stress towards the three phase contact line increases. These Marangoni stresses dominate the stress due to pinning on the structured surface.

The analysis of the emptying mechanism showed, that the gravure cells do not empty completely after the contact line moves over them. Some liquid remains in the cells and the remaining liquid evaporates afterwards. How this remaining liquid influences the wetting behaviour is not clear yet and it needs further investigation to understand this influence as well.

6 Flow profile on a microscopic length scale

6.1 Materials and methods

A new setup was designed, which allows to investigate the flow profile in the liquid close to the moving contact line down to a length scale of 10 µm. The idea of the setup is to image the area near the CL with a confocal microscope. Therefore, a drop will be deposited on a glass slide. Thereby it should be possible to move the glass slide during the drop is hold on one position, to enable the imaging of the area around the moving CL. In figure 6.1 the idea of the specially designed setup is depicted. This setup allows to image a moving contact line stationary above a microscope objective.

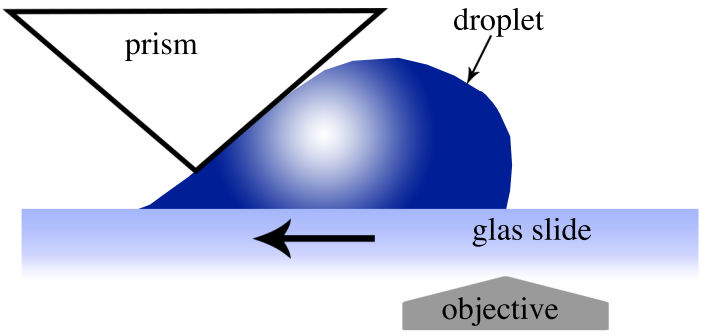

Figure 6.1.: Schematic sketch of the idea of the setup to measure the CL with a higher spatial resolution than the one described in section 2.8.3.

6.2 Development of the microscopic setup

To realize the idea of a stationary moving contact line, it was necessary to find a possibility to move the glass slide continuously linear. If the motion is not continuously linear and makes instead small steps, capillary waves in the drop could be generated, which could results in changes in the flow profile. The travel distance must be bigger than 20 mm to allow the measurement during an stationary motion in the drop. Furthermore a variation of the velocities was required to allow investigations at different velocities. All necessary criteria of the motor are summarized in table 6.1.

Table 6.1.: Necessary criteria of the glass slide motion and data of the use motor.

	necessary criteria	piezo stage LPS-45
travel range	20 mm	26 mm
maximum velocity	$> 5\,\mathrm{mm\,s^{-1}}$	$10\,\mathrm{mm\,s^{-1}}$
minimum velocity	$<0.1\,\mathrm{mm\,s^{-1}}$	$0.001\,\mathrm{mm\,s^{-1}}$
aberration in z-direction	a few micrometer	$\pm 2\,\mu\mathrm{m}$

The realization of the stepless motion was the biggest problem during the development of the new setup, since most small linear motors with a large travel range are stepper motors and therefore the motion is not stepless. To realize a stepless motion the piezo stick slip motor LPS-45 from Physik Instrumente[1] (figure 6.2 (A)) is used. The working principle is a piezo motor, which moves the whole motor a specific distance and slips to the next position and moves the motor again. The exact working mechanism is a company secret. The data given by the manufacturer of that motor is listed in table 6.1. To image the area close to the contact line with a microscope, the whole setup must fit on top of the microscope stage. To enable on one hand a view from the bottom with a microscope on the glass slide on the other hand the glass slide (B) has to be mounted onto the motor to enable the motion of the glass slide, an extension (C) is necessary. A parallel motion of the glass slide to the objective is necessary. Therefore, an adapter plate (D) with three micrometer screws (E) was designed. To apply an initial load on the micrometer screws, two additional screws with rubber rings (F) are used to generate the initial load.

To hold the contact line of the moving drop on the imaging position during the measurement a 60° prism (G) (coated with Trichloro (1H, 1H, 2H, 2H-perfluorooctyl) silane) with a length of 25 mm is used. For precise positioning of the prism, the prism is mounted on a mirror mount (I) (mirror mount kinematic, with fine-thread screws, K 25-FGS, Owis GmbH[2]) which is placed on a vertical stage (H) (Aluminium Ball Bearing Vertical Stages, 7VT174-5, Standa[3]). This enables an exact positioning of the prism in x, y and z direction to realize that the corner of the prism is parallel and close to the glass slide. The prism is glued with sealing wax to an adapter plate, which is glued also with sealing wax to the mirror mount. A 3-D drawing of the setup is shown in figure 6.2.

The technical drawings of this setup can be found in appendix figure A.25 - figure A.39.

[1] Physik Instrumente (PI) GmbH & Co. KG, Auf der Römerstraße 1, 76228 Karlsruhe, Deutschland, www.physikinstrumente.de

[2] Owis GmbH, Im Gaisgraben 7, 79219 Staufen im Breisgau, Deutschland, www.owis.eu

[3] Standa, Švitrigailos g. 4, Vilnius 03222, Litauen, www.standa.lt

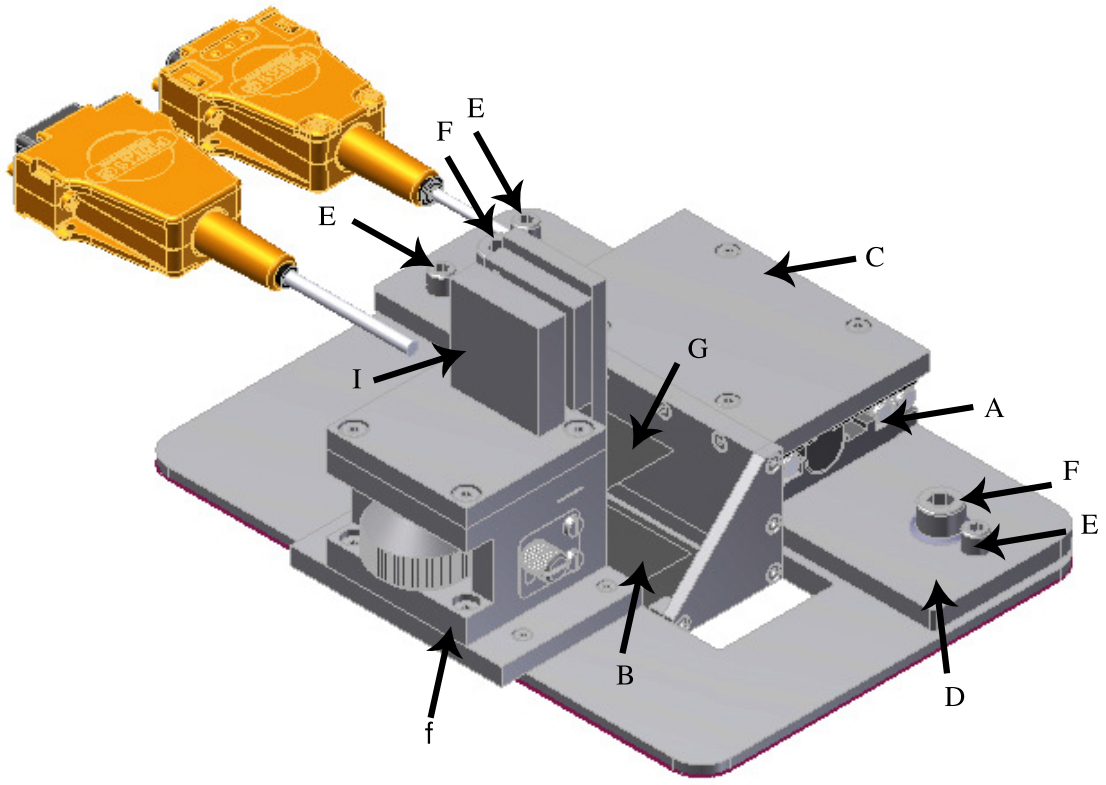

Figure 6.2.: 3D drawing of the microscope setup: (A) Piezo stick slip motor, (B) glass slide, (C) extension, (D) adapter plate, (E) micrometer screws, (F) screws with rubber rings, (G) 60° prism, (H) vertical stage, (I) mirror mount.

6.2.1 Analyzing the linearity of the motion

To determine the continuously linear motion of the glass slide motion a small amount of 7 µm silica particles were placed on the glass slide. The setup was placed on a Leica DMI 6000 B microscope with an Olympus UPLAPO60XW/1.20 UIS-OBJ, WD0.25 objective. The glass slides were driven with different velocities with the new setup. The particle motion was imaged with the high speed camera Photron S1. The single particles were tracked by "Particle Detector and Trackers" plugin in ImageJ. To guarantee a motionless connection between the glass slide and the extension, the glass slide (thickness: 170 µm) is glued with sealing wax on the extension of the motor.

The extension was fixed in three different ways onto the motor to find the most linear motion. Either the extension was screwed to the motor, glued with tesa Powerstrips®[4], or a polydimethylsiloxane (PDMS) layer was placed between the motor and the extension and weighted down to avoid a tilting of the extension. The PDMS layer

[4] tesa SE, Hugo-Kirchberg-Straße 1, 22848 Norderstedt, Deutschland, www.tesa.com

is approximately 1 mm thick and is build out of SYLGARD®184 (silicone elastomer) in a ratio of 10:1.

Table 6.2.: Three different connections methods were tested concerning their continuous linear motion at different velocities. A continuous linear motion is labeled as linear, all motions where the motion is not step free were labeled nonlinear. The velocities of the Piezo stick slip motor depending of the specific frequency changed in the software. To resolve the motion the frame rate of the high speed camera was varied.

frequency [Hz]	frame rate [fps]	velocity [mm s^{-1}]	screwed	glued	PDMS
151	5400	0.07	nonlinear	nonlinear	nonlinear
313	5400	0.13	nonlinear	nonlinear	nonlinear
500	5400	0.22	nonlinear	nonlinear	linear
1510	30000	0.70	nonlinear	nonlinear	linear
3011	40000	1.33	linear	linear	linear
10011	54000	3.87	linear	linear	linear
25000	54000	10.97	linear	linear	linear

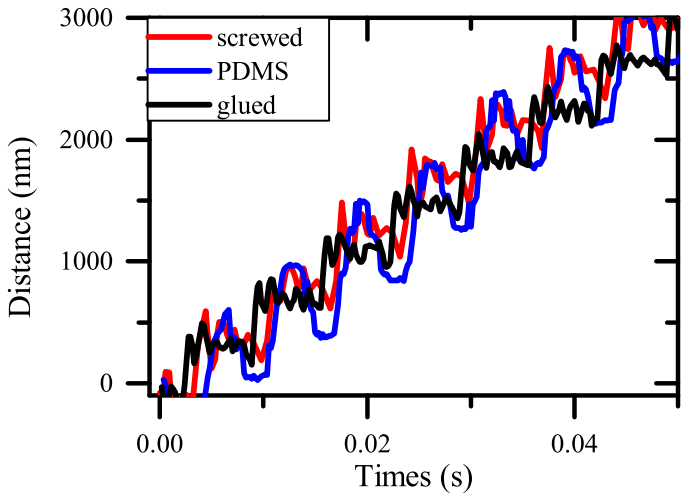

Figure 6.3.: Nonlinear motion of the Piezo stick slip motor for the different mounting versions at 151 Hz. The uncertainty of the measurements is around 200 nm.

For changing the velocity of the motor it is necessary to change a frequency in the software of the motor. What exactly this frequency changes is a company secret. It is possible to vary this frequency between 150 Hz and 25 000 Hz. Since the resulting velocities were not known a priori, it was necessary to analyze the velocity. Additionally the continuous linear motion was proved. To resolve the motion at all frequencies the

frame rate of the high speed camera was adjusted for the current frequency. The measured frequencies as well as the used frame rates are summarize in table 6.2.

The measurement of the motion shows, that for the frequencies $< 300\,\mathrm{Hz}$ all kind of connection shows a nonlinear motion. Clear steps of the motion are detectable by tracking the particles (figure 6.3). The steps in the motion results from the type of motor, which is a piezo stick slip motor. Thereby a piezo motor moves the whole motor a specific distance (for the used motor 400 nm) and slips to next position and moves the motor again. I assume, that the visible steps are the slip motion of the piezo motor.

For the PDMS layer connection the motion of the glass slide is for frequencies $> 500\,\mathrm{Hz}$ continuously linear in the measurement uncertainties. In contrast to the measurements for lower frequencies the motion of the tracer particles and therefore also the motion of the glass slide is linear (figure 6.4). All higher frequencies show similar behaviour for the PDMS layer connection. Since in contrast to the PDMS layer connection the screwed as well as the glued connection, show still steps at $< 3\,\mathrm{kHz}$ and show only a continuously linear motion at even higher frequencies, the PDMS layer connection was chosen for all following experiments. The continuously linear motion for lower frequencies for the PDMS connection results from the damping effect of the PDMS layer. In comparison to the other connections it damps the still existing steps and results in a continuously linear motion of the glass slide.

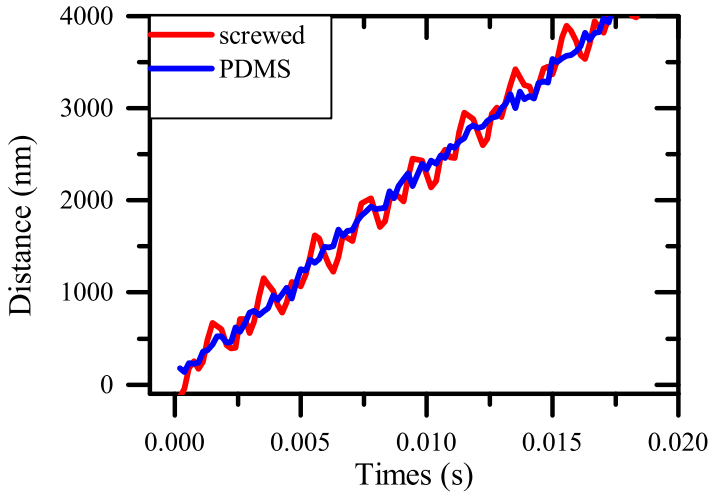

Figure 6.4.: Linear motion of the piezo stick slip motor for the PDMS connection and a stepwise motion for the screwed connection at 500 Hz. The uncertainty of the measurements is around 200 nm.

The frequency dependence of the velocity is not linear for the whole frequency range as visible in figure 6.5. Only for velocities $< 10\,\mathrm{kHz}$ a linear dependency exist. Nevertheless

the motor can move the glass slides linear in the velocity range between $0.2\,\mathrm{mm\,s^{-1}}$ and $10\,\mathrm{mm\,s^{-1}}$ continuously linear motion withour visible steps.

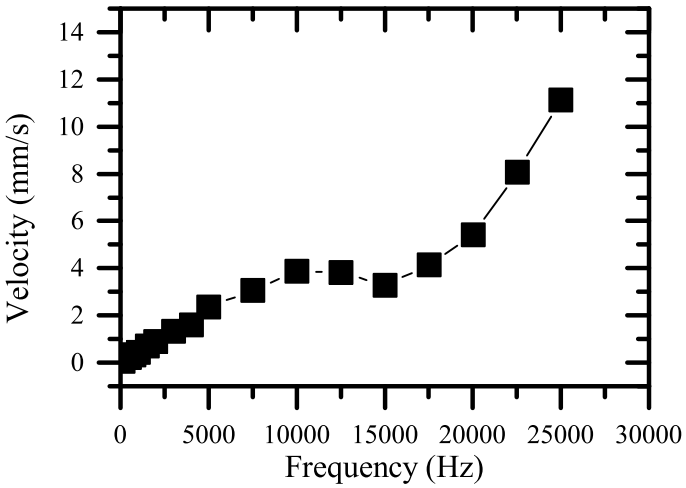

Figure 6.5.: Frequency dependence of the velocity in the piezo slip stick motor LPS-45.

6.2.2 Modifications of the confocal microscope

To image the flow profile close to the contact line a confocal microscope is used. For the lowest linear velocity, which is possible with the setup ($v = 0.2\,\mathrm{mm\,s^{-1}}$), the slow mode of the confocal microscope is not fast enough to resolve the motion of the particles. Therefore, the fast mode of the home built setup (see section 2.9) has to be used. As already mentioned the fast mode of the confocal setup has some disadvantages in the alignment and the usage of flipping mirrors. Since there is no possibility to use no flip mirrors for the fast mode or the slow mode all screws used in the optical path of both modes of the confocal microscope were fixed additionally with loctite 222[5]. All mirrors and the beam splitter were pointwise clued with two component epoxy to avoid temperature induced motion and therefore misalignment of the optical path. The additional fixing counteracts as well the misalignment of the optical path due to the external force by flipping the mirrors.

For an easier alignment of the fast mode an additional flip mirror was placed in the optical path of the fast mode. Due to this mirror an alignment of the fast mode is possible without misaligning the slow mode. This has in addition the positive effect, that the photon detectors (slow mode) can be used, even if for the rest of the optical path the fast mode path is used (blue arrows in figure 6.6). This benefits in a more

[5] Henkel AG & Co. KGaA Standort München, Gutenbergstraße 3, 85748 Garching, www.loctite.de

precise surface detection of the sample, by flipping only one mirror. The modifications of the fast mode beam path are shown in figure 6.6.

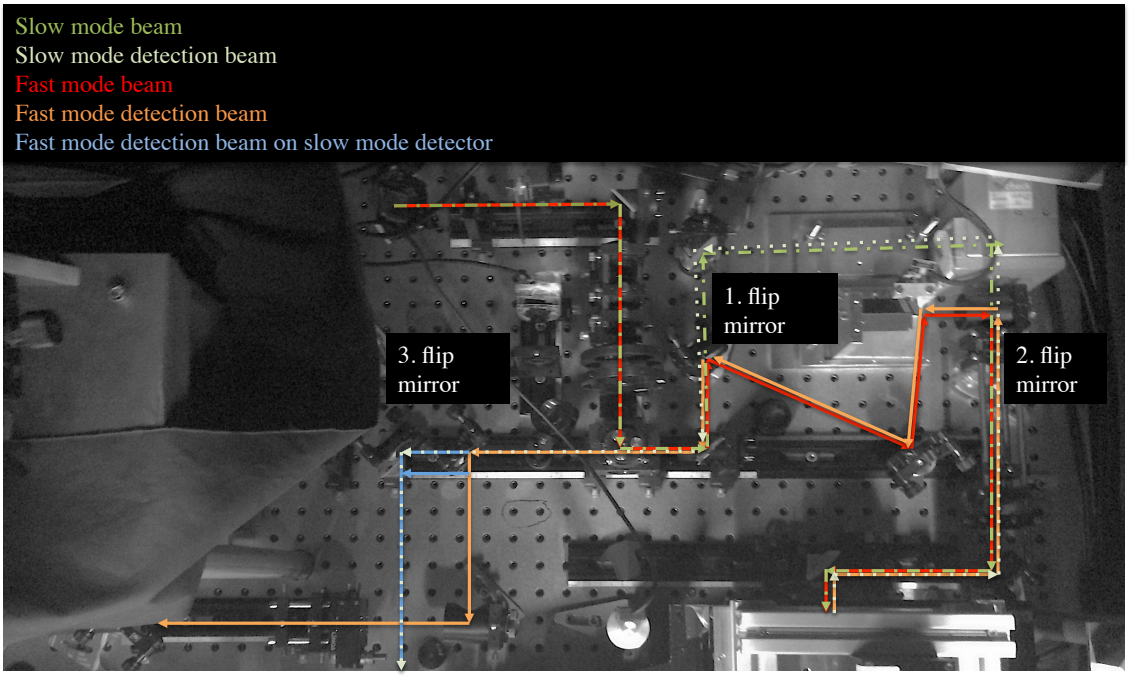

Figure 6.6.: Modification of the fast mode beam path to allow a faster alignment. The red arrows show the modified fast mode beam path, the orange one the detection beam path of the fast mode, the dashed green one shows the beam path of the slow mode.

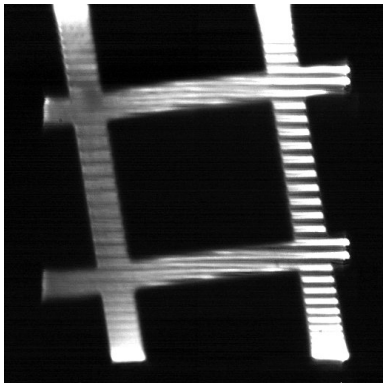

Figure 6.7.: 400 Hz frame rate image of a micrometer grid. The square has a dimension of 50 µm. The stripes in the image result from the limited number of lines during the scanning process.

Even if a third flip mirror has to be used in the modified beam path the alignment of the fast mode is faster and more precise, which allows to use a 20 µm pinhole to reach a

higher z resolution of the image. An example image with 400 Hz frame rate done with the modified alignment of the fast mode is shown in figure 6.7. The stripes in the image result from the limited number of lines during the scanning process. The used objective in this thesis is a 60x water immersion objective (Olympus UPLAPO60XW/1.20 UIS-OBJ, WD0.25)[6], to have as low refractive index changes as possible and therefore a deep view in the sample.

6.3 Experimental method and procedure

6.3.1 Material

To prove the hypothesis (see section 2.7 and 4.4) of the wetting behaviour close to the contact line in the presence of surfactants, I investigate the dewetting behaviour of surfactant solutions on a microscopic length scale. Therefore, I used the surfactants CTAB and C_8E_3, purchased from Sigma-Aldrich (same surfactants as used in the previous sections). To analyze the flow profile PS particles (home made by Gabriel Schäfer, Max Planck Institute for Polymer Research) with a diameter of 4 µm were added to the solution. In contrast to commercially bought particle, the presence of surfactants on the particle surface can be excluded. The particle size was chosen, since on one hand they are clearly detectable, on the other hand they are small enough to follow the flow behaviour at the length scale where the changes by adding surfactant are expected. As mentioned in section 2.7 and 2.8.3 the length scale changes are expected is around 20 µm.

In a water solution the particles sediment due to the density difference between water and PS. This has to be avoided, since the sedimentation would influence the flow behaviour. To overcome the sedimentation a density adjusted solution was used. Therefore, instead of pure water a 1:1 mixture of water (H_2O) and deuterium oxide (D_2O) was used. In this solution the particles show no sedimentation during at least 6 h. As H_2O milli Q water was used, which was prepared by using an Arium®611 ultra pure water system (Sartorius) or Arium ®pro VF/UF & DI/UV (Sartorius) at a resistivity of 18.2 MΩ m. The D_2O was purchased from Sigma-Aldrich, with a purity of 99 %.

To realize a stable contact line position in the imaged view field a clean glass slide was necessary to avoid pinning of the contact line. Due to optical reasons it was necessary, that the liquid drop of the solution has a contact angle smaller than 90°. If the contact

[6] OLYMPUS EUROPA SE & CO. KG, Wendenstraße 14-18, 20097 Hamburg, Deutschland, http://www.olympus-lifescience.com

angle would be higher then 90° the optical path passes the glass slide and than the air between the drop and the glass slide to image the area slightly above the glass slide. This would reduce the image quality significantly and has therefore to be avoided. To reach this contact angle the glass slides (thickness 170 µm, Menzel) were cleaned with isopropanol and a clean room tissue mechanically. Afterwards the glass slides were coated in gas phase with Tricloro(1H,1H,2H,2H-perfluorooctyl)silane purchased from Sigma Aldrich. Therefore, the glass slides were placed in a box and a drop of the coating liquid was placed next to it. For a homogeneous coating a magnetic stirrer was also placed in the box to distributed the Tricloro(1H,1H,2H,2H-perfluorooctyl)silane homogeneously in the gas phase. The box was closed for two minutes, afterwards the glass slides were immediately moved out of the box. The static contact angle of pure water is around 78° on these glass slides.

6.3.2 Experimental procedure

The clean glass slides were glued with sealing wax on the extension. Afterwards the whole setup was placed on top of the confocal microscope. All experiments were done in the reflective mode of the confocal microscope (see section 2.9.1). Before the experiment is started the focus is placed on the glass slide of the sample. Therefore, the detectors of the slow mode are used (blue line in figure 6.6). Since the refractive index of the glass and air is different the reflex of the glass surface it clearly visible. Because the detectors of the slow mode are more sensitive than the CCD-chip of the fast mode the detection of the surface by using the single photon detector is faster and easier. After the surface is detected the mirror 3 is flipped to change the beam path to the CCD-chip. For all experiments 20 µL of the solution were placed on the glass slide with an Eppendorf pipette. The drop is placed as close as possible to the prism, but without touching it, to avoid contaminations. The movement of the glass slide was started and the area close to the CL was imaged with 200 Hz. To minimize the influence of the prism on the flow profile close to the contact line, the contact line on the opposite side of the drop was imaged, as sketched in figure 6.8. As soon as the glass starts to move, the CL changes the position and has to be moved back in the imaged area. During this time the drop moves >1 mm. It can be assumed, that this distance is enough to reach a stationary flow profile close to the contact line.

The view field ($\approx$ 80 x80 µm) was positioned as seen in figure 6.8 to have a straight CL in the images. The zoomed out picture shows an image done with the fast mode confocal setup. The image is taken from the bottom of the drop and shows a horizontal cut, 2-10 µm above the glass slide. The dark area is the liquid and the bright area

the refection of the glass slide, the transition between the dark and the bright area is the contact line. The bright parts in the liquid are the tracer particles. The imaged plane was roughly 2-10 µm above the glass slide for all experiments. The glass slide was aligned as parallel as possible to the objective, the angle was less than 5°(see section 6.4.4).

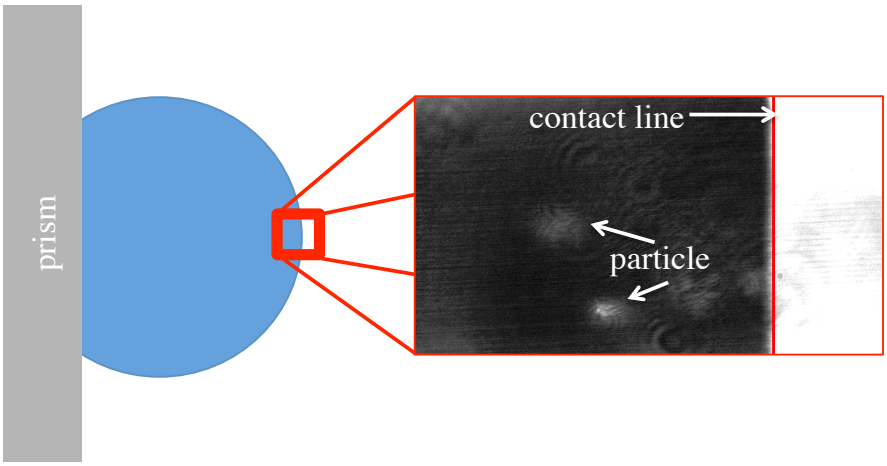

Figure 6.8.: View field position in the drop, bottom view of the drop (blue circle). The red square shows the imaging region and the zoomed out region is a confocal image of this area. The dark part is the drop, the bright part the refection of the glass slide. The bright spots in the drop are tracer particles. The red line is the contact line calculated in figure 6.9

Every glass slide was only used for one drop, to eliminate the possibility of contaminations on the next experiments. By reusing the glass slide, the contact line was not moving continuously anymore but rather pinned on the surface. During the movement of a drop with tracer particles over the glass slide, some tracer particles remain on the glass slide and affected therefore the next drop, which is moving over this already used glass slide.

6.3.3 Strategies for the data analysis

Due to optical limitations not all the tracer particles are shown in the images as round circles. Therefore, the particles could not be tracked with the same procedure as described in section 6.2.1. To track the particles the pixel with the local brightness peak was tracked. Normally this was the pixel in the center of the particle. Some particles had two local brightness peaks, then the pixel coordinates were averaged afterwards. To track the particles as described in the whole video, an ImageJ macro was used to detect the maxima in more than one image and save the x and y coordinates of the

particles. This macro is based on the "find maximum" plugin of image J and can be found in appendix A.2.1.

To detect the contact line the brightness profile of all images in the analyzed area was saved with another ImageJ macro based on the plugin plot profile (see appendix A.2.1). Since the contact line is the transition between the dark and the bright area it is shown as jump in the plot profile. The contact line is defined at the position of 90 % of the gray value of the glass reflection (see figure 6.9 dashed red line.) The contact line find with this method is marked in figure 6.8 as red line.

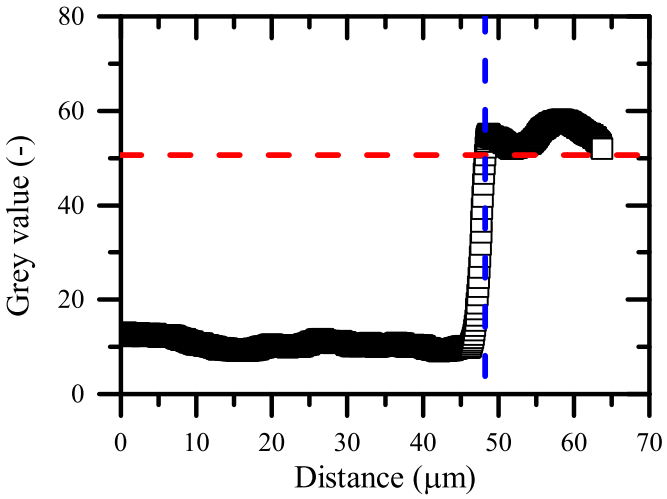

Figure 6.9.: To determine the contact line a brightness profile of the image was calculated. The high gray values is the reflecting glass side and the lower values the water. The contact line is defined as 90 % of the average gray value of the glass slide (dashed red and blue lines).

By imaging a micrometer grid a scaling factor between pixel and micrometer could be calculated. The movement of the particles in the image were translated into the movement of the particles related to the contact line. This allows to compare the movement of particles of different experiments, since the motion of the particles relative to the contact line represents the flow in the drop in the imaged plane. The experimental results are explained in the following sections.

The contact angle can not be measured during the experiment due to optical reasons. The size of the setup had to be small enough to fit on top of the microscope. Additionally the working distance between objective and glass slide must be small enough for the confocal microscope measurements. This does not allow the measurement of the contact angle during the experiments on the confocal microscope. To measure the contact angle the high speed camera Photron S1 with two times magnification and illumination

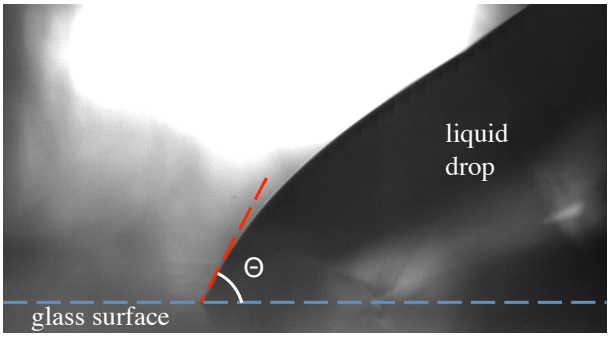

Figure 6.10.: Image of the contact line area in side view. The contact angle can not be measured during the confocal microscope measurement and has to be done afterwards on a similar preprepared glass slide. The dashed blue line represents the glass surface and the dashed red line the liquid surface. The angle in-between is the measured contact angle. The shape of the drop differs from a sphere, since it is pinned on the right side on the prism. The image has a dimension in x direction of around 5 mm.

through the objective was used. To allow the side view imaging of the contact line area from one side, the prism was glued to another extension. The contact angles were analyzed by fitting one straight line on the glass surface and a second one to the liquid air interface close to the contact line. The angle between these two lines was determined as the contact angle (figure 6.10). The measurement uncertainties of this contact angle measurement technique are 5°.

6.4 Experimental results

6.4.1 Dynamic contact angle

On one hand, as already mentioned, the contact angle can not be measured during the experiment on top of the confocal microscope. On the other hand, the glass slides can only be used for one experiment since otherwise the flow contact line is pinned by particles, that remained on the surface. This would also change the contact angle. Therefore, it is not possible to measure the contact angle and the flow profile on the same glass slide. Nevertheless the contact angle was measured on a fresh glass slide preprepared in the same way as the glass slides for the confocal measurements. To verify, that the measured contact angle is comparable to the one in the flow profile measurements, the contact angle was measured on four fresh surfaces for every concentration. The averaged results are shown in figure 6.11. Comparable to all experiments shown before, the contact angle decreases with increasing surfactant concentration. For

pure water the receding contact angle at a velocity of $0.2\,\mathrm{mm\,s^{-1}}$ is around 58° and decreases for a concentration of 30 % CMC down to 41° for CTAB and 38° for C_8E_3.

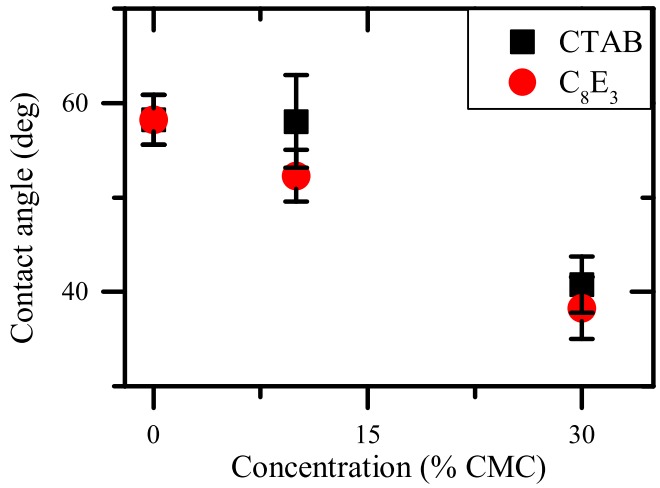

Figure 6.11.: Contact angle depending on the relative surfactant concentration (% CMC) at a velocity of $0.2\,\mathrm{mm\,s^{-1}}$ with increasing surfactant concentration the contact angle decreases.

6.4.2 Water

The tracking of tracer particles in water shows two kinds of typical behaviour (figure 6.12). One is a motion with a constant velocity, the other behaviour is a slowing down of the particles towards the contact line. The two different behaviours can be explained by the fact, that some particles stick to the glass slide and do not freely move in the liquid. These particles do not slow down. The velocity of these particles is the velocity of the glass slide, measured by particle tracking (see section 6.3.2). Therefore I assume these particles stick to the glass surface. In contrast the particles, which slow down, can freely move in the liquid and follow therefore the flow of the liquid. Nevertheless, all particles following the flow profile have a similar behaviour (figure 6.13). First they have a constant velocity in x direction towards the CL and around 30 µm away from the CL the particles slow down in x direction. It can be assumed, that the particles change their direction and move out of the imaged area in y direction. In order to get an average value of the motion close to the CL, the motion of all measured particles was averaged (orange line, figure 6.13).

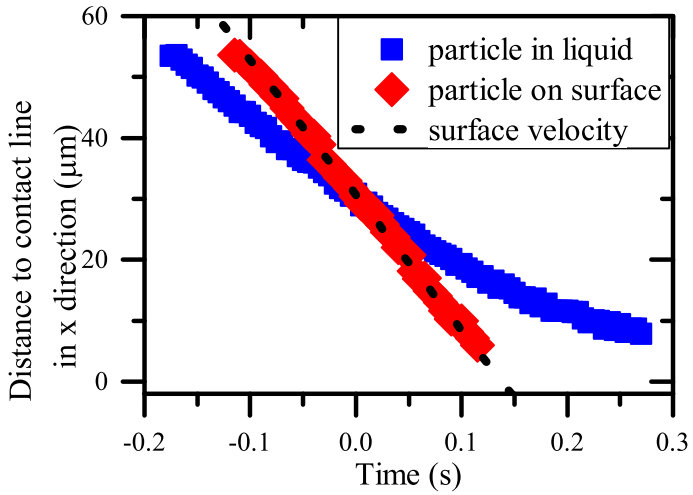

Figure 6.12.: Two different flow behaviours of particles at a velocity of $0.2\,\mathrm{mm\,s^{-1}}$. The particles represented by the red symbols stick to the glass slide, while the particles represented by the blue symbols can follow the liquid flow. The dashed black line is the velocity of the glass slide, measured by particle tracking (see section 6.3.2).

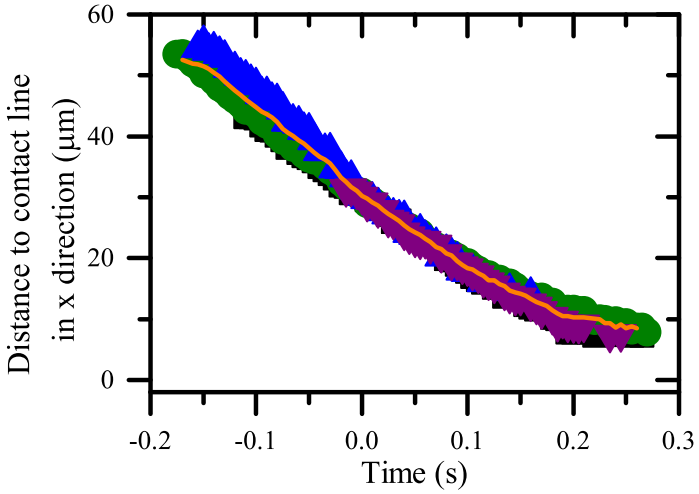

Figure 6.13.: Flow behaviour close to the CL at a velocity of $0.2\,\mathrm{mm\,s^{-1}}$. The particles slow down in x direction towards the contact line. The orange line represents the average motion.

6.4.3 Surfactant solutions

To investigate the influence of surfactants on the flow behaviour, the same experiment was done with two different surfactants (CTAB and C_8E_3), each with two different concentrations (10 % CMC and 30 % CMC). In general, the behaviour for the surfactant solution is comparable to the one for pure water. Some particles stick to the surface and have the velocity of the glass surface. All other measured particles flow towards the CL and slow down near the CL in x direction (figure 6.14). To exclude the influence of charge of the surfactant molecules, two differently charged surfactants were measured, the cationic surfactant CTAB and the nonionic surfactant C_8E_3.

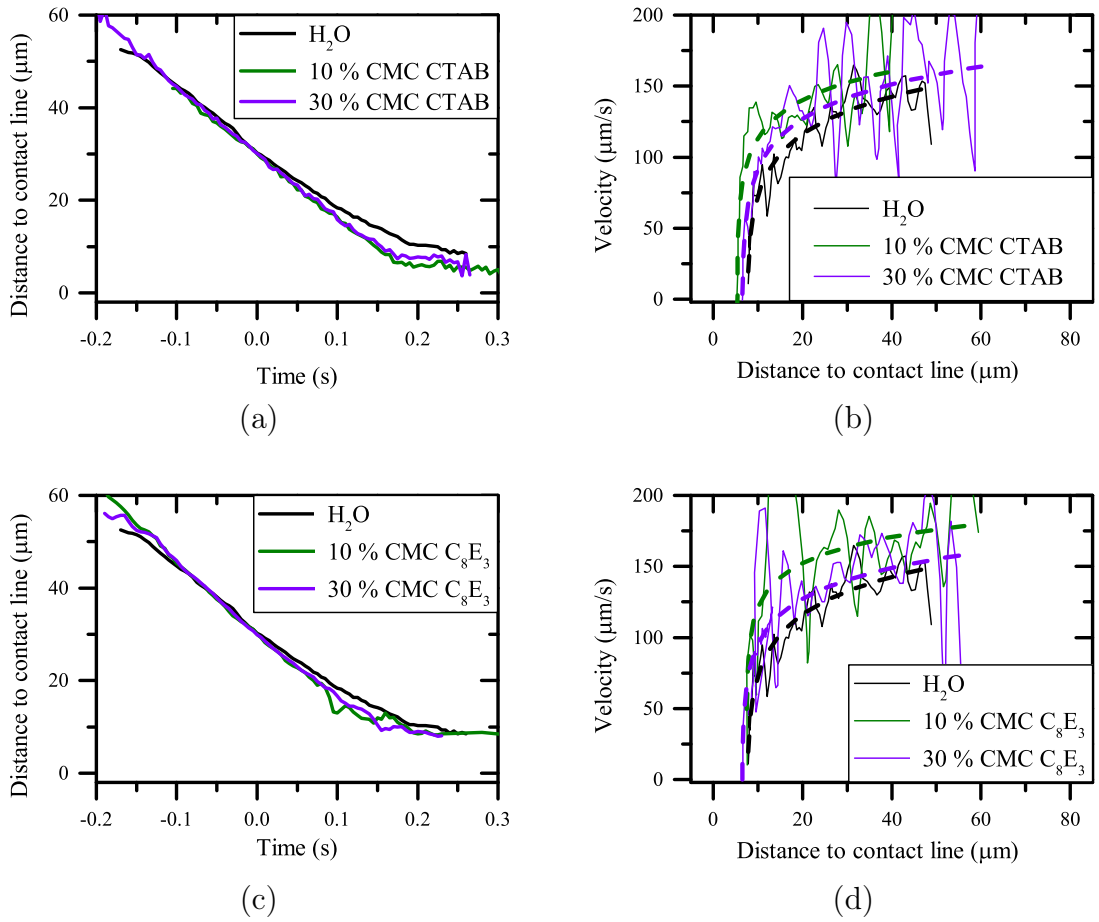

Figure 6.14.: Comparison of the flow behaviour with and without surfactants close to the CL at a velocity of $0.2\,\mathrm{mm\,s^{-1}}$.Panel (a), (b) shows CTAB measurements, panel (c), (d) C_8E_3 measurements. The dashed lines in the right figures are guides for the eye.

In comparison with water, both surfactants show a change in the flow profile (figure 6.14). This is a weak but reproducible effect of the surfactants. In presence of

surfactant the decrease of the velocity in x direction happens closer to the contact line (≈15 µm) than for pure water (≈30 µm). The time derivative of the measured data is the velocity in x direction close to the contact line (figure 6.14 (b), (c)). To reduce the measurement noise, I averaged the derivative over six measurements.

6.4.4 Comparison with the theoretically predicted flow profile

Moffatt [113] predicted the flow profile near a sharp corner. Effects on the nanoscopic as well as mesoscopic length scale, like for example the slip length as described in [38, 73], will not play a role at the investigated length scale of 20 µm. Moffatt solved the flow profile for a flat plate drawn in a liquid with one free surface. There he neglected the surface tension effects and assumed, that the gravity keeps the surface horizontal. He calculated the flow in a planar coordinate system (see figure 6.15). In the measurements, shown in this section, the flow behaviour should be similar. Therefore I compared the measured data with the predicted flow profile.

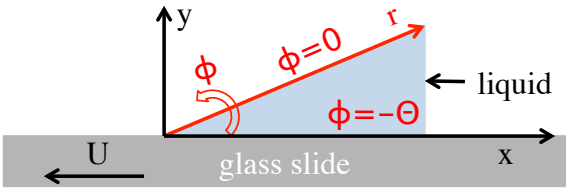

Figure 6.15.: Definition of the polar (red) and Cartesian coordinate system (black).

To do so I have to transform the coordinate system from the given planar coordinate system to the used Cartesian coordinate system in the measurements (figure 6.15). [113] calculated in the polar coordinate system that the velocity is

$$v_r = U \cdot f_1'(\phi), \tag{6.1}$$

$$v_\phi = -U \cdot f_1(\phi). \tag{6.2}$$

Where U is the velocity of the glass surface and

$$f_1(\phi) = \frac{\phi\cos(\phi)\sin(\Theta) - \Theta\cos(\Theta)\sin(\phi)}{\sin(\Theta)\cos(\Theta) - \Theta}. \tag{6.3}$$

The velocities in x and y can be calculated due to coordination transformation with

$$v_x = v_r \cos(-\Theta - \phi) + v_\phi \sin(-\Theta - \phi), \tag{6.4}$$

$$v_y = -v_r \sin(-\Theta - \phi) + v_\phi \cos(-\Theta - \phi), \tag{6.5}$$

with

$$\phi = \arctan 2\,(x\cos(\Theta) + y\sin(\Theta), -x\sin(\Theta) + y\cos(\Theta)). \tag{6.6}$$

This transformation allows to predict the flow profile close to the contact line in the same coordinate system as the experimental results. Figure 6.16 shows the predicted flow profile for a contact angle of 58° and a velocity of $0.2\,\mathrm{mm\,s^{-1}}$. The blue arrows represent the flow in the bulk of the liquid and the black arrow the motion of the glass surface. The liquid moves, close to the glass surface, towards the three phase contact line and slows down, changes the direction and flows back near the surface to the bulk.

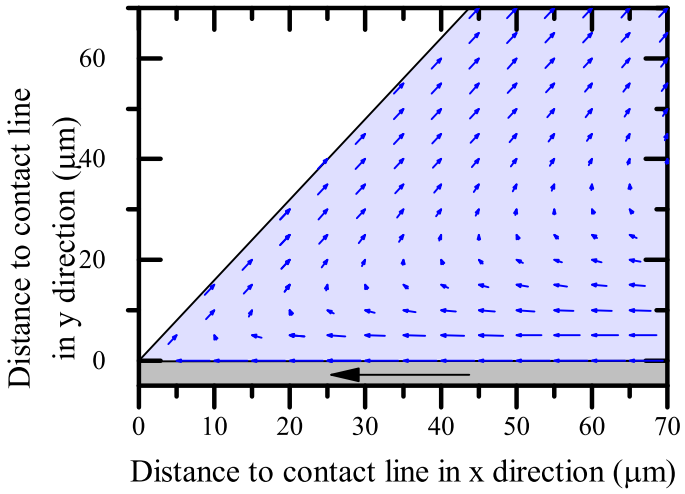

Figure 6.16.: Calculated flow profile with Eq. 6.1 - Eq. 6.6 for a contact angle $\Theta = 58°$ and a velocity of $0.2\,\mathrm{mm\,s^{-1}}$. The blue arrows represent the flow in the liquid (blue background) and the gray background represent the glass slide.

To compare this predicted flow profile with the measured values, it is necessary to calculate the distance to the contact line in y direction (distance to the glass surface) since it was not possible to extract this information from the measurement data. To calculate the distance to the contact line in y direction for every measurement point I

used the Eq. 6.1 - Eq. 6.6. Thereby I used the measured velocity in x direction and the distance x to the contact line and compared them with the calculated values, to predict the distance to the contact line in y direction. To do so, I assume that the glass slide is vertical to the optical axis within the measurements uncertainties. In reality, the glass slide can be tilted to the optical axis of the microscope by a few degrees. To verify the calculated distance to the contact line in y direction I use the fact, that the image plane is flat. Therefore, it must be possible to fit all calculated values of the distance to the contact line in y direction with a straight line. This line can be slightly tilted, due to the slightly tilted glass slide. The quality of the fit can be used as an indicator for the accuracy of the flow profile by Moffatt for the surfactant measurements. In this analysis, I used the macroscopically measured contact angle of the liquids, as well as the measured velocity in x direction and the distance in x towards the contact line.

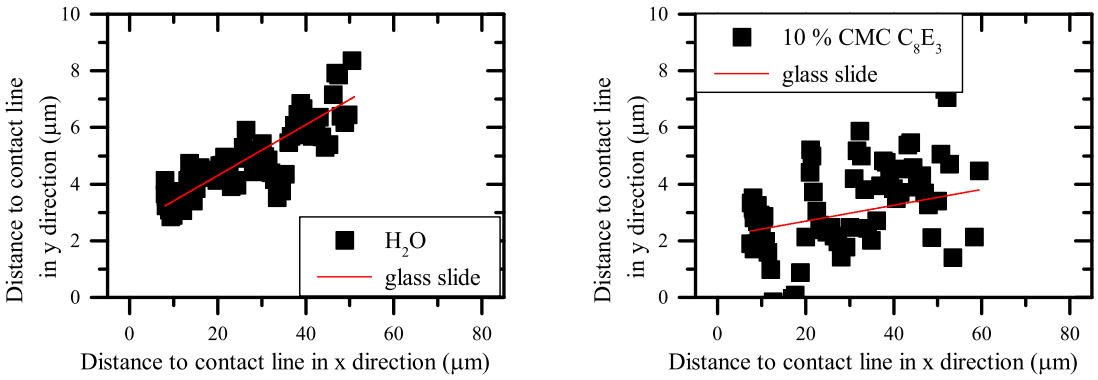

Figure 6.17.: Calculated y position over the measured distance to the contact line. The fit (red line) represents the glass slide. (a) the fit shows a relatively good agreement with the water measurement. Whereas in panel (b) the fit does not show a good agreement with the 10 % CMC C_8E_3 measurement.

For the water measurements the fit works relatively good (figure 6.17 (a)). The data shows a good agreement with a fitted line with an angle of around 5°. To estimate the quality of the fit I use the reduced chi-squared value. The closer the value is to unity the better the fit is. For water this value is 0.6874.

For all surfactant solutions the value is lower than 0.3 (table 6.3, figure 6.17(b)). These low values indicate that the data cannot be fitted with a straight line. This implies, that to overlap the surfactant solutions measurement with the theoretic flow profile, the glass surface would have to be bended. Since this is not the case, it is a clear indication, that the flow profile close to the contact line changes in the presence of surfactant. Therefore, it can not be compared with the flow profile predicted in [113].

Table 6.3.: Reduced chi-squared value of the glass surface fit for all measured liquids.

liquid	reduced chi-squared value of the glass surface fit
water	0.6874
10 % CMC CTAB	0.10614
30 % CMC CTAB	0.21615
10 % CMC C_8E_3	0.05497
30 % CMC C_8E_3	0.25762

The deviation from the predicted flow profile predicted by Moffatt [113] for surfactant solutions indicates, that for surfactant solution an additional effect must be present. As mentioned before at a distance closer than 30 µm the water flow behavior is different from the one of surfactant solution, which also indicates, that an additional effect must be present for surfactant solutions. This additional effect can be explained by the hypothesis (see section 2.7). Close to the contact line a fresh surface, with a lower surfactant concentration, is created which leads to a Marangoni force towards the three phase contact line to reduce the resulting gradient in surface tension. This additional force towards the CL leads to the different decrease of velocity in x direction. However, it has to be considered, that the contact angle decreases with increasing surfactant concentration, which also influenced the flow behaviour (see section 4.2).

Nevertheless, for water I observed a relatively good agreement between the measured velocity data and the model by Moffatt. The velocity in y direction can be calculated with Eq. 6.1 - Eq. 6.6. The velocity in y direction increases towards the contact line while the velocity in x direction decreases towards the contact line (figure 6.18 (a)). I assume, that the remaining difference comes from the measurement uncertainty due to optical reasons as well as from the fact, that I had to make the assumption that the microscopic contact angle is equal to the measured macroscopic contact angle. Additionally the used tracer particles might also influence the flow behaviour marginally. Ongoing experiments showed, that influence of the particle size on the flow behaviour is marginal, but might depend on the particle concentration. The direct comparison of the calculated as well as the measured and back calculated values are shown in figure 6.18 (b).

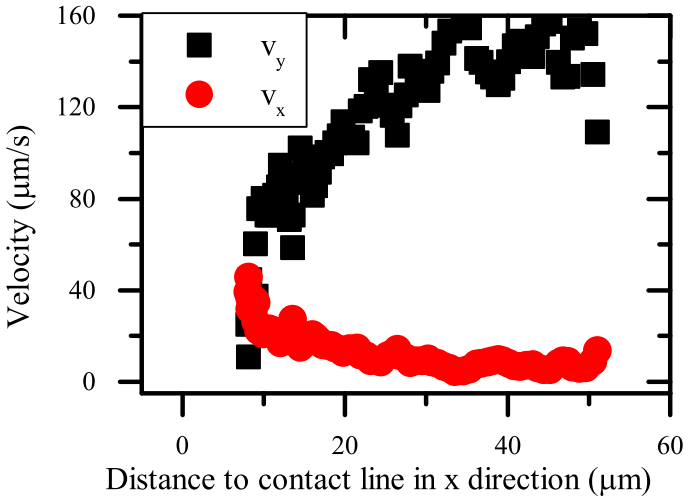

(a)

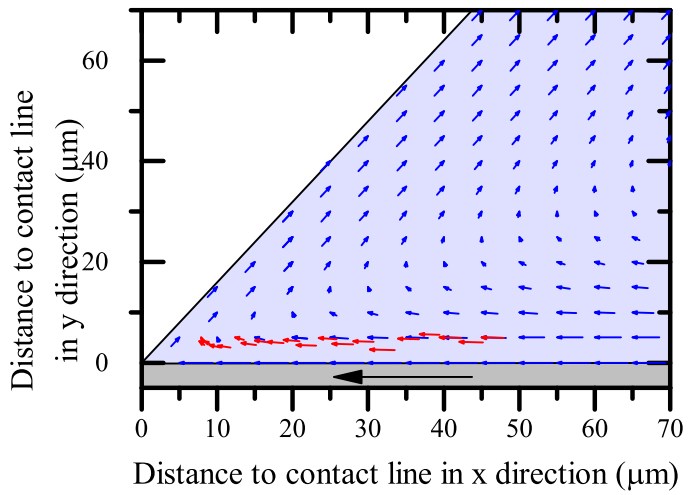

(b)

Figure 6.18.: (a) Measured absolute values of velocity in x direction v_x and the calculated values of the velocity in y direction v_y for water. (b) Calculated flow profile with Eq. 6.1 - Eq. 6.6 for a contact angle $\Theta = 58°$ and a velocity of $0.2\,\mathrm{mm\,s^{-1}}$. The blue arrows represent the flow in the liquid (light blue background) and the gray background represent the glass slide. The measured velocity of water in x and calculated velocity in y results in the red arrows, which show a good agreement with the predicted flow profile.

6.5 Conclusion of the flow profile on a microscopic length scale

A new experimental setup was designed to measure the flow profile near the three phase contact line. For pure water, the measured flow profile is comparable to the predicted flow profile near a sharp corner by [113] on the observed micrometer length scale. Close to the moving solid surface the liquid follows the movement direction towards the receding contact line. With decreasing distance to the contact line, the velocity v_x decreases . The decrease in the velocity happens in the last 30 µm. In contrast to the velocity in x direction the velocity in y direction, predicted with the model by [113] increases in the last 15 µm.

By adding surfactant to a liquid, the flow profile close to the receding contact angle changes. The flow profile of surfactant solution can not be predicted with the theoretical model by [113]. The velocity in x direction decreases towards the CL comparable to water. Nevertheless the decrease in velocity happens at a closer distance to the contact line. This is in agreement with the hypothesis, that close to the CL a surface is created which is not completely covered with surfactant molecules. This leads to a gradient in surface tension resulting in a Marangoni force towards the receding contact line. This additional force is the reason for the difference in decrease of the velocity in x direction with and without surfactant.

To proof this further I suggest, that the microscopic setup should to be modified to allow imaging a cut vertical with a frame rate in the order of 200 Hz to measure the two dimensional flow profile in x and y direction with and without surfactant.

7 Conclusion and Outlook

Wetting and dewetting of liquids on a solid surface is an important issue in many technical applications. A decent amount of studies showed, that surfactants influence the wetting behaviour [3, 23, 32, 34, 48, 55, 56, 57, 59, 68, 74, 83, 84, 93, 103, 107, 110, 149, 151, 160, 162, 166]. The majority of these studies investigated the influence of surfactants on spontaneous spreading. Less work was done on forced wetting and dewetting of surfactant solutions [34, 55, 56, 57]. It was figured out, that the presence of surfactant effects the forced dewetting behaviour, even at concentrations well below the critical micelle concentration. With increasing surfactant concentration, the receding contact angle and film formation velocity decreases.

Nevertheless, previously it was not understood how exactly the dewetting behaviour was influenced by the surfactants. Therefore I investigated in this thesis the macroscopic as well as microscopic dewetting behaviour close to the contact line. The macroscopic experiments were done in a rotating drum setup comparable to the experiments in [55, 56, 57]. This rotating drum setup allows to investigate the dewetting behaviour on different surfaces. For a better cleaning procedure and a nondestructive exchange of the surfaces, a new setup was designed within this thesis. The exchangeable surfaces allow to investigate the additional influence of structured surfaces during the dewetting of surfactant solutions.

Before the influence on structured surfaces can be understood, the mechanism of forced dewetting on a smooth surface required further investigations. Therefore, I measured the velocity dependent receding contact angle in the rotating drum setup for different kinds of surfactants. For all measured surfactant solutions, the receding contact angle decreases with increasing concentration as well as with increasing velocity. The critical velocity, where the contact line starts to get unstable and film formation begin, decreases with increasing surfactant concentration as well. The investigated surfactants were CTAB, S-1DeS, C_4E_1, C_8E_3 and $C_{12}E_5$. It can be assumed, that the decrease in the contact angle results from the Marangoni stress driven by a gradient in surface tension. This additional force towards the three phase contact line influences the wetting behaviour close to the contact line and decreases the contact angle. All surfactants influence the wetting behaviour in a similar way. Since effects due to charges were not visible in the measurement results, I assume that the charge of the surfactant does not have a significant influence on the wetting behaviour. The material property with the by far strongest effect is the critical micelle concentration. The still remaining

differences in the change of contact angle are small compared to the rescaling the surfactant concentration by CMC. The CMC was varied by more than four orders of magnitude and the residual differences after scaling with CMC was only a factor of three. The rescaling by CMC allows to compare the different surfactants. With this approach, the influence on the wetting behaviour of other surfactant solutions can be predicted.

The receding contact angle as well as the critical velocity of film formation increases comparable to previous studies [57, 55, 56], due to a smoother surface. The wider velocity range allows a comparison of the experimental results with the hydrodynamic model. For velocities higher than $10\,\mathrm{mm\,s^{-1}}$ all measurements can be fitted with the hydrodynamic model, even if surfactants are present; although, the model is only developed for simple liquids. The influence of the surfactants can be summarized in the logarithmic part of the hydrodynamic model - the so called friction parameter. This friction parameter shows a small influence caused by the charge of the surfactant, while the non charged surfactants have a constant friction parameter. For the positively and negatively charged surfactants it increases with increasing concentration. The fact, that the experimental data can only be fitted at higher velocities, can be explained by the fact that at low velocities the forces due to surface roughness dominate the hydrodynamic forces.

For a better understanding of the influence of the surface roughness and the structure, the dewetting behaviour on structured surfaces was investigated. Unused printing plates, with differently structured areas, were used as structured surface and mounted on the surface of the rotating drum. The dewetting behaviour on the structured surfaces showed, that the contact angle decreases with increasing velocity and surfactant concentration, comparable to the dewetting on the smooth surface. Nevertheless the structured surfaces have an influence on the dewetting behaviour. On the structured surfaces the contact line is pulled up higher than on an unstructured surface area of the same material. With increasing surfactant concentration this influence decreases. The decreasing influence can be explained by the increasing Marangoni force towards the contact line with increasing surfactant concentration. This Marangoni stress dominates the effect of the surface roughness, therefore the influence of surface roughness decreases.

For a more detailed investigation of the dewetting behaviour, microscopic studies of the dewetting behaviour were realized. Therefore a new setup was designed, which allows imaging of the area close to the contact line during the movement. A drop is placed on a moving glass slide and hold at a fixed position. This allows a stable position of the CL area relative to the optics used for observation, during the movement of the

drop. Due to this, the region close to the contact line can be imaged with a fast confocal microscope. This technique allows to analyze the flow behaviour close to the three phase contact line. Therefore tracer particles were added to the drop, which follow the flow in the drop. By tracking the particles, the flow close to the contact line was measured parallel to the glass slide to determine the flow profile in direction of the contact line. This was done for pure water as well as for surfactant solutions. The water measurements show a slow-down of the velocity towards the contact line. These measurement results can be compared with the predicted flow profile by [113], which allows to calculate the two dimensional flow profile. For surfactant solution the flow behaviour changes and the velocity decreased closer to the contact line compared to pure water. Due to the different flow profiles, the measurement results using surfactant solutions were not in accordance with the predicted flow profile by [113] and the two dimensional flow profile could not be calculated. Nevertheless, the change in the flow profile supports the hypothesis, that close to the contact line a fresh surface is created, which generates a gradient in surface tension and leads to a Marangoni stress towards the three phase contact line.

To proof this hypothesis, the confocal microscope has to be modified to allow an imaging of q section plane vertical to the glass slide with a comparable high frame rate of 200 Hz to measure the flow profile of a liquid drop with and without surfactant.

The two newly developed and built setups allow the investigation of further wetting and dewetting experiments. Macroscopically different liquids than water can be investigated to understand how different liquids behave with and without additives. Also all kinds of surfaces can be mounted to investigate the wetting behaviour on these surfaces. The microscopic setup allows as well to use other liquids and other transparent surfaces to investigate the flow behaviour close to the contact line.

List of Figures

List of Tables

Bibliography

[1] R. Ablett. XXV. an investigation of the angle of contact between paraffin wax and water. Philosophical Magazine Series 6, 46(272):244–256, 1923.

[2] N. K. Adam and G. Jessop. CCL.-angles of contact and polarity of solid surfaces. Journal of the Chemical Society, Transactions, 127(0):1863–1868, 1925.

[3] Y. Amarouchene, G. Cristobal, and H. Kellay. Noncoalescing drops. Physical Review Letters, 87(20):206104, 2001.

[4] M. Anyfantakis, D. Fell, H.-J. Butt, and G. K. Auernhammer. Time-dependent dynamic receding contact angles studied during the flow of dilute aqueous surfactant solutions through fluorinated microtubes. Chemistry Letters, 41(10):1232–1234, 2012.

[5] M. Apel-Paz and A. Marmur. Spreading of liquids on rough surfaces. Colloids and Surfaces A: Physicochemical and Engineering Aspects, 146(1-3):273–279, 1999.

[6] G.K. Auernhammer, M. Roth, and H.J. Butt. Optisches Rastermikroskop mit zwei Scaneinheiten. Patent, 2013.

[7] F. Bartell and J. Shepard. Surface roughness as related to hysteresis of contact angles. ii. the systems paraffin - 3 molar calcium chloride solution - air and paraffin - glycerol - air. The Journal of Physical Chemistry, 57(4):455–458, 1953.

[8] H. Benkreira and J. B. Ikin. Dynamic wetting and gas viscosity effects. Chemical Engineering Science, 65(5):1790–1796, 2010.

[9] M. K. Bernett and W. A. Zisman. Relation of wettability by aqueous solutions to the surface constitution of low-energy solids. The Journal of Physical Chemistry, 63(8):1241–1246, 1959.

[10] B. Bhushan and Y. C. Jung. Wetting, adhesion and friction of superhydrophobic and hydrophilic leaves and fabricated micro/nanopatterned surfaces. Journal of Physics: Condensed Matter, 20(22):225010, 2008.

[11] B. Bhushan and Y. C. Jung. Natural and biomimetic artificial surfaces for superhydrophobicity, self-cleaning, low adhesion, and drag reduction. Progress in Materials Science, 56(1):1–108, 2011.

[12] J. Bico, U. Thiele, and D. Quéré. Wetting of textured surfaces. Colloids and Surfaces a-Physicochemical and Engineering Aspects, 206(1-3):41–46, 2002.

[13] W. C. Bigelow, D. L. Pickett, and W. A. Zisman. Oleophobic monolayers: I. films adsorbed from solution in non-polar liquids. Journal of Colloid Science, 1(6):513–538, 1946.

[14] J. Billingham and A. C. King. The interaction of a moving fluid/fluid interface with a flat plate. Journal of Fluid Mechanics, 296:325–351, 1995.

[15] B. P. Binks, A. J. Johnson, and J. A. Rodrigues. Inversion of 'dry water' to aqueous foam on addition of surfactant. Soft Matter, 6(1):126–135, 2010.

[16] T. D. Blake. The physics of moving wetting lines. Journal of Colloid and Interface Science, 299(1):1–13, 2006.

[17] T. D. Blake and J. M. Haynes. Kinetics of liquidliquid displacement. Journal of Colloid and Interface Science, 30(3):421–423, 1969.

[18] T. D. Blake and K. J. Ruschak. A maximum speed of wetting. Nature, 282(5738):489–491, 1979.

[19] T. D. Blake and K. J. Ruschak. Wetting: static and dynamic contact lines, pages 63–97. Springer Netherlands, Dordrecht, 1997.

[20] T. D. Blake and Y. D. Shikhmurzaev. Dynamic wetting by liquids of different viscosity. Journal of Colloid and Interface Science, 253(1):196–202, 2002.

[21] K. B. Blodgett. Monomolecular films of fatty acids on glass. Journal of the American Chemical Society, 56(2):495–495, 1934.

[22] R. Blossey. Self-cleaning surfaces - virtual realities. Nat Mater, 2(5):301–306, 2003.

[23] D. Bonn, J. Eggers, J. Indekeu, J. Meunier, and E. Rolley. Wetting and spreading. Reviews of Modern Physics, 81(2):739–805, 2009.

[24] M. Bracke, F. De Voeght, and P. Joos. The kinetics of wetting: the dynamic contact angle, pages 142–149. Springer, 1989.

[25] J. B. Brzoska, I. Ben Azouz, and F. Rondelez. Silanization of solid substrates: A step toward reproducibility. Langmuir, 10(11):4367–4373, 1994.

[26] R. Burley and B. S. Kennedy. An experimental study of air entrainment at a solid/liquid/gas interface. Chemical Engineering Science, 31(10):901–911, 1976.

[27] H.-J. Butt, G. K. Auernhammer, and D. Vollmer. Oberflächen mit Phobie. Physik Journal, (2):25–32, 2015.

[28] H.-J. Butt, K. Graf, and M. Kappl. Physics and chemistry of interfaces. Wiley Online Library, 2003.

[29] H.-J. Butt, K. Graf, and M. Kappl. Contact Angle Phenomena and Wetting, pages 118–144. Wiley-VCH Verlag GmbH & Co. KGaA, 2004.

[30] A. B. D. Cassie and S. Baxter. Wettability of porous surfaces. Transactions of the Faraday Society, 40:546–551, 1944.

[31] N. T. Chamakos, M. E. Kavousanakis, A. G. Boudouvis, and A. G. Papathanasiou. Droplet spreading on rough surfaces: Tackling the contact line boundary condition. Physics of Fluids, 28(2):022105, 2016.

[32] D. Y. Chan, M. H. Uddin, K. L. Cho, II Liaw, R. N. Lamb, G. W. Stevens, F. Grieser, and R. R. Dagastine. Silica nano-particle super-hydrophobic surfaces: the effects of surface morphology and trapped air pockets on hydrodynamic drainage forces. Faraday Discuss, 143:151–68; discussion 169–86, 2009.

[33] T. S. Chan, T. Gueudré, and J. H. Snoeijer. Maximum speed of dewetting on a fiber. Physics of Fluids (1994-present), 23(11):112103, 2011.

[34] R. G. Chaudhuri and S. Paria. Dynamic contact angles on ptfe surface by aqueous surfactant solution in the absence and presence of electrolytes. Journal of Colloid and Interface Science, 337(2):555–562, 2009.

[35] H.-H. Chen, J. Shi, and C.-L. Chen. Wetting dynamics of multiscaled structures. Applied Physics Letters, 103(17):171601, 2013.

[36] B. W. Cherry and C. M. Holmes. Kinetics of wetting of surfaces by polymers. Journal of Colloid and Interface Science, 29(1):174–176, 1969.

[37] Z. Chu and S. Seeger. Superamphiphobic surfaces. Chemical Society Reviews, 43(8):2784–2798, 2014.

[38] R. G. Cox. The dynamics of the spreading of liquids on a solid surface. part 1. viscous flow. Journal of Fluid Mechanics, 168(1):169–194, 1986.

[39] J. C. Crocker and D. G. Grier. Methods of digital video microscopy for colloidal studies. Journal of colloid and interface science, 179(1):298–310, 1996.

[40] B. Cuenot, J. Magnaudet, and B. Spennato. The effects of slightly soluble surfactants on the flow around a spherical bubble. Journal of Fluid Mechanics, 339:25–53, 1997.

[41] P. G. De Gennes. Wetting: statics and dynamics. Reviews of Modern Physics, 57(3):827–863, 1985.

[42] P.-G. De Gennes, F. Brochard-Wyart, and D. Quéré. Capillarity and wetting phenomena: drops, bubbles, pearls, waves. Springer Science & Business Media, 2003.

[43] G. Delon, M. Fermigier, J. H. Snoeijer, and B. Andreotti. Relaxation of a dewetting contact line. part 2. experiments. Journal of Fluid Mechanics, 604:55–75, 2008.

[44] X. Deng, L. Mammen, H.-J. Butt, and D. Vollmer. Candle soot as a template for a transparent robust superamphiphobic coating. Science, 335(6064):67–70, 2012.

[45] B. Derjaguin. Trimness of liquid layer adhering to walls of vessels on their emptying and the theory of photo- and motion picture film coating. CR (Dokl.) Acad. Sci. URSS, 39:13–16, 1943.

[46] R. H. Dettre and R. E. Johnson Jr. Contact angle hysteresis. IV. contact angle measurements on heterogeneous surfaces. The Journal of Physical Chemistry, 69(5):1507–1515, 1965.

[47] E. B. Dussan. On the spreading of liquids on solid surfaces: static and dynamic contact lines. Annual Review of Fluid Mechanics, 11(1):371–400, 1979.

[48] V. Dutschk, K. G. Sabbatovskiy, M. Stolz, K. Grundke, and V. M. Rudoy. Unusual wetting dynamics of aqueous surfactant solutions on polymer surfaces. Journal of Colloid and Interface Science, 267(2):456–462, 2003.

[49] J. Eggers. Existence of receding and advancing contact lines. Physics of Fluids (1994-present), 17(8):082106, 2005.

[50] T. F. Eibach, D. Fell, H. Nguyen, H.-J. Butt, and G. K. Auernhammer. Measuring contact angle and meniscus shape with a reflected laser beam. Review of Scientific Instruments, 85(1):013703, 2014.

[51] A. Eifert, D. Paulssen, S. N. Varanakkottu, T. Baier, and S. Hardt. Simple fabrication of robust water-repellent surfaces with low contact-angle hysteresis based on impregnation. Advanced Materials Interfaces, 1(3):n/a–n/a, 2014.

[52] A. Einstein. Über die von der molekularkinetischen Theorie der Wärme geforderte Bewegung von in ruhenden Flüssigkeiten suspendierten Teilchen. Annalen der Physik, 322(8):549–560, 1905.

[53] H. B. Eral and J. M. Oh. Contact angle hysteresis: a review of fundamentals and applications. Colloid and Polymer Science, 291(2):247–260, 2013.

[54] H. Y. Erbil, A. L. Demirel, Y. Avci, and O. Mert. Transformation of a simple plastic into a superhydrophobic surface. Science, 299(5611):1377–1380, 2003.

[55] D. Fell. Dynamic wetting of complex liquids. Thesis, 2013.

[56] D. Fell, G. K. Auernhammer, E. Bonaccurso, C. Liu, R. Sokuler, and H.-J. Butt. Influence of surfactant concentration and background salt on forced dynamic wetting and dewetting. Langmuir, 27(6):2112–2117, 2011.

[57] D. Fell, N. Pawanrat, E. Bonaccurso, H.-J. Butt, and G. K. Auernhammer. Influence of surfactant transport suppression on dynamic contact angle hysteresis. Colloid and Polymer Science, 291(2):361–366, 2013.

[58] G. E. Fogg. Quantitative studies on the wetting of leaves by water. Proceedings of the Royal Society of London. Series B-Biological Sciences, 134(877):503–522, 1947.

[59] B. Frank and S. Garoff. Surfactant self-assembly near contact lines: control of advancing surfactant solutions. Colloids and Surfaces A: Physicochemical and Engineering Aspects, 116(1-2):31–42, 1996.

[60] G. L. Gaines Jr. On the history of Langmuir-Blodgett films, pages viii–xiii. Elsevier, Oxford, 1983.

[61] L. Gao and T. J. McCarthy. Contact angle hysteresis explained. Langmuir, 22(14):6234–6237, 2006.

[62] E. B. Gutoff and C. E. Kendrick. Dynamic contact angles. AIChE Journal, 28(3):459–466, 1982.

[63] R. A. Hayes and J. Ralston. Forced liquid movement on low energy surfaces. Journal of colloid and interface science, 159(2):429–438, 1993.

[64] F. Henrich, D. Fell, D. Truszkowska, M. Weirich, M. Anyfantakis, T.-H. Nguyen, M. Wagner, G. K. Auernhammer, and H.-J. Butt. Influence of surfactants in forced dynamic dewetting. Soft Matter, 12(37):7782–7791, 2016.

[65] F. Henrich, D. Linke, H. M. Sauer, E. Dörsam, S. Hardt, H.-J. Butt, and G. K. Auernhammer. Forced dynamic dewetting of structured surfaces: Influence of surfactants. ArXiv:1803.10601, 2018.

[66] S. Herminghaus. Roughness-induced non-wetting. EPL (Europhysics Letters), 52(2):165, 2000.

[67] S. Herminghaus, M. Brinkmann, and R. Seemann. Wetting and dewetting of complex surface geometries. Annual Review of Materials Research, 38(1):101–121, 2008.

[68] R. M. Hill. Superspreading. Current Opinion in Colloid & Interface Science, 3(3):247–254, 1998.

[69] W. Hopf and T. Geidel. The dynamic contact angle I. dependence of the receding contact angle on velocity in the surfactant-containing three-phase system. Colloid and Polymer Science, 265(12):1075–1084, 1987.

[70] W. Hopf and H. Stechemesser. Three-phase contact line movement in systems with and without surfactant. Colloids and Surfaces, 33:25–33, 1988.

[71] H. Hu and R. G. Larson. Marangoni effect reverses coffee-ring depositions. The Journal of Physical Chemistry B, 110(14):7090–7094, 2006.

[72] S. Huang, G. Pessot, P. Cremer, R. Weeber, C. Holm, J. Nowak, S. Odenbach, A. M. Menzel, and G. K. Auernhammer. Buckling of paramagnetic chains in soft gels. Soft Matter, 12(1):228–237, 2016.

[73] C. Huh and L. E. Scriven. Hydrodynamic model of steady movement of a solid/liquid/fluid contact line. Journal of Colloid and Interface Science, 35(1):85–101, 1971.

[74] J. Hyypia. Measurement of rates of spread of solutions of surface active agents. Analytical Chemistry, 20(11):1039–1043, 1948.

[75] C. Ishino and K. Okumura. Wetting transitions on textured hydrophilic surfaces. The European Physical Journal E, 25(4):415–424, 2008.

[76] A. Jerschow and N. Müller. Suppression of convection artifacts in stimulated-echo diffusion experiments. double-stimulated-echo experiments. Journal of Magnetic Resonance, 125(2):372–375, 1997.

[77] T.-S. Jiang, O. H. Soo-Gun, and J. C. Slattery. Correlation for dynamic contact angle. Journal of Colloid and Interface Science, 69(1):74–77, 1979.

[78] J. F. Joanny and P.-G. De Gennes. A model for contact angle hysteresis. The Journal of Chemical Physics, 81(1):552–562, 1984.

[79] P. Kim, T.-S. Wong, J. Alvarenga, M. J. Kreder, W. E. Adorno-Martinez, and J. Aizenberg. Liquid-infused nanostructured surfaces with extreme anti-ice and anti-frost performance. ACS Nano, 6(8):6569–6577, 2012.

[80] A. C. King, J. Billingham, and D. F. Popple. The moving contact line between two wedges of fluid on a flat plate. The Quarterly Journal of Mechanics and Applied Mathematics, 52(3):453–468, 1999.

[81] S. F. Kistler and P. M. Schweizer. Coating Science and Technology: An Overview, pages 3–15. Springer Netherlands, Dordrecht, 1997.

[82] T. Koishi, K. Yasuoka, S. Fujikawa, T. Ebisuzaki, and X. C. Zeng. Coexistence and transition between cassie and wenzel state on pillared hydrophobic surface. Proceedings of the National Academy of Sciences of the United States of America, 106(21):8435–8440, 2009.

[83] N. M. Kovalchuk, A. Barton, A. Trybala, and V. Starov. Surfactant enhanced spreading: Catanionic mixture. Colloids and Interface Science Communications, 1(0):1–5, 2014.

[84] R. Krechetnikov and G. M. Homsy. Surfactant effects in the landau-levich problem. Journal of Fluid Mechanics, 559:429–450, 2006.

[85] B. Kronberg, K. Holmberg, and B. Lindman. Surface Chemistry of Surfactants and Polymers. John Wiley and Sons, 2014.

[86] J. W. Krumpfer and T. J. McCarthy. Contact angle hysteresis: a different view and a trivial recipe for low hysteresis hydrophobic surfaces. Faraday Discussions, 146(0):103–111, 2010.

[87] D. Y. Kwok, T. Gietzelt, K. Grundke, H. J. Jacobasch, and A. W. Neumann. Contact angle measurements and contact angle interpretation. 1. contact angle measurements by axisymmetric drop shape analysis and a goniometer sessile drop technique. Langmuir, 13(10):2880–2894, 1997.

[88] D. Y. Kwok, R. Lin, M. Mui, and A. W. Neumann. Low-rate dynamic and static contact angles and the determination of solid surface tensions. Colloids and Surfaces A: Physicochemical and Engineering Aspects, 116(1-2):63–77, 1996.

[89] L. Landau and B. Levich. Dragging of a liquid by a moving plate. Acta Physicochimica Urss, 17:42–54, 1942.

[90] P. Langevin. Sur la théorie du mouvement brownien. CR Acad. Sci. Paris, 146(530-533):530, 1908.

[91] I. Langmuir. The constitution and fundamental properties of solids and liquids. II. liquids. Journal of the American Chemical Society, 39(9):1848–1906, 1917.

[92] H. P. Latscha, U. Kazmaier, and H. Klein. Organische Chemie: Chemie-Basiswissen II. Springer-Verlag, 2008.

[93] K. S. Lee, N. Ivanova, V. M. Starov, N. Hilal, and V. Dutschk. Kinetics of wetting and spreading by aqueous surfactant solutions. Advances in Colloid and Interface Science, 144(1-2):54–65, 2008.

[94] X.-M. Li, D. Reinhoudt, and M. Crego-Calama. What do we need for a superhydrophobic surface? A review on the recent progress in the preparation of superhydrophobic surfaces. Chemical Society Reviews, 36(8):1350–1368, 2007.

[95] R. Lipowsky, P. Lenz, and P. S. Swain. Wetting and dewetting of structured and imprinted surfaces. Colloids and Surfaces A: Physicochemical and Engineering Aspects, 161(1):3–22, 2000.

[96] J. Lopez, C. A. Miller, and E. Ruckenstein. Spreading kinetics of liquid drops on solids. Journal of Colloid and Interface Science, 56(3):460–468, 1976.

[97] M. Ma and R. M. Hill. Superhydrophobic surfaces. Current Opinion in Colloid & Interface Science, 11(4):193–202, 2006.

[98] G. Macdougall and C. Ockrent. Surface energy relations in liquid/solid systems. I. The adhesion of liquids to solids and a new method of determining the surface tension of liquids. Physical and Engineering Sciences, 180(981):151–173, 1942.

[99] M. Maillard, L. Motte, A. T. Ngo, and M. P. Pileni. Rings and hexagons made of nanocrystals: A marangoni effect. The Journal of Physical Chemistry B, 104(50):11871–11877, 2000.

[100] M. Maleki, E. Reyssat, D. Quéré, and R. Golestanian. On the landau-levich transition. Langmuir, 23(20):10116–10122, 2007.

[101] M. Maleki, M. Reyssat, F. Restagno, D. Quéré, and C. Clanet. Landau-levich menisci. Journal of Colloid and Interface Science, 354(1):359–363, 2011.

[102] K. Malysa, M. Krasowska, and M. Krzan. Influence of surface active substances on bubble motion and collision with various interfaces. Advances in Colloid and Interface Science, 114-115(0):205–225, 2005.

[103] O. Manor, I. U. Vakarelski, X Tang, S. J. OâĂŹShea, G. W. Stevens, F. Grieser, R. R. Dagastine, and D. Y. C. Chan. Hydrodynamic boundary conditions and dynamic forces between bubbles and surfaces. Physical Review Letters, 101(2):024501, 2008.

[104] C. Marangoni. Über die Ausbreitung der Tropfen einer Flüssigkeit auf der Oberfläche einer anderen. Annalen der Physik, 219(7):337–354, 1871.

[105] A. Marmur. Equilibrium and spreading of liquids on solid surfaces. Advances in Colloid and Interface Science, 19(1):75–102, 1983.

[106] A. Marmur. The lotus effect: Superhydrophobicity and metastability. Langmuir, 20(9):3517–3519, 2004.

[107] A. Marmur and M. D. Lelah. The spreading of aqueous surfactant solutions on glass. Chemical Engineering Communications, 13(1-3):133–143, 1981.

[108] J. A. Marsh and A. M. Cazabat. Dynamics of contact line depinning from a single defect. Physical Review Letters, 71(15):2433–2436, 1993.

[109] J. A. Marsh, S. Garoff, and E. B. Dussan V. Dynamic contact angles and hydrodynamics near a moving contact line. Physical Review Letters, 70(18):2778–2781, 1993.

[110] H. C. Mayer and R. Krechetnikov. Landau-levich flow visualization: Revealing the flow topology responsible for the film thickening phenomena. Physics of Fluids, 24(5), 2012.

[111] M. Minsky. Microscopy apparatus. Patent, 1961.

[112] M. Minsky. Memoir on inventing the confocal scanning microscope. Scanning, 10(4):128–138, 1988.

[113] H. K. Moffatt. Viscous and resistive eddies near a sharp corner. Journal of Fluid Mechanics, 18(01):1–18, 1964.

[114] P. Mukerjee and K. J. Mysels. Critical micelle concentrations of aqueous surfactant systems. DTIC Document, 1970.

[115] V. A. Nierstrasz and G. Frens. Marginal regeneration and the marangoni effect. Journal of Colloid and Interface Science, 215(1):28–35, 1999.

[116] A. D. Nikolov, D. T. Wasan, A. Chengara, K. Koczo, G. A. Policello, and I. Kolossvary. Superspreading driven by marangoni flow. Advances in Colloid and Interface Science, 96(1-3):325–338, 2002.

[117] M. Nosonovsky and P. K. Rohatgi. Artificial Self-Cleaning Surfaces, volume 152 of Springer Series in Materials Science, book section 13, pages 355–374. Springer New York, 2012.

[118] P. Papadopoulos, L. Mammen, X. Deng, D. Vollmer, and H.-J. Butt. How superhydrophobicity breaks down. Proceedings of the National Academy of Sciences, 110(9):3254–3258, 2013.

[119] A. Paszternák, É. Kiss, and P. Jedlovszky. Structure of the nonionic surfactant triethoxy monooctylether C_8E_3 adsorbed at the free water surface, as seen from surface tension measurements and monte carlo simulations. The Journal of Chemical Physics, 122(12):124704, 2005.

[120] M. Paven, H. Mayama, T. Sekido, H.-J. Butt, Y. Nakamura, and S. Fujii. Light driven delivery and release of materials using liquid marbles. Advanced Functional Materials, 26(19):3199–3206, 2016.

[121] J. Perrin. Mouvement brownien et réalité moléculaire. In Annales de Chimie et de Physique, volume 18, pages 5–104, 1909.

[122] I. R. Peters, J. H. Snoeijer, A. Daerr, and L. Limat. Coexistence of two singularities in dewetting flows: regularizing the corner tip. Physical Review Letters, 103(11):114501, 2009.

[123] J. G. Petrov and P. G. Petrov. Forced advancement and retraction of polar liquids on a low energy surface. Colloids and Surfaces, 64(2):143–149, 1992.

[124] P. Petrov and I. Petrov. A combined molecular-hydrodynamic approach to wetting kinetics. Langmuir, 8(7):1762–1767, 1992.

[125] T. Podgorski, J.-M. Flesselles, and L. Limat. Corners, cusps, and pearls in running drops. Physical Review Letters, 87(3):036102, 2001.

[126] D. Quéré. Rough ideas on wetting. Physica A: Statistical Mechanics and its Applications, 313(1-2):32–46, 2002.

[127] D. Quéré. Wetting and roughness, volume 38 of Annual Review of Materials Research, pages 71–99. Annual Reviews, Palo Alto, 2008.

[128] S. Rafaï, D. Sarker, V. Bergeron, J. Meunier, and D. Bonn. Superspreading: Aqueous surfactant drops spreading on hydrophobic surfaces. Langmuir, 18(26):10486–10488, 2002.

[129] E. Ramé. The interpretation of dynamic contact angles measured by the wilhelmy plate method. Journal of Colloid and Interface Science, 185(1):245–251, 1997.

[130] O. Reynolds. An experimental investigation of the circumstances which determine whether the motion of water shall be direct or sinuous, and of the law of resistance in parallel channels. Proceedings of the royal society of London, 35(224-226):84–99, 1883.

[131] G. Roberts. Langmuir-blodgett films. Springer Science & Business Media, 2013.

[132] L. Románszki, M. Mohos, J. Telegdi, Z. Keresztes, and L. Nyikos. A comparison of contact angle measurement results obtained on bare, treated, and coated alloy samples by both dynamic sessile drop and wilhelmy method. Periodica Polytechnica. Chemical Engineering, 58(Supplement):53, 2014.

[133] M. J. Rosen, A. W. Cohen, M. Dahanayake, and X. Y. Hua. Relationship of structure to properties in surfactants. 10. surface and thermodynamic properties of 2-dodecyloxypoly(ethenoxyethanol)s, $C_{12}H_{25}(OC_2H_4)_xOH$, in aqueous solution. The Journal of Physical Chemistry, 86(4):541–545, 1982.

[134] M. J. Rosen and J. T. Kunjappu. Surfactants and interfacial phenomena. John Wiley & Sons, 2012.

[135] M. Roth. Rheology of arrested colloids : a parameter study using novel experimental methods. Thesis, 2012.

[136] M. Roth, C. Schilde, P. Lellig, A. Kwade, and G. K. Auernhammer. Colloidal aggregates tested via nanoindentation and quasi-simultaneous 3d imaging. The European Physical Journal E, 35(11):124, 2012.

[137] F. Schellenberger, N. Encinas, D. Vollmer, and H.-J. Butt. How water advances on superhydrophobic surfaces. Physical Review Letters, 116(9):096101, 2016.

[138] R. V. Sedev, C. J. Budziak, J. G. Petrov, and A. W. Neumann. Dynamic contact angles at low velocities. Journal of Colloid and Interface Science, 159(2):392–399, 1993.

[139] R. V. Sedev and J. G. Petrov. Influence of geometry on steady dewetting kinetics. Colloids and surfaces, 62(1-2):141–151, 1992.

[140] Y. D. Shikhmurzaev. The moving contact line on a smooth solid surface. International Journal of Multiphase Flow, 19(4):589–610, 1993.

[141] Y. D. Shikhmurzaev. Mathematical modeling of wetting hydrodynamics. Fluid Dynamics Research, 13(1):45–64, 1994.

[142] J. H. Snoeijer and B. Andreotti. A microscopic view on contact angle selection. Physics of Fluids (1994-present), 20(5):057101, 2008.

[143] J. H. Snoeijer and B. Andreotti. Moving contact lines: scales, regimes, and dynamical transitions. Annual Review of Fluid Mechanics, 45:269–292, 2013.

[144] J. H. Snoeijer, B. Andreotti, G. Delon, and M. Fermigier. Relaxation of a dewetting contact line. part 1. a full-scale hydrodynamic calculation. Journal of Fluid Mechanics, 579:63–83, 2007.

[145] J. H. Snoeijer, N. Le Grand-Piteira, L. Limat, H. A. Stone, and J. Eggers. Cornered drops and rivulets. Physics of Fluids, 19(4):042104, 2007.

[146] J. H. Snoeijer, J. Ziegler, B. Andreotti, M. Fermigier, and J. Eggers. Thick films of viscous fluid coating a plate withdrawn from a liquid reservoir. Physical Review Letters, 100(24), 2008.

[147] J. Spurk. Strömungslehre: Einführung in die Theorie der Strömungen. Springer-Verlag, 2013.

[148] V. M. Starov, S.R. Kosvintsev, and M. G. Velarde. Spreading of surfactant solutions over hydrophobic substrates. Journal of Colloid and Interface Science, 227(1):185–190, 2000.

[149] V. M. Starov, M. G. Velarde, and C. J. Radke. Wetting and spreading dynamics. CRC press, 2007.

[150] E. O. Stejskal and J. E. Tanner. Spin diffusion measurements: spin echoes in the presence of a time - dependent field gradient. The Journal of Chemical Physics, 42(1):288–292, 1965.

[151] T. Stoebe, R. M. Hill, M. D. Ward, and H. T. Davis. Enhanced spreading of aqueous films containing ionic surfactants on solid substrates. Langmuir, 13(26):7276–7281, 1997.

[152] Y. Su, B. Ji, Y. Huang, and K.-C. Hwang. Nature's design of hierarchical superhydrophobic surfaces of a water strider for low adhesion and low-energy dissipation. Langmuir, 26(24):18926–18937, 2010.

[153] W. Sutherland. Lxxv. a dynamical theory of diffusion for non-electrolytes and the molecular mass of albumin. Philosophical Magazine Series 6, 9(54):781–785, 1905.

[154] T. F. Svitova, M. J. Wetherbee, and C. J. Radke. Dynamics of surfactant sorption at the air/water interface: continuous-flow tensiometry. Journal of Colloid and Interface Science, 261(1):170–179, 2003.

[155] K. Szymczyk, A. Zdziennicka, B. Jańczuk, and W. Wójcik. The wettability of polytetrafluoroethylene and polymethyl methacrylate by aqueous solution of two cationic surfactants mixture. Journal of Colloid and Interface Science, 293(1):172–180, 2006.

[156] S. Takagi and Y. Matsumoto. Surfactant effects on bubble motion and bubbly flows. Annual Review of Fluid Mechanics, 43(1):615–636, 2011.

[157] L. H. Tanner. The spreading of silicone oil drops on horizontal surfaces. Journal of Physics D: Applied Physics, 12(9):1473, 1979.

[158] J. Thomson. Xlii. on certain curious motions observable at the surfaces of wine and other alcoholic liquors. Philosophical Magazine Series 4, 10(67):330–333, 1855.

[159] S. M. Troian, E. Herbolzheimer, and S. A. Safran. Model for the fingering instability of spreading surfactant drops. Physical Review Letters, 65(3):333–336, 1990.

[160] S. M. Troian, X. L. Wu, E. Herbolzheimer, and S. A. Safran. Fingering Instability of a Spreading Drop, volume 211 of NATO ASI Series, book section 23, pages 245–248. Springer US, 1989.

[161] D. Truszkowska, F. Henrich, J. Schultze, K. Koynov, H. J. Räder, H.-J. Butt, and G. K. Auernhammer. Forced dewetting dynamics of high molecular weight surfactant solutions. Colloids and Surfaces A: Physicochemical and Engineering Aspects, 2016.

[162] K. S. Varanasi and S. Garoff. Unsteady motion of receding contact lines of surfactant solutions: The role of surfactant re-self-assembly. Langmuir, 21(22):9932–9937, 2005.

[163] J. Venzmer. Superspreading - 20 years of physicochemical research. Current Opinion in Colloid & Interface Science, 16(4):335–343, 2011.

[164] O. V. Voinov. Hydrodynamics of wetting. Fluid Dynamics, 11(5):714–721, 1976.

[165] J. Wang, M. Do-Quang, J. J. Cannon, F. Yue, Y. Suzuki, G. Amberg, and J. Shiomi. Surface structure determines dynamic wetting. Scientific Reports, 5:8474, 2015.

[166] X. Wang, L. Chen, and E. Bonaccurso. Comparison of spontaneous wetting and drop impact dynamics of aqueous surfactant solutions on hydrophobic polypropylene surfaces: scaling of the contact radius. Colloid and Polymer Science, 293(1):257–265, 2015.

[167] R.N. Wenzel. Resistance of solid surfaces to wetting by water. Industrial and Engineering Chemistry, 28(8):988–994, 1936.

[168] J. Wenzl. Wet and dry model granulates under mechanical load : a confocal microscopy study. Thesis, 2014.

[169] J. Wenzl, R. Seto, M. Roth, H.-J. Butt, and G. K. Auernhammer. Measurement of rotation of individual spherical particles in cohesive granulates. Granular Matter, 15(4):391–400, 2013.

[170] L. Wilhelmy. Über die Abhängigkeit der Capillaritäts-Constanten des Alkohols von Substanz und Gestalt des benetzten festen Körpers. Annalen der Physik, 195(6):177–217, 1863.

[171] K. G. Winkels, I. R. Peters, F. Evangelista, M. Riepen, A. Daerr, L. Limat, and J. H. Snoeijer. Receding contact lines: from sliding drops to immersion lithography. The European Physical Journal Special Topics, 192(1):195–205, 2011.

[172] T.-S. Wong, S. H. Kang, S. K. Y. Tang, E. J. Smythe, B. D. Hatton, A. Grinthal, and J. Aizenberg. Bioinspired self-repairing slippery surfaces with pressure-stable omniphobicity. Nature, 477(7365):443–447, 2011.

[173] T. Young. An essay on the cohesion of fluids. Philosophical Transactions of the Royal Society of London, 95:65–87, 1805.

[174] Y. Yuan and T. R. Lee. Contact Angle and Wetting Properties, pages 3–34. Springer Berlin Heidelberg, Berlin, Heidelberg, 2013.

[175] W. Zhang, M. Wahlgren, and B. Sivik. Membrane characterization by the contact angle technique: Ii. characterization of uf-membranes and comparison between the captive bubble and sessile drop as methods to obtain water contact angles. Desalination, 72(3):263–273, 1989.

[176] Y.-L. Zhang, H. Xia, E. Kim, and H.-B. Sun. Recent developments in superhydrophobic surfaces with unique structural and functional properties. Soft Matter, 8(44):11217–11231, 2012.

[177] W. A Zisman. Relation of the Equilibrium Contact Angle to Liquid and Solid Constitution, volume 43 of Advances in Chemistry, book section 1, pages 1–51. American chemical society, 1964.

Glossary and Acronyms

Glossary

name	description	unit
Ai	Airy function	-
$\frac{dAi}{dx}$	first derivation of the Airy function	-
α	numerical constant depending on the geometry	-
Ca	capillary number	-
d	diameter	mm
η	viscosity	$\mathrm{Pa\,s}$
g	gravity acceleration	$\mathrm{m\,s^{-2}}$
Γ	surface excess	-
γ	surface tension	$\mathrm{mN\,m^{-1}}$
γ_L	inter-facial tension of the liquid	$\mathrm{mN\,m^{-1}}$
γ_S	inter-facial tension of the solid	$\mathrm{mN\,m^{-1}}$
γ_{SL}	inter-facial tension between solid and liquid	$\mathrm{mN\,m^{-1}}$
h	characteristic macroscopic length scale	m
h_F	Thickness of the film	m
κ^0	characteristic frequency	Hz
$\mathrm{k_B}$	Bolzmann constant	$\mathrm{J\,K^{-1}}$
λ	characteristic distance	m
μ	chemical potential	-
R	Universal gas constant	$\mathrm{J\,mol^{-1}\,K^{-1}}$
Re	Reynolds number	-
ρ	density	$\mathrm{kg\,m^{-3}}$
S	spreading coefficient	-
T	absolute temperature	K
Θ	contact angle	°
$\Theta_{0\,\%\mathrm{CMC}}$	contact angle of pure water	°
Θ_0	contact angle at zero velocity	°
Θ_{adv}	advaning contact angle	°

name	description	unit
Θ_{0adv}	advancing contact angle at zero velocity	°
$\Delta\Theta$	change in contact angle	°
Θ_{rec}	receding contact angle	°
Θ_{0rec}	receding contact angle at zero velocity	°
$\Theta_{X\,\%\,\mathrm{CMC}}$	contact angle at X % CMC	°
v	velocity	$\mathrm{m\,s^{-1}}$

Acronyms

C_4E_1	butyl glycol.
C_8E_3	octyltriglycol.
$C_{12}E_5$	dodecyl pentaglycol.
CA	contact angle.
CL	three phase contact line.
CMC	critical micelle concentration.
CTAB	cetyl trimethylammonium bromide.
D_2O	deuterium oxide.
H_2O	water.
HDT	hydrodynamic theory.
MKT	molecular kinetic theory.
PDMS	polydimethylsiloxane.
PS	polystyrene.
PTFE	polytetrafluoroethylene.
PVC	polyvinyl chloride.
S-1DeS	sodium 1-decanesulfonate.
SDS	sodium dodecyl sulfate.
THF	tetrahydrofuran.

Lebenslauf

Franziska Monika Henrich

Puplikationen

Y. Yao, S. Alexandris, F. Henrich, G. K. Auernhammer, M. Steinhart, H.-J. Butt, G. Floudas. Complex dynamics of capillary imbibition of poly (ethylene oxide) melts in nanoporous alumina.The Journal of Chemical Physics, 2017.

F. Henrich, D. Fell, D. Truszkowska, M. Weirich, M. Anyfantakis, T.-H. Nguyen, M. Wagner, G. K. Auernhammer, H.-J. Butt. Influence of surfactants in forced dynamic dewetting. Soft Matter., 2016.

T. Hessberger, L.B. Braun, F. Henrich, C. Müller, F. Gießelmann, C. Serram, R. Zentel. Co-flow microfluidic synthesis of liquid crystalline actuating Janus particles. Journal of Materials Chemistry C, 2016.

D. Truszkowska, F. Henrich, J. Schultze, K. Koynov, HJ. Räder, H-J Butt and G.K. Auernhammer. Forced dewetting dynamics of high molecular weight surfactant solutions. Colloids and Surfaces A: Physicochemical and Engineering Aspects, 2016.

A. Kumar, L. Gilson, F. Henrich, V. Dahl, J. Klein, T. Gambaryan-Roisman and J Venzmer. Intact deposition of cationic vesicles on anionic cellulose fibers: Role of vesicle size, polydispersity, and substrate roughness studied via streaming potential measurements. Journal of colloid and interface science, 473:152-161, 2016.

F. Henrich, H. Rahn and S. Odenbach. Heat transition during magnetic heating treatment: Study with tissue models and simulation. Journal of Magnetism and Magnetic Materials, 2014.

F. Henrich, H. Rahn and S. Odenbach. Investigation of heat distribution during magnetic heating treatment using a polyurethane-ferrofluid phantom-model. Journal of Magnetism and Magnetic Materials, 351:1-7, 2014.

Danksagung

A Appendix

A.1 Technical Drawings

A.1.1 Rotating Drum Setup

Liquid container

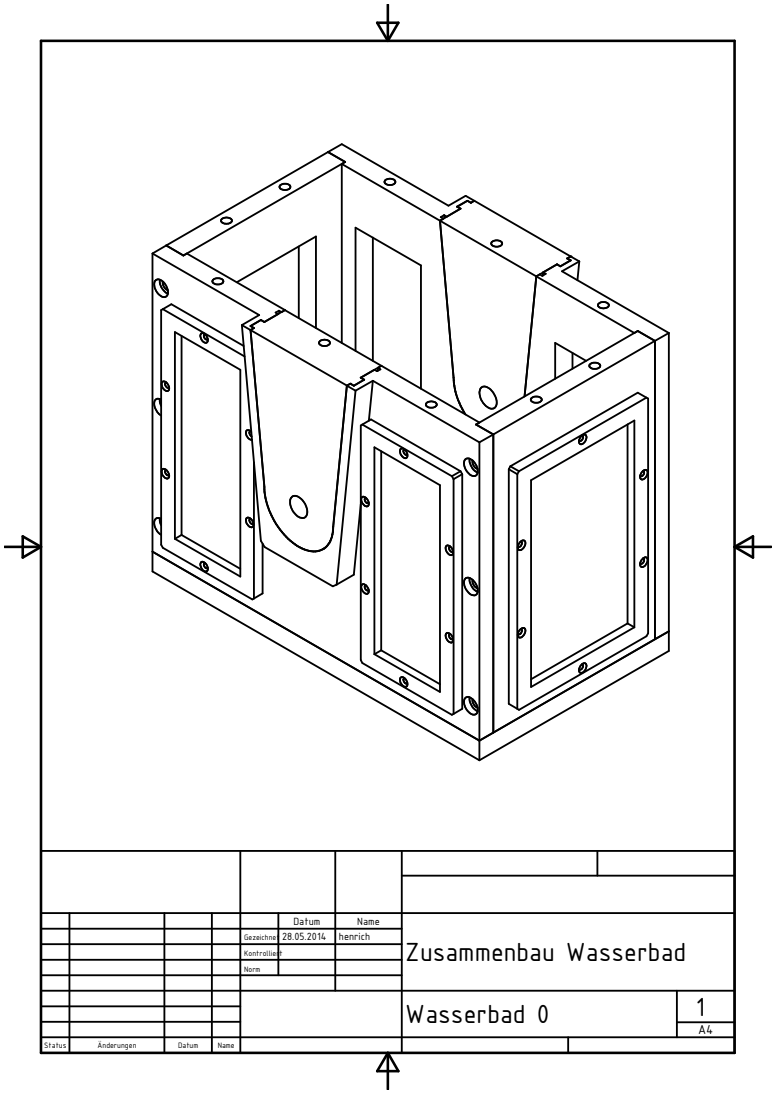

Figure A.1.: Technical drawing of the mounted rotating drum liquid container.

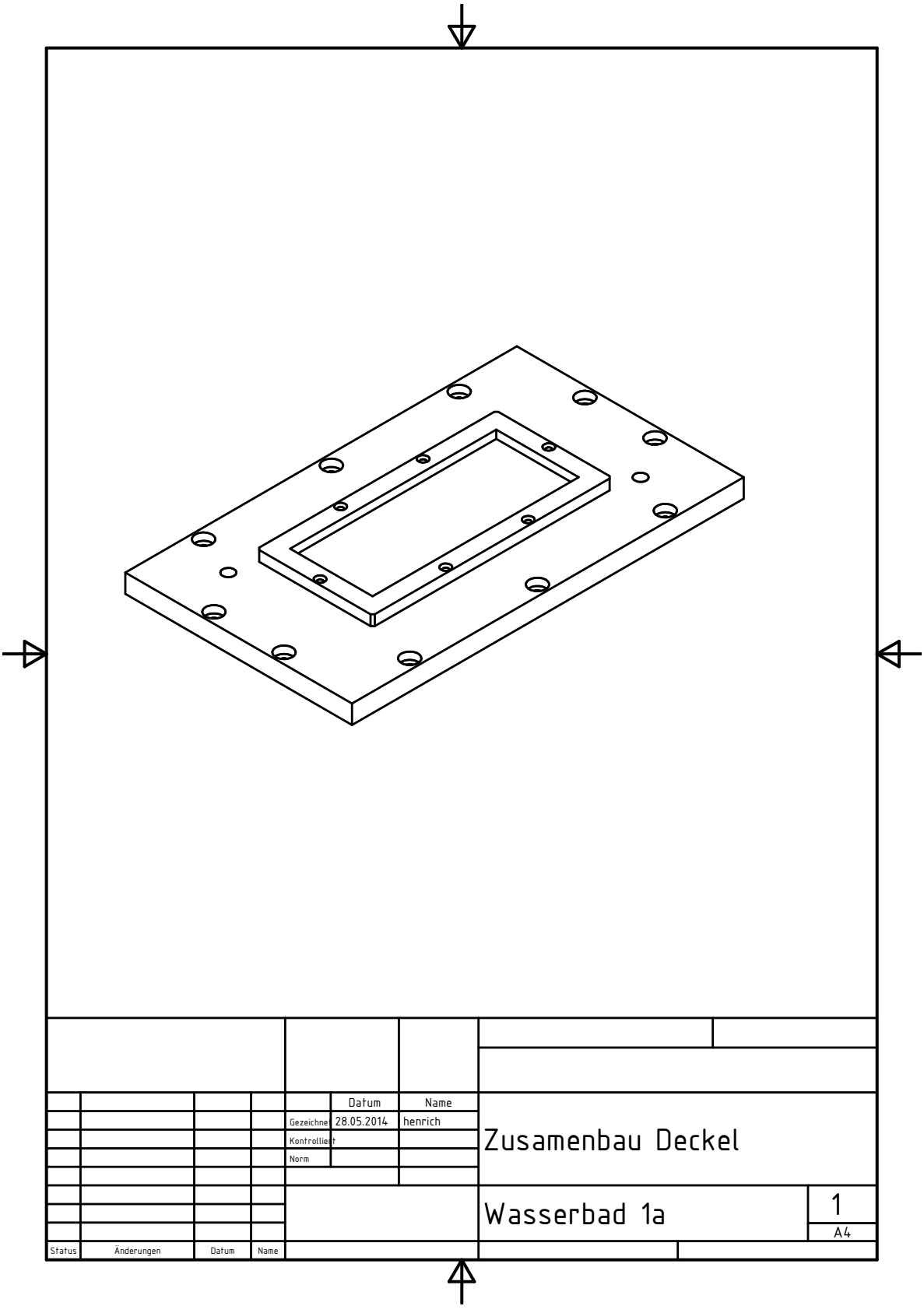

Figure A.2.: Technical drawing of the mounted liquid container top.

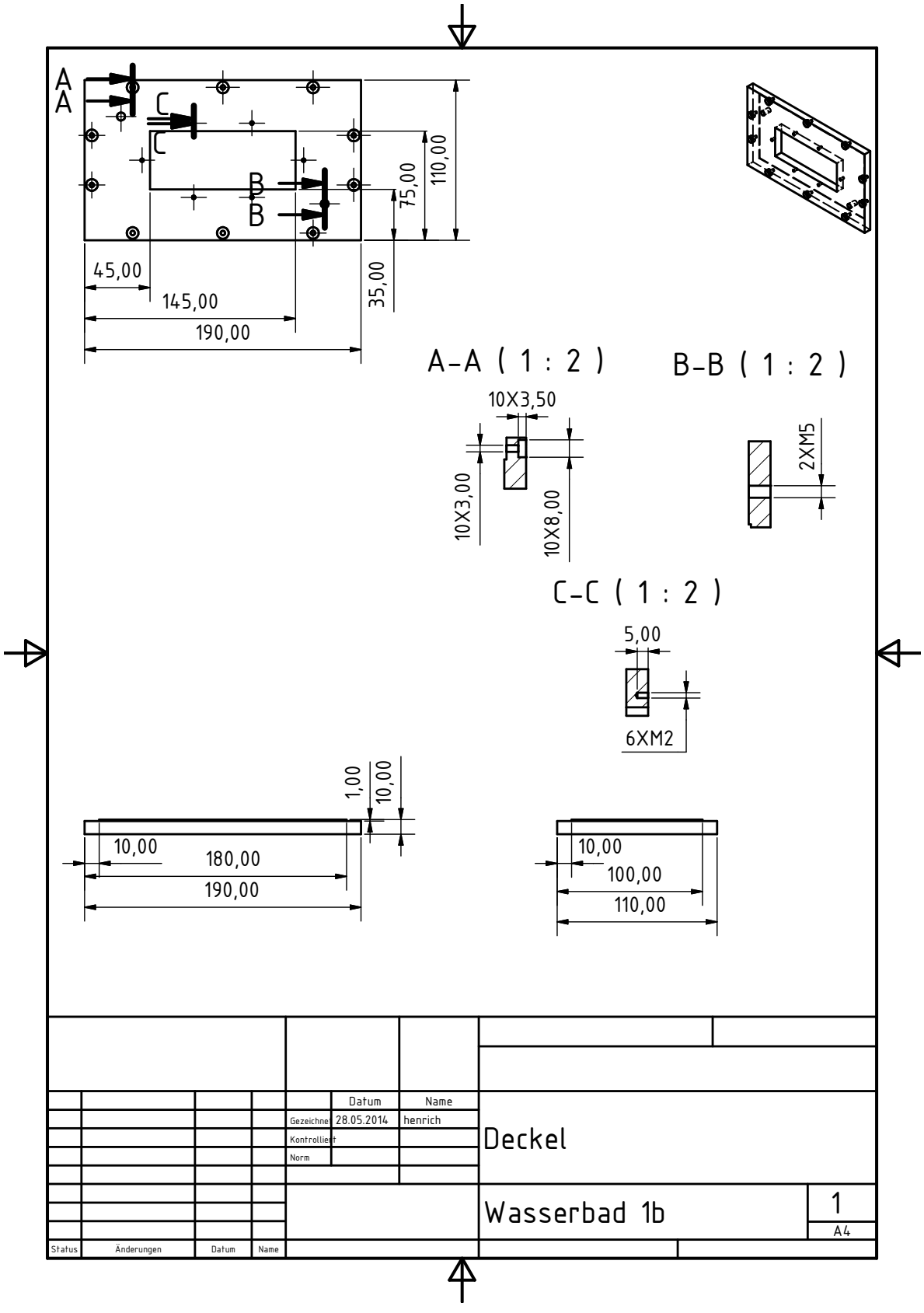

Figure A.3.: Technical drawing of the liquid container top.-part 1

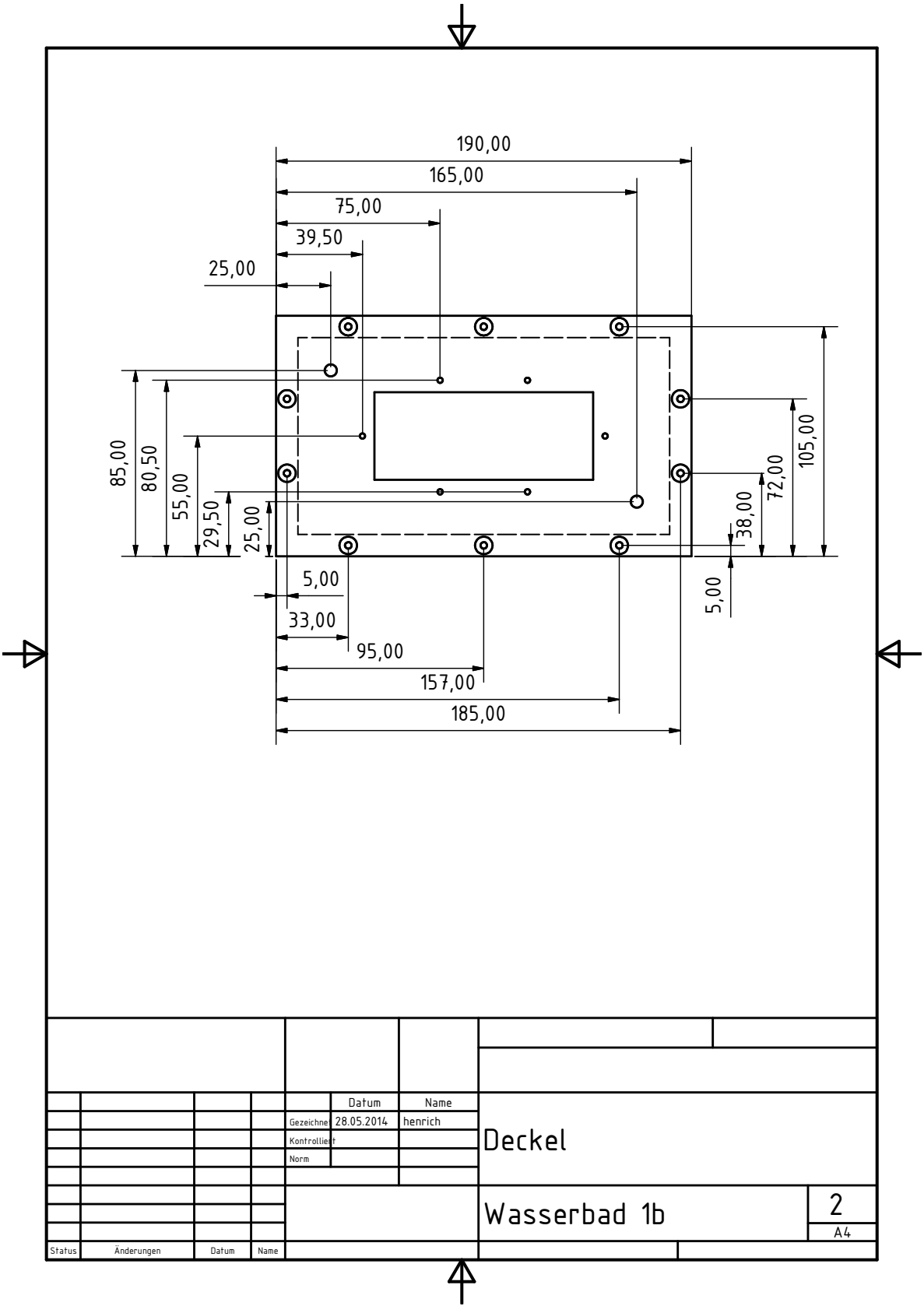

Figure A.4.: Technical drawing of the liquid container top.-part 2

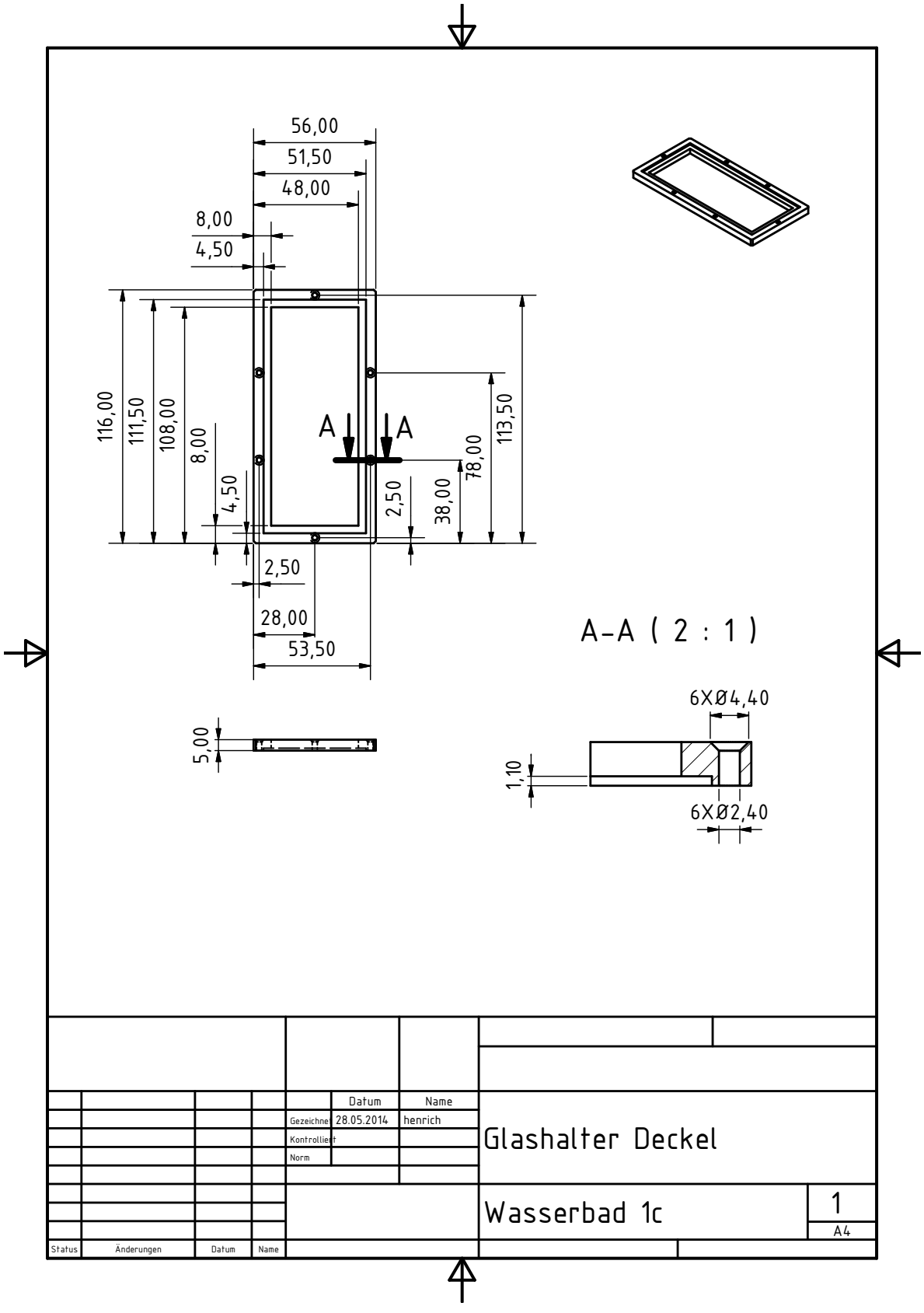

Figure A.5.: Technical drawing of the glasholder top.

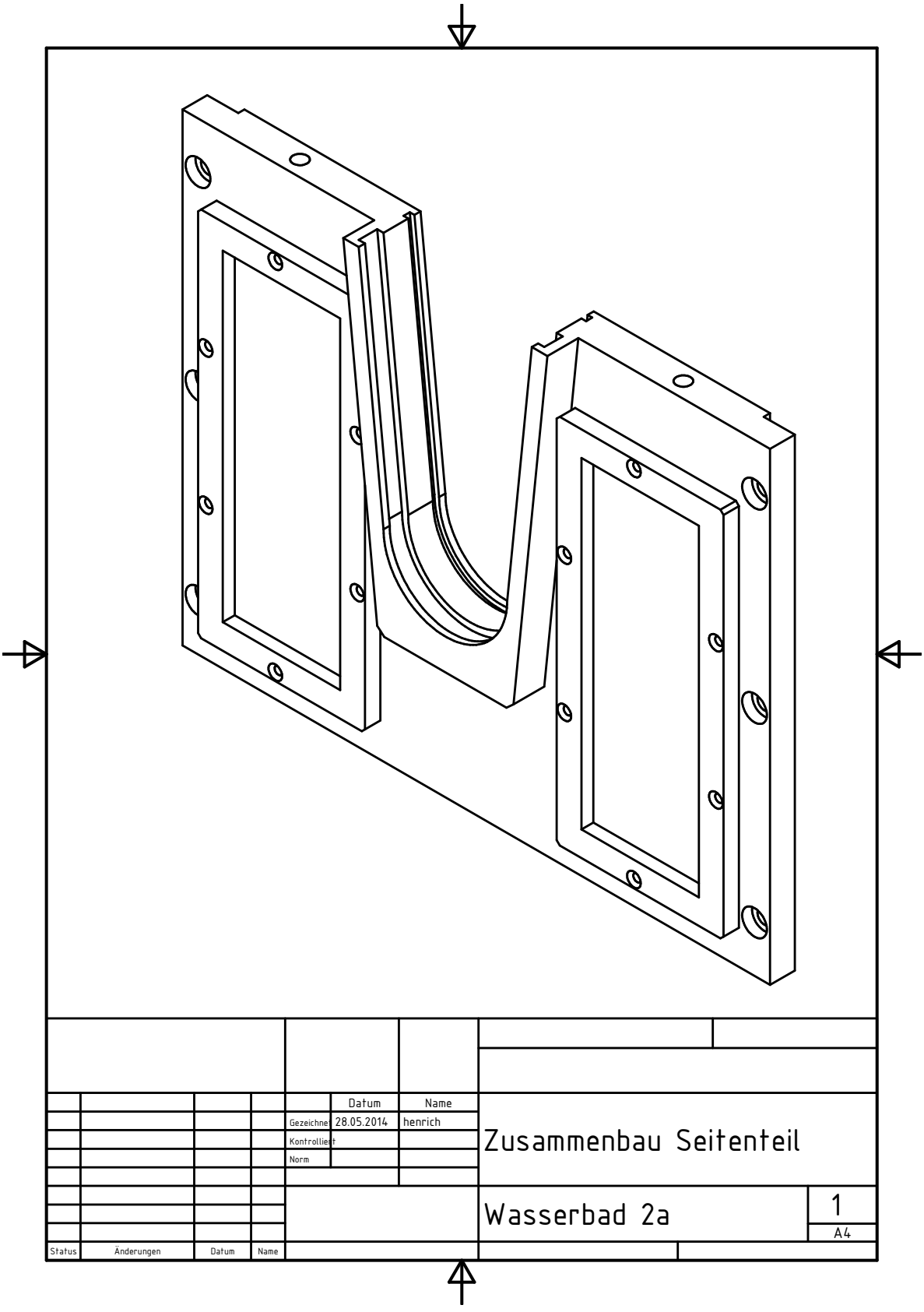

Figure A.6.: Technical drawing of the monted liquid container side right and left.

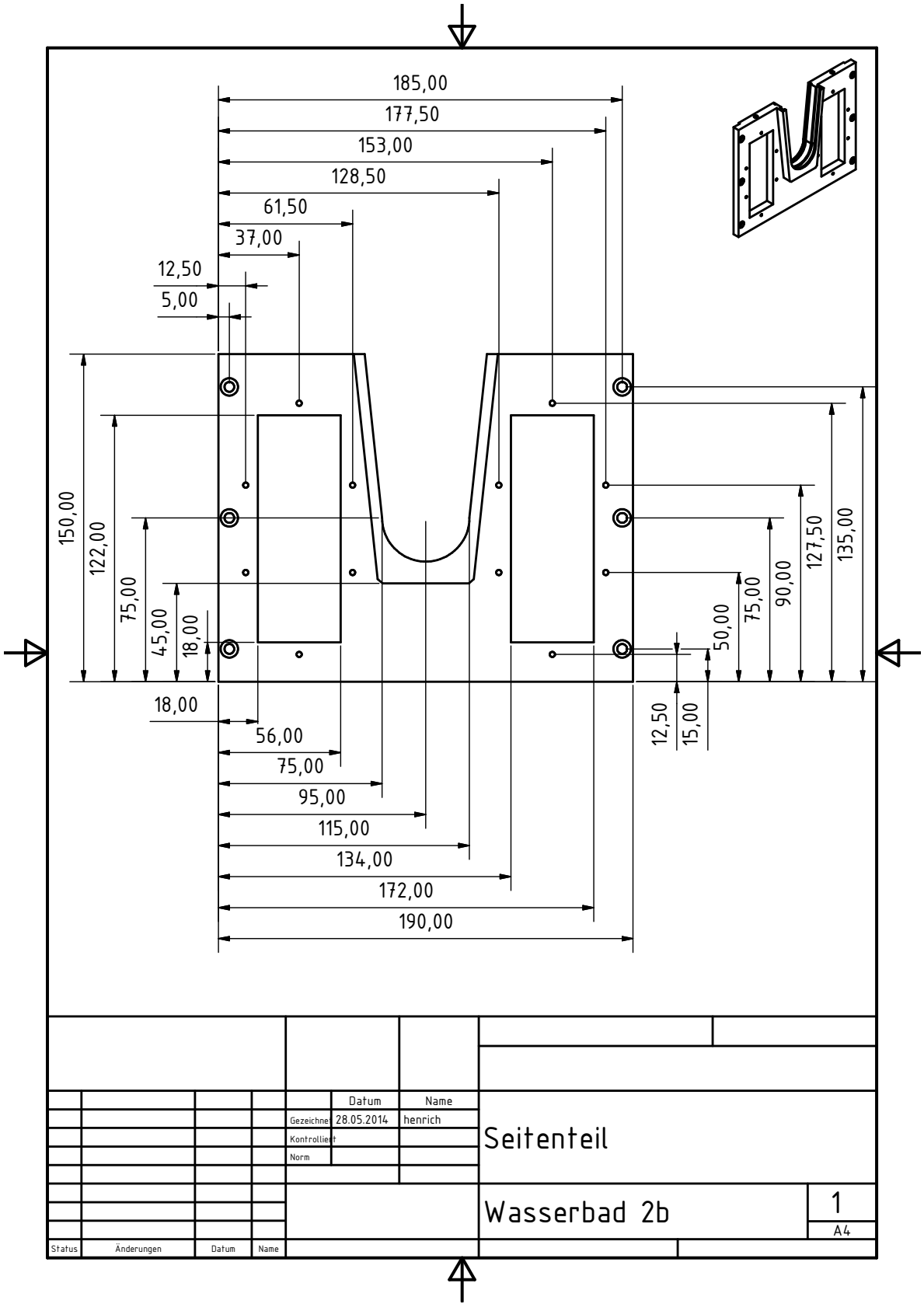

Figure A.7.: Technical drawing of the liquid container right and left.- part 1

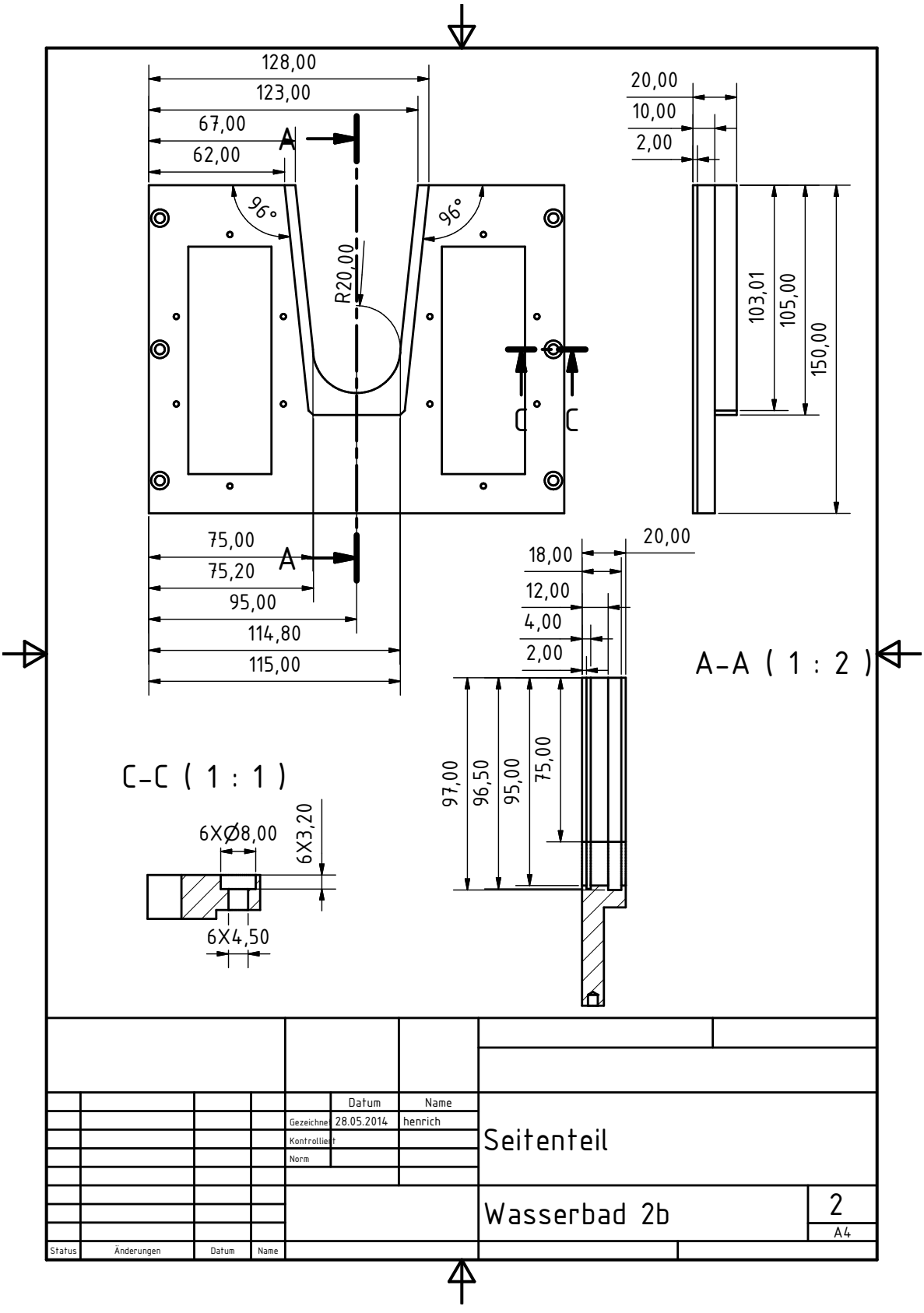

Figure A.8.: Technical drawing of the liquid container right and left.- part 2

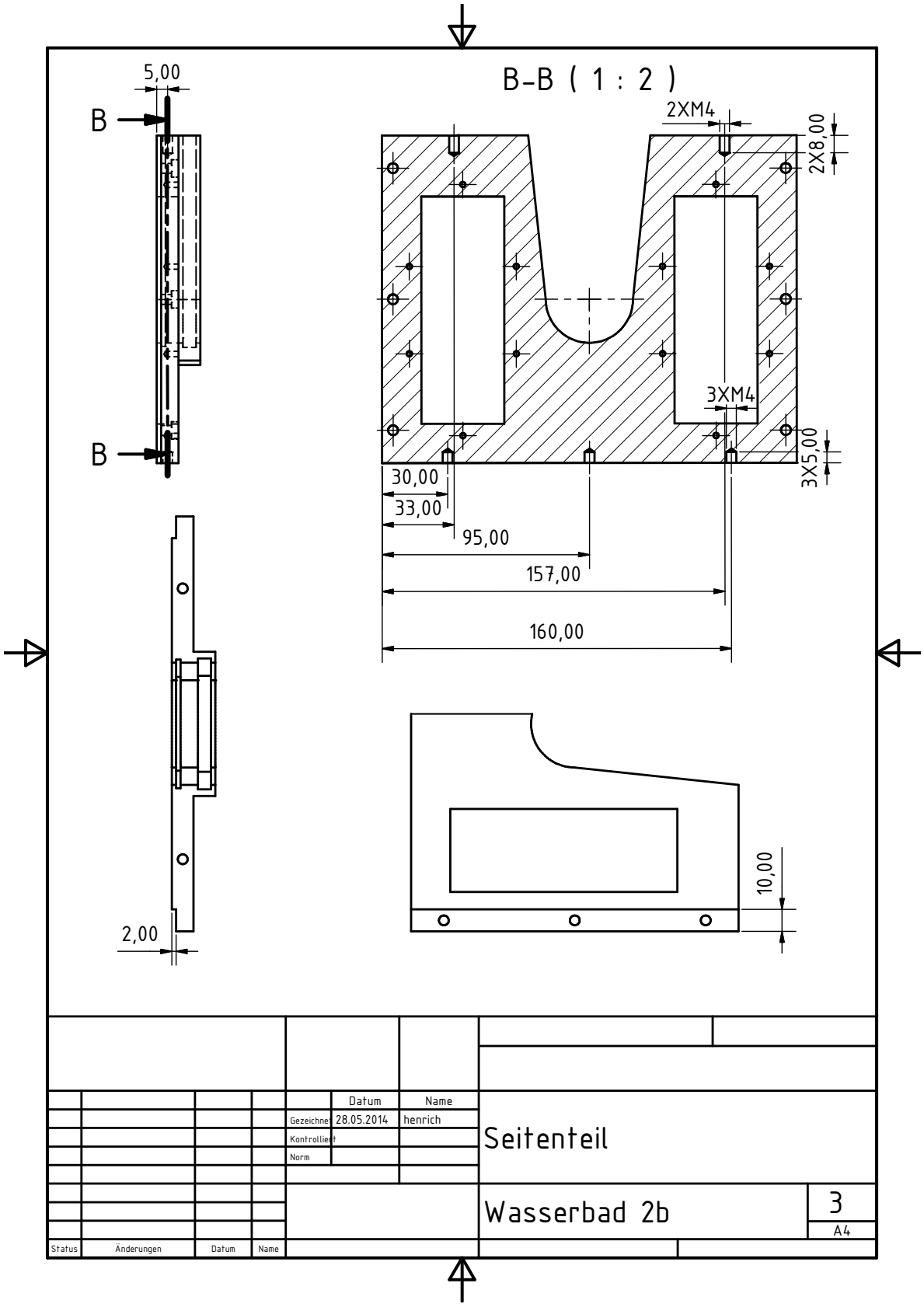

Figure A.9.: Technical drawing of the liquid container right and left.- part 3

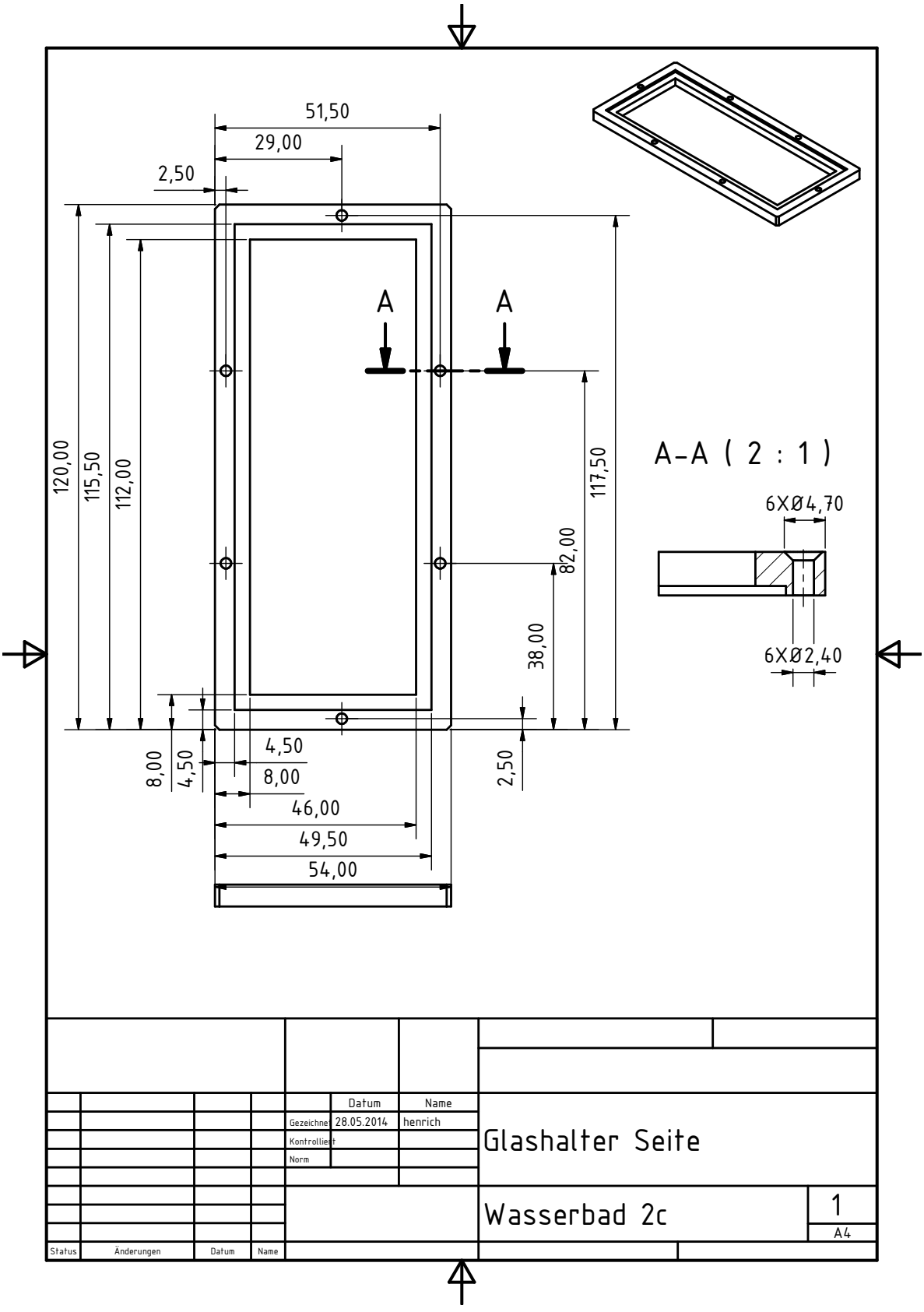

Figure A.10.: Technical drawing of the window holder right and left

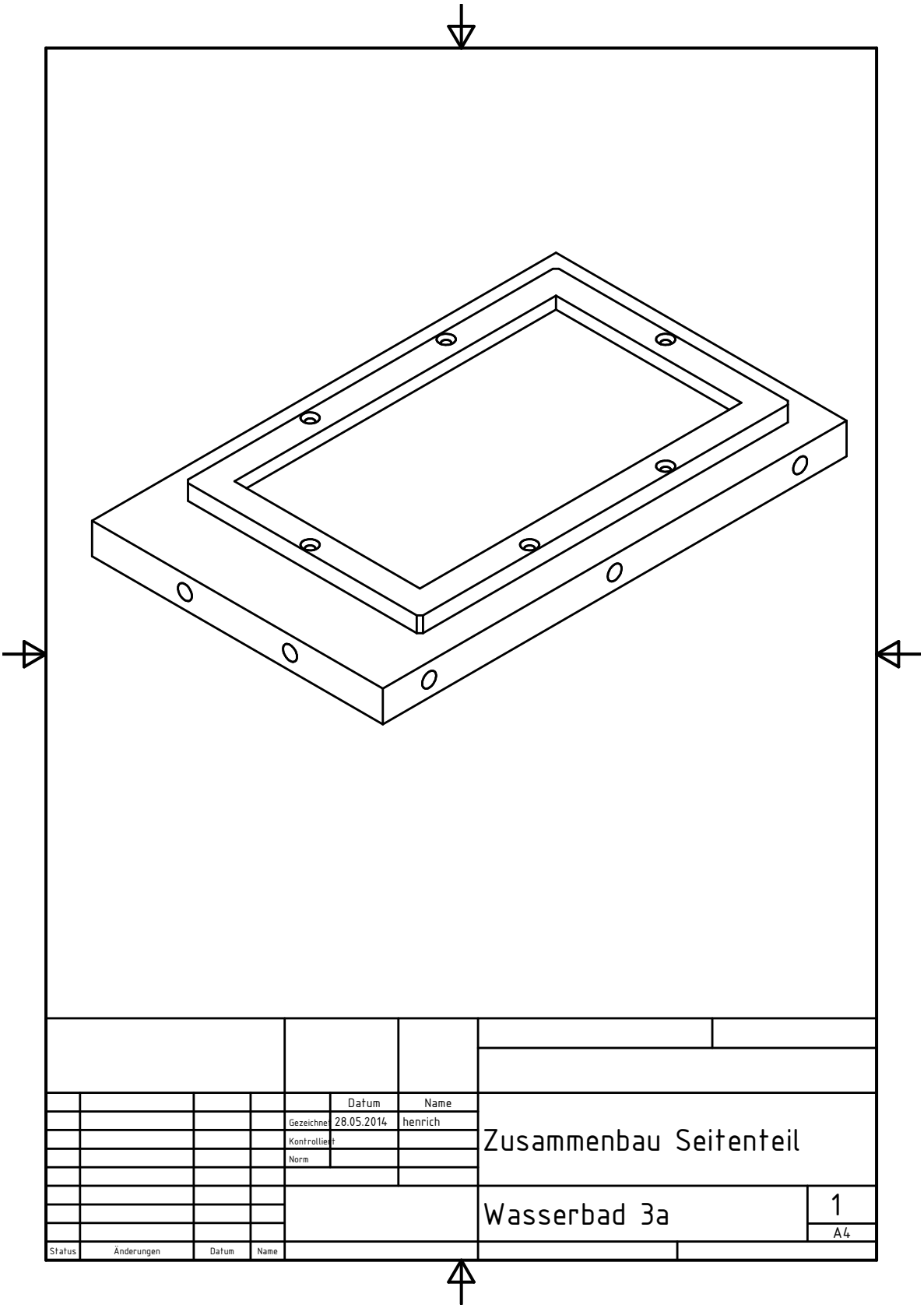

Figure A.11.: Technical drawing of the mounted liquid container front and back

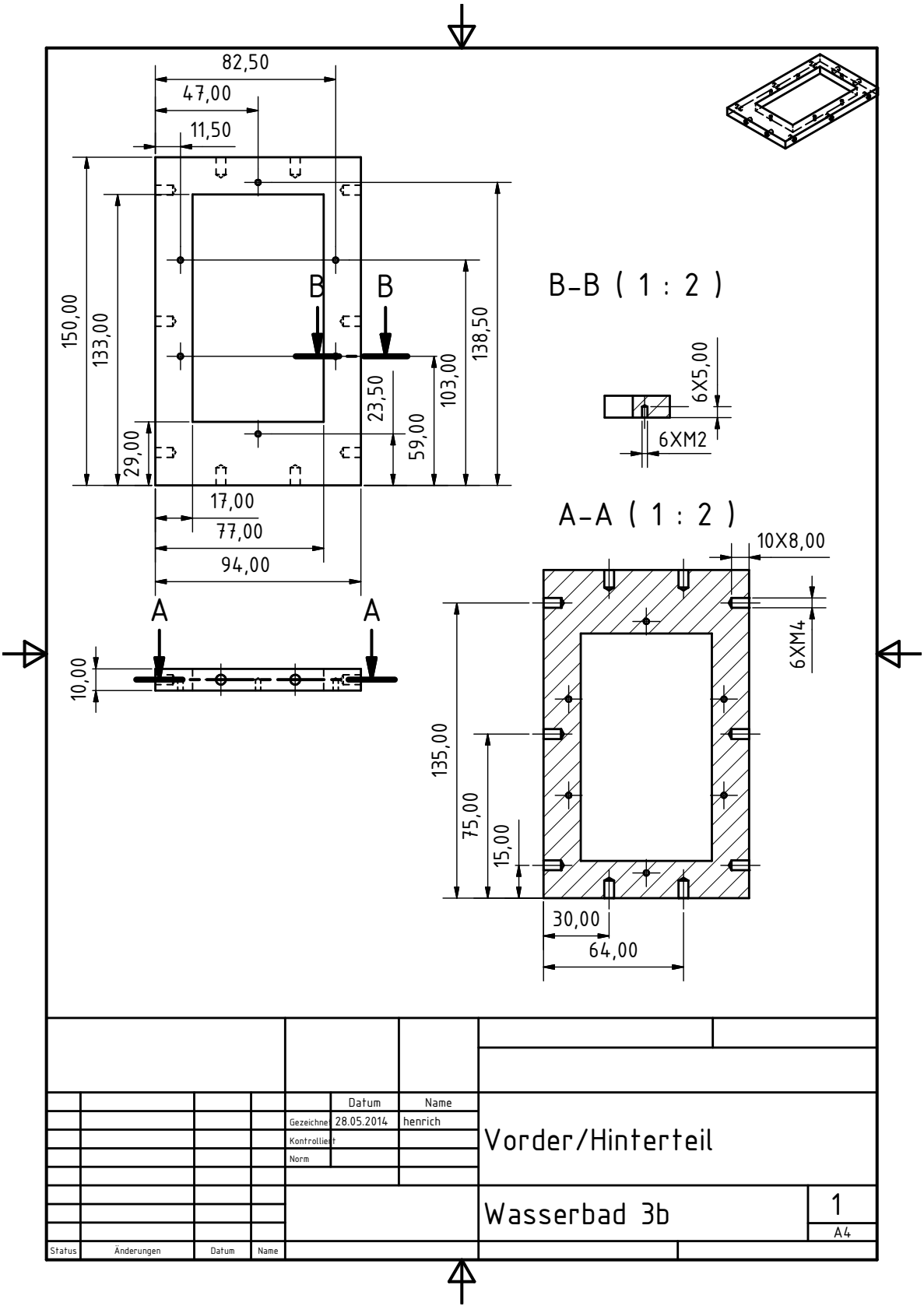

Figure A.12.: Technical drawing of the liquid container front and back

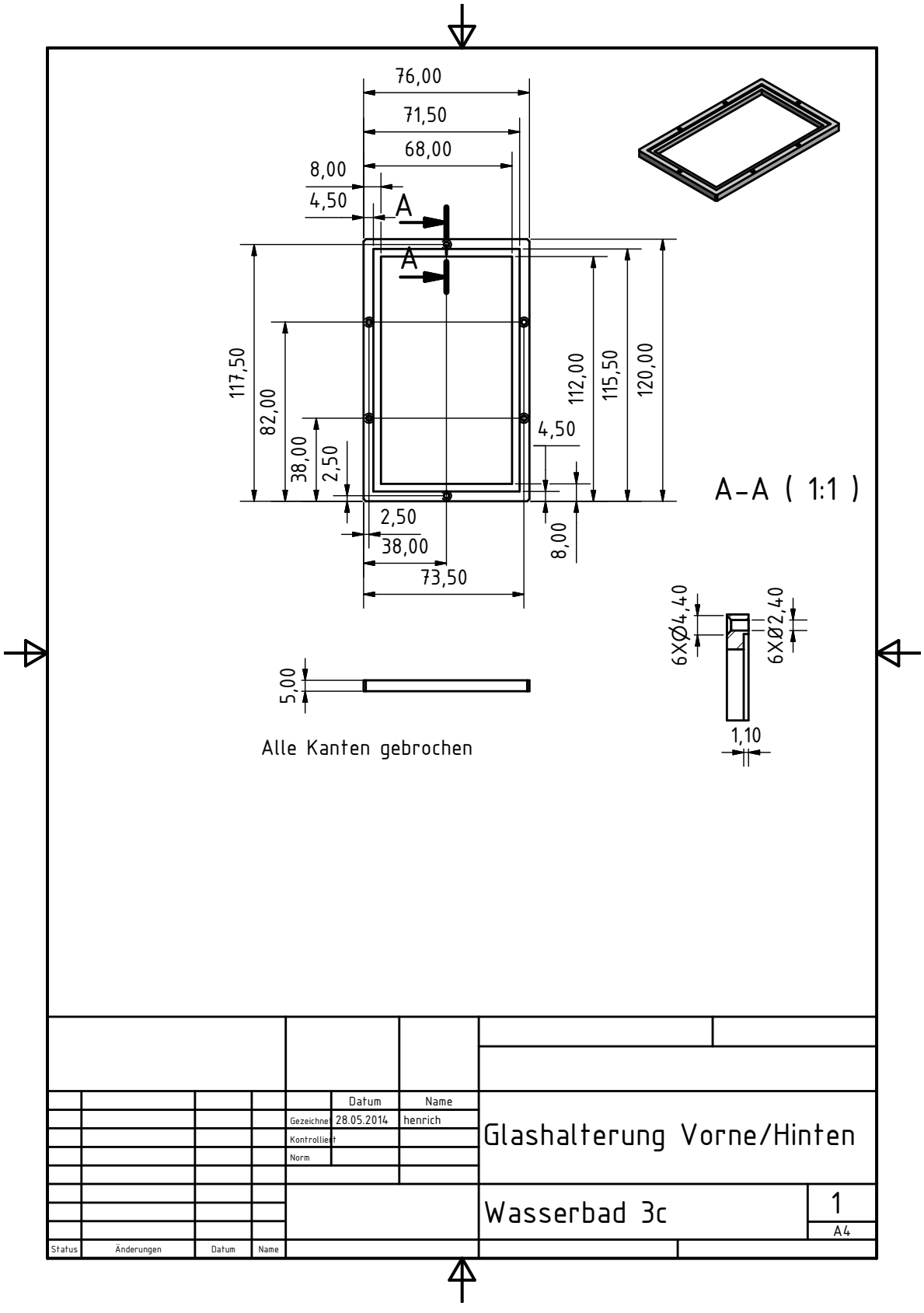

Figure A.13.: Technical drawing of the window holder front and back

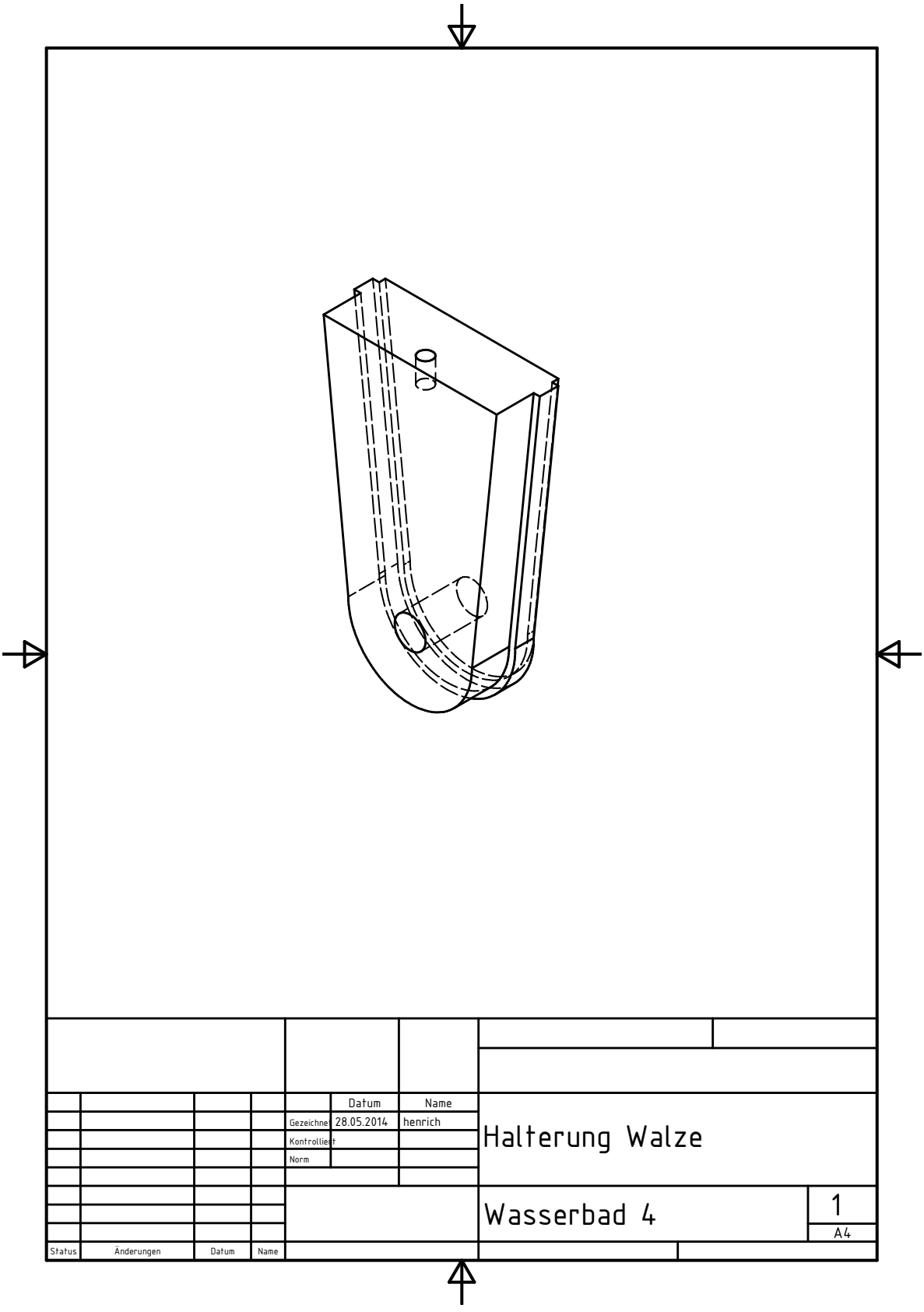

Figure A.14.: Technical drawing of the drum holder

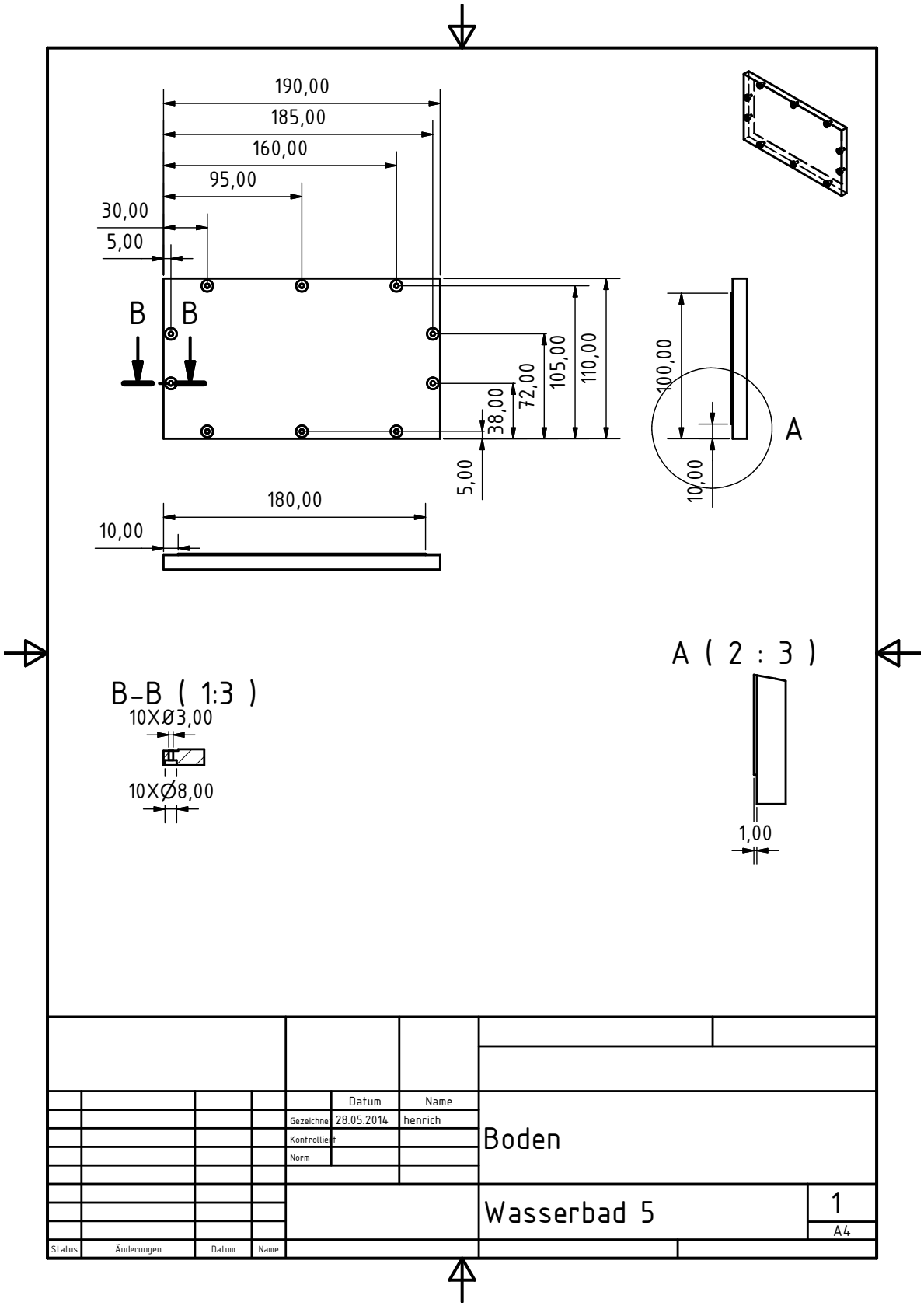

Figure A.15.: Technical drawing of the bottom part of the liquid container

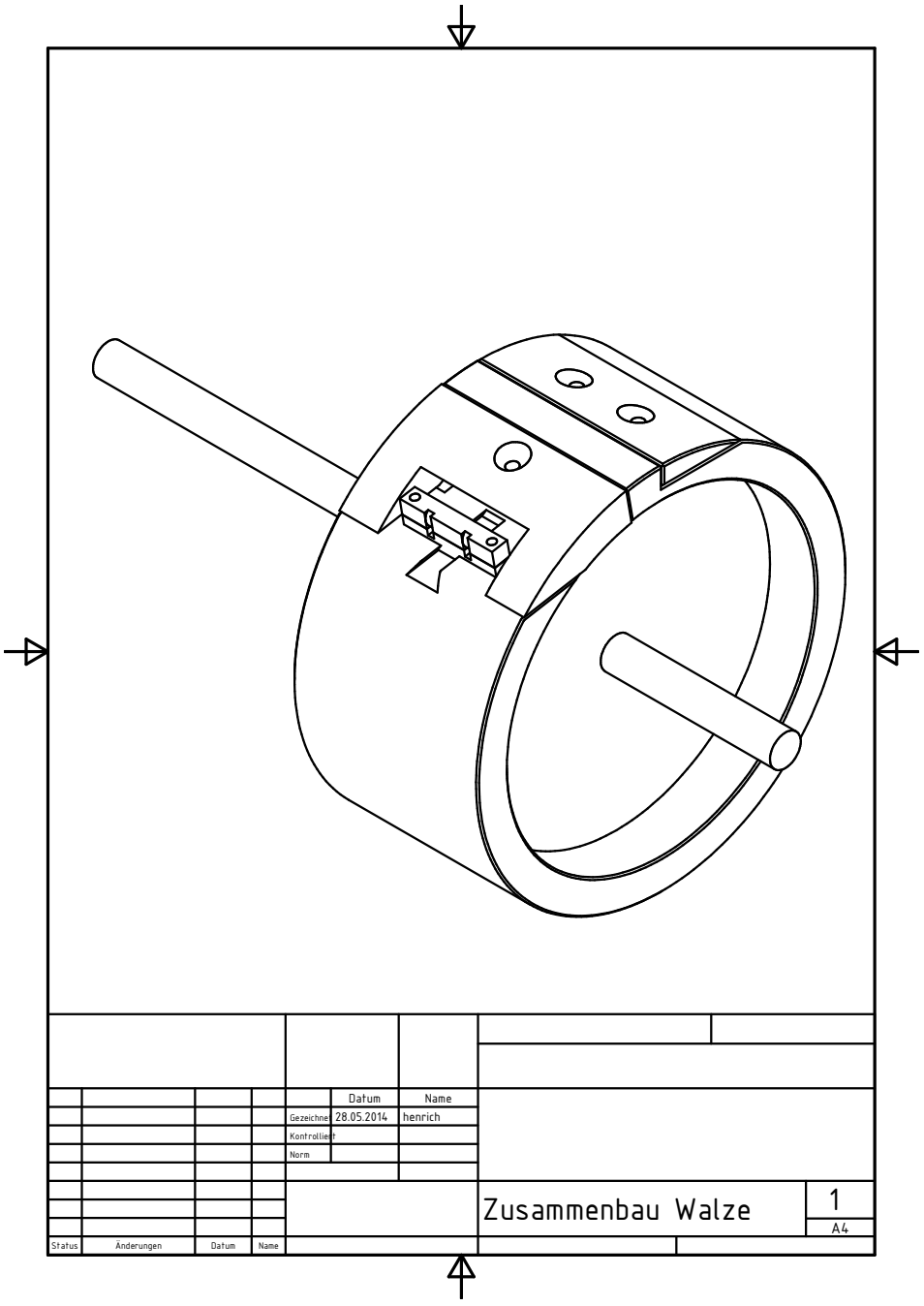

Figure A.16.: Technical drawing of the mounted drum

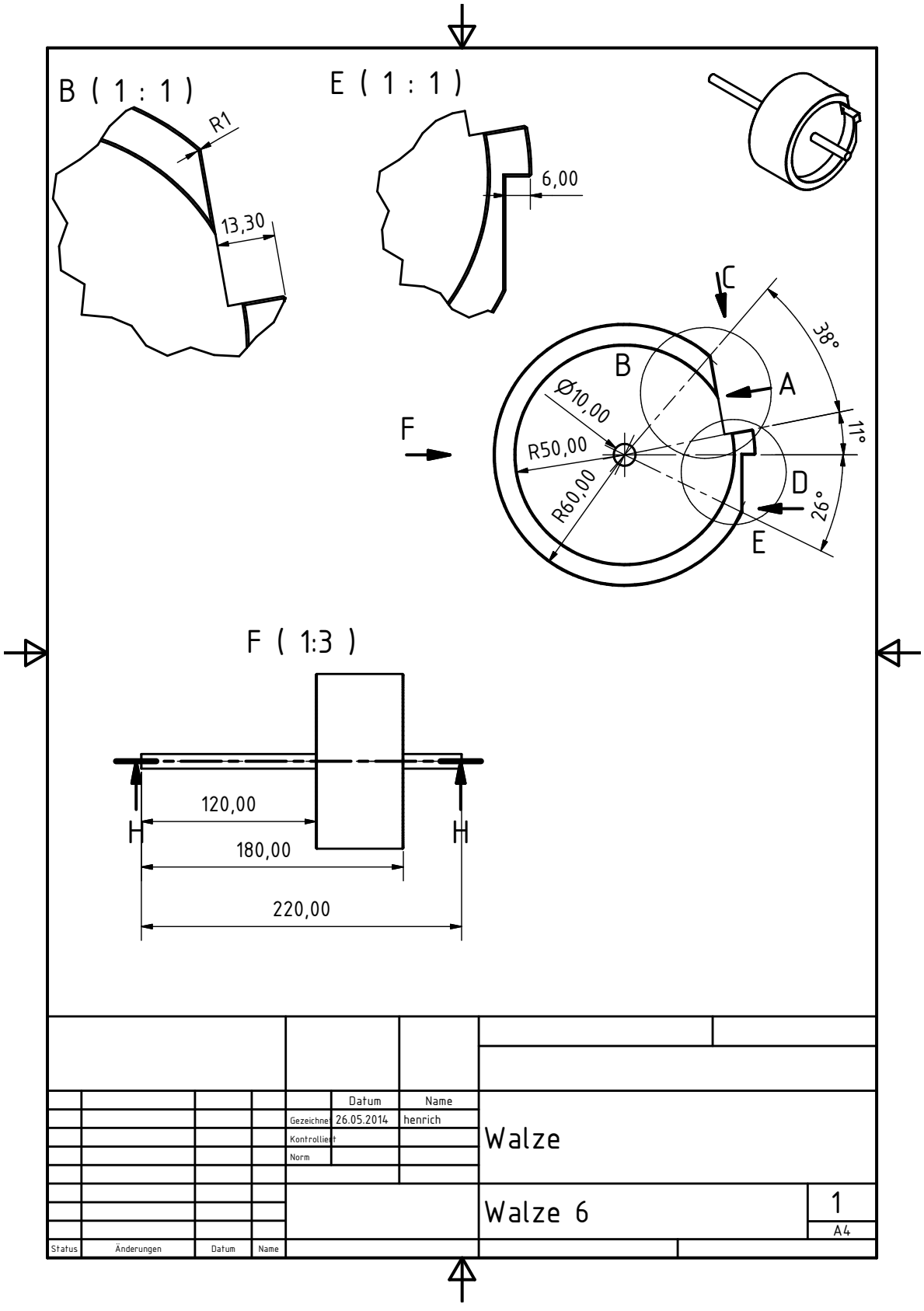

Figure A.17.: Technical drawing of the rotating drum-part 1

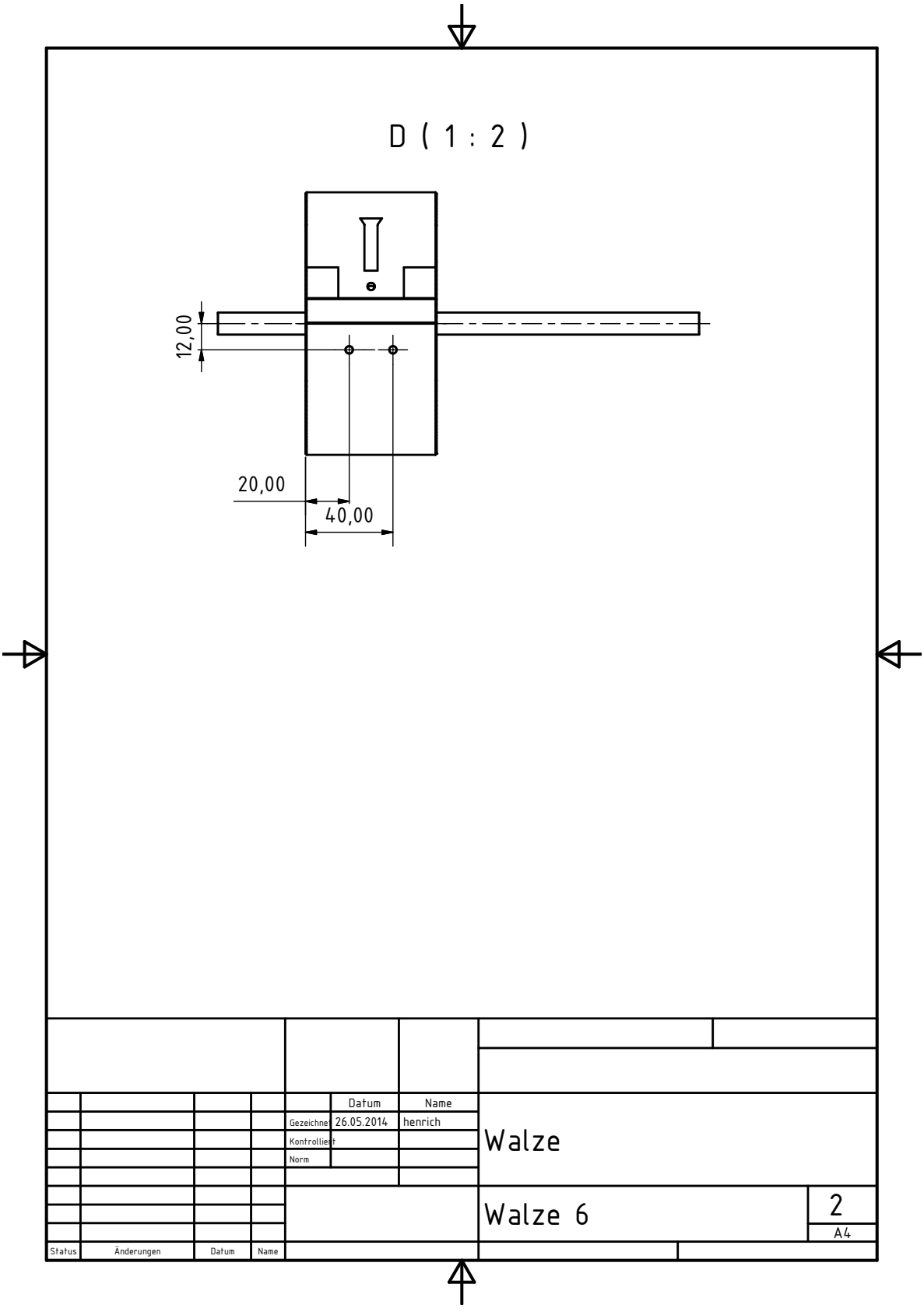

Figure A.18.: Technical drawing of the rotating drum-part 2

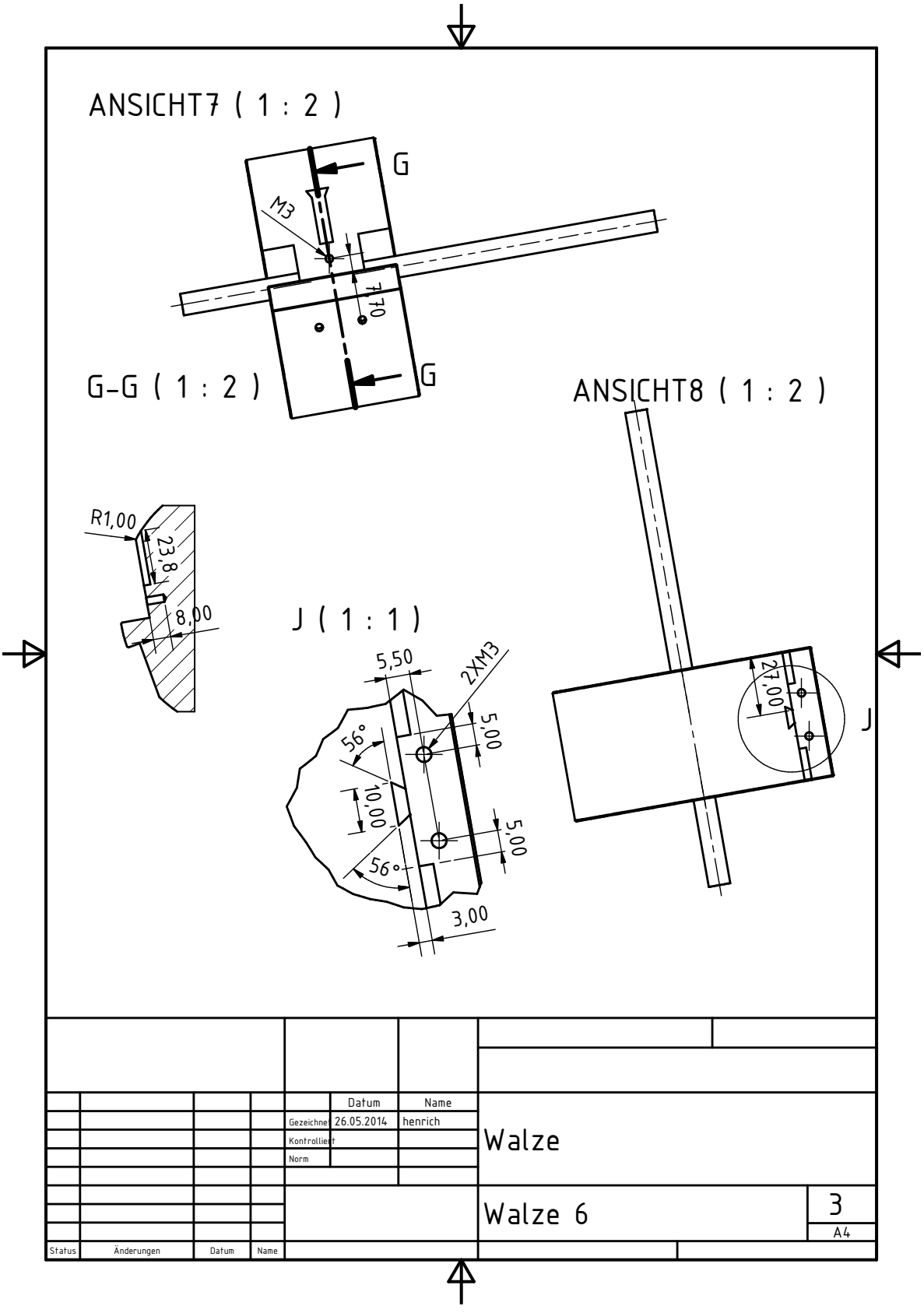

Figure A.19.: Technical drawing of the rotating drum-part 3

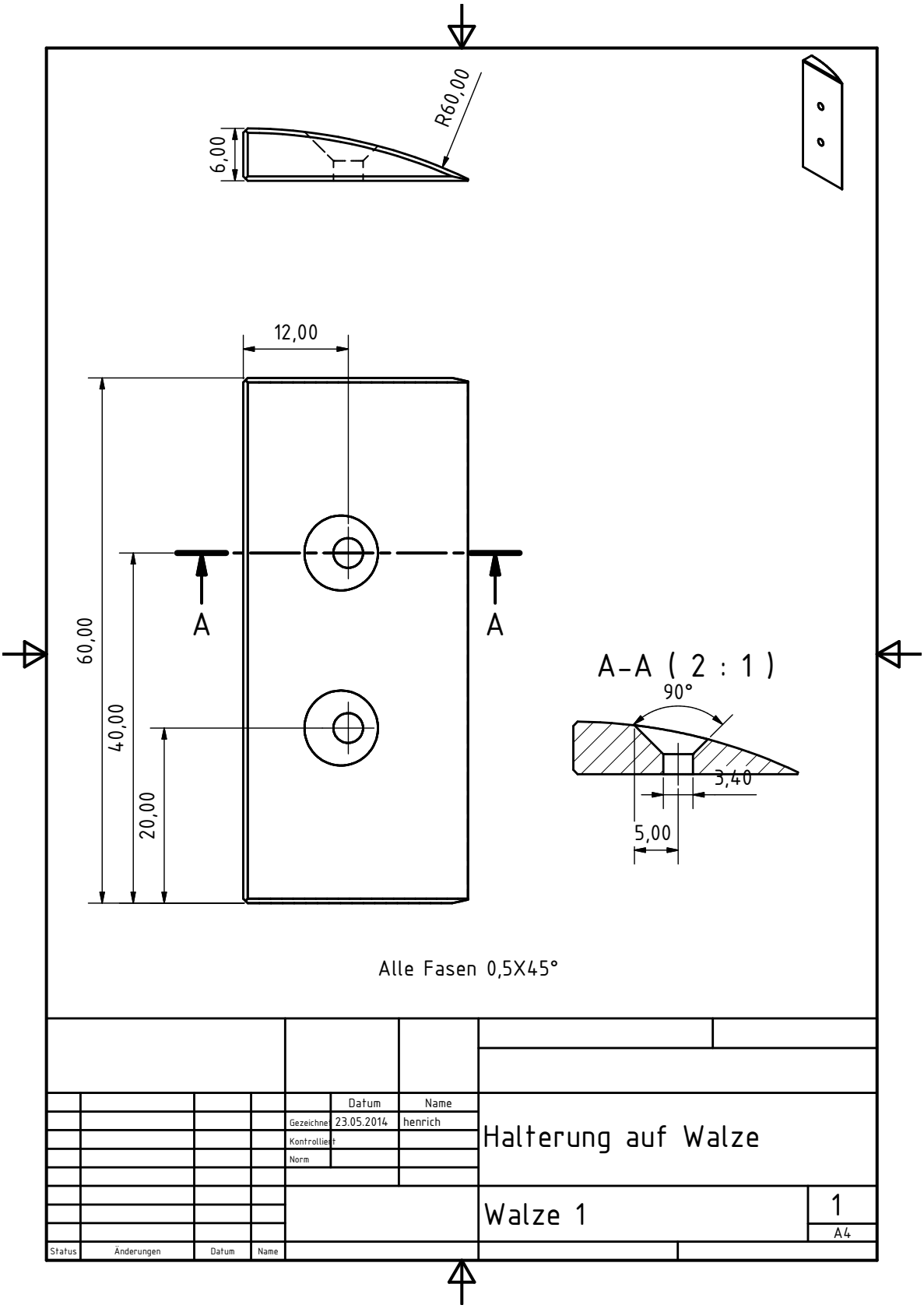

Figure A.20.: Technical drawing of the fixing part direct on the drum

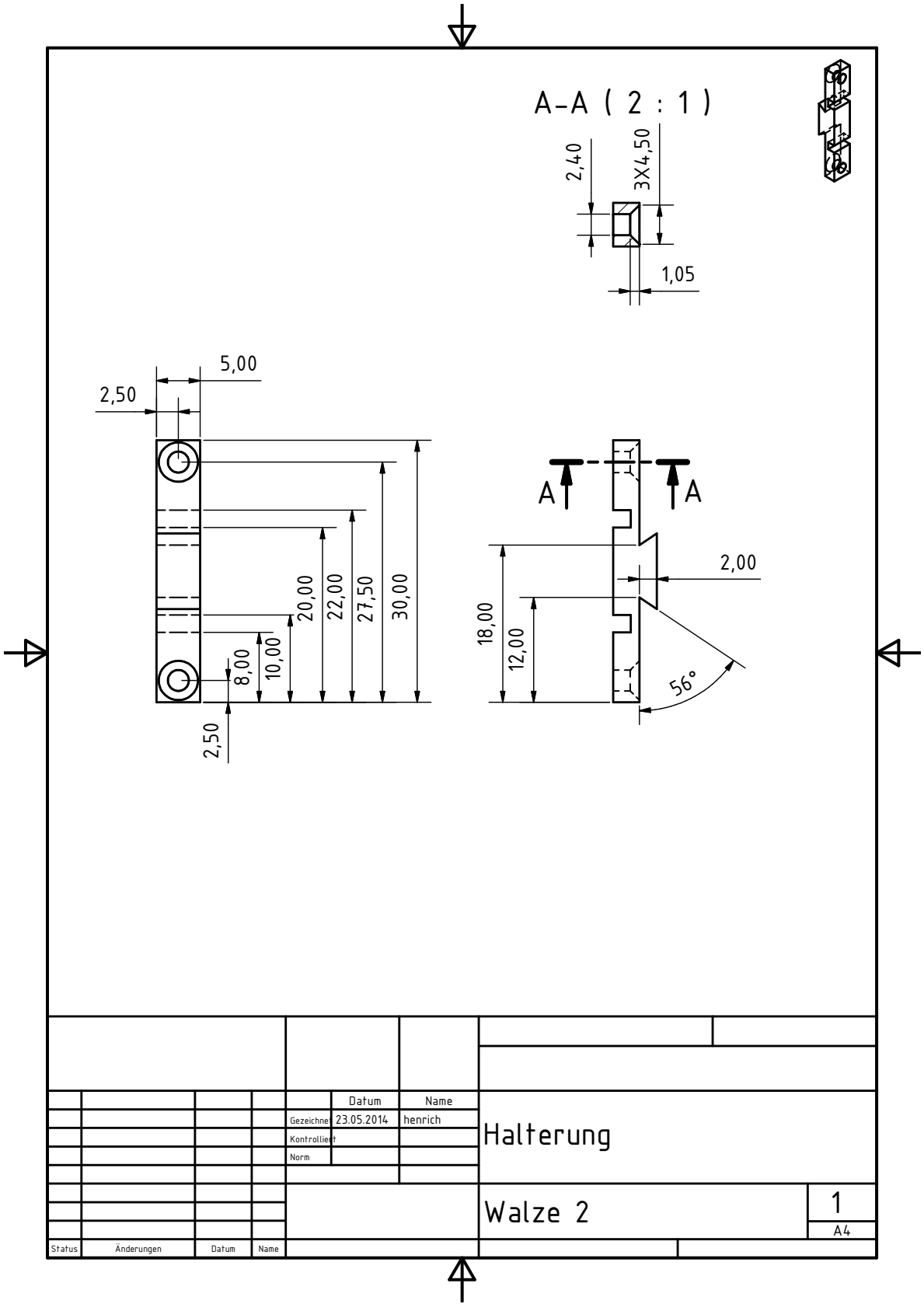

Figure A.21.: Technical drawing of the fixing part with dovetail connection

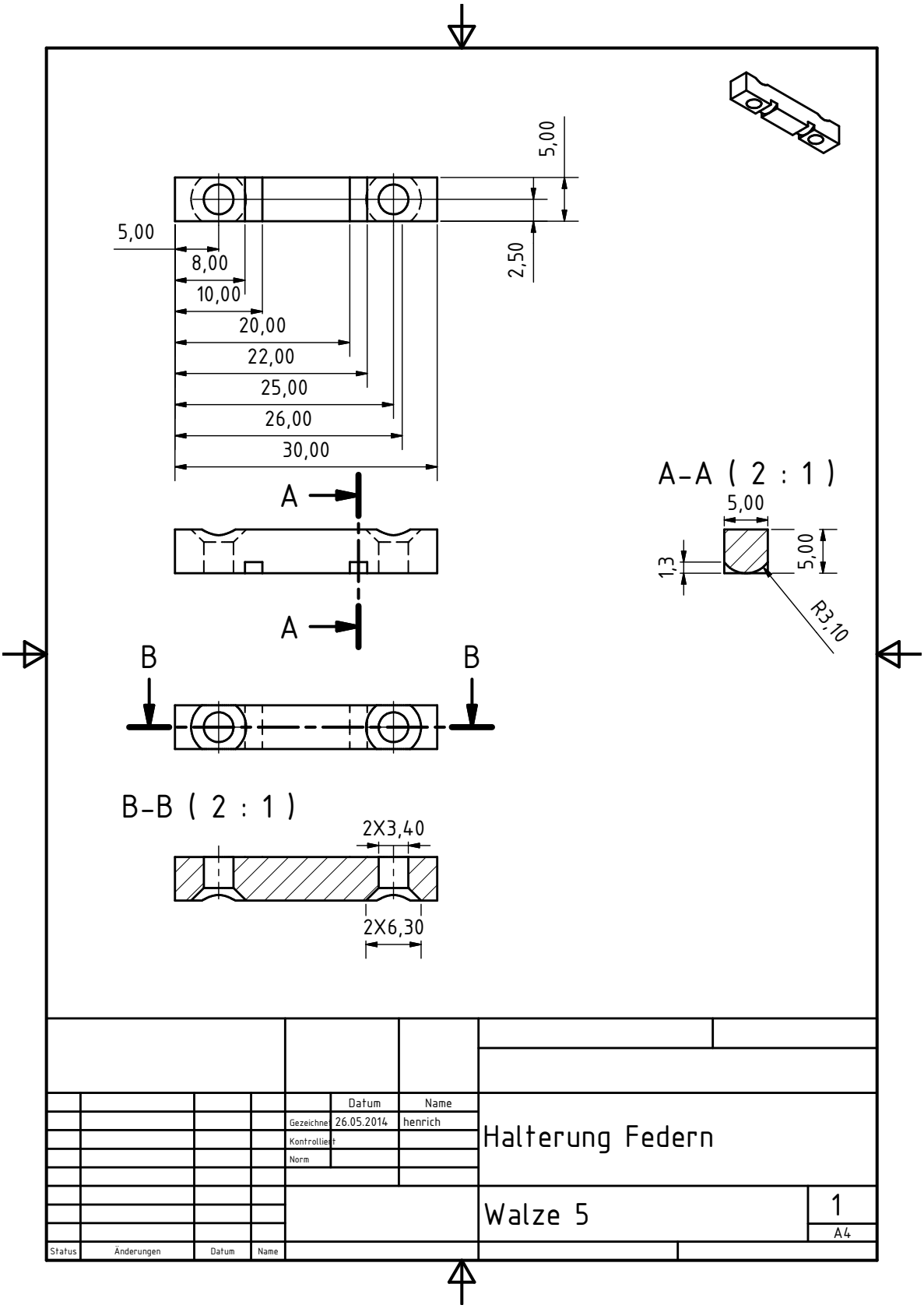

Figure A.22.: Technical drawing of the fixing part with spring holder

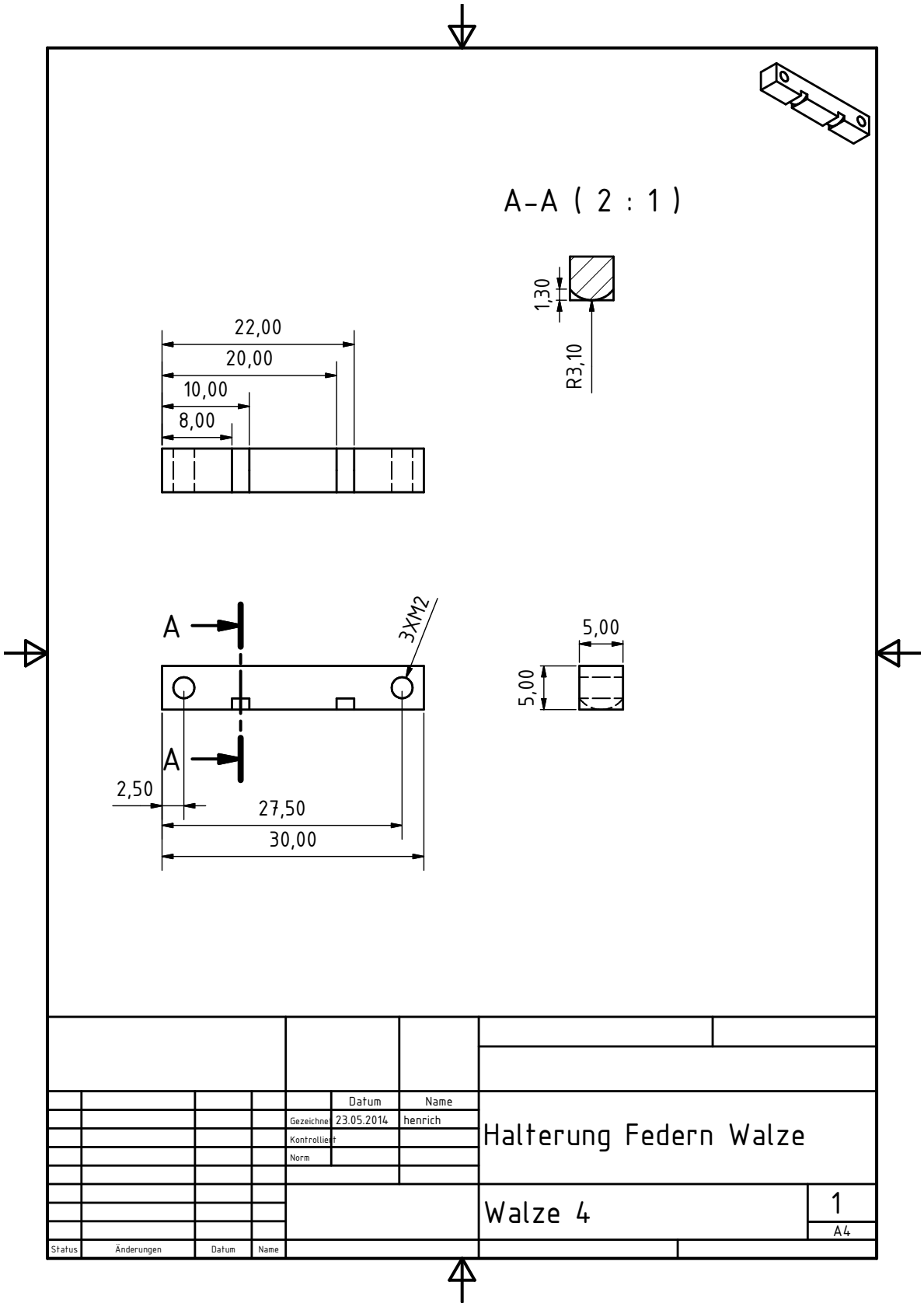

Figure A.23.: Technical drawing of the spring holder conneted directly to the drum

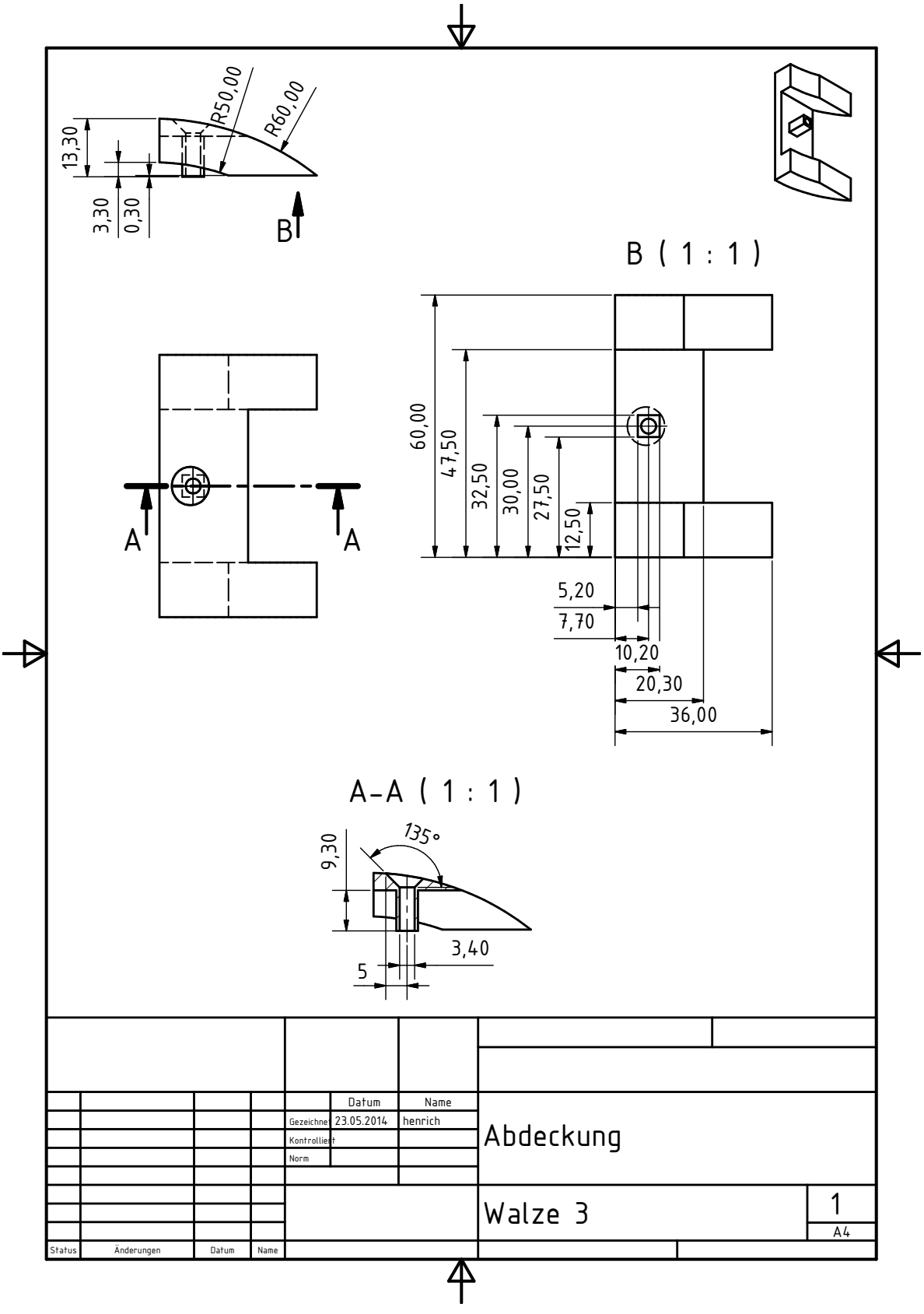

Figure A.24.: Technical drawing of the fixation cover

A.1.2 Mircoscope Setup

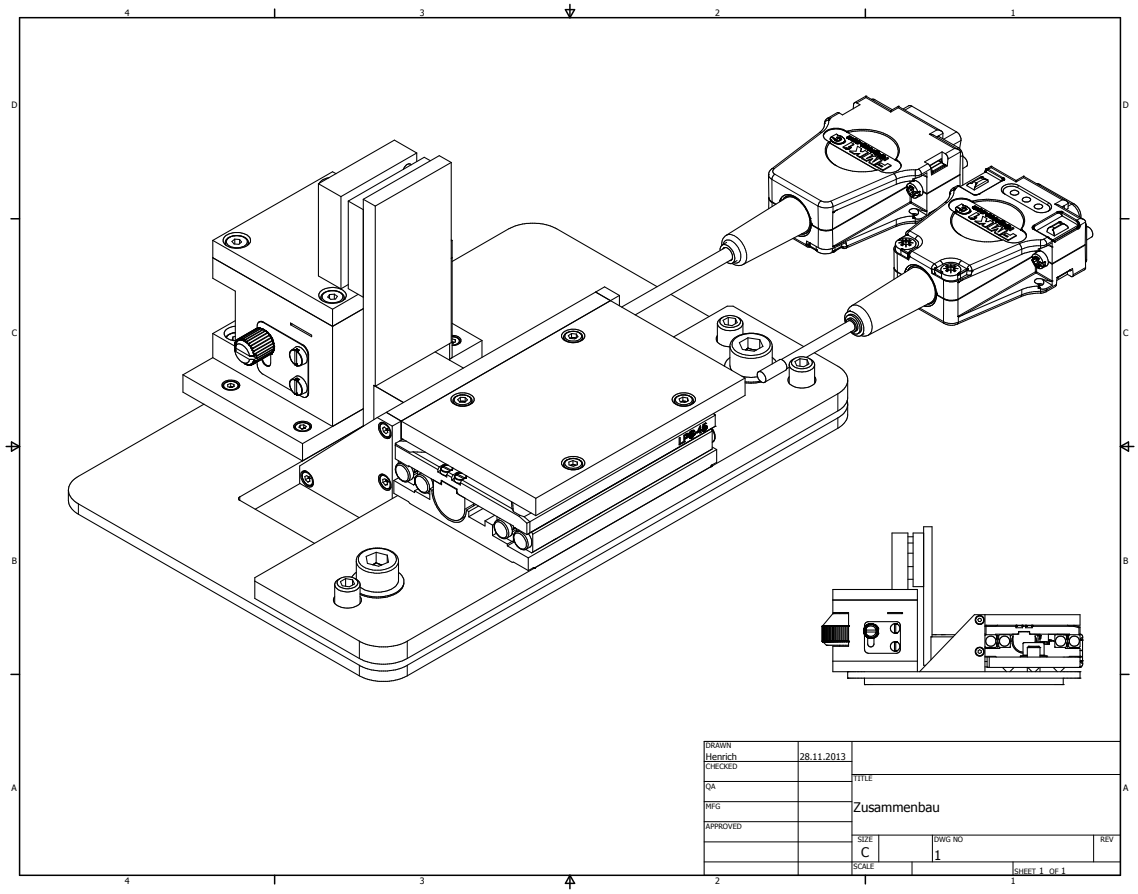

Figure A.25.: Technical drawing of the mounted microscope setup.

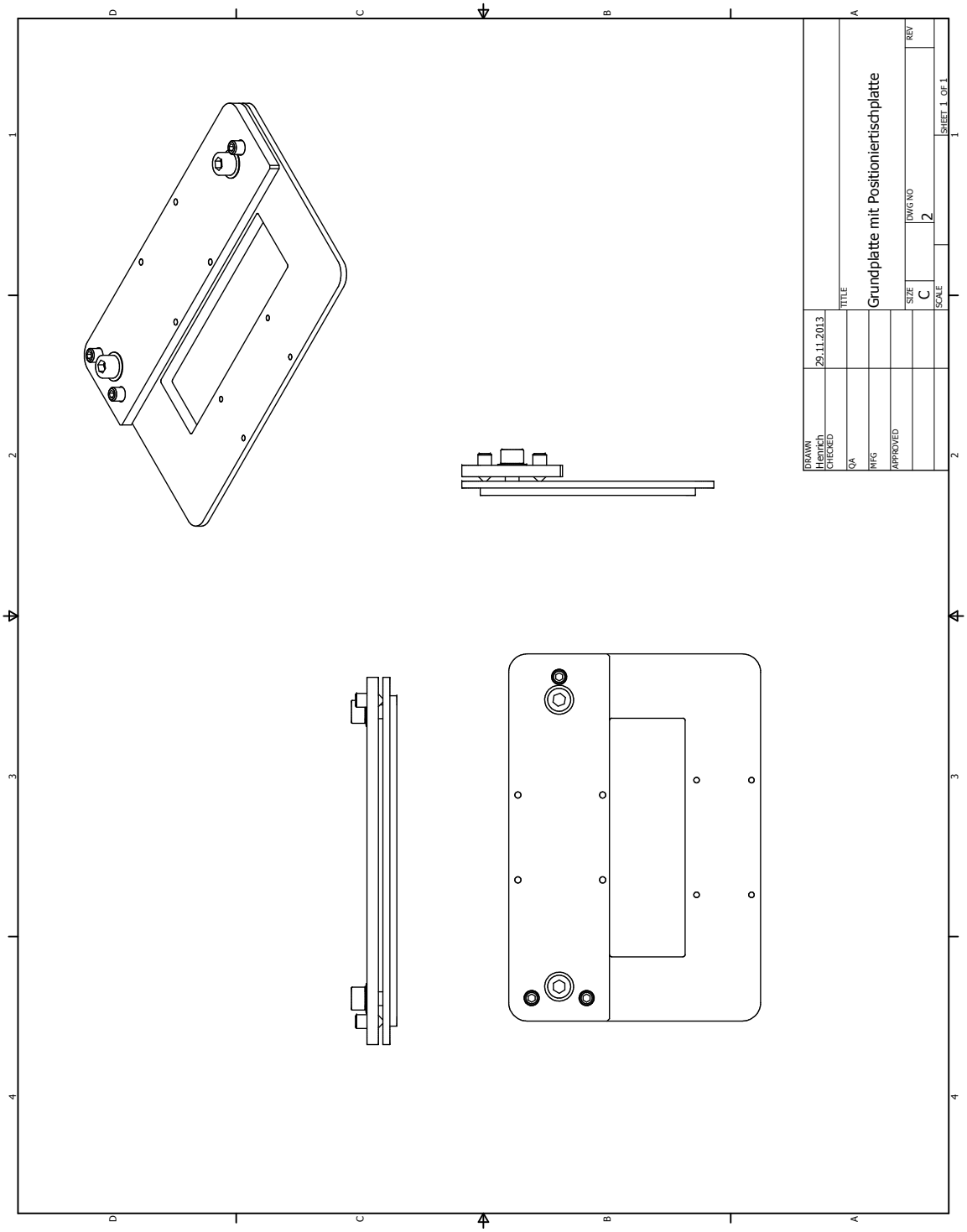

Figure A.26.: Technical drawing of the mounted ground plate.

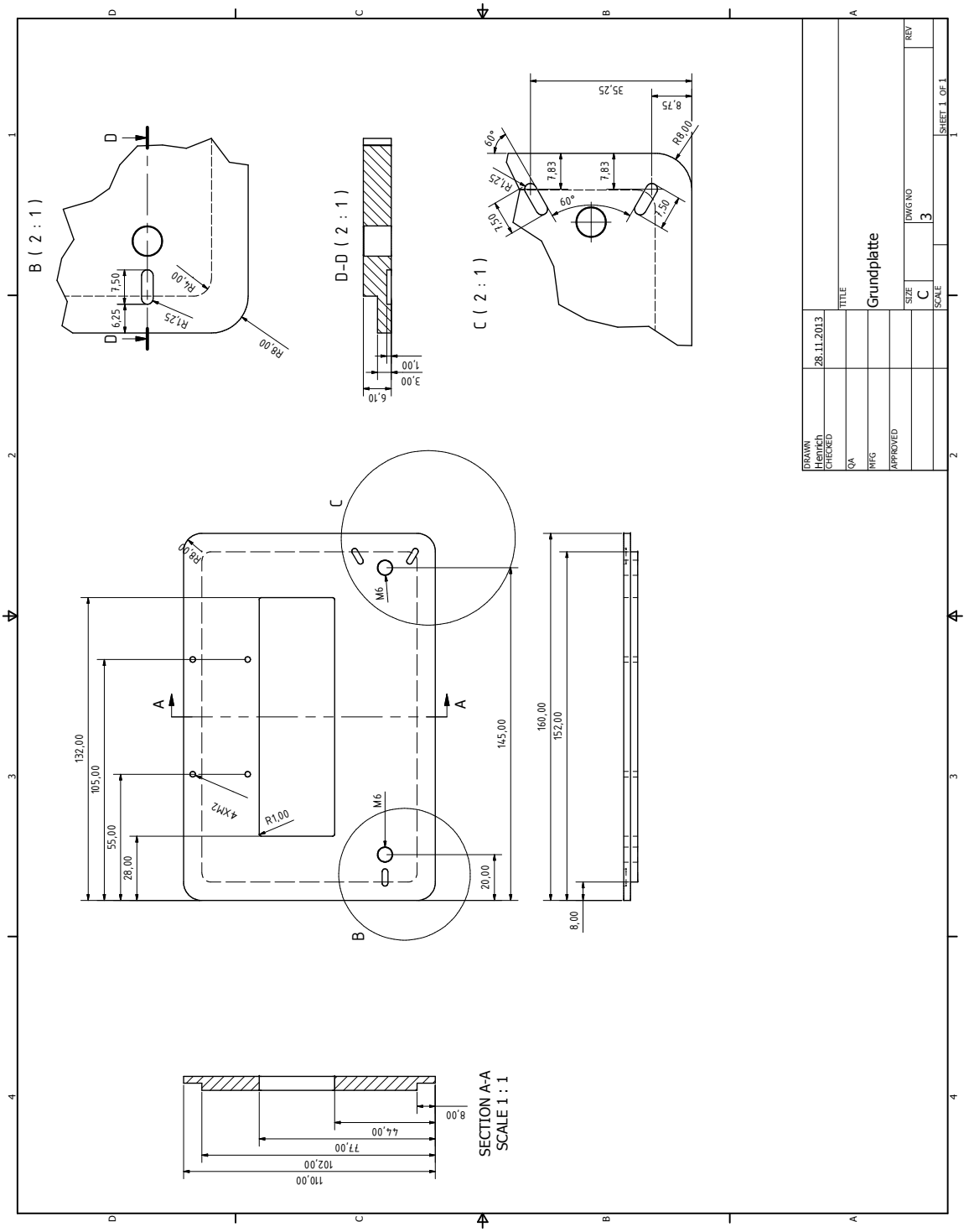

Figure A.27.: Technical drawing of the ground plate.

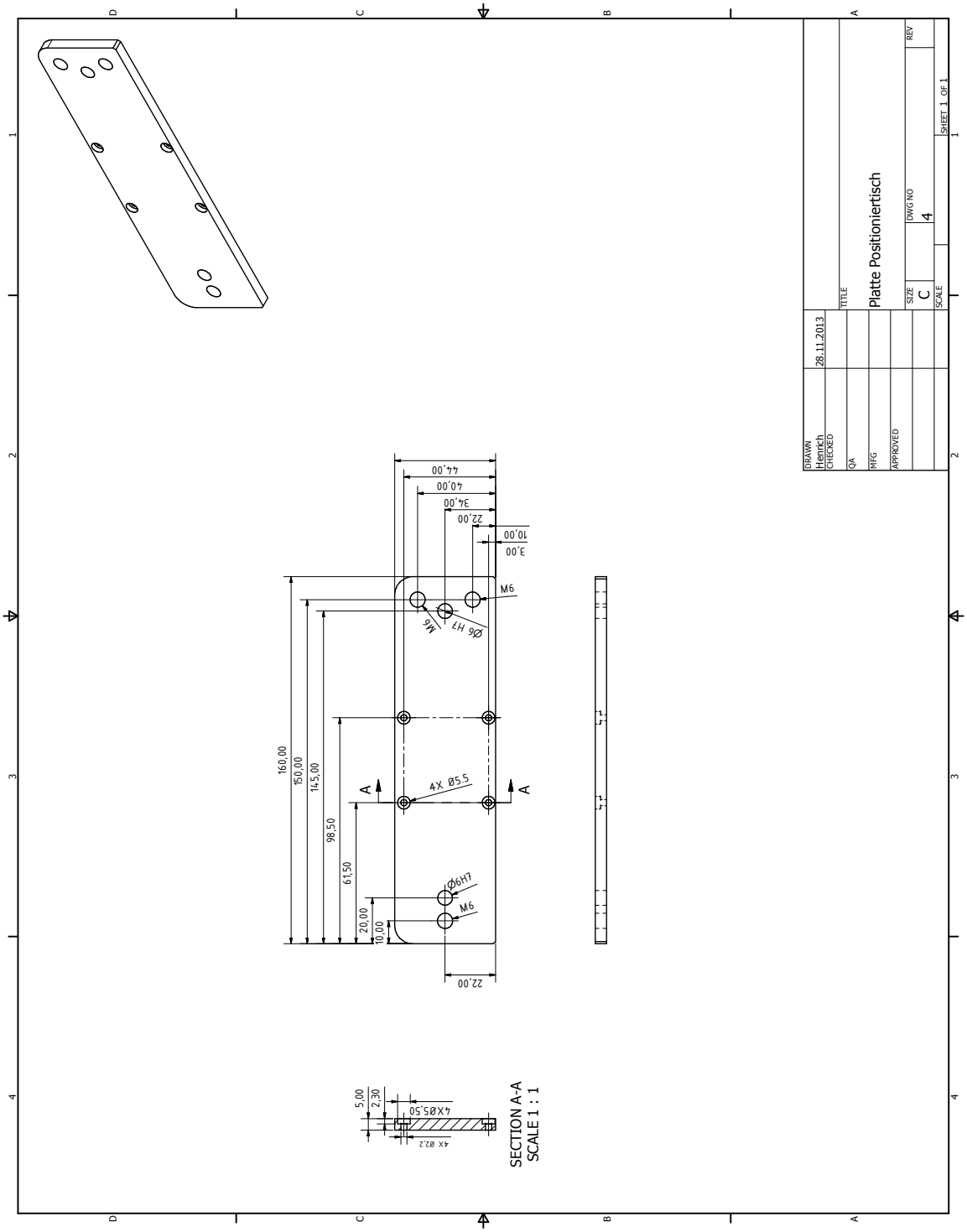

Figure A.28.: Technical drawing of the adapter plate.

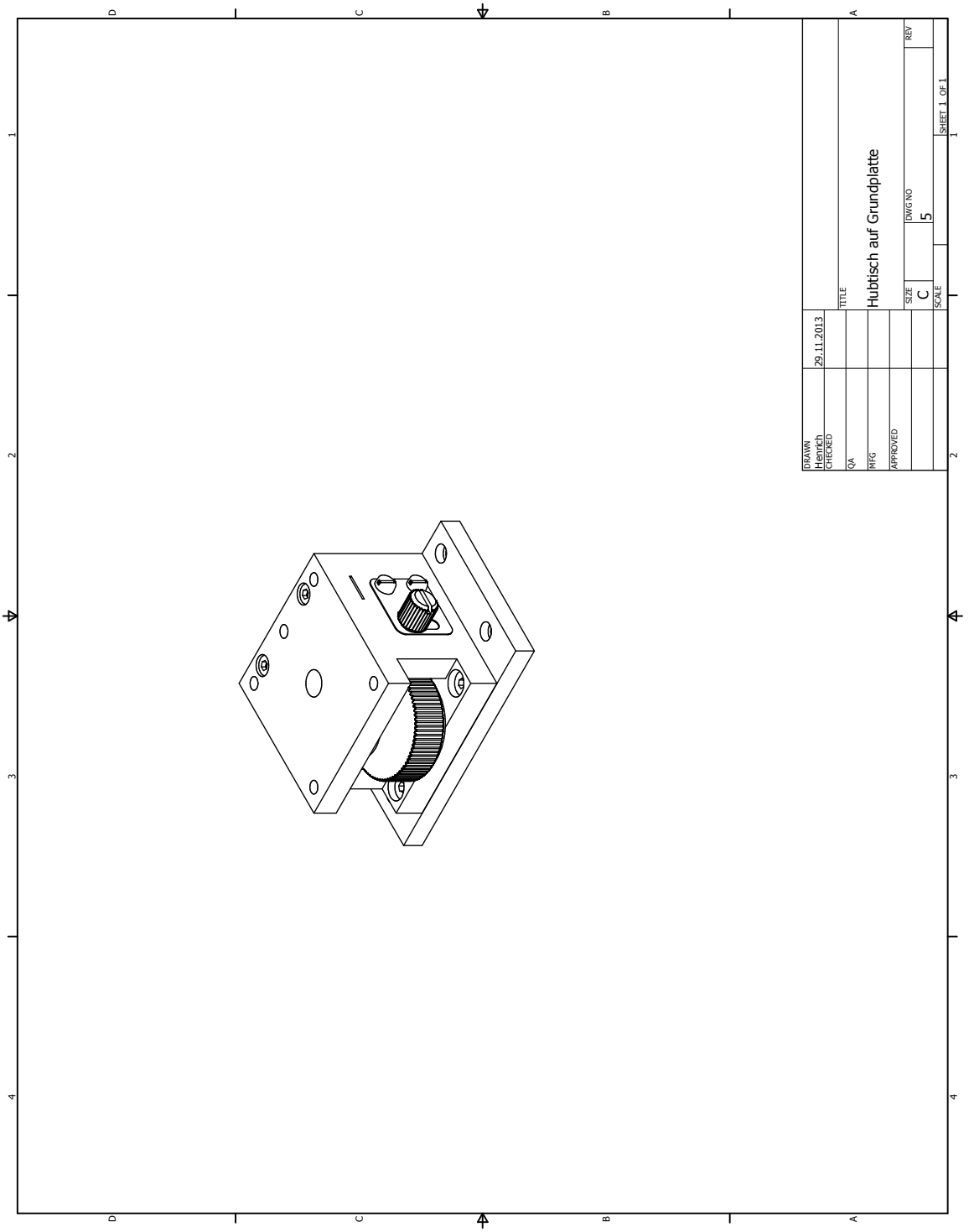

Figure A.29.: Technical drawing of the used vertical stage.

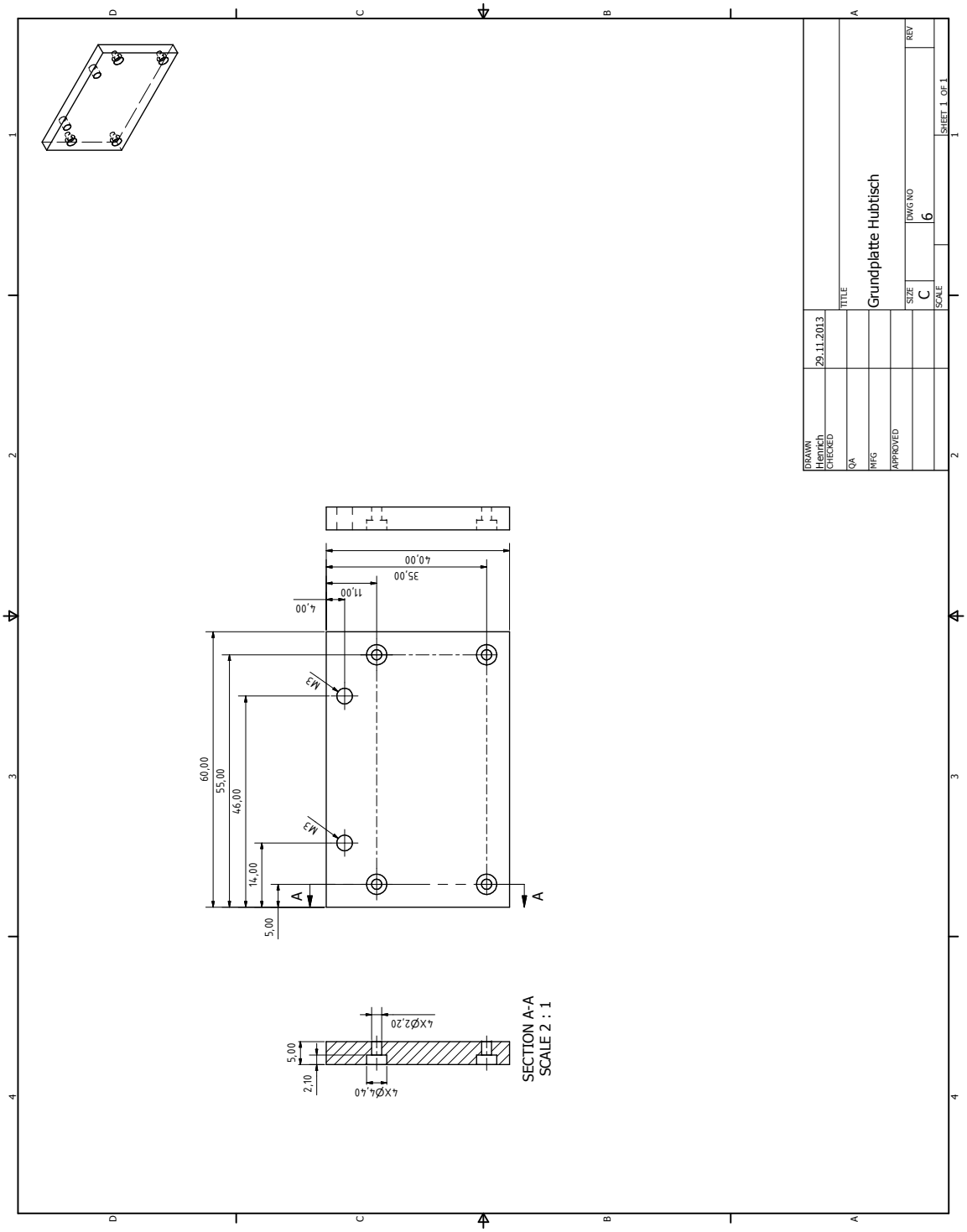

Figure A.30.: Technical drawing of the ground plate of the vertical stage.

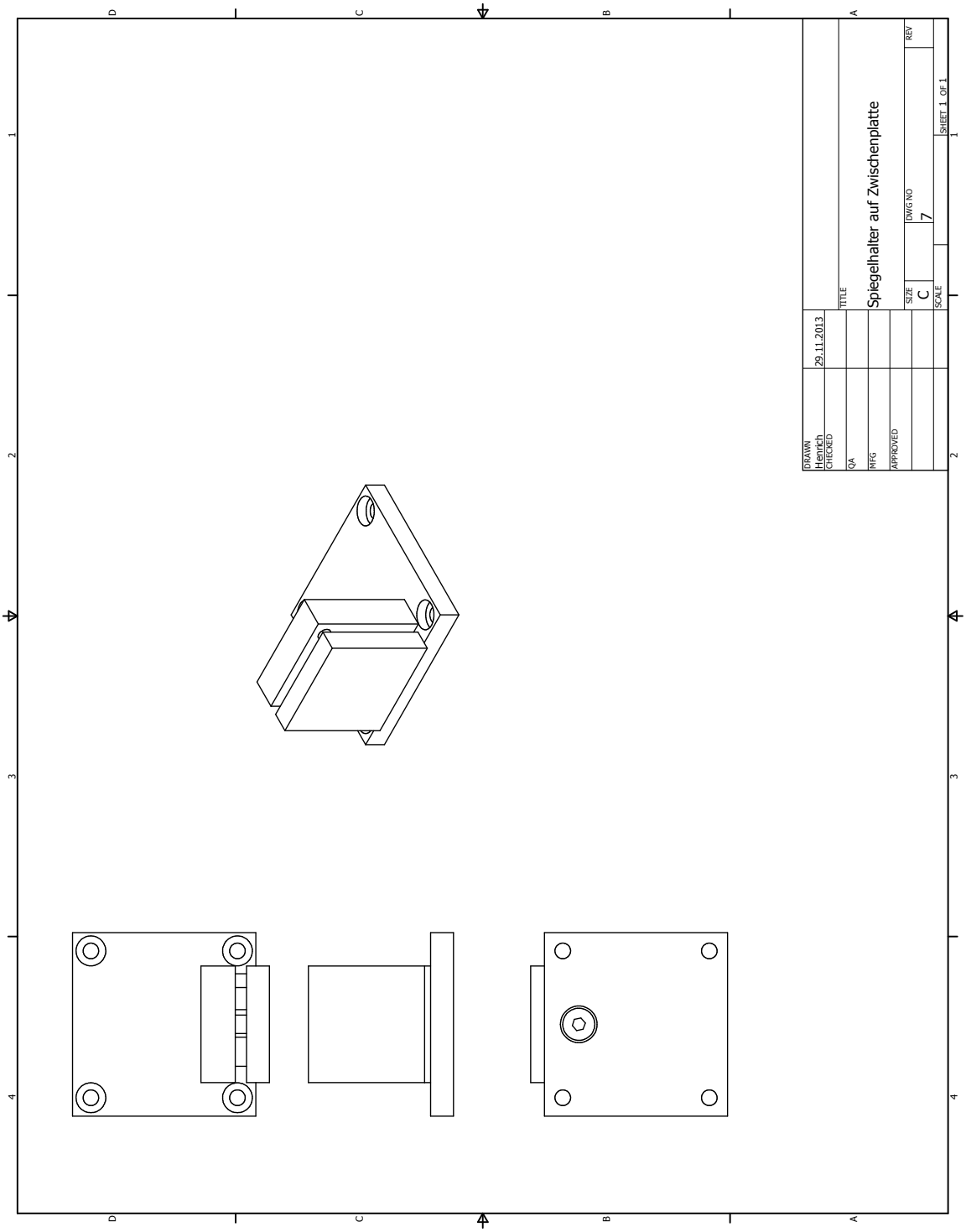

Figure A.31.: Technical drawing of the mirror mount on the adapter plate.

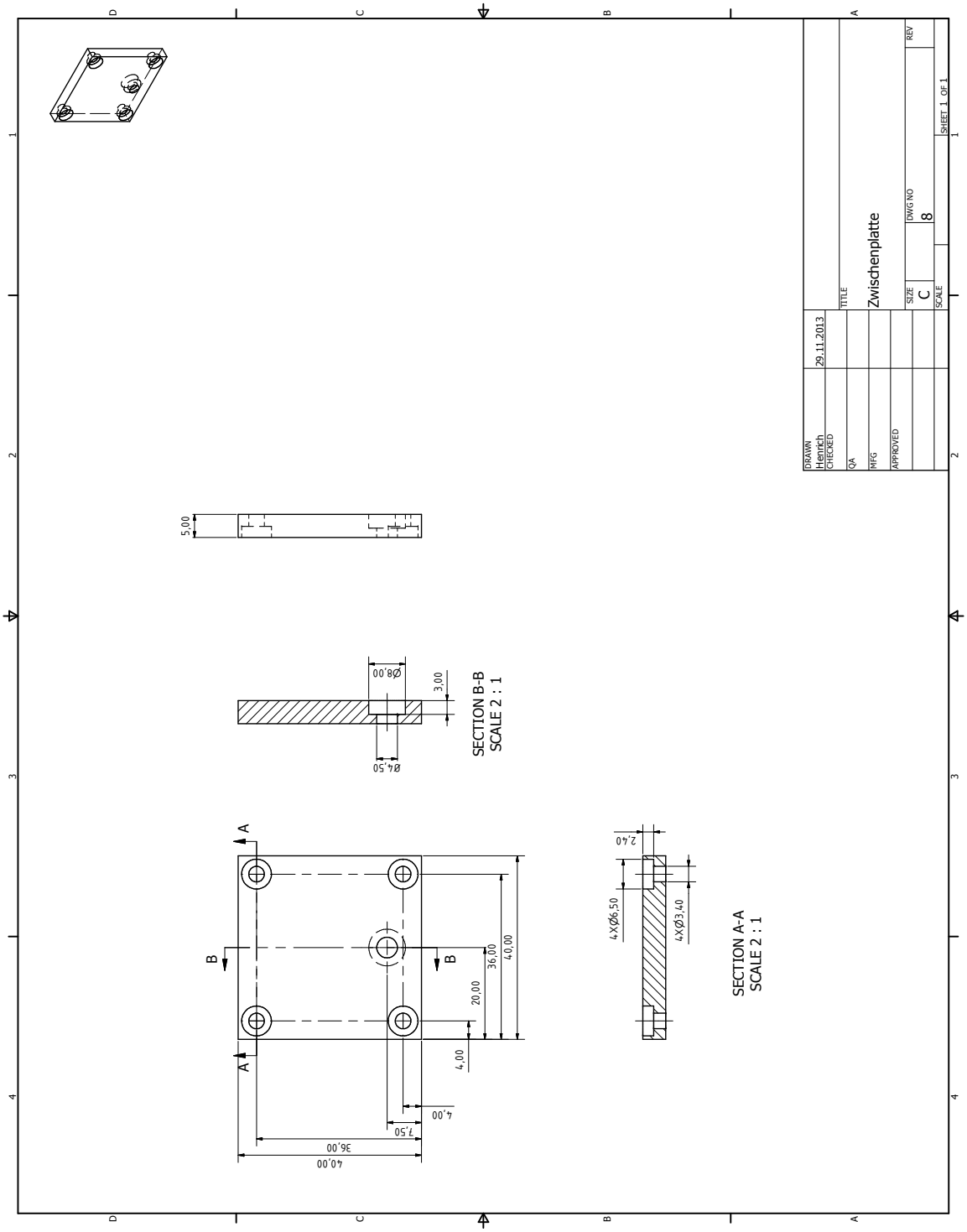

Figure A.32.: Technical drawing of the adapter plate for the mirror mount.

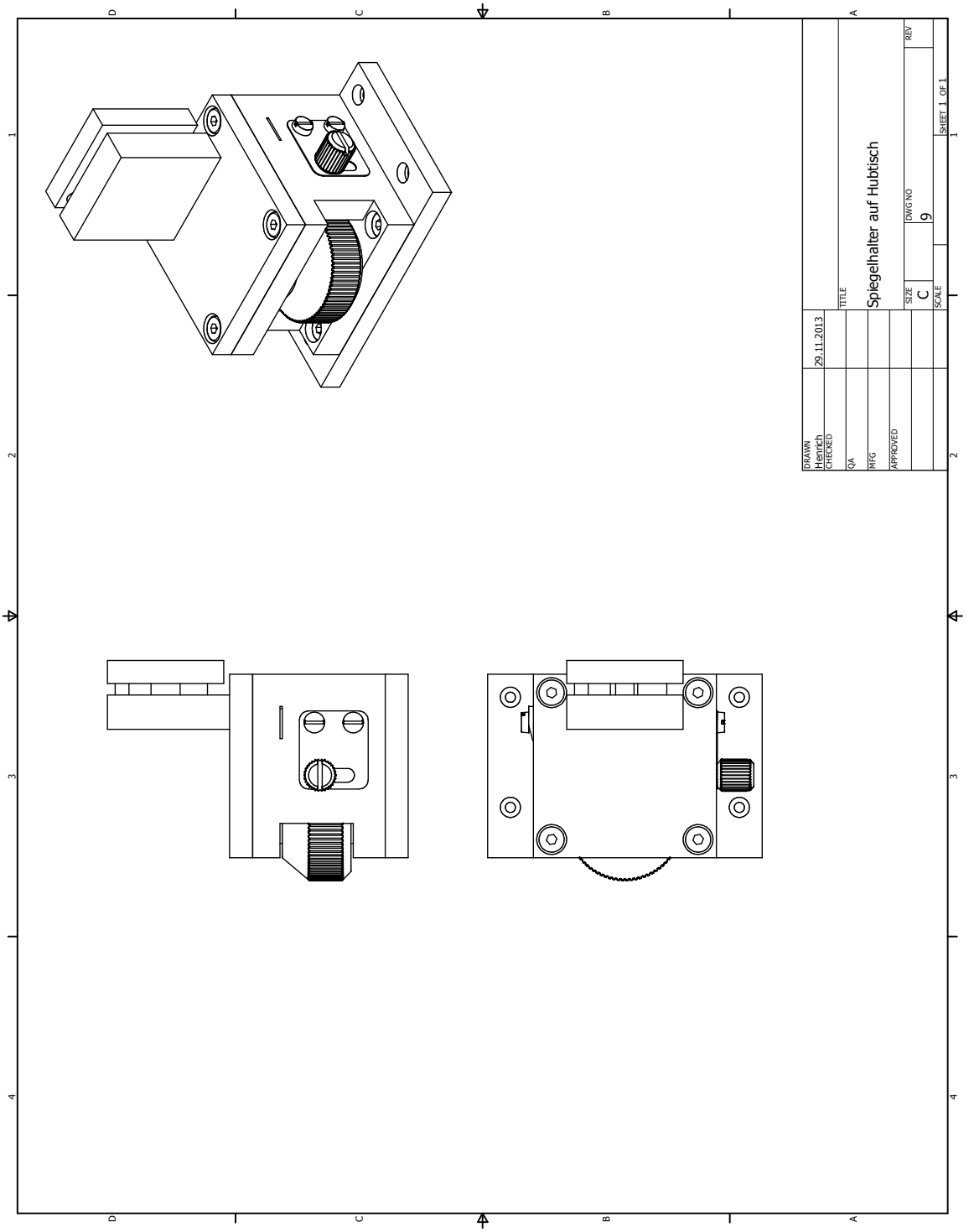

Figure A.33.: Technical drawing of the mirror mount the vertical stage.

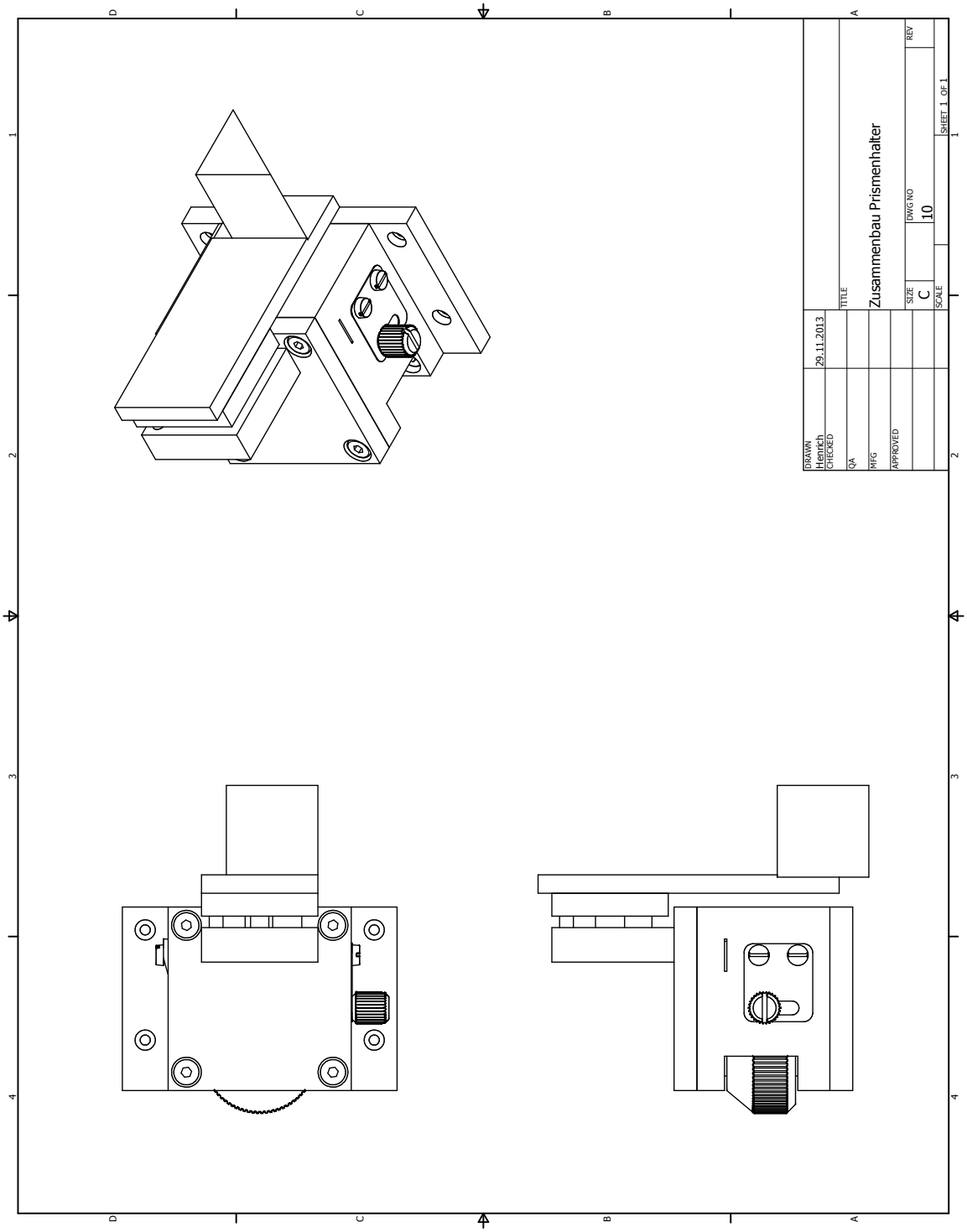

Figure A.34.: Technical drawing of the mounted prism on the vertical stage.

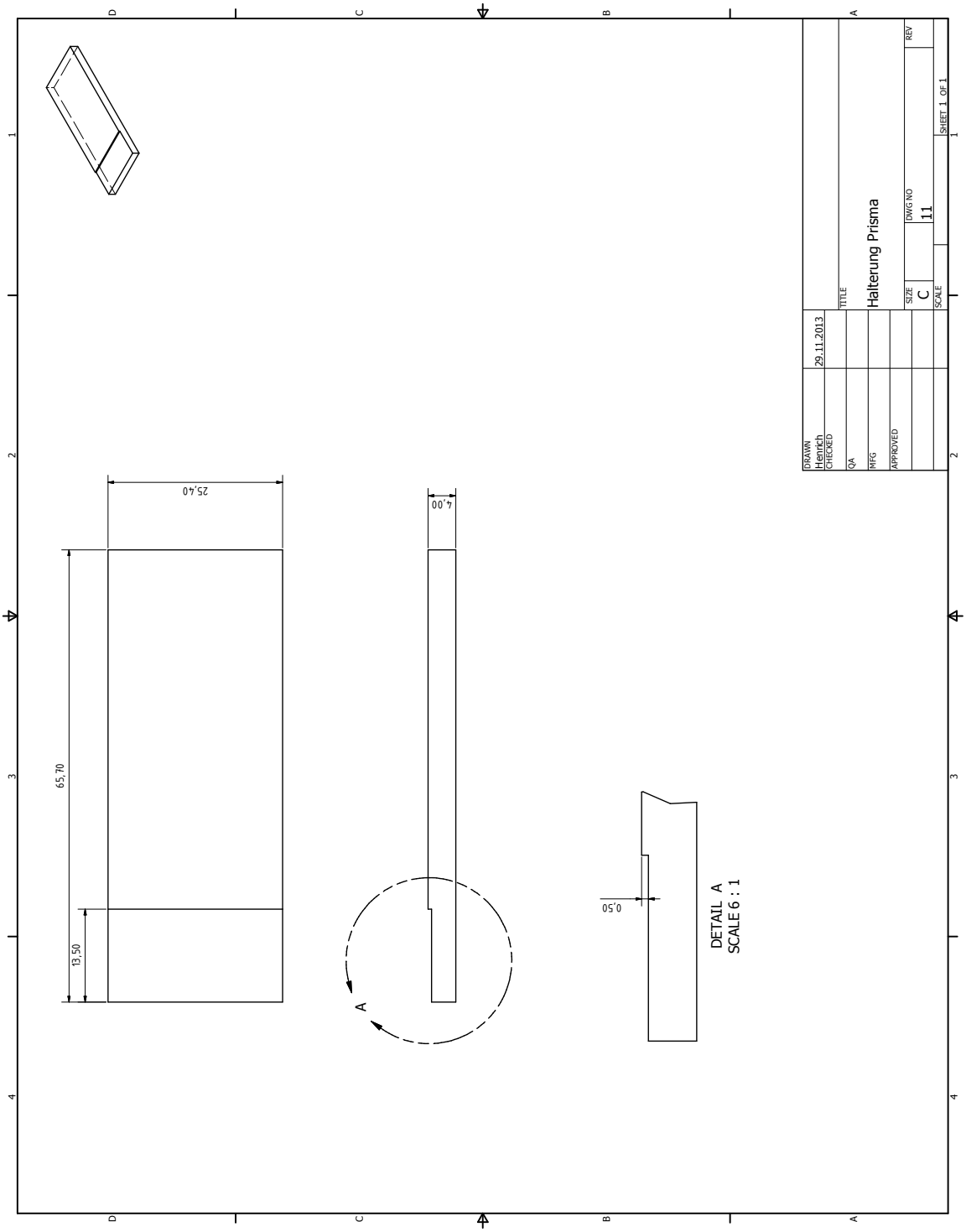

Figure A.35.: Technical drawing of prism holder.

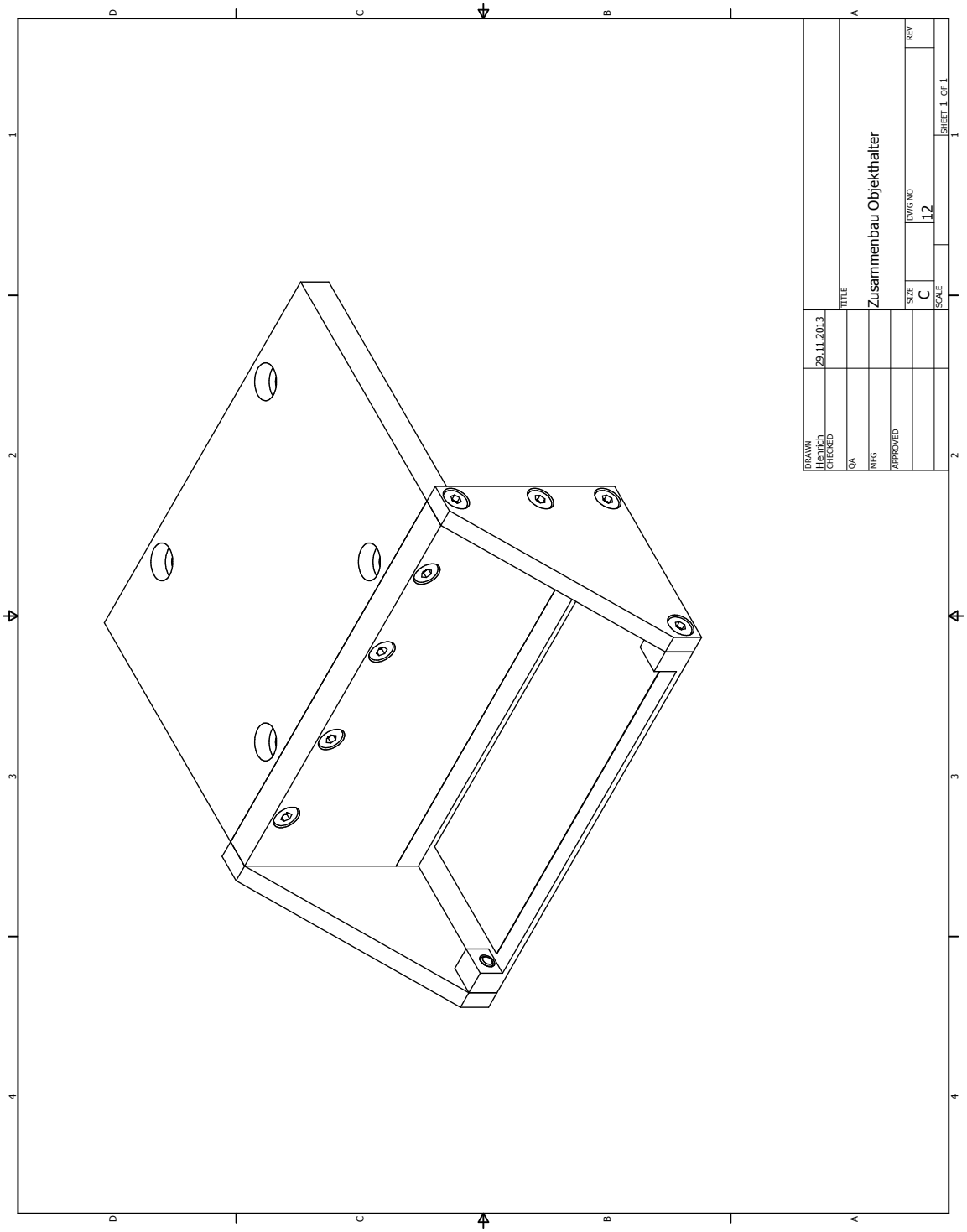

Figure A.36.: Technical drawing of the mounted glass slide extension.

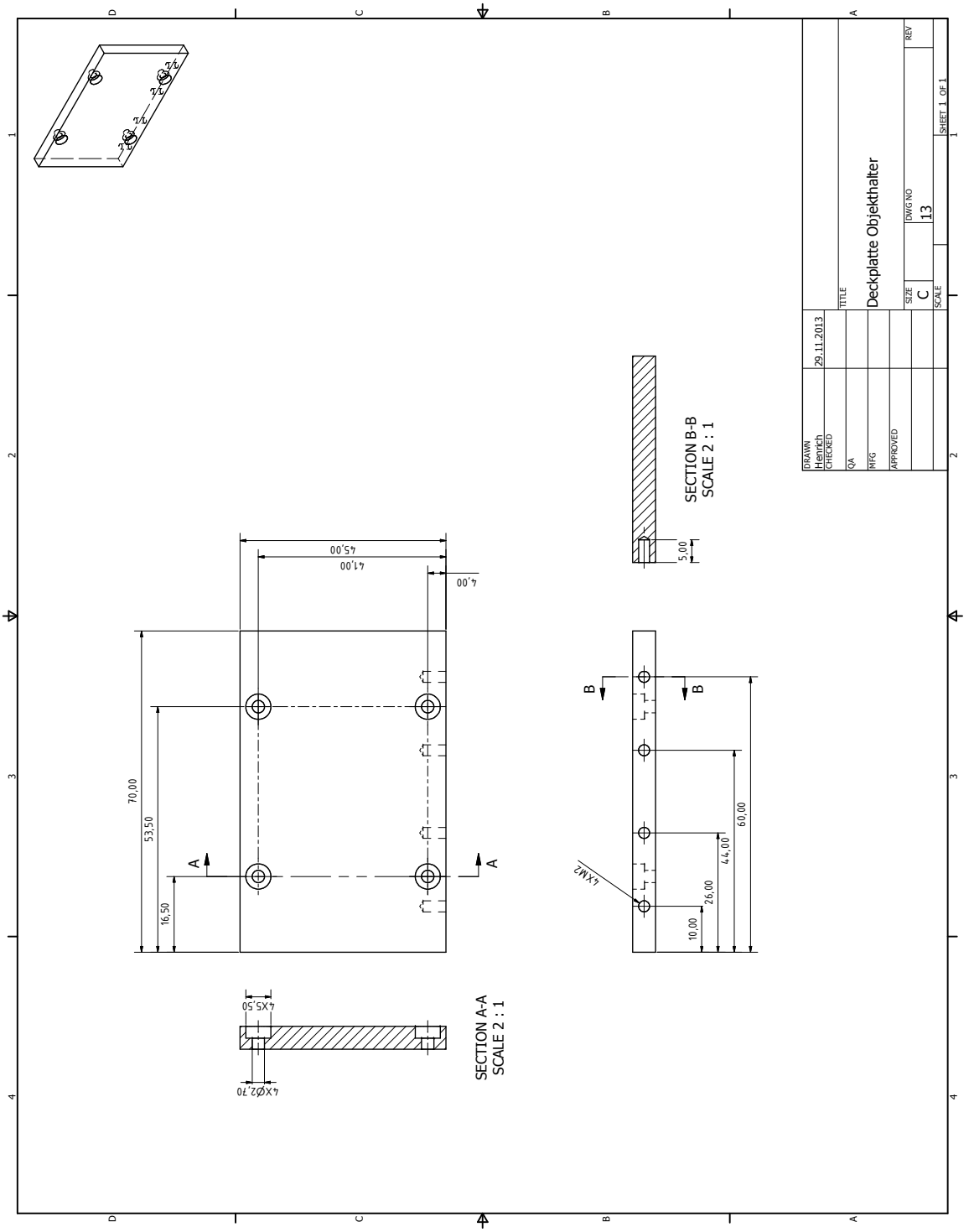

Figure A.37.: Technical drawing of the ground plate of the glass slide extension.

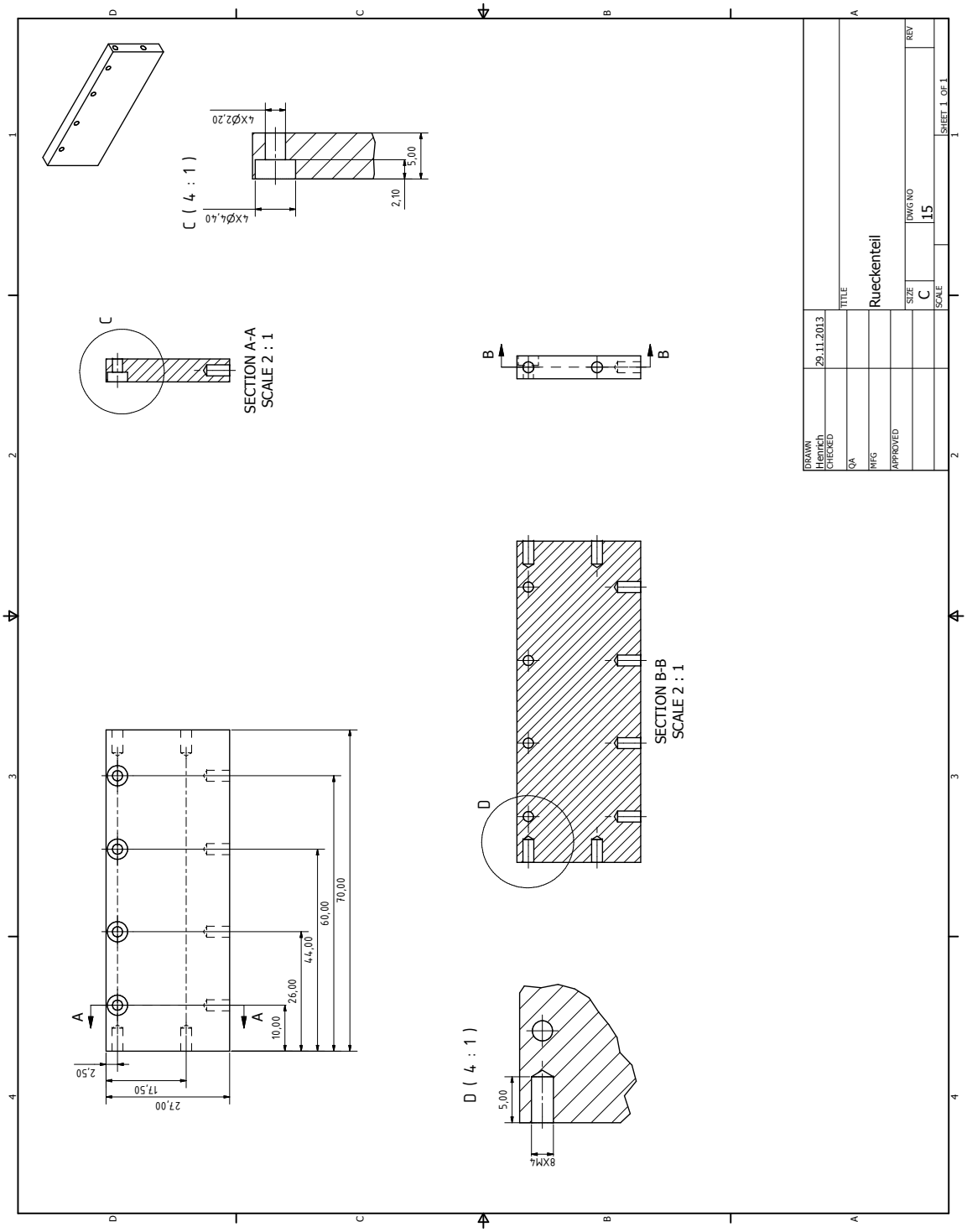

Figure A.38.: Technical drawing of the backside of the glass slide extension.

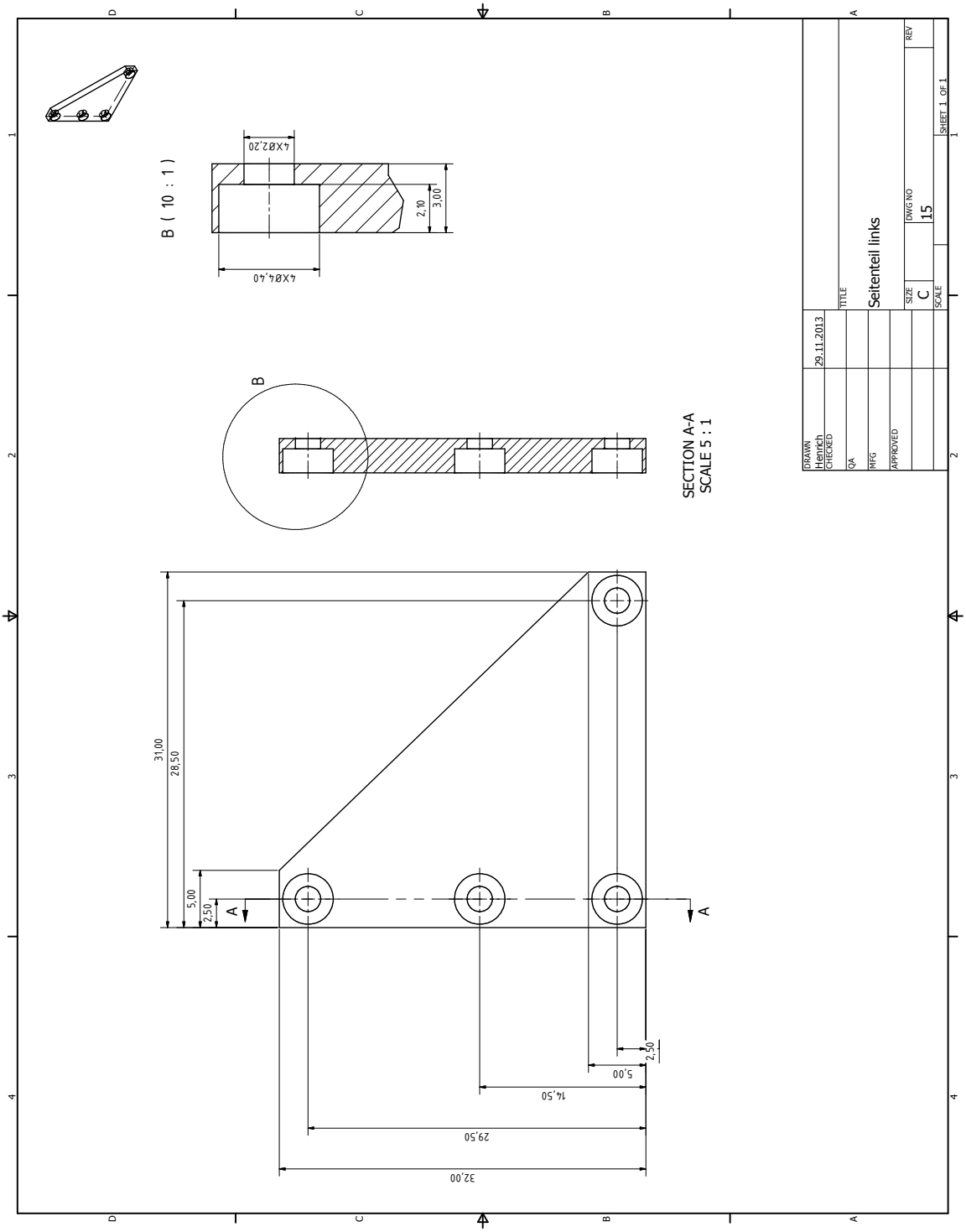

Figure A.39.: Technical drawing of the left side plate of the glass slide extension.

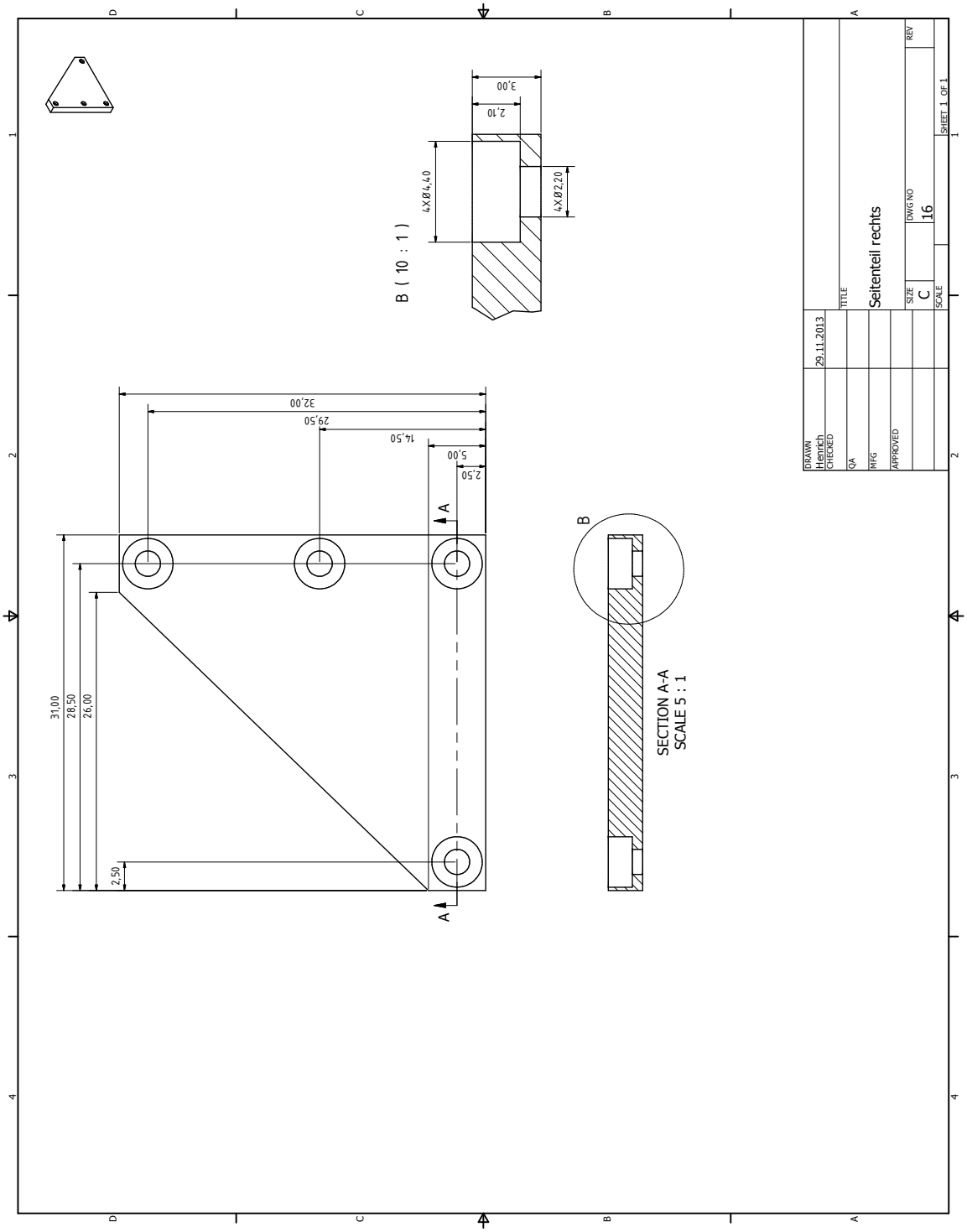

Figure A.40.: Technical drawing of the right side plate of the glass slide extension.

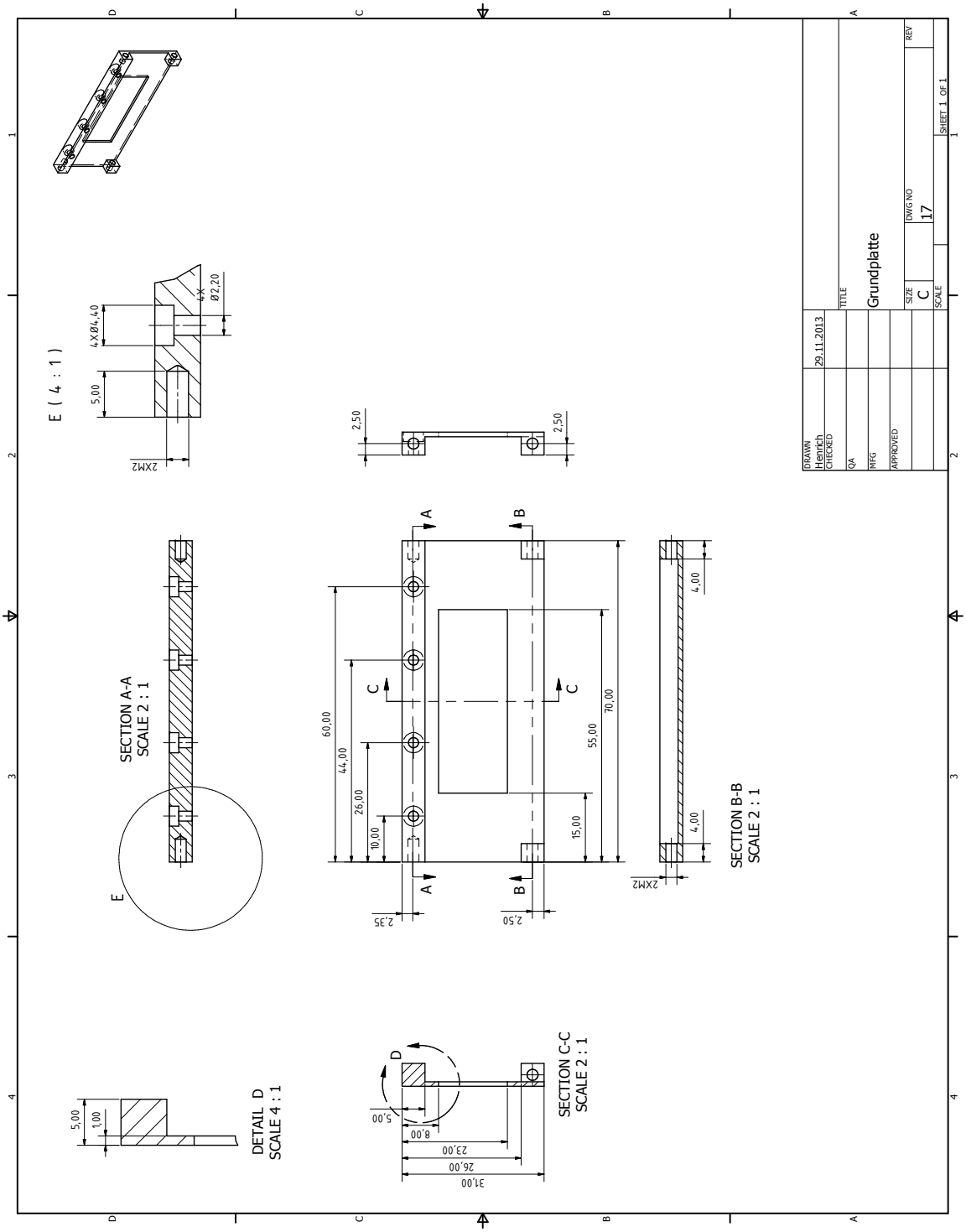

Figure A.41.: Technical drawing of the left bottom plate of the glass slide extension.

A.2 ImageJ macros

A.2.1 Macro for particle tracking

The following macro was used in section 6 to track the tracer particles in the moving liquid drop.

```
   tolerance = 50;
type = "Point Selection";
excludeEdgeMaxima = false;
lightBackground =false;
options = " ";
if (excludeEdgeMaxima) options = options + " exclude";
if (lightBackground) options = options + " light";
run("Clear Results");
for (n=1; n<=nSlices; n+) {
showProgress(n, nSlices);
setSlice(n);
run("Find Maxima...", "noise=&tolerance output=&type"+options);
counter = nResults();
if (selectionType<0) { setResult("px0", counter, -1);
setResult("py0", counter, -1);
} else { getSelectionCoordinates(x, y);
count = x.length;
if (count>25) exit("Too many maxima: "+count);
for (i=0; i<count; i++) {
setResult("px"+i, counter, x[i]);
setResult("py"+i, counter, y[i]);
}
}
}
updateResults;
run("Select None");
```

A.2.2 Macro for contact line detection

For detecting the three phase contact line the following macro was used.

```
  macro "Stack profile Plot" {
ymin = 0;
ymax = 255;
saveSettings();
if (nSlices==1)
exit("Stack required");
run("Profile Plot Options...",
"width=400 height=200 minimum="+ymin+" maximum="+ymax+" fixed");
setBatchMode(true);
stack1 = getImageID;
stack2 = 0;
n = nSlices;
for (i=1; i<n; i++) {
showProgress(i, n);
selectImage(stack1);
setSlice(i);
run("Plot Profile");
run("Copy");
w = getWidth; h = getHeight;
close();
if (stack2==0) {
newImage("Plots", "8-bit", w, h, 1);
stack2 = getImageID;
} else {
selectImage(stack2);
run("Add Slice");
}
run("Paste");
}
setSlice(1);
setBatchMode(false);
restoreSettings();
}
```